(This article was initially submitted to the UKMK 2016 (National Chemical Engineering Congress) and finally evaluated by the JOTCSB editorial staff).

Production of Bioadditive Ethyl Levulinate in the Catalytic Membrane Reactor

Derya Unlu[1,*], Nilufer Hilmioglu[1]

[1] Kocaeli University, Engineering Faculty, Chemical Engineering Department, Umuttepe, Kocaeli, 41380, Turkey

Abstract: Fuel bioadditive ethyl levulinate is the biofuel of the future. Reactants of ethyl levulinate are produced from biomass. Therefore, esterification of ethanol and levulinic acid is an environmentally friendly green process for the production of ethyl levulinate. In this study, synthesis of ethyl levulinate was carried out in the batch reactor and in the catalytic membrane reactor by using sulfated zirconia loaded catalytic membrane. Catalytic membrane reactor (CMR) has higher conversion values than the conventional batch reactor. Optimum operation conditions were specified as T=70°C, M=1:1, and C_{cat}=8 g/L. The levulinic acid conversion reached 36 % and 89% in the batch reactor (BR) and in the CMR, respectively.

Keywords: Bioadditive; Ethyl levulinate; Catalytic Membrane Reactor.

Submitted: September 15, 2016**. Revised:** October 05, 2016**. Accepted:** November 02, 2016**.**

Cite this: Ünlü D, Hilmioğlu N. Production of Bioadditive Ethyl Levulinate in the Catalytic Membrane Reactor. JOTCSB. 2017;1(1):1–12.

*Corresponding author. E-mail: derya.unlu@kocaeli.edu.tr.

INTRODUCTION

Global warming caused by greenhouse gases is known as one of the serious environmental problems in our age. As a result of the usage of fossil-derived fuels and also the reduction of the vegetation cover, the amount of carbon dioxide in the atmosphere has been increasing. Except for CO_2, during combustion of other gases occur, such as chlorofluorocarbons, hydrocarbons, methane, nitrous oxide (NO_x) and sulfur oxides (SO_x). This situation increases the effect of greenhouse gases. Greenhouse gases cause the global warming and climate change. Utilization of biofuels reduces the effect of greenhouse gas and acid rains. As an option of renewable fuel, while biodiesel and bioethanol have been used in the recent time, Fischer-Tropsch diesel-derived biomass and additives derived cellulosic biomass will be important in the medium term. Ethyl levulinate is an important bioadditive material. The use of ethyl levulinate as biofuel provides higher motor efficiency, long operation life, less carbon monoxide (CO) and NO_x emissions. Diesel engines have a high exhaust and NO_x emissions. Therefore, they have a negative effect to environment. The addition of oxygenates to fossil fuels is one of the most important methods to eliminate these problems. Levulinates are known as oxygenate additive. Ethyl levulinate has properties such as high flash temperature (low ignition temperature) and 33% oxygen content, clean combustion with high efficiency [1-4].

Levulinic acid and ethanol are used as the reactants for the ethyl levulinate production. Each reactant is biomass-based. While levulinic acid is obtained by the acidic hydrolysis of cellulose, ethanol can be produced from biological and waste sources such as sugars, starch, cereal grains, and agricultural and wood residues. The use of biomass based reactants for ethyl levulinate production makes the process the environmentally friendly green production process [5].

Reaction products of ethanol and levulinic acid are ethyl levulinate and water. For the usage of ethyl levulinate as fuel additive, ethyl levulinate must be obtained as pure. Distillation, which is one of the conventional separation methods, is used for the purification in literature researches. Distillation is quite a costly process to obtain a pure product. In this situation, new separation processes are investigated by researchers. Membrane reactor is one of the developing membrane separation process and it is used for obtaining pure products economically [6].

Production of ethyl levulinate occurs in the presence of homogeneous or heterogeneous catalysts.

For overcoming the equilibrium limit, excess amount of limiting reactant is used or by-products are removed by conventional methods such as reactive distillation and reactive stripping. The utilization of excess reactant increases the operating costs and results in the formation of undesired by-products. Reactive distillation is not suitable for azeotropic liquids. The use of membrane reactor is more attractive at this point, because the processing cost reduces by the minor amount of reactants and high conversions are obtained too [7].

The system, which uses a catalytic membrane, is called as the catalytic membrane reactor (CMR). CMR integrates the reaction and separation into one single unit. Catalytic membranes are used in this process. Reaction is carried out on the catalytic layer of the membrane and reaction products are obtained. As a result of the reaction, the formed product is selectively removed through the membrane. The continuous removal of selective product from the reaction mixture shifts the reaction equilibrium to the product side. Therefore, it facilitates the enhancement of reaction conversion [8-9].

In this study, catalytic membranes, which had catalytic and separation properties, were prepared. The purpose of the combination of the catalyst and membrane is to make the reaction in one step. Hydrophilic biodegradable polymer hydroxyethyl cellulose was used in this study [10]. Sulfated zirconium oxide (SO_4^{2-}/ZrO_2) is used as a catalyst. SO_4^{2-}/ZrO_2 was chosen for the esterification reactions due to their acidic properties. High conversion values were obtained while SO_4^{2-}/ZrO_2 was used in similar esterification reactions. SO_4^{2-}/ZrO_2 has a problem as leaching. This situation caused the catalytic activity loss. Therefore, catalyst was embedded into the polymeric membranes as an alternative. In this case, recovery of the catalytic membrane and reuse were easy and practical. Also, leaching problems were prevented when the SO_4^{2-}/ZrO_2 catalytic membranes were utilized. The effects of reaction parameters such as temperature, catalyst concentration, and the molar feed ratio on conversion were examined.

MATERIALS AND METHODS

Chemicals

Hydroxyethyl cellulose polymer and ethanol, levulinic acid, isopropanol, sodium hydroxide, and phosphoric acid were obtained from Sigma Aldrich and Merck.

Experimental procedure

Preparation of catalytic composite membrane: The catalytic composite membrane was prepared by the solution casting method. The composite membrane consisted of catalytic layer and separation layer. The aqueous HEC polymeric membrane solution was first prepared for the separation layer. The polymeric membrane solution was mixed for 24 hours at room temperature. Then, the solution was poured on PMMA surface. After one day, diluted polymeric membrane solution was prepared by the addition of 2, 5 and 8 g/L of catalyst SO_4^{2-}/ZrO_2. The prepared catalytic polymer solution was poured onto the separation HEC layer. After drying, membrane was immersed in isopropanol-water and phosphoric acid solution for crosslinking. Finally, the membrane was washed with pure water and dried in the oven [11-12]. The pristine and catalytic composite membrane were characterized by Scanning Electron Microscopy.

Esterification reaction

The esterification reaction of ethanol with levulinic acid was carried out by using catalytic membrane as catalyst under the various conditions. The experiments of batch reactor were performed in a 100 mL round-bottom flask fitted with a reflux condenser, magnetic stirrer and thermometer. The prepared catalytic membrane was cut into small pieces and added in the batch reactor. Scheme of the batch reactor was shown in Figure 1.

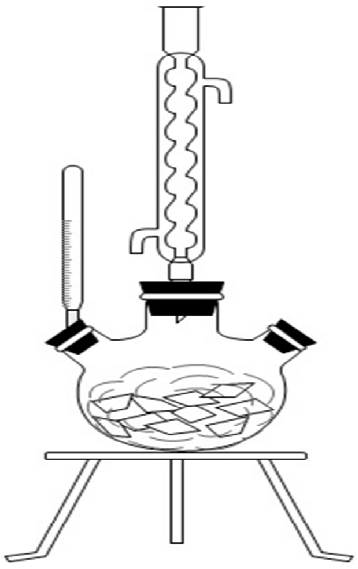

Figure 1. Batch reactor.

Levulinic acid conversion values are calculated by the titration with NaOH. Conversion values were calculated by using the following Equation (1).

$$x = \frac{N_{Ao} - N_A}{N_{Ao}} \qquad \text{(Eq. 1)}$$

In this equation, N_{Ao} is the number of moles of levulinic acid at t = 0, N_A is the number of moles of levulinic acid at any of the time of the reaction [13].

The esterification reaction of levulinic acid and ethanol was conducted in the catalytic membrane reactor by using SO_4^{2-}/ZrO_2 loaded catalytic composite membrane. Reactants were fed into the membrane cell. The reaction occured in the catalytic layer of the membrane. Reactants are converted to products by the reaction. According to affinity of the membrane, one of the products was removed through the membrane. Figure 2 shows the CMR process.

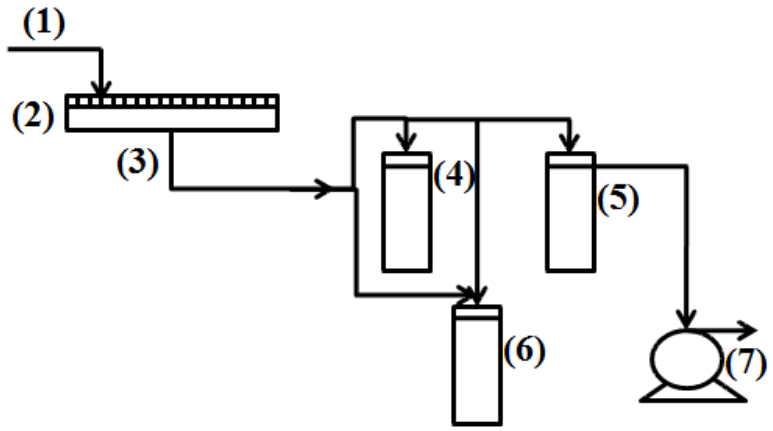

Figure 2. CMR process (1) Feed (2) Catalytic membrane (3) Permeate (4), (5), (6) Cold trap (7) Vacuum pump.

Levulinic acid conversion values were determined by titration and GC analysis. Obtained conversion values were compared with batch reactors and efficiency of CMR for increment of conversion was exhibited.

RESULTS AND DISCUSSION

Membrane Characterization by SEM

The surface and cross-section images of the catalytic composite membrane were viewed by SEM. Figure 3 shows pristine membrane surface (a), catalytic membrane surface (b), pristine membrane cross-section (c) and catalytic membrane cross-section (d), respectively.

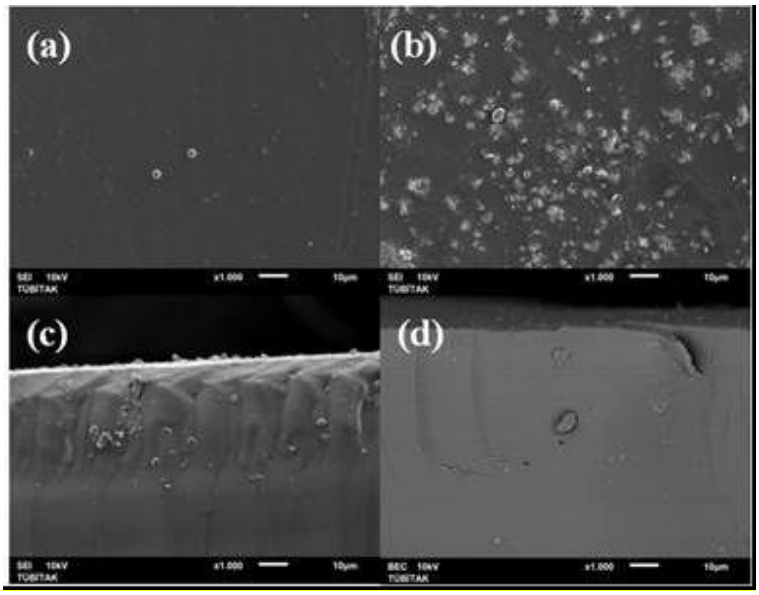

Figure 3. SEM images of the pristine and catalytic membrane: (a) pristine membrane surface and (b) catalytic membrane surface (c) pristine membrane cross-section (d) catalytic membrane cross-section.

As shown in Figure 3(a) the pristine HEC membrane has a homogeneous surface. In Figure 3(b) catalysts of SO_4^{2-}/ZrO_2 are dispersed on the catalytic layer of the composite membrane. Fig. 3(c) shows the cross-section of pristine membrane. It has only a single layer. Cross section image of catalytic composite membrane is shown in Figure 3(d). It was observed in Figure 3(d), catalytic composite membrane has two layers: catalytic layer and separation layer. Also, the compatibility of the separation layer and catalytic layer can be seen in Figure 3(d).

Effect of the temperature on levulinic acid conversions in the batch reactor and in the CMR

Experiments of CMR and BR were realized by using 8 g/L of SO_4^{2-}/ZrO_2 loaded catalytic membrane with equimolar condition (M=1) at temperature of 50 °C, 60 °C, and 70 °C. The effect of the temperature on levulinic acid conversion was shown in Figure 4.

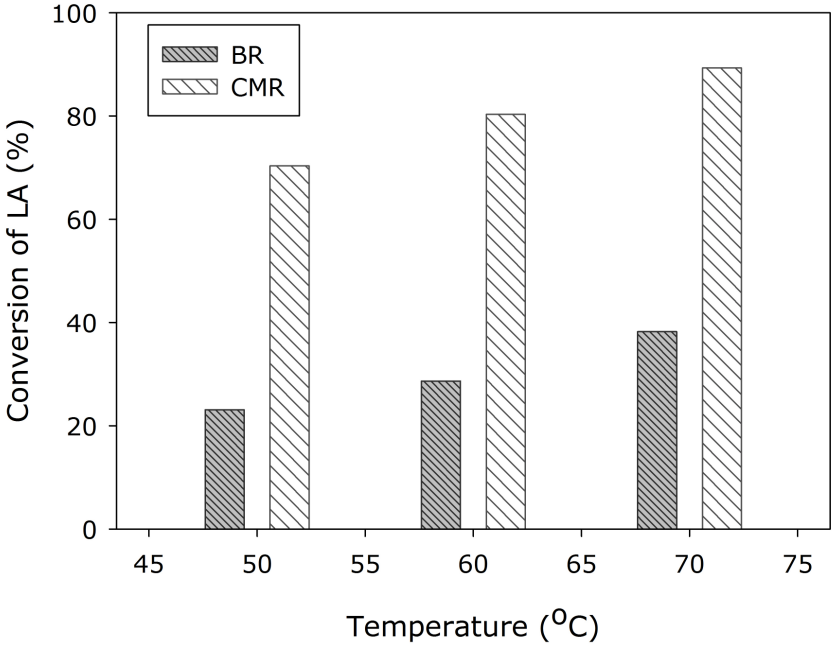

Figure 4. Effect of the temperature on conversion (8 g/L catalyst loaded membrane, M=1).

Conversion was increased by temperature in both BR and CMR. However, conversion of CMR was higher than conversion of BR. In CMR, water, which occurred from the result of the reaction, was removed from the reaction medium. Therefore, reaction equilibrium shifted toward the products. Thermal mobility of the polymer chains increased with increasing temperature. This situation created free volume in the membrane matrix. Transport of selected components increased through the membrane. Thus, by removing the water had improved the conversion [14-16].

After 7 hours, the highest conversion was obtained as 38% at 70 °C in the batch reactor. Under the same reaction conditions, the highest conversion was obtained as 89% in the CMR [17].

Effect of the catalyst concentration on levulinic acid conversions in the batch reactor and in the CMR

Different ratios of SO_4^{2-}/ZrO_2 loaded catalytic membranes were prepared and experiments were performed by using equimolar reactant (M=1) at 70 °C. Figure 5 shows the change of levulinic acid conversion values in the different catalyst loading amounts.

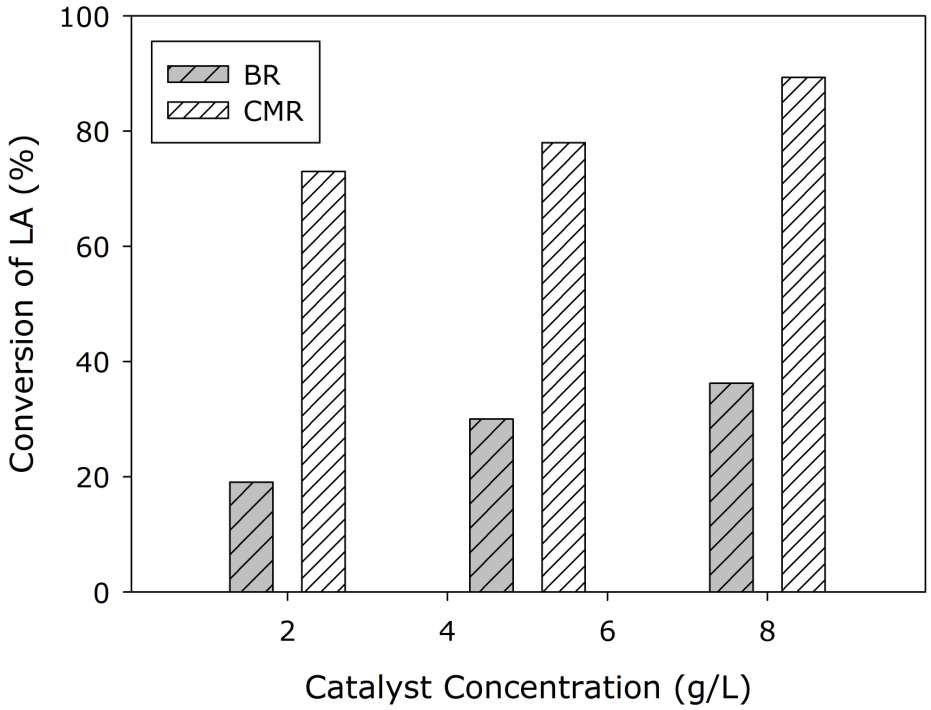

Figure 5. Effect of the catalyst concentration on conversion (70°C, M=1).

Levulinic acid conversion increased with increasing catalyst concentration. Higher conversion was obtained in the CMR in the first hours of reaction. The increase in catalyst concentration of the membrane provided the intense catalyst distribution on the membrane surface and the reactants could be reached easily active site of the catalyst [18-20]. Conversions obtained in the CMR was higher than in the BR. While the 36% of conversion was obtained by 8 g/L SO_4^{2-}/ZrO_2 catalyst loaded membrane for 7 hours in the batch reactor, 89% of conversion was obtained under the same reaction conditions in the CMR [17].

Effect of the molar feed ratio of alcohol to acid on levulinic acid conversions in the batch reactor and in the CMR

BR and CMR experiments were carried out by using 8 g/L SO_4^{2-}/ZrO_2 catalyst loaded HEC catalytic membrane at 70°C, different alcohol/acid molar feed ratios. Figure 6 shows the change of conversion of levulinic acid with molar feed ratio.

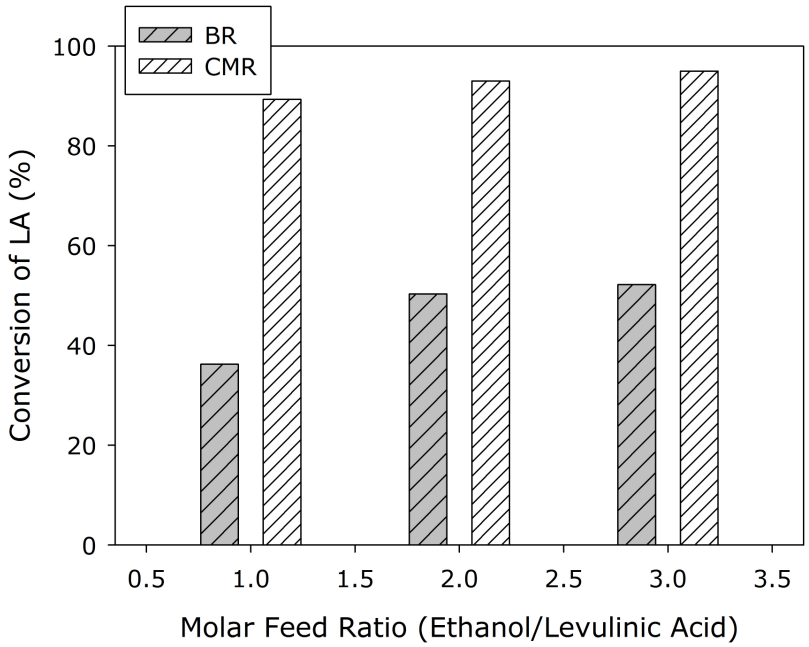

Figure 6. Effect of molar feed ratio on conversion (8 g/L catalyst loaded membrane, T=70 °C).

Conversions obtained in the CMR were higher than in the BR, because the water was removed through the membrane continuously and equilibrium was shifted towards the products. While the conversion was obtained as 52% at M=3 for 7 h in the batch reactor, conversion was obtained as 95% in the CMR under the same reaction conditions [17].

Levulinic acid conversion was increased by the molar feed ratio. One of the ways for increasing the conversion is usage of excess reactant. According to Le Châtelier's principle, the utilization of excess reactant changes the reaction equilibrium towards the product. Therefore, conversion increases. Besides, the usage of excess reactant increases the possibility of contact of all reactants, levulinic acid conversion increases [3 , 21]. However, the aim of the CMR was increasing the conversion by the removal of one of products, therefore (M=1) was chosen as an appropriate value.

CONCLUSIONS

In this study, the esterification reaction was performed by the catalytic membrane in both BR and CMR. Compared to BR, higher conversion was obtained in CMR. Because reaction equilibrium was changed towards the product by removal of byproduct water and so conversion was increased. Results of experimental studies show that the CMR is a suitable method for the synthesis of ethyl levulinate.

ACKNOWLEDGMENTS

The authors gratefully acknowledge the financial support from The Scientific and Technological Research Council of Turkey, TÜBİTAK (Project No. 114M147) and Kocaeli University Scientific Research Projects Unit (Project No. 2014/076).

REFERENCES

1. Wang Z, Lei T, Liu L, Zhu J, He X, Li Z. Performance Investigations Of A Diesel Engine Using EthylLevulinate-Diesel Blends. BioResources. 2012;7(4):5972-5982. URL: http://ojs.cnr.ncsu.edu/index.php/BioRes/article/view/BioRes_07_4_5972_Wang_Diesel_Engine_Performance .

2. Kashinath S, Manan Z, Hashim H, Alwi S. Design of green diesel from biofuels using computer aided technique. Computers & Chemical Engineering. 2012 June;41:88–92, DOI: 10.1016/j.compchemeng.2012.03.006.

3. Nandiwale K, Sonar S, Niphadkar P, Joshi P, Deshpande S, Patil V, Bokade V. Catalytic upgrading of renewable levulinic acid to ethyl levulinate biodiesel using dodecatungstophosphoricacid supported on desilicated H-ZSM-5 as catalyst. Applied Catalysis A: General. 2013 June;460–461:90–98, DOI: 10.1016/j.apcata.2013.04.024.

4. Nandiwale K, Niphadkar P, Deshpande S, Bokade V. Esterification of renewable levulinic acid to ethyl levulinate biodiesel catalyzed by highly active and reusable desilicated H-ZSM-5. Journal of Chemical Technology and Biotechnology. 2014 October; 89:1507-1515. DOI: 10.1002/jctb.4228.

5. Fernandes DR, Rocha AS, Mai EF, Mota JA, Silva V. Levulinic acid esterification with ethanol to ethyl levulinate production over solid acid catalysts. Applied Catalysis A: General. 2012 May;425–426:199–204, DOI: 10.1016/j.apcata.2012.03.020.

6. Smitha B, Suhanya D, Sridhar S, Ramakrishna M. Separation of organic–organic mixtures by pervaporation a review. Journal of Membrane Science. 2004 September;241:1-21 DOI: 10.1016/j.memsci.2004.03.042.

7. Khajavi S, Jansen JC, Kapteijn F. Application of a sodalite membrane reactor in esterification-Coupling reaction and separation. Catalysis Today. 2010 October;156:132–139. DOI: 10.1016/j.cattod.2010.02.042.

8. Ceia, T.F., Silva, A.G., Ribeiro, C.S., Pinto, J.V., Casimiro, M.H., Ramos, A.M., Vital, J., 2014. PVA composite catalytic membranes for hyacinth flavour synthesis in a pervaporation membrane reactor. Catal. Today. 236, 98-107. DOI: 10.1016/j.cattod.2014.02.052.

9. Zhang, W., Qing, W., Chen, N., Ren, Z., Chen, J., Sun, W., 2014. Enhancement of esterification conversion using novel composite catalytically active pervaporation membranes. J. Memb. Sci. 451, 285-292. DOI: 10.1016/j.memsci.2013.10.001.

10. Peters TA. Catalytic pervaporation membranes for close integration of reaction and separation, PhdThesis, Technische Universiteit Eindhoven, Eindhoven, 2006. URL: https://pure.tue.nl/ws/files/2367271/200610481.pdf.

11. Sridhar S, Ganga D, Smitha B, Ramakrishna M. Dehydration of 2-Butanol by Pervaporation Through Blend Membranes of Chitosan and Hydroxy Ethyl Cellulose. Separation Science and Technology. 2007 Feb; 40:2889-2908. DOI: 10.1080/01496390500333186 .

12. Kalyani S, Smitha B, Sridhar S, Krishnaiah A. Blend membranes of sodium alginate and hydroxyethyl cellulose for pervaporation-based enrichment of t- butyl alcohol. Carbohydrate Polymers. 2006 May;64:425–432. DOI: 10.1016/j.carbpol.2005.12.012.

13. Liu QL, Chen HF. Modeling of esterification of acetic acid with n-butanol in the presence of $Zr(SO_4)^{2-}.4H_2O$ coupled pervaporation. Journal of Membrane Science. 2002 Feb;196:171-178. DOI: 10.1016/S0376-7388(01)00543-9.

14. Wasewar K, Patidar S, Agarwal VK. Esterification of lactic acid with ethanol in a pervaporation reactor: modeling and performance study. Desalination. 2009 July; 243:305–313. DOI: 10.1016/j.desal.2008.04.030.

15. Delgado P, Sanz MT, Beltran S. Pervaporation of the quaternary mixture present during the esterification of lactic acid with ethanol. Journal of Membrane Science. 2009 April; 332:113–120. DOI: 10.1016/j.memsci.2009.01.044.

16. Veerapur SK, Gudasi KB, Sairam M, Shenoy RV, Netaji M, Raju KVSN, Sreedhar B, Aminabhavi TM. Novel sodium alginate composite membranes prepared by incorporating cobalt(III) complex particles used in pervaporation separation of water–acetic acid mixtures. Journal of Materials Science. 2007 June; 42: 4406–4417. DOI: 10.1007/s10853-006-0652-0.

17. Unlu D, Ilgen O, Hilmioglu ND. Biodiesel additive ethyl levulinate synthesis by catalytic membrane: SO_4^{-2}/ZrO_2 loaded hydroxyethyl cellulose. Chemical Engineering Journal. 2016 October; 302:260–268. DOI: 10.1016/j.cej.2016.05.047.

18. Alhassan FH, Rashid U, Yunus R, Sirat K, Lokman IM, Taufiq-Yap YH. Synthesis of Ferric–Manganese Doped Tungstated Zirconia Nanoparticles as Heterogeneous Solid Superacid Catalyst for Biodiesel Production From Waste Cooking Oil. International Journal of Green Energy. 2015 Jan;12:987−994. DOI: 10.1080/15435075.2014.880843.

19. Jiang Y, Lu J, Sun K, Ma L, Ding J. Esterification of oleic acid with ethanol catalyzed by sulfonated cation exchange resin: Experimental and kinetic studies. Energy Conversion and Management. 2013 December; 76:980−985. DOI: 10.1016/j.enconman.2013.08.011.

20. Ma J, Zhang M, Lu L, Yin X, Chen J, Jiang Z. Intensifying esterification reaction between lactic acid and ethanol by pervaporation dehydration using chitosan–TEOS hybrid membranes. Chemical Engineering Journal. 2009 December; 155:800–809. DOI: 10.1016/j.cej.2009.07.044.

21. Çimenler Ü, Investıgatıon of the esterıfıcatıon reactıon for the productıon of butyl propionate in pervaporation membrane reactor using Amberlite Ir-120 catalyst, Master Thesis, Yıldız Technical University, Graduate School of Natural and Applied Sciences, İstanbul, 2011. DOI: https://tez.yok.gov.tr/UlusalTezMerkezi/.

Türkçe Öz ve Anahtar Kelimeler

Katalitik Membran Reaktörde Biyokatkı Maddesi olan Etil Levulinatın Üretimi

Derya Unlu, Nilufer Hilmioglu

Öz: Yakıt katkı maddesi olan etil levulinat geleceğin biyoyakıtıdır. Etil levulinatı oluşturacak reaktifler biyokütleden üretilmektedir. Bu sebeple, etanol ve levulinik asidin esterleştirilmesi, etil levulinatın üretimi için çevreyle dost ve yeşil bir süreç olarak karşımıza çıkmaktadır. Bu çalışmada, etil levulinatın sentezi kesikli ve katalitik membran reaktörde yapılmıştır ve katalitik membran olarak sülfatlı zirkonya yüklenmiş membran kullanılmıştır. Katalitik membran reaktör (CMR) geleneksel kesikli reaktörden daha yüksek dönüşüm değerleri vermiştir. En uygun operasyon koşulları T=70°C, M=1:1, and C_{cat}=8 g/L olarak tespit edilmiştir. Levulinik asit dönüşümü kesikli reaktörde (BR) %36 ve CMR'de %89 olarak elde edilmiştir.

Anahtar kelimeler: Biyokatkı maddesi; etil levulinat; katalitik membran reaktörü.

Gönderme: 15 Eylül 2016**. Düzeltme**: 05 Ekim 2016**. Kabul:** 02 Kasım 2016**.**

(This article was initially submitted to the UKMK 2016 (National Chemical Engineering Congress) and finally evaluated by the JOTCSB editorial staff)

Effects of Material Characteristics on the Performance of Hydrocracking Catalysts

Melek Bardakcı Türkmen[1]*, Burcu Yüzüak[1], Deniz Onay Atmaca[1], Ayşegül Bayat[1], Volkan Balci[1], Seçil Ünsal[2], Can Erkey[2] and Ersen Ertaş[1]

[1]Turkish Petroleum Refineries Corporation, R&D, Kocaeli, Turkey
[2]Koc University, Chemical and Biological Engineering Department, İstanbul, Turkey

Abstract: Hydrocracking is a refinery process used to convert heavy hydrocarbon fractions to lighter cuts with high added value. The products that usually range from heavy diesel to light naphtha involving middle distillate as targeted cut are obtained as a result of hydrocracking process of feeding with higher molecular weights and lower hydrogen/carbon ratios. Hydrocracking reactions occur under high hydrogen partial pressures and temperatures in the presence of catalyst in order to remove impurities such as sulfur compounds and crack heavy hydrocarbon molecules to high added value lighter cuts. Hydrocracking catalysts are bifunctional in which metal function with hydrogenation consisting group VIB or group VIIIB is for removal of impurities and acidic support consisting amorphous oxides and/or crystalline zeolites to realize cracking function. In this study, the association between the performance test results obtained from laboratory scale reactor system and the material characteristics of the catalysts are viewed. Selectivity, hydrocracking, and hydrogenation activities within the performance parameters of the catalysts are calculated based on the fraction ratios and feed-product properties. Furthermore, the effect of hydro-treating activity on hydrocracking activity is also highlighted. The surface area and pore size, crystallinity, chemical composition of the material and acidic properties are investigated within the scope of material characteristics of the catalysts by using BET, XRD, XRF, NH_3-TPD techniques, respectively.

Keywords: Hydrocracking; catalyst; characterization; structure-performance relationship.

Submitted: September 02, 2016. **Revised:** October 06, 2016. **Accepted:** November 02, 2016.

Cite this: Bardakcı Türkmen B, Yüzüak B, Atmaca D, Bayat A, Balcı V, Ünsal S, et al. Effects of Material Characteristics on the Performance of Hydrocracking Catalysts. JOTCSB. 2017;1(1):13–24.

*Corresponding author. E-mail: melek.bardakciturkmen@tupras.com.tr.

INTRODUCTION

Hydrocracking is a refining technology within the scope of hydro-processing which is used for the conversion of a variety of feedstocks to a range of products by adding hydrogen, removing impurities in the presence of catalyst. Hydrocracking technology for conversion of coal to liquid fuels was developed in Germany as early as 1915. The forerunner of the hydrocracking is Bergius process which may be considered as the first commercial plant and brought on stream in Germany in 1927 for hydrogenation of distillates derived brown coal (1,2). During World War II, hydrocracking processes played an important role in producing aviation gasoline. Nevertheless, after World War II, the emergent availability of Middle Eastern crude removed the incentive to convert coal to liquid fuels which caused the development of hydrocracking technology to become less important as newly developed fluid catalytic cracking processes were much more economical than hydrocracking for converting high-boiling petroleum oils to fuels. In the mid-1950s, manufacturing of high performance cars with high-compression ratio engines of the automobile industry required high-octane gasoline, where the switch of railroads from steam to diesel engines and the introduction of commercial jet aircraft in the late 1950s increased the demand for diesel fuel and jet fuel (1). Thus in the early 1960s, with the increasing demand for gasoline, diesel, and jet fuel, by-product hydrogen at low cost and in large amounts from catalytic reforming operations and environmental concerns limiting sulfur and aromatic compound concentrations, hydrocracking technology gained importance again. Moreover, in 1958, the first modern distillate hydrocracker had been put into commercial operation by Standard Oil of California (now Chevron). It grew in other parts of the world, starting in the 1970s primarily for the production of middle distillates, while hydrocracking was used in the United States primarily in the production of high-octane gasoline (1-3).

Hydrocracking reactions proceed through a bifunctional mechanism which is one that requires two distinct types of catalytic sites. These two functions to catalyze separate steps in the reactions are the acidic function, which provides for the cracking and isomerization and the metallic function which provides for the olefin formation and hydrogenation. The number and strength of the acid sites of the acidic supports consisting of amorphous oxides and/or crystalline zeolite plus binder, or a mixture of them, designate the acidic characteristics and thus the cracking function of the catalyst. The metals providing metal function consisting of noble metal or base metal sulfides from groups VIA and VIIIA, make the feedstock more reactive for cracking and heteroatom removal (4-6). In some studies, organic acids are reported to be used as modifying agents of supports that enhance activity and stability of the catalyst improving secondary pore volume, crystallinity, and silica–alumina ratio (7-10). Some studies are also related with uniformity of alumina–silica

dispersion to inhibit the molecular sieve agglomeration or channel blocking (11). Nevertheless, strength, ratio, balance, and distance of the acid and hydrogenation functions of the bifunctional catalyst are also important with regard to catalytic performance. For instance, a catalyst with a strong hydrogenation and a weak acidic function has low activity but good selectivity for middle distillates and requires low severe operating condition (12). Overall, the activity and selectivity within the relevant activities indicate the performance of the catalyst.

The selection of the hydrocracking catalyst concerning commercial units is a crucial step in terms of its performance, cost, and required operational conditions. The characteristics of the materials in terms of acidity, composition, surface area, pore structure, *etc*. strongly influence the hydrogenation and cracking activities of the catalyst as known from the literature. Therefore in this study, the association of the material characteristics and the performance of the relevant catalysts are viewed to investigate the consideration of the material characteristics for the selection of the hydrocracking catalyst in the future. The material characteristics of the catalysts are analyzed by several instrumental analysis methods using BET, XRD, XRF, NH_3-TPD techniques where the performance of the catalysts is calculated based on the laboratory scale test results. Furthermore in this study, the effect of hydro-treating activity on hydrocracking activity is also highlighted for revealing that the higher hydro-treating activity causes hydrocracking activity to enhance hydrocracking reactions.

MATERIALS AND METHODS

Chemicals

Three fresh, Ni-W-based hydrocracking catalysts coded as C(F), D(F), E(F) were selected for all performance tests and characterization.

Apparatus

All surface area and pore size measurements were carried out through BET (Brunauer–Emmett–Teller) technique with Micromeritics Asap 2020 N_2 Adsorption-Desorption. The crystal properties were investigated by XRD (X-ray Diffraction) analysis with Bruker – D8 Advanced. The chemical compositions of the material were carried out by XRF (X-ray Fluorescence) technique with Bruker – Tiger 8S and the acidic properties were characterized by NH_3-TPD (Temperature Programmed Desorption) analysis through Micromeritics Chemisorp 2750. The performance tests of the

catalysts were carried out in a laboratory scale reactor system, Parr 5402C providing a down flow continuous trickle bed operation in an isothermal mode by independent temperature control of three zone electric furnace (Figure 1). The distillation data of VGO (Vacuum Gas Oil) as feed and TLP (Total Liquid Product) which indicated hydrocracking activity of the catalysts were obtained through GC (Gas Chromatography) technique by AC Analytical Controls Simulated Distillation Analyzer on Agilent 7890. The sulfur & nitrogen content of the feed and the TLP which represented hydrotreating activity of the catalysts were analyzed by using Antek MultiTek N-S 115V/230V.

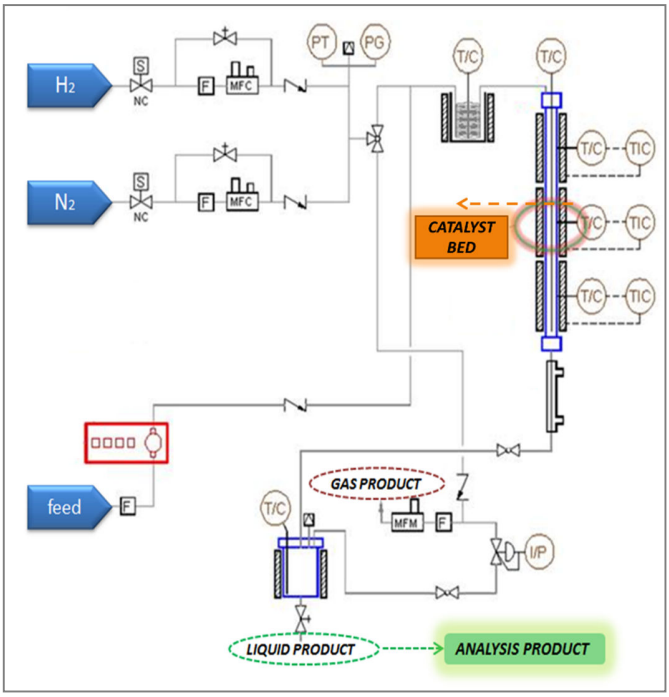

Figure 1. Schematic diagram of laboratory-scale reactor system.

Experimental procedure

The material characteristics of the catalysts were analyzed in terms of surface area and pore size by using BET (ASTM 3663, 4222, 4641, 4365), crystallinity by using XRD spectra with measurement range between 2θ degrees of 10-90°, chemical composition by XRF analysis and acidic properties by NH_3-TPD analysis, respectively.

Process parameters that play an important role in the operation of the hydrocracking unit are reactor temperature, LHSV (Liquid Hourly Space Velocity), operating pressure and H_2/oil ratio. These operating conditions held constant during the performance tests to avoid the effect of process parameters on the performance of the catalysts. The experiments of the performance

tests were performed at a temperature of 380°C, a pressure of 120 bar, a LHSV of 1.14, a H_2 flow rate of 400 mL/min and a feed flow rate of 0.33 mL/min over 17.54 mL of catalyst through a laboratory scale reactor system. Initially the hydrogen flow was set at a required level that has been calculated from LHSV and H_2/oil ratio of the commercial hydrocracker unit. The amounts of the catalysts were calculated according to the LHSV values and determined based on bulk densities of each catalyst. The catalysts are loaded to the reactor by mixing with an equal volume of SiC (Silicon carbide) to ensure homogeneous flow distribution and catalyst wetting through reactor during performance tests. The pressure of the reactor is controlled by a BPR (Back Pressure Controller) located at the gas outlet of high pressure separator.

At the end of the performance tests, the liquid and gas samples were collected for analysis of GC and product properties. Therefore, hydrocracking activity and selectivity of the catalysts were calculated as based on the distillation data of the feed and the TLP. The hydro-treating activity of the catalysts was also determined according to the total sulfur & nitrogen content of the feed and the TLP.

The surface area and the pore size are shown in Figure 2 revealing that the catalyst D (F) has the highest surface area with 270.2 m^2/g but the lowest total pore volume with 0.368 cm^3/g. The lowest surface area belongs to the catalyst C (F) having a higher total pore volume of 0.404 cm^3/g.

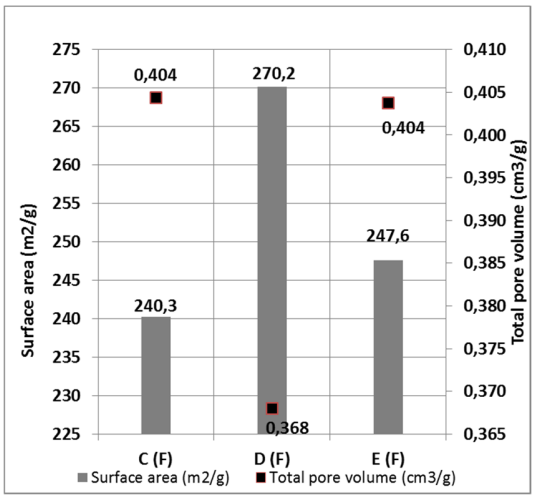

Figure 2. Surface area and pore size of the catalysts.

The content of NiO and WO_3 measured through XRF technique reveals that catalyst C (F) has the highest content of NiO and WO_3 where the content of NiO and WO_3 of the catalysts D (F) and E (F)

are similar and lower than that of catalyst C (F) as seen in Figure 3.

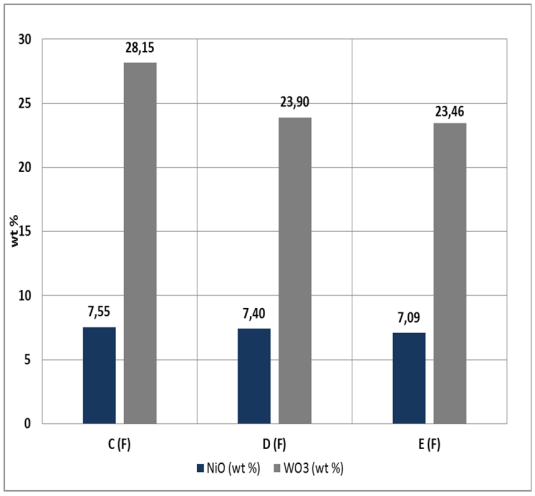

Figure 3. NiO and WO_3 content of the catalysts.

The crystallinity of the catalysts obtained from XRD patterns are given in Figure 4. According to the figure, catalyst C (F) and D (F) have zeolite structures whereas catalyst E (F) has an amorphous structure. The catalyst D (F) and E (F) are also assumed to have poor distribution of metal phase as WO_3 peaks are seen through related patterns.

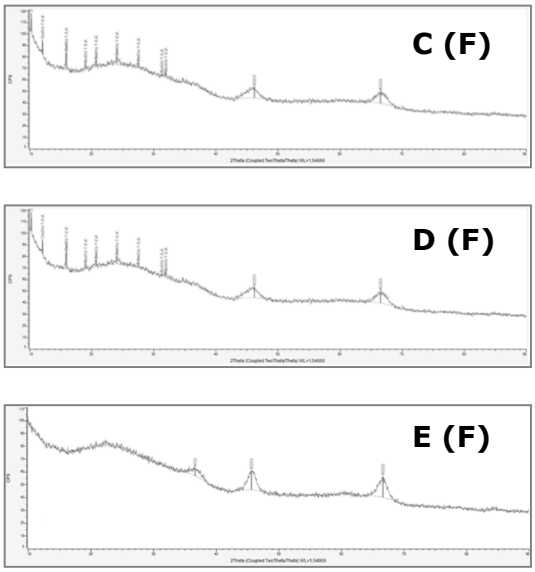

Figure 4. XRD patterns of the catalysts.

The acidic properties of the catalysts studied by NH_3-TPD analysis. According to the Figure 5, the catalyst D (F) has the highest total and medium acidic strength where the catalyst E (F) has the lowest total acidic strength.

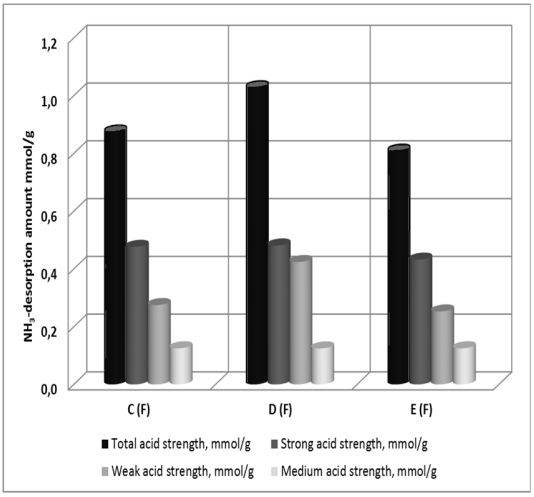

Figure 5. Acidic properties of the catalysts.

The hydrocracking and hydro-treating activities of the catalysts performed through the laboratory scale reactor system are given in Figures 6 and 7. The selectivity and hydrocracking activity of the catalysts are calculated through the distillation data of the TLPs which have been obtained from performance test of each catalyst.

According to Figure 6, the catalyst E (F) has the highest selectivity and conversion value as more fractions are observed and the amount of UCO (unconverted oil) in the TLP is the lowest. The catalysts C (F) and D (F) have similar values of selectivity and conversion due to similar fractions and UCO amount.

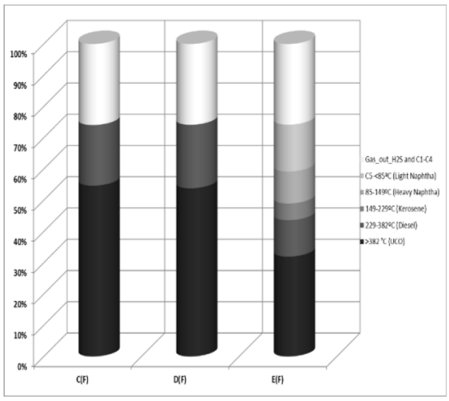

Figure 6. Selectivity and conversion performance of the catalysts.

The sulfur and nitrogen removal activities within the hydro-treating performance and the conversion activities within the hydrocracking performance of the catalysts are seen in Figure 7. The relevant activities are studied based on distillation data and sulfur and nitrogen content of both feed and TLP. The catalyst E (F) has both the highest conversion value and sulfur and nitrogen removal activity representing the hydrocracking and hydro-treating performances, respectively. The catalysts C (F) and D (F) have similar values of conversion and sulfur and nitrogen removal activity.

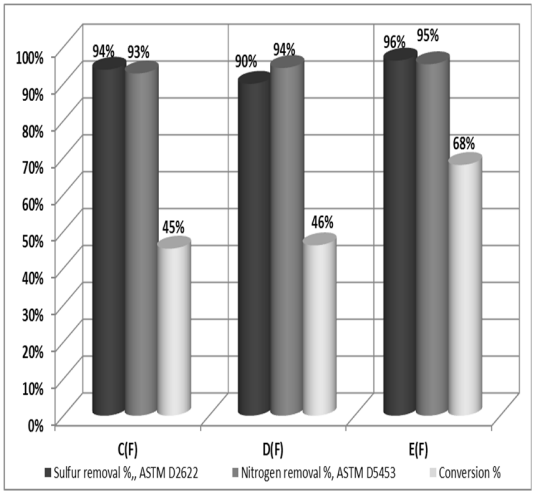

Figure 7. Hydrotreating activities and conversion performances of the catalysts.

RESULTS AND DISCUSSION

The metal phases of the catalyst C (F) are not bulk according to the XRD data. As a result, homogenous distribution of the available metal phases is observed to enhance the hydrotreating

activity (Figure 4). The similarity of the hydrocracking activities of the catalysts C (F) and D (F) even though the higher surface area and acidity of the catalyst D (F) may be associated with the higher total pore size and hydrotreating activity of the catalyst C (F) (Figure 5, 6 and 7).

The hydrotreating activity of the catalyst D (F) which has the lowest value may be associated with the lower content of NiO and WO_3 and poor distribution of metal phases of the catalyst (Figures 3 and 7). The WO_3 peak which is seen in XRD pattern also confirms the formation of the bulk metal phases in patches (Figures 4 and 7). The hydrocracking activity of the catalyst D (F) is relatively low despite high surface area and acidity of the catalyst. This may be explained by relatively lower pore size and hydro-treating activity of the catalyst D (F) (Figure 2, 4 and 7).

The enhancement of hydrotreating activity of the catalyst E (F) seen in Figure 7 may reveal the prospective metal-support interaction. Moreover, high mesopore/micropore ratio, large distribution of pore size, low SAR (Silica to Alumina Ratio) value, relatively high acidity and amorphous structure of the catalyst E (F) promotes high conversion activity of the catalyst even when using heavy feed such as VGO.

In general, the effect of hydro-treating activity on hydrocracking activity may be associated with consecutive nature of the hydrocracking and hydro-treating reactions. Therefore, the higher hydro-treating activity may promote hydrocracking activity to enhance hydrocracking reactions. It is concluded that the bulk metal formation of NiO and/or WO_3 phases or poor distributions of metal phases of the catalyst observed from XRD patterns has a negative effect on hydro-treating activity.

In future studies, the inclusion of the material characteristics for selection of the relevant hydrocracking catalysts within commercial unit operations will be investigated. Furthermore, the effect of hydro-treating activity on hydrocracking activity and the possible influence of consecutiveness of the hydrocracking and hydro-treating reactions will be examined in detail.

ACKNOWLEDGMENTS

This work was performed with support from The Scientific and Technological Research Council of Turkey, TÜBİTAK (Project No: P1.15AP.05). We appreciate the support of Koç University, Chemical and Biological Engineering discipline in performing NH_3-TPD analysis.

REFERENCES

1. James H. Gary, Glenn H. Handwerk, Mark J. Kaiser. Catalytic Hydrocracking. In: James H. Gary, Glenn H. Handwerk, Mark J. Kaiser. editors. Petroleum Refining: Technology and Economics. 5 ed. Boca Raton: CRC Press; 2007. p. 161-79. ISBN: 978-0-203-90792-4.

2. Alain Billon, Pierre-Henri Bigeard. Hydrocracking. In: Pierre Leprince. editor. Petroleum Refining. Vol. 3 Conversion Processes. : Institut Français Du Petrole Publication; 2001. p. 288. ISBN: 2-7108-0779-3

3. Adrian Gruia. Distillate Hydrocracking. In: David S. J. "Stan" Jones, Peter R. Pujadó, editors. Handbook of Petroleum Processing. Dordrecht: Springer Netherlands; 2006. p. 287-320. ISBN: 978-1-4020-2819-9.

4. Patricia Rayo Mayoral, Juarez Jorge Ancheyta , Marroquin Sanchez Gustavo Jesus, Centeno Nolasco Guillermo, Jorge Fernando Ramirez Solis, Mesoporous Composite Of Molecular Sieves for Hydrocracking of Heavy Crude Oils and Residues, US20140124410, filed in December 19, 2012, issued in January 26, 2014. URL: https://patents.google.com/patent/US20140124410A1/en.

5. Marchand Karin, Chaumonnot Alexandra, Bonduelle Audrey, Dufaud Veronique, Lefebvre Frederic, Bader Manuela, Lopes Silva Susana, Process for the Hydrocrackıng of Hydrocarbon Cuts Using A Catalyst Based on Heteropolyanıons Trapped in A Mesostructured Oxide Support, US20130334099, filed in December 15, 2011, issued in December 19, 2013. URL: https://patents.google.com/patent/US20130334099A1/en.

6. Omer Refa Koseoglu, Adnan Al-Hajji, Ali Mahmood Al-Somali, Ali H. Al-Abdul'Al, Mishaal Al-Thukair, Masaru Ushio, Ryuzo Kuroda, Takashi Kameoka, Koji Nakano, Yuichi Takamori, Hydrocracking Catalyst for Hydrocarbon Oil, Method for Producing Hydrocracking Catalyst, and Method for Hydrocracking Hydrocarbon Oil with Hydrocracking Catalyst, filed August 02, 2011, and issued July 11, 2013. URL: https://patents.google.com/patent/WO2012018819A1/en?q=%22Hydrocracking+Catalyst+for+Hydrocarbon+Oil%2c+Method+for+Producing+Hydrocracking+Catalyst%2c+and+Method+for+Hydrocracking+Hydrocarbon+Oil+with+Hydrocracking+Catalyst%22.

7. Qi Bangfeng, Gan Weğmin, Meng Fanmei, Silicon-Aluminum Carrier Containing Two Modified Molecular Sieves, Preparation Method and Application Thereof, filed July 22, 2013, and issued December 31, 2014. URL: https://patents.google.com/patent/CN104250010A/en?q=%22Silicon-Aluminum+Carrier+Containing+Two+Modified+Molecular+Sieves%2c+Preparation+Method+and+Application+Thereof%22.

8. Zhang Zhihua, Yan Zifeng, Dai Baoqin, Liu Xinmei, Tian Ran, Li Haiyan, Sun Famin, Qin Lihong, Zhang Wencheng, Lyu Qian, Xie Bin, Wang Dongqing, Wang Fucun, Guo Shuzhi, Zhang Qingwu, Wang Yan, Yu Xiujuan, Bing Shuqiu, Usy Molecular Sieve Modification Method, filed April 03, 2013, and issued October 15, 2014. URL: https://patents.google.com/patent/CN104096586A/en?q=%22Molecular+Sieve+Modification+Method%22.

9. Kwan Young Lee, Hee Jun Eom, Seong Min Kim, Young Gul Hur, Method for Preparing Light Distillate from Extra-Middle Distillate by Using Heteropolyacid Catalyst Substituted with Cesium, and Method for Regenerating Catalyst, filed August 14, 2013, and issued October 09, 2014. URL: https://patents.google.com/patent/WO2014163252A1/en?q=%22Method+for+Preparing+Light+Distillate+from+Extra-Middle+Distillate+by+Using+Heteropolyacid+Catalyst+Substituted+with+Cesium%2c+and+Method+for+Regenerating+Catalyst%22.

10. Lu Yinhua, Fan Lichuang, Liu Feipeng, Hao Kun, Tao Zhichao, Yang Yong, Li Yongwang, Non-Sulfur Catalyst as well as Preparation Method and Application Thereof, filed July 11, 2013, and issued September 18, 2013. URL: https://patents.google.com/patent/CN103301872A/en?q=%22Non-Sulfur+Catalyst+as+well+as+Preparation+Method+and+Application+Thereof%22.

11. Dong Songtao, Dong Jianwei, Nie Hong, Shi Yahua, Li Dadong, Hydrocracking Catalyst, Preparation

and Application Thereof, filed March 15, 2013, and issued September 17, 2014. URL: https://patents.google.com/patent/CN104043478A/en?q=%22Hydrocracking+Catalyst%2c+Preparation+and+Application+Thereof%22.

12. Melek Bardakcı Türkmen. Recent Developments in Hydrocracking Catalysts – Patent and Open Literature Survey. In: Deniz Üner. editor. Advances in Refining Catalysis. :CRC Press; in press. ISBN: 9781498729970.

Türkçe Öz ve Anahtar Kelimeler

Effects of Material Characteristics on the Performance of Hydrocracking Catalysts

Melek Bardakcı Türkmen, Burcu Yüzüak, Deniz Onay Atmaca, Ayşegül Bayat, Volkan Balci, Seçil Ünsal, Can Erkey and Ersen Ertaş

Öz: Hidro-kraking ağır hidrokarbon fraksiyonlarını daha küçük ve katma değeri daha fazla olanlara çevirmek için kullanılan bir rafineri sürecidir. Hedeflenen kısımlar olarak orta distilatları içeren ağır dizelden hafif naftaya kadar uzanan bir seri elde edilir daha yüksek moleküler ağırlık ve dah a düşük hidrojen/karbon oranları elde edilmiş olur. Hidro-kraking tepkimeleri yüksek hidrojen kısmi basınçları ve yüksek sıcaklıklarda, katalizör varlığında oluşur, kükürtlü bileşikler gibi safsızlıklar bu esnada ortamdan uzaklaştırılmış olur ve ağır hidrokarbon molekülleri yüksek katma değerli ve daha hafif türevlere dönüşür. Hidro-kraking katalizörleri iki fonksiyonludur ve VIB veya VIIIB grubundan bir metal hidrojenlemede safsızlıkları gidermek için ve amorf oksitler ve/veya kristal zeolitler de kraking işlevini yerine getirecek asidik fonksiyonları barındırır. Bu çalışmada, laboratuar reactor sisteminden gelen performans test sonuçları ile katalizörlerin malzeme karakteristikleri arasındaki uyum izlenecektir. Katalizörlerin performans parametreleri içindeki seçimlilik, hidro-kraking ve hidrojenleme aktiviteleri fraksiyon oranlar ıve akış ürün özelliklerine dayanan hesaplamalarla bulunmuştur. Bunun ötesinde, hidrokraking aktivitesi üzerine hidro-muamele aktivitesinin etkisi de ortaya konmuştur. Yüzey alanı ve gözenek boyutu, kristallik, malzemenin kimyasal bileşimi ve asidik özellikleri sırasıyla BET, XRD, XRF, NH_3-TPD teknikleri ile yapılmıştır.

Anahtar kelimeler: Hidrokraking; katalizör; karakterizasyon; yapı-performans ilişkisi.

Sunulma: 02 Eylül 2016. **Düzeltme:** 06 Ekim 2016. **Kabul:** 02 Kasım 2016.

(This article was initially submitted to the UKMK 2016 (National Chemical Engineering Congress) and finally evaluated by the JOTCSB editorial staff).

Ethyl Acetate Synthesis by Chitosan/ Poly(Vinylpyrrolidone) Blend Membrane in Pervaporation Membrane Reactor

Derya Unlu[1,*], Aynur Hacıoglu[1], Nilufer Hilmioglu[1]

[1] Kocaeli University, Engineering Faculty, Chemical Engineering Department, Umuttepe, Kocaeli, 41380, Turkey

Abstract: In this study, polymeric blend membranes were prepared for using the esterification reaction. Aluminum potassium sulfate dodecahydrate was used as catalyst. Chitosan and poly(vinylpyrrolidone) polymers were utilized for blend membrane solution. The membrane was prepared by solution casting method. The reaction of ethanol and acetic acid was chosen as a model reaction. Effect of the temperature, amount of catalyst, and initial molar ratio of reactants on the conversion of acetic acid, pervaporation flux, and selectivity were investigated and interpreted. When 10% of conversion value was obtained in batch reactor, 49.76% of conversion was obtained in pervaporation membrane reactor under the same reaction conditions (65 °C, catalyst amount of 5 wt.%, M =6 :1). Compared to the batch reactor, conversion values show the performance of the pervaporation membrane reactor. Pervaporation membrane reactor displayed higher performance with regard to the batch reactor.

Keywords: Ethyl acetate; chitosan; pervaporation membrane reactor; poly(vinylpyrrolidone).

Submitted: September 22, 2016. **Revised:** October 17, 2016. **Accepted:** November 08, 2016.

Cite this: Ünlü D, Hacıoğlu A, Hilmioğlu N. Ethyl Acetate Synthesis by Chitosan/ Poly(Vinylpyrrolidone) Blend Membrane in Pervaporation Membrane Reactor. JOTCSB. 2017;1(1):25–38.

*Corresponding author. E-mail: derya.unlu@kocaeli.edu.tr.

INTRODUCTION

The increment of industrial application of pervaporation is related to the advantages of this membrane separation technology. Hybrid process "pervaporation membrane reactor" (PVMR) is a combined reaction and separation and one of the pervaporation technology. Pervaporation membrane reactors are membrane-aided processes and reaction and separation occur simultaneously. The membrane permits the selective permeability of one of the products from the reaction mixture. Therefore, membrane reactors provide an increment of conversion values in the thermodynamic equilibrium limited reactions (1).

Esterification reactions have an important position in the industry (2). Esterification reactions are reversible equilibrium reactions. Generally, two methods are used for shifting the reaction equilibrium: One of the reactants is used as excess or one or more of the products are removed by reactive distillation. The usage of excess reactant increases the cost of operation and causes the formation of undesirable byproducts. The reactive distillation is not a suitable process for the close-boiling-point mixtures and azeotropes. The use of membrane reactor becomes an attractive option for these reasons. High conversion values can be obtained by the use of minimum reactants under the mild operating conditions in the membrane reactor. Thus, both reaction yield increases and cost of operation reduces. Also, compared to conventional batch reactor, reaction time decreases by using membrane reactor for achieving maximum conversion in esterification (3).

Separation efficiency of PVMR is not limited by relative volatility, it relies on sorption and transport properties of the membrane (4-5). When the feed solution contacts with upper surface of the membrane, one of the components is adsorbed by it. This component diffuses through the membrane, and then collected as vapors on the bottom side of the membrane. Vacuum or gas purge is used to obtain a partial pressure difference in the diffusion of molecules (3, 6).

Reaction and separation mechanism of the pervaporation membrane reactor takes place as follows. Selective membrane is placed in the reactor. One of the reaction products is removed through the membrane during the reaction and the reaction equilibrium changes towards the products. Therefore, both conversion increases and purification occurs (7).

Ethyl acetate, which is commonly used in the chemical industry, is produced by the esterification reaction of ethyl alcohol and acetic acid. Ethyl acetate is mostly synthesized by the reactive distillation in the industry. Ethyl acetate, water and waste ethanol are obtained at the end of the reaction. Double or triple azeotropes are formed in this case. It is not possible to separate the azeotrope with conventional distillation. Therefore, azeotropic distillation or extractive distillation

processes should be used for the purification of ethyl acetate. Both processes consume relatively high energy and require large investment costs. Pervaporation is used for separation of the azeotrope and close boiling point mixture. Pervaporation has low energy consumption and it is also an environmentally friendly membrane technology (8).

In this study, ethyl acetate was synthesized by chitosan/poly(vinylpyrrolidone) blend membrane in the presence of aluminum potassium sulfate dodecahydrate catalyst in the pervaporation membrane reactor. There are similar PVMR studies for the esterification reaction of ethanol and acetic acid, but different membranes and catalysts are used. Chitosan/PVP blend membranes were used only for dehydration by pervaporation. There is no PVMR application by using chitosan/PVP membrane in the literature. Also, aluminum potassium sulfate dodecahydrate catalyst was not used in esterification. The effect of reaction parameters such as temperature, amount of catalyst, and molar feed ratio was examined on reaction conversion, flux, and selectivity.

MATERIALS AND METHODS

Chemicals

In this study, chitosan (CS) and poly(vinylpyrrolidone) (PVP) polymers and high purity grade of ethanol, acetic acid, sulfuric acid, and acetone were used and all of these chemicals were supplied from Sigma-Aldrich and Merck.

Experimental procedure

Chitosan/PVP blend membrane preparation: Dense, nonporous membrane prepared by solution casting method. The 2 wt.% solution of CS and the 2 wt.% solution of PVP were mixed separately. The blend of PVP/CS (20 wt%/80 wt%) was prepared by physically mixing both solutions. The blend polymeric solution was stirred for 24 hours. The prepared polymeric solution was poured onto poly(methyl methacrylate) surface by solution casting techniques and dried in room conditions. Crosslinking process is applied to improve physical and chemical resistance of the membrane. Membrane had been treated with 0.005 M sulfuric acid in 50 vol.% acetone-50 vol.% water solution for crosslinking. After the membrane was immersed in the crosslinking bath for 5 min, the blend membrane was washed with distilled water and dried at room conditions. Chitosan/PVP blend membrane was characterized by FTIR.

Synthesis of Ethyl Acetate in PVMR: Esterification of ethyl alcohol and acetic acid was carried out by chitosan/PVP blend membrane in the pervaporation membrane reactor. Reactants of ethanol and acetic acid and catalyst of aluminum potassium sulfate dodecahydrate catalyst were placed into three-necked reactor and reaction mixture was transferred to the membrane cell by the feed pump.

A thermocouple is used for temperature control of the reactor, a heating magnetic stirrer is used for the mixing and heating and the condenser is used to avoid solvent losses. Hydrophilic chitosan/PVP blend membranes were placed in the membrane cell. Vacuum is applied to the underside of the membrane cell and product is collected in a Dewar flask. The PVMR experiment system is shown in Figure 1.

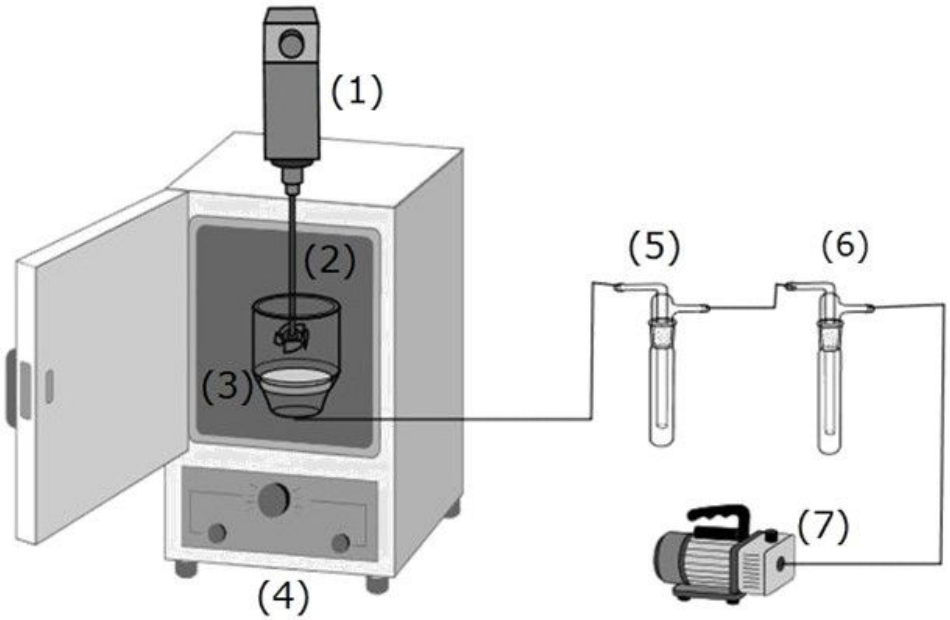

Figure 1. PVMR process (1) Mixer (2) Reactor (3) Membrane (4) Drying oven (5), (6) Cold trap (7) Vacuum pump.

Samples of permeate and reaction mixture were injected to gas chromatography at every hour of analysis. GC-7820A installed with TCD and HP-FFAP capillary column was used to analyze concentrations. Detector and column temperatures were 280 and 220 °C, respectively. Conversion, flux, and selectivity values were calculated.

Conversion values were calculated using Equation 1.

$$x = \frac{N_{Ao} - N_A}{N_{Ao}} \qquad \text{(Eq. 1)}$$

In this equation, N_{Ao} is the number of moles of acetic acid at t = 0, N_A is the number of moles of acetic acid at any time of the reaction (9).

Flux is defined as the mass of the collected permeates in the cold trap. Flux is determined as mass

amount per unit time, per unit area of the membrane. Flux (J) (kg/m^2.h) and selectivity (α) values are calculated by Equations 2 and 3.

$$J = \frac{m}{A.t} \quad \text{(Eq. 2)}$$

$$\alpha = \frac{Y_a / Y_b}{X_a / X_b} \quad \text{(Eq. 3)}$$

In these equations, t is the time (h), A is the membrane area (m^2), m is the amount of sample taken from traps (kg). X and Y are the weight fractions of feed and permeate streams, respectively. Parameter a is the component of selectivity of membrane, b represents all of the other materials. Selectivity is a unitless parameter.

RESULTS AND DISCUSSION

Membrane characterization by FTIR spectroscopy

Figure 2 shows the FTIR spectra of PVP/CS blend membrane.

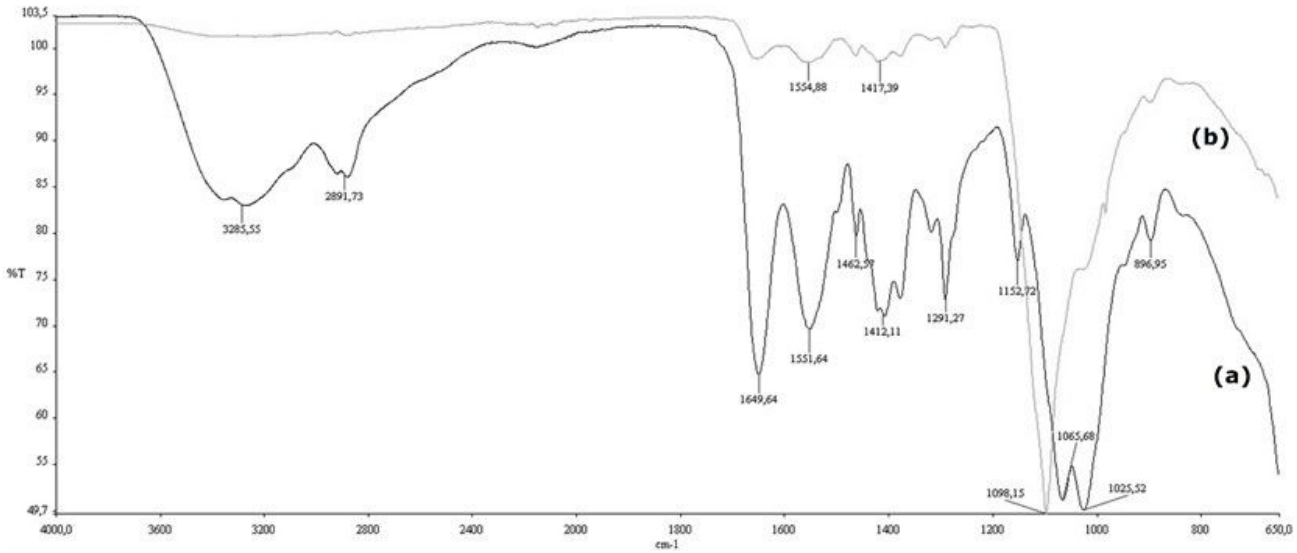

Figure 2. FT-IR spectra of PVP/CS blend membrane (a) uncross-linked (b) cross-linked.

Spectrum a in Figure 2 represents the uncross-linked blend membranes. The characteristic O−H peak can be seen between 2800-3500 cm^{-1}. FTIR spectra shows the functional groups of polymers. The peak around 1649.64 cm^{-1} shows a single carbonyl band of CS/PVP blend. This bond is formed between amine groups of CS and carbonyl group of PVP. The peak at 1291.27 cm^{-1} is assigned to

the absorbance of C-N bonds. The peak at 1551.64 cm^{-1} is assigned to the specific absorbance of N–H bonds in NH_3^+ groups. Spectrum a of Figure 2 represents the cross-linked blend membranes. For the PVP/CS blend, crosslinked with H_2SO_4, the appearance of a new peak at 1554.88 cm^{-1} and 1417.39 cm^{-1} is due to crosslinking with sulfuric acid. This could be due to the crosslinking reaction occurring between amino groups of chitosan and sulfate ions of sulfuric acid (Zhang *et al.,* 2009 and Devi *et al.,* 2006 and Caetano *et al.,* 2013).

Degree of swelling

Figure 3 presents how the swelling degree of membrane in water varies with time. When the cross-linking degree of the membrane is good, the mobility of polymer chains decreases. In this experiment, H_2SO_4 was used as crosslinking agent. As seen in Figure 3, membrane had low swelling degree, because H_2SO_4 had high crosslinking properties. Rigidity of the membrane increased by using H_2SO_4 as a crosslinking agent. Therefore, diffusivity of membrane decreased and swelling degree of membrane was lower.

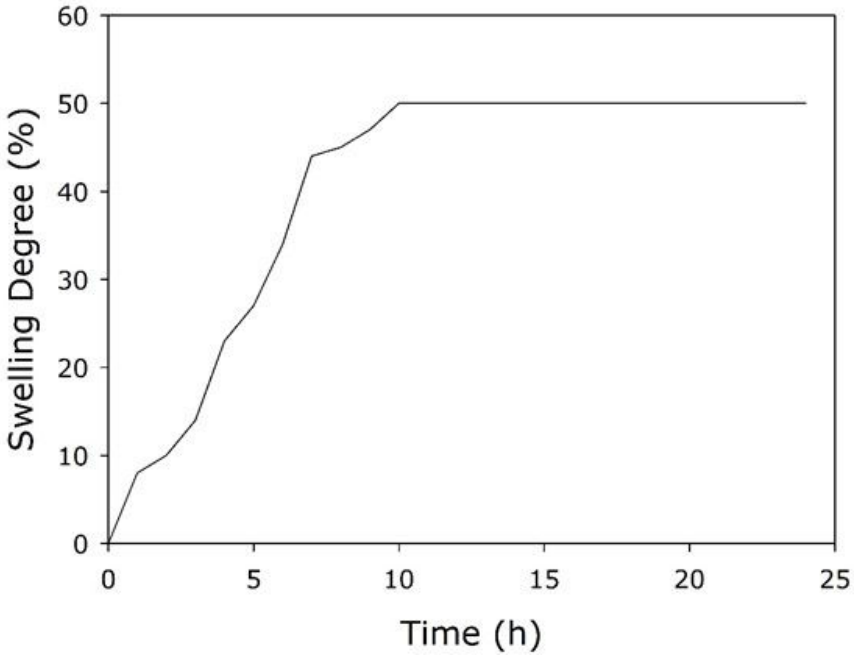

Figure 3. Swelling degree of membrane in water.

Effect of the temperature in PVMR

The effect of temperature on the PVMR process was investigated in the temperature of 55 ^oC, 65 ^oC, and 75 ^oC. The change of the conversion of acetic acid with temperature is given in Figure 4.

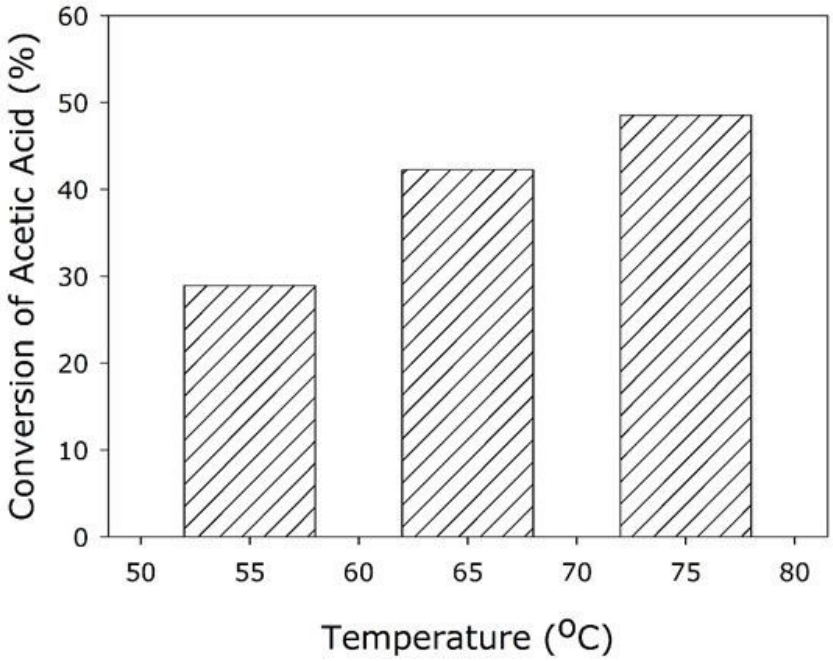

Figure 4. Effect of the different temperatures on the conversion (catalyst amount of 5 wt.%, M = 6: 1).

Conversion increased with increasing reaction temperature. The temperature has an important effect on both of pervaporation performance and the reaction kinetics (13). Increasing the reaction temperature led to an increase in the rate constant and the rate of reaction (14). Relation between temperature and reaction rate constant can be explained by the Arrhenius' equation. The activation energy, which is needed to start a reaction, is provided by the kinetic energy of the reactants. Therefore, increment of the reaction temperature resulted in the high kinetic energy of the reactant molecules hence reaction rate is increased. Esterification of acetic acid with ethanol is an endothermic reaction. Increment of the temperature shifts the equilibrium in the direction of the products and conversion increases.

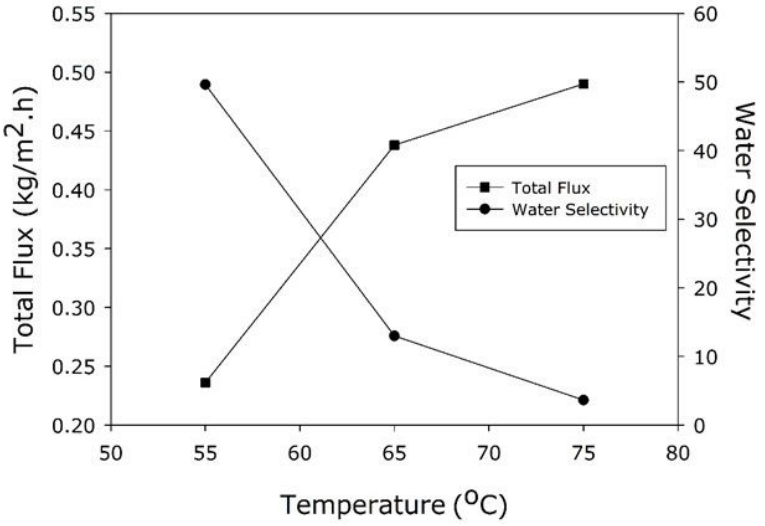

Figure 5. Effect of the different temperatures on flux and selectivity (catalyst amount of 5 wt.%, M = 6: 1).

The increase in temperature not only affects the reaction rate but also the pervaporation rate. As the reaction rate is increased, water amount in the reaction mixture rises. In this study, chitosan and PVP were chosen as membrane materials. Chitosan and PVP have hydrophilic structure interacting with water. Therefore, water was removed from the reaction mixture by the chitosan/PVP blend membrane. Removal of water changed the reaction equilibrium towards the products and conversion is increased. PVMR has higher conversion values than the batch reactor.

Polymer molecules also had a more flexible structure at the higher temperature, the diffusion rate of components increased. The reaction equilibrium shifted towards the product side by the increment of diffusion of water. Increasing the diffusion rate caused an increase of free volume of the membrane. Flux increased with free volume and this free volume also facilitated the transport of other components and consequently the selectivity of water was decreased (15). Figure 5 presents the flux and the selectivity for chitosan/PVP membrane for different reaction temperatures. As seen in Figure 5, while total flux increased, water selectivity decreased with the temperature.

Effect of the amount of catalyst in PVMR

To determine the effect of the catalyst amount on conversion, 2.5 wt.%, 5 wt.%, and 7.5 wt. % of catalyst was added into the reaction mixture. The change of the conversion of acetic acid with amount of catalyst is given in Figure 6.

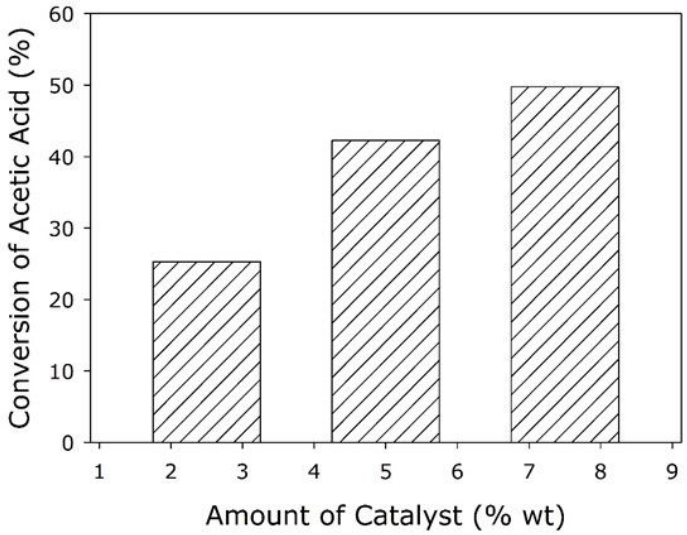

Figure 6. Effect of the different catalyst amounts on the conversion (65°C, M = 6: 1).

Conversion increased with increasing amount of the catalyst. The reaction rate is directly related to the number of active groups in the catalyst. Conversion increased with increasing amount of the catalyst. The reaction rate is directly related to the number of active groups in the catalyst. The number of the active groups was increased by increasing catalyst amount in the reaction medium. Reactants easily contact with active groups of the catalyst and acetic acid conversion increased. The catalyst amount based on the weight of acetic acid varied as 2.5%, 5%, and 7.5 %, respectively.

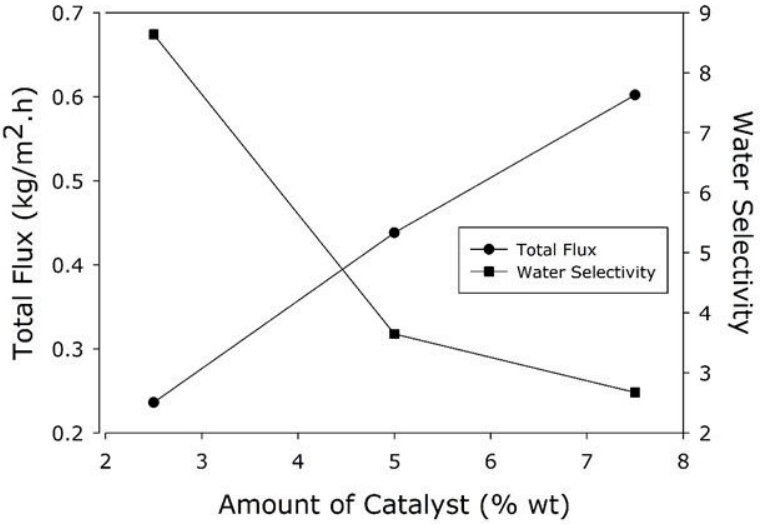

Figure 7. Effect of the amount of catalyst on flux and selectivity (65°C, M = 6: 1).

As the conversion of the acid increased, the amount of product (ethyl acetate and water) increased too. Increment of water amount resulted in the increase of concentration gradient. The driving force of the PVMR process is concentration gradient. High concentration gradient facilitated the diffusion of water and flux of water increased. Esterification of acetic acid and ethanol is a kind of reversible

reaction. If water is removed from the reaction mixture, reaction equilibrium shifts towards the products and thus leads to an increased conversion of acetic acid (18). Chitosan/PVP membrane is swollen by high amount of water. The other components with water diffused through the membrane and water selectivity decreased. Figure 4 shows the change of flux and selectivity with the amount of catalyst.

Effect of the initial molar ratio in PVMR

Three different alcohol / acid initial molar ratios were studied in PVMR, M = 3: 1, M = 6: 1, and M = 9: 1. Figure 8 shows the effect of the initial molar ratio on conversion values.

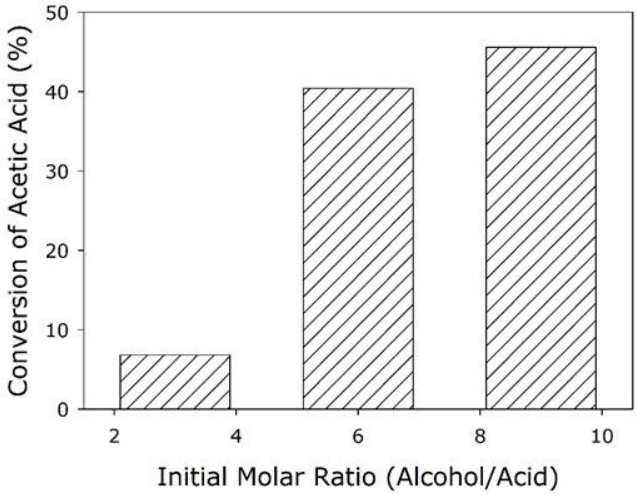

Figure 8. The effect of different initial molar ratios on conversion (65°C, catalyst amount of 5 wt.%).

Usage of excess reactant or removal of one of the products are two methods for increment of conversion. The use of excess reactant is conventional and favored method for obtaining higher conversion values in the reversible reaction. As seen in Figure 5, conversion increased with increasing initial molar ratios. High conversion values are obtained with respect to Le Châtelier's principle when excess amount of one of reactants is used in the esterification, because the usage of excess reactant shifts the reaction equilibrium towards the products [19].

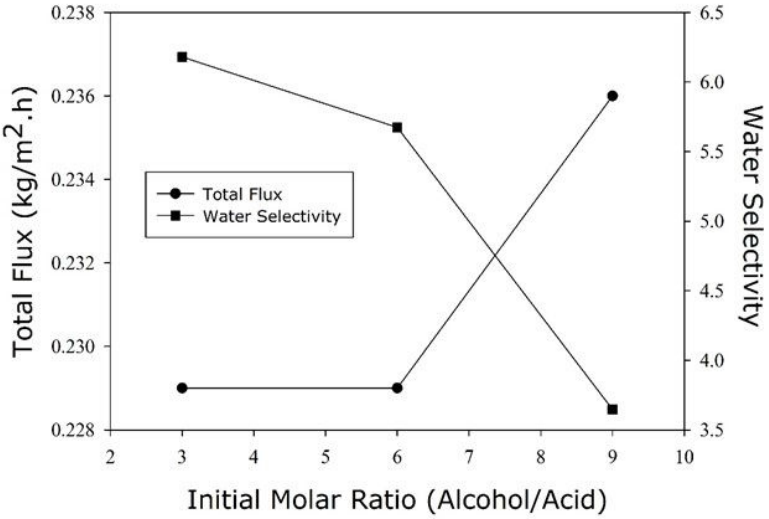

Figure 9. The effect of different initial molar ratios on flux and selectivity (65°C, catalyst amount of 5 wt.%).

Water formation increased with increment of conversion and hence the rate of water diffusion increased. In PVMR, water was removed from the reaction mixture by the hydrophilic chitosan/PVP membrane and conversion was increased. As a result of the increment of water amount, polymer transport channel expanded and flux increased, selectivity decreased, because of increment in free volume in the membrane [20]. The effect of the initial molar ratio on flux and selectivity values is shown in Figure 6.

CONCLUSIONS

The esterification of acetic acid with ethyl alcohol for the production of ethyl acetate and water was carried out under different operating conditions in PVMR. The effect of reaction temperature, the initial molar ratio of reactants and the amount of the catalyst on reaction conversion and pervaporation performance were investigated. The membrane which was prepared in the laboratory was used in the research. Chitosan/PVP blend membrane was preferred for good hydrophilic and high selectivity properties. Aluminum potassium sulfate dodecahydrate as a catalyst was used in PVMR and at the end of the reaction, 49.76% conversion was obtained. Under the same reaction conditions, 10% conversion value is obtained in batch reactor in previous studies [21]. The reaction performance of the PVMR and batch reactor was compared, and it can be seen that the PVMR displayed higher performance with regard to the batch reactor. These results indicate that the PVMR is a good alternative to the conventional batch reactor. The usage of the PVMR for the synthesis of ethyl acetate is economical and environmental technology.

ACKNOWLEDGMENTS

The authors gratefully acknowledge the financial support from Kocaeli University, Scientific Research Projects Unit (Project No. 2014/076).

REFERENCES

1. Parulekar SJ. Analysis of pervaporation-aided esterification of organic acids. Industrial & Engineering Chemistry Research. 2007 October; 46(25):8490-8504, DOI: 10.1021/ie061157o.

2. Sanz MT, Gmehling J. Esterification of acetic acid with isopropanol coupled with pervaporation Part I: Kinetics and pervaporation studies. Chemical Engineering Journal. 2006 October; 123(1-2):1–8, DOI: 10.1016/j.cej.2006.06.006.

3. Han Y, Lv E, Ma L, Lu J, Chen K, Ding J. Coupling membrane pervaporation with a fixed-bed reactor for enhanced esterification of oleic acid with ethanol. Energy Conversion and Management. 2015 December; 106:1379–1386, DOI: 10.1016/j.enconman.2015.10.075.

4. Sert E, Atalay FS. n-Butyl acrylate production by esterification of acrylic acid with n-butanol combined with pervaporation. Chemical Engineering and Processing: Process Intensification. 2014 July; 81: 41–47, DOI: 10.1016/j.cep.2014.04.010.

5. Khajavi S, Jansen JC, Kapteijn F. Application of a sodalite membrane reactor in esterification—Coupling reaction and separation. Catalysis Today. 2010 October; 156(3-4):132–139, DOI: 10.1016/j.cattod.2010.02.042.

6. Jia Z, Wu G. Metal-organic frameworks based mixed matrix membranes for pervaporation. Microporous and Mesoporous Materials. 2016 November; 235:151-159, DOI: 10.1016/j.micromeso.2016.08.008.

7. Wasewar K, Patidar S, Agarwal VK. Esterification of lactic acid with ethanol in a pervaporation reactor: modeling and performance study, Desalination. 2009 July; 243(1-3):305–313, DOI: 10.1016/j.desal.2008.04.030.

8. Xia S, Dong X, Zhu Y, Wei W, Xiangli F, Jin W. Dehydration of ethyl acetate–water mixtures using PVA/ceramic composite pervaporation membrane. Separation and Purification Technology. 2011 February; 77(1):53–59, DOI: 10.1016/j.seppur.2010.11.019.

9. Liu QL, Chen HF. Modeling of esterification of acetic acid with n-butanol in the presence of Zr(SO4)2.4H2O coupled pervaporation. Journal of Membrane Science. 2002 February; 196(2):171-178, DOI: 10.1016/S0376-7388(01)00543-9.

10. Devi DA, Smitha B, Sridhar S, Aminabhavi TM. Novel crosslinked chitosan/poly(vinylpyrrolidone) blend membranes for dehydrating tetrahydrofuran by the pervaporation technique. Journal of Membrane Science. 2006 September; 280(1-2):45–53, DOI: 10.1016/j.memsci.2006.01.003.

11. Caetano CS, Caiado M, Farinha J, Fonseca IM, Ramos AM, Vital J, Castanheiro JE. Esterification of free fatty acids over chitosan with sulfonic acid groups. Chemical Engineering Journal. 2013 August; 230:567–572, DOI: 10.1016/j.cej.2013.06.050.

12. Zhang XH, Liu QL, Xiong Y, Zhu AM, Chen Y, Zhang QG. Pervaporation dehydration of ethyl acetate/ethanol/water azeotrope using chitosan/poly (vinyl pyrrolidone) blend membranes. Journal of Membrane Science. 2009 February; 327 (1-2):274–280, DOI: 10.1016/j.memsci.2008.11.034.

13. Delgado P, Sanz MT, Beltrán S, Núñez LA. Ethyl lactate production via esterification of lactic acid with ethanol combined with pervaporation. Chemical Engineering Journal. 2010 December; 165(2):693–700, DOI: 10.1016/j.cej.2010.10.009.

14. Acartürk F., Reaksiyon Kinetiği ve Stabilite, URL: www.e-kutuphane.teb.org.tr.

15. Veerapur SK, Gudasi KB, Sairam M, Shenoy RV, Netaji M, Raju KVSN, Sreedhar B, Aminabhavi TM. Novel sodium alginate composite membranes prepared by incorporating cobalt (III) complex particles used in pervaporation separation of water–acetic acid mixtures at different temperatures. Journal of Materials Science. 2007 June; 42(12):4406–4417, DOI: 10.1007/s10853-006-0652-0.

16. Alhassan FH, Rashid U, Yunus R, Sirat K, Lokman IM, Taufiq-Yap YH. Synthesis of Ferric–Manganese Doped Tungstated Zirconia Nanoparticles as Heterogeneous Solid Superacid Catalyst for Biodiesel Production From Waste Cooking Oil. International Journal of Green Energy. 2015 September; 12(9):987−994, DOI: 10.1080/15435075.2014.880843.

17. Jiang Y, Lu J, Sun K, Ma L, Ding J. Esterification of oleic acid with ethanol catalyzed by sulfonated cation exchange resin: Experimental and kinetic studies. Energy Conversion and Management. 2013 December; 76:980−985, DOI: 10.1016/j.enconman.2013.08.011.

18. Liu Q, Zhang Z, Chen H. Study on the coupling of esterification with pervaporation. Journal of Membrane Science. 2001 February; 182(1−2):173−181, DOI: 10.1016/S0376-7388(00)00568-8.

19. Çimenler Ü, Investigation of the esterification reaction for the production of butyl propionate in pervaporation membrane reactor using Amberlite Ir-120 catalyst. Master Thesis, Yıldız Technical University, Graduate School of Natural and Applied Sciences, Istanbul, (2011), URL: https://tez.yok.gov.tr/UlusalTezMerkezi/TezGoster?key=zqI_ZOq-b18GC2rT9c2JGlmbUEtqEZJt1bJBbhtjJJqWhMcrCpf4Ick83Dn9zVrn.

20. Korkmaz S, Salt Y, Hasanoglu A, Ozkan S, Salt I, Dincer S. Pervaporation membrane reactor study for the esterification of acetic acid and isobutanol using polydimethylsiloxane membrane. Applied Catalysis A: General. 2009 September; 366(1):102–107, DOI: 10.1016/j.apcata.2009.06.037.

21. Unlu D, Hacıoglu A, Hilmioglu N. Preparation And Application Of AlK(SO4)2.12H2O Loaded Chitosan/ Polyvinylpyrrolidone Catalytic Membrane. NCC6-The 6th Catalysis Conference. 2016 April; Page:146, ISBN / 978-605-9332-00-2, Bursa, Turkey.

Türkçe Öz ve Anahtar Kelimeler

Pervaporasyon Membran Reaktörde Kitosan / Poli(vinilpirolidon) Blend Membran ile Etil Asetat Sentezi

Derya Unlu, Aynur Hacıoglu, Nilufer Hilmioglu

Öz: Bu çalışmada, polimerik blend membranlar esterleştirme reaksiyonlarında kullanılmak için hazırlanmıştır. Alüminyum potasyum sülfat dodekahidrat katalizör olarak kullanılmıştır. Kitosan ve poli(vinilpirolidon) polimerleri blend membran çözeltisi için kullanılmıştır. Membran çözeltiden döküm yöntemiyle hazırlanmıştır. Etanol ve asetik asit tepkimesi model reaksiyon olarak seçilmiştir. Sıcaklık, katalizör miktarı ve reaktanların ilk molar oranının asetik asidin dönüşümü, pervaporasyon akısı ve seçicilik üzerindeki etkisi araştırılmış ve yorumlanmıştır. Kesikli reaktörde %10 dönüşüm elde edilirken pervaporasyon membran reaktördeki dönüşümün %49,76 olduğu bulunmuştur (tepkime koşulları aynıdır, 65 °C, ağırlıkça %5 katalizör ve M = 6:1). Kesikli reaktörle kıyaslandığında, dönüşüm değerleri pervaporasyon membran reaktörün performansını göstermektedir. Pervaporasyon membran reaktör, kesikli reaktöre göre daha yüksek performans göstermiştir.

Anahtar kelimeler: Etil asetat; kitosan; pervaporasyon membran reaktör; poli(vinilpirolidon).

Sunulma: 22 Eylül 2016. **Düzeltme:** 17 Ekim 2016. **Kabul:** 08 Kasım 2016.

(This article was initially submitted to the UKMK 2016 (National Chemical Engineering Congress) and finally evaluated by the JOTCSB editorial staff)

Growth Kinetics of Calcium Sulfate Dihydrate in the Presence of Oxalic Acid

Sevgi POLAT*, Sibel TİTİZ-SARGUT, Perviz SAYAN

Chemical Engineering Department, Marmara University, Istanbul, 34722, TURKEY

Abstract: This study is focused on the crystallization kinetics of calcium sulfate dihydrate. The reactive crystallization of calcium sulfate dihydrate in the absence and presence of 250 ppm, 1000 ppm, and 2500 ppm oxalic acid concentrations was carried out in a mixed-suspension-mixed-product-removal (MSMPR) type crystallizer. The growth kinetic of calcium sulfate dihydrate crystals was analyzed in accordance with size-independent and size-dependent growth models. It was found that the growth rates of calcium sulfate dihydrate crystals depend on the particle size and the kinetic parameters were evaluated according to Bransom, MJ2, and MJ3 models. Also, the relative coefficient, mean square error, and the mean square deviation were determined for each model and the results showed that MJ3 model was the best fitting model to the experimental data.

Keywords: Calcium sulfate dihydrate; crystallization kinetic models; oxalic acid.

Submitted: October 08, 2016. **Revised:** November 17, 2016. **Accepted:** November 19, 2016.

Cite this: Polat S, Titiz-Sargut S, Sayan P. Growth Kinetics of Calcium Sulfate Dihydrate in the Presence of Oxalic Acid. JOTCSB. 2017;1(1):39–48.

*Corresponding author. E-mail: sevgi.polat@marmara.edu.tr.

INTRODUCTION

Calcium sulfate dihydrate ($CaSO_4.2H_2O$) is one of the most common components encountered in several industrial and environmental precipitation processes. It is a by-product of both the production of phosphoric acid from phosphate rock and the production of boric acid from colemanite ore. In both processes, the most important point is separation of the calcium sulfate dihydrate crystals via filtration. It is well known that achieving good filtration process depends on the produced crystals having homogeneous crystal size distribution [1]. The crystal size distribution depends on the nucleation and growth rate as well as residence time in the crystallizer. It is possible to investigate all of these functions for both steady and unsteady state functions by population balance theory. The continuous mixed-suspension mixed-product-removal (MSMPR) types are the most suitable crystallizers in order to apply population balance theory [2]. There are some assumptions to analyze the MSMPR crystallizer based on the population balance theory. These assumptions are (a) steady-state operation, (b) no particles in the feed, (c) no attrition of the particles [3]. As a result of these assumptions, the general population balance equation is demonstrated in Eq. (1).

$$\frac{\mathrm{d}[\mathrm{G(L)n(L)}]}{\mathrm{dL}} + \frac{\mathrm{n(L)}}{\tau} = 0 \qquad (1)$$

G(L) is the crystal growth rate, L is the crystal size, n(L) is the population density at and τ is the residence time of suspension in the crystallizer [4]. As considering the crystal growth rate obeys the McCabe ΔL law, the growth of crystals rate is size independent. That is dG(L)/dL=0 and G(L)=G=constant. The population density distribution in MSMPR crystallizer could be presented as shown in below.

$$\mathrm{n(L)} = \mathrm{n_0} \exp\left(-\frac{\mathrm{L}}{\mathrm{G}\tau}\right) \qquad (2)$$

n_0 is the $\lim_{L\to 0} n(L)$, the zero size population density. In this situation, if the graph of ln (n) versus L is drawn, a straight line is produced with the intercept n_0 and the slope $-1/(G\tau)$ and from which the crystal growth rate could be calculated [5].

A non-linearity in ln (n) vs. L plot has been observed in many crystallization systems. Such curvature can result from various reasons such as secondary nucleation, size-dependent growth, abrasion, growth rate dispersion, agglomeration, and breaking. If the crystal growth rate does not obey the McCabe ΔL law and the line deviates from linearity, this case indicates to the existence of size dependent growth. Therefore, the population density distribution will not follow the simple exponential relationship given by Eq. (2). The relationship between crystal size and growth rate has been studied by a number of authors and certain models have been offered such as Bransom, Canning and Randolph (C-R), Abegg Stevens and Larson (ASL) two parameter (MJ2) and three parameter (MJ3) size dependent growth models [6]. While C-R and ASL models can be reduced to Bransom models, MJ2 and MJ3 are the latest proposed models. Therefore, in the literature mostly and notably Bransom, MJ2, and MJ3 models are preferred. Several

examples are given in the literature in which small amount of carboxylic acids alter the crystal growth, shape of the crystals and their agglomeration or dispersion behavior, yet the exact role of carboxylic acids is not yet fully disclosed. Furthermore, the effects of oxalic acid containing two carboxyl functional groups on calcium sulfate dihydrate crystallization has not been investigated and there is no kinetic study about calcium sulfate dihydrate crystallization in the presence of oxalic acid in the literature. Therefore, this study is focused on the examination of the crystallization kinetics of calcium sulfate dihydrate crystal produced in the absence and presence of oxalic acid using Bransom, MJ2 and MJ3 size dependent growth models.

Bransom Model. The growth rate equation of this size dependent model proposed by Bransom is written as

$$\mathrm{G(L)} = \mathrm{a}L^{b} \tag{3}$$

Using the Eq. (3), Eq. (1) can be integrated to obtain the population balance equation

$$\mathrm{n(L)} = n_0 \exp\left[\frac{1}{\mathrm{a\tau(b-1)}}\left(\mathrm{L}^{1-\mathrm{b}} - \mathrm{L}^{*(1-\mathrm{b})}\right) - \ln\left(\frac{\mathrm{L}}{\mathrm{L}^{*}}\right)^{\mathrm{b}}\right] \tag{4}$$

MJ2 Model. The MJ2 model was suggested by Mydlarz and Jones with two parameters and the equation is shown as

$$G(L) = G_m[1 - \exp(-aL)] \tag{5}$$

$$b = a\tau G_m$$

The population balance equation in accordance with MJ2 model can be defined as

$$n(L) = n^{*} exp[a(L - L^{*})]\left(\frac{\exp(aL) - 1}{\exp(aL^{*}) - 1}\right)^{\frac{(-1-b)}{b}} \tag{6}$$

MJ3 Model. Mydlarz and Jones three-parameter model (MJ3) was improved from MJ2 model, the equation is

$$G(L) = G_m\left[1 - \exp[-a(L + c)]\right] \tag{7}$$

$$\mathrm{b} = \mathrm{a\tau G_m}$$

By replacing Eq. (9) into the general population equation, the following population balance equation is obtained as

$$n(L) = n_0 \exp(aL)\left(\frac{\exp[a(L + c)] - 1}{\exp(ac) - 1}\right)^{\frac{(-1-b)}{b}} \tag{8}$$

a, b, c are the growth model parameters. G_0 is the growth rate of nuclei, G_m is the limiting growth rate of large crystal, L* is the chosen crystal size, and n* is population density at L*[2-9]. In this study, the modified procedure of models was used and the experimental data concerning crystallization kinetics of calcium sulfate dihydrate were presented. The kinetic parameter values were evaluated according to size-independent and size-dependent growth models.

MATERIALS AND METHODS

Chemicals

The solution of calcium carbonate ($CaCO_3$) and sulfuric acid (H_2SO_4) were prepared with distilled water. Calcium carbonate and sulfuric acid were used to prepare formation of calcium sulfate dihydrate crystals ($CaSO_4.2H_2O$) and were supplied by Merck Company. In addition, oxalic acid ($C_2H_2O_4$) was used as additive in this study.

Experimental procedure

Calcium carbonate solution (20% w/w) was reacted with sulfuric acid (20% w/w) solution in 1-liter double jacketed glass crystallizer in pure media and in the presence of oxalic acid at a residence time of 0.5 h, 2.5 pH and 65°C to carry out calcium sulfate dihydrate crystallization. The experiments were conducted at three different oxalic acid concentrations as 250 ppm, 1000 ppm and 2500 ppm. The exact control of temperature within the crystallizer was achieved using a thermostatted system. During the experiments, pH in the crystallizer was kept at 2.5 by feeding concentrated sulfuric acid solution. Stirring of the solution was performed via a three-blade propeller located in the center of crystallizer including three flow breakers and one draft-tube. The feed solutions were continuously fed into the crystallizer using peristaltic pumps. At the end of each experiment, the crystals were separated from suspension via vacuum filtration and washed with saturated calcium sulfate solution. Then the crystals dried at room temperature to constant weight. The obtained crystals were subjected to morphology observation by scanning electron microscopy (SEM) to investigate the change of crystal habit and the zeta potential of the produced crystals were also measured. The crystal size distribution was gathered via laser diffraction particle size analyzer. Furthermore, the values of kinetic parameter were calculated in accordance with size-independent and size-dependent growth models.

RESULTS AND DISCUSSION

In this study, the effect of oxalic acid over the growth rate of calcium sulfate dihydrate was investigated and the kinetic parameters were evaluated according to size-independent growth model and size-dependent growth models using population balance theory. Figure 1 demonstrated both linear regression between population density ln (n) and crystal size (L) and the relation of different models estimation with experimental data. When Figure 1 was examined, the deviation was observed from McCabe's ΔL law and the size independent growth rate model was not appropriate for describing the crystal growth of calcium sulfate dihydrate. In the present study, the size dependent growth was considered and Bransom, MJ2, and MJ3 size dependent growth models were utilized to describe the growth rate of calcium sulfate. The kinetic parameters of these models were determined using modified population balance equations and the parameters values were given in Table 1.

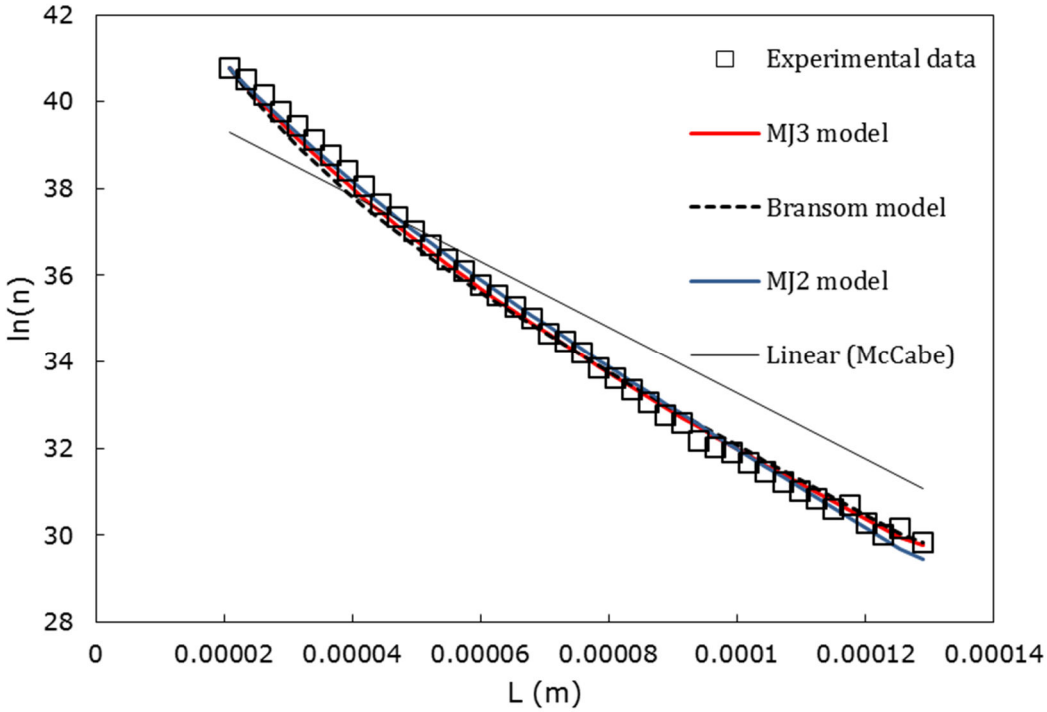

Figure 1. Population density evaluation according to the size-independent and size dependent models for calcium sulfate dihydrate obtained in the presence of 1000 ppm oxalic acid.

Table 1. Kinetic parameters of Bransom, MJ2 and MJ3 models.

Oxalic Acid Concentration	Model	Model parameters			
		$a \times 10^6$ (m^{-1})	b	$c \times 10^6$ (m)	$G_m \times 10^{-8}$ ($m.s^{-1}$)
Pure media	Bransom	4	0.456	-	-
	MJ2	0.020	0.402	-	1.117
	MJ3	0.005	0.201	40.8	2.233
250 ppm	Bransom	3.8	0.400	-	-
	MJ2	0.031	0.480	-	0.860
	MJ3	0.016	0.219	40.2	0.760
1000 ppm	Bransom	5	0.340	-	-
	MJ2	0.029	0.380	-	0.728
	MJ3	0.024	0.280	39	0.648
2500 ppm	Bransom	3.2	0.500	-	-
	MJ2	0.031	0.380	-	0.681
	MJ3	0.018	0.130	37.0	0.040

In order to find the model which best fitted the experimental data, relative coefficient, mean square error and mean square deviation of each model were evaluated and the results were presented in Table 2. By comparison, it was found that the MJ3 size-dependent growth model was the best model to characterize the experimental data with high relative coefficient and small square deviation.

Table 2. R, MSE and variance values for the kinetic models.

Oxalic Acid Concentration	Model	R	MSE	Variance
Pure media	McCabe ΔL	0.9758	-	-
	Bransom	0.9989	0.4072	0.0171
	MJ2	0.9984	0.4744	0.0242
	MJ3	0.9991	0.3496	0.0128
250 ppm	McCabe ΔL	0.9742	-	-
	Bransom	0.9984	0.5817	0.0416
	MJ2	0.9986	0.4743	0.0242
	MJ3	0.9992	0.3442	0.0124
1000 ppm	McCabe ΔL	0.9882	-	-
	Bransom	0.9978	0.0571	0.7898
	MJ2	0.9984	0.0725	0.7765
	MJ3	0.9991	0.0330	0.5402
2500 ppm	McCabe ΔL	0.9759	-	-
	Bransom	0.9995	0.7003	0.0522
	MJ2	0.9988	0.4849	0.0278
	MJ3	0.9997	0.3178	0.0130

The MJ3, a three-parameter growth rate model, also satisfied all essential size dependent growth model conditions because of predicting zero-size crystal growth. Therefore, the MJ3 size dependent growth rate model could predict the calcium sulfate dihydrate growth rate well all through the entire size range. Application of MJ3 model to the experimental data, nucleation rates was calculated range from 2.8×10^{9} to 7.8×10^{9} $m^{-3}.s^{-1}$ and as the concentrations of oxalic acid increased, the nucleation rates of crystals decreased. It was determined that oxalic acid as additive in the media affected the calcium sulfate dihydrate growth rate. In other words, growth mechanism of the crystals was changed in the presence of oxalic acid. This situation was supported by SEM analysis and zeta potential measurements.

The SEM image of the calcium sulfate dihydrate crystals obtained in pure media was given in Figure 2. As can be clearly seen in Figure 2, calcium sulfate dihydrate crystals were of needle-like shape in pure media. While the calcium sulfate dihydrate crystals produced in the presence of 2500 ppm oxalic acid preserved basically the same needle-like form, the length/width ratio of the crystals decreased compared to the crystals obtained in the pure media. That is oxalic acid favored the formation of needle shaped crystals smaller, thinner, and weaker than the crystals obtained in pure media. This kind of weak structures could be broken easily by the hydrodynamic conditions of the media [10].

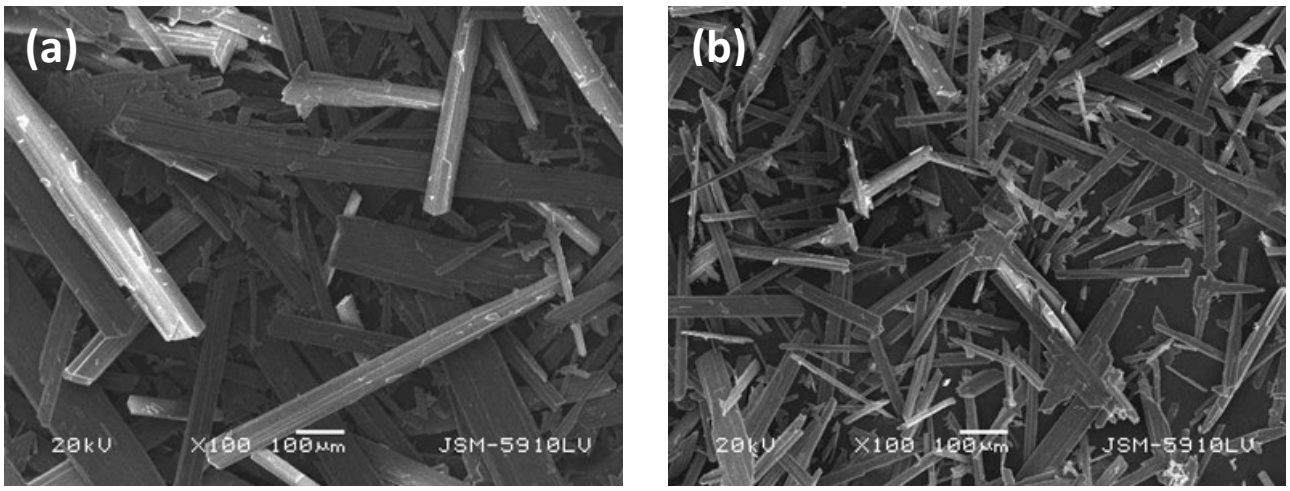

Figure 2. SEM images of the calcium sulfate dihydrate crystals. (a) Pure media (b) 2500 ppm oxalic acid.

The results of zeta potential measurements were given in Figure 3. As seen on Figure 3, calcium sulfate dihydrate crystals produced in pure media had a -13.3 mV surface charge in its own saturated solution.

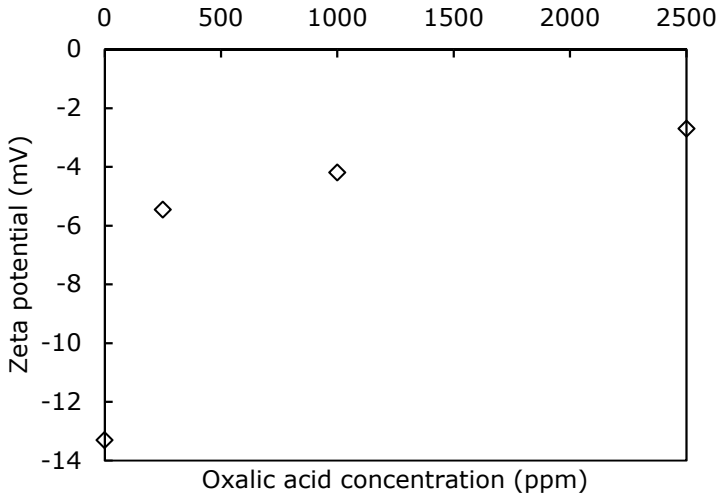

Figure 3. Influence of oxalic acid concentration on zeta potential of calcium sulfate dihydrate.

Oxalic acid had a significant effect on the surface charge of crystals. As the oxalic acid concentration increased from 0 to 2500 ppm, the zeta potentials of crystals varied from -13.3 mV to -2.7 mV. This change that occurred in the zeta potential values indicated that oxalic acid could adsorb on the crystal surface.

CONCLUSIONS

The crystallization kinetic models of calcium sulfate dihydrate in pure media and in the presence of oxalic acid were studied. It was detected that the growth rates of calcium sulfate dihydrate crystals depend on crystal size. Evaluations were carried out in accordance with the Bransom,

MJ2, and MJ3 size-dependent growth models. By comparison of experimental population density data obtaining from these models, it was determined that the MJ3 model was the most appropriate model among the other used models. It was also found that oxalic acid in the media affected both crystal shape and crystal growth rate.

ACKNOWLEDGMENTS

This work was supported by Marmara University Scientific Research Projects Commission under the funding BAPKO FEN-A-080715-0340.

REFERENCES

1. Titiz-Sargut S, Sayan P, Avcı B. Influence of citric acid on calcium sulfate dihydrate crystallization in aqueous media. Cryst Res Technol. 2007; 42(2):119-126. DOI: 10.1002/crat.200610783.

2. Mydlarz J, Jones A.G. On numerical computation of size-dependent crystal growth rates. Computers Chem. Eng. 1989; 8:959-965. DOI: 10.1016/0098-1354(89)85068-9.

3. Mullin, J.W. Crystallization. London: 4rd Edition; Butterworth-Heinmann, Oxford; 2001.

4. Wierzbowska B, Piotrowski K, Koralewska J, Hutnik N, Matynia A. Kinetics of nucleation and growth of L-sorbose crystals in a continuous MSMPR crystallizer with draft tube: Size-independent growth model approach. Korean J. Chem. Eng. 2009; 26:175-181. DOI: 0.1007/s11814-009-0029-6.

5. Mydlarz J, Jones A.G. On the estimation of size-dependent crystal growth rate functions in MSMPR crystallizers. Chem. Eng. J. 1993; 53:125-135. DOI: http://dx.doi.org/10.1016/0923-0467(93)85003-E.

6. Mydlarz J, Jones A.G. An assessment of MSMPR crystallization kinetics data for systems modelled by size-dependent crystal growth rate functions. Chem. Eng. J. 1994; 55:69-80. DOI: http://dx.doi.org/10.1016/0923-0467(94)87008-X.

7. Li X, Song X, Liu G, Yu J. Size-dependent nucleation and growth kinetics model for potassium chloride—Application in Qarhan salt lake. J. Cryst. Growth. 2009; 311:3167-3173. DOI: http://dx.doi.org/10.1016/j.jcrysgro.2009.03.007.

8. Hongxun H, Jingkang W, Yongli, W, Baohong H. Crystal growth models of dexamethasone sodium phosphate in a MSMPR reactive crystallizer. Chinese J. Chem. Eng. 2005; 13(3):350-354. URL: http://www.cjche.com.cn/EN/article/downloadArticleFile.do?attachType=PDF&id=687.

9. Mydlarz J. Modeling of crystal size distribution in a mixed suspension, mixed product removal crystallizer when growth is size dependent, Separ. Technol. 1993; 3(4):212-220. DOI: http://dx.doi.org/10.1016/0956-9618(93)80020-R.

10. Sayan P, Titiz-Sargut S, Avcı B. Effect of trace metals on reactive crystallization of gypsum. Cryst Res Technol. 2007; 42(10):961-970. DOI: 10.1002/crat.200710939.

Türkçe Öz ve Anahtar Kelimeler

Oksalik Asit Varlığında Kalsiyum Sülfat Dihidratın Büyüme Kinetiği

Sevgi POLAT, Sibel TİTİZ-SARGUT, Perviz SAYAN

Öz: Bu çalışma, kalsiyum sülfat dihidratın kristalizasyon kinetiği üzerine odaklanmaktadır. Kalsiyum sülfat dihidrat kristalizasyonu, sürekli beslemeli ve sürekli ürün çekişli (MSMPR) bir kristalizörde saf ortamda ve 250, 1000 ve 2500 ppm oksalik asit konsantrasyonlarında gerçekleştirilmiştir. Kalsiyum sülfat dihidrat kristallerinin büyüme kinetiği tane boyutundan bağımsız ve tane boyutuna bağlı büyüme modellerine göre analiz edilmiştir. Kalsiyum sülfat dihidrat kristal büyüme hızının tane boyutuna bağlı olduğu bulunmuş ve kinetik parametreler Bransom, MJ2 ve MJ3 modellerine göre değerlendirilmiştir. Ayrıca korelasyon katsayı, ortalama hata karesi ve varyans değerleri her model için hesaplanmış; MJ3 modelinin sistemi en iyi karakterize eden model olduğu bulunmuştur.

Anahtar kelimeler: Kalsiyum sülfat dihidrat; kristalizasyon kinetik modelleri; oksalik asit.

Sunulma: 08 Ekim 2016. **Düzeltme:** 17 Kasım 2016. **Kabul:** 19 Kasım 2016.

This article was initially submitted to the UKMK 2016 (National Chemical Engineering Congress) and finally evaluated by the JOTCSB editorial staff.

Improvement of the Sorption Performance of Nanosilica and Polymeric Solid Supports by Impregnation with Ionic Liquid for the Removal of Cr(VI) Ions from Aqueous Solutions

Nilay Gizli[1]*, Merve Arabacı[1]

[1]Ege University, Faculty of Engineering, Chemical Engineering Department, 35100, Bornova İzmir-Turkey.

Abstract: In this study, supported ionic liquid phase (SILP) adsorbents were prepared by immobilizing the ionic liquids (ILs) onto nanosilica and styrene-divinylbenzene copolymer (SDVB) particles for the removal of hexavalent chromium, Cr(VI) ions from aqueous solutions. Three types of ionic liquids such as tricapryl methyl ammonium nitrate [A336][NO_3], tricapryl methyl ammonium chloride (Aliquat® 336) and 1-ethyl-3-methylimidazolium bis(trifluoromethylsulfonyl)imide (EMIMTf_2N) were successfully impregnated onto solid supports by following physical impregnation method through ultrasonication. The structural and morphological characterizations of the adsorbents were investigated by FTIR, SEM, and BET analysis. The thermal stabilities of the ionic liquid impregnated solid particles were also characterized by TGA analysis. Metal sorption performances of the prepared sorbents were investigated by considering Cr(VI) ions' sorption regarding the thermodynamic and kinetic aspects. The effects of various analytical parameters on the sorption of Cr(VI) ions such as IL loading ratio, pH of the solution, adsorbent dosage, initial metal ion concentration were studied. Cr(VI) ions were quantitatively adsorbed in the pH range of 2-4 with the impregnation ratio of 1 g-IL/g-support by all type of adsorbents. Moreover, the removal percentages of chromium ions were found to be 99.53%, 99.50% and 100% for TT600-TS, MOX80-TS and XAD-A, respectively. Sorption isotherms were also fitted with Langmuir equation and they were exhibited favorable sorption behavior.

Keywords: Adsorption; ionic liquid; supported ionic liquid phase (SILP); chromium.

Submitted: October 03, 2017. **Revised:** November 16, 2016. **Accepted:** December 03, 2016.

Cite this: Gizli N, Arabacı M. Improvement of the Sorption Performance of Nanosilica and Polymeric Solid Supports by Impregnation with Ionic Liquid for the Removal of Cr(VI) Ions from Aqueous Solutions. JOTCSB. 2016;1(1):49–70.
*Corresponding author. E-mail: nilay.gizli@ege.edu.tr.

INTRODUCTION

In recent years, various methods have been extensively studied for the removal of heavy metal ions from wastewater. These technologies include chemical precipitation (1), ion-exchange (2), adsorption (3), membrane filtration (4), coagulation, flocculation, flotation, and electrochemical methods (5). Among all these methods, adsorption is considered as the effective technique for the removal of heavy metals from wastewater (6). Generally, there are several factors specifying the efficiency of the adsorption such as the surface area, pore size, and distribution as well as the surface chemistry of the adsorbents. Porous materials (*e.g.* silica, macroporous polymer beads) are employed as promising sorbents for heavy metal removal due to their good physicochemical properties such as porosity and high surface area. However, they do not lead satisfactory efficiency with respect to weak binding properties (7). Consequently, the modification of porous sorbents by immobilization or incorporation of the functional groups is particular concern to increase the surface adsorption and to enhance the removal efficiency. In many applications, ionic liquids (ILs) can be used as chelating agent due to their unique properties (8).

ILs are salts consisting completely of organic cations and inorganic or organic anions. Their better charge distribution and larger ion size compared to classical inorganic salts result in melting points below 100 °C. By variation of anions and cations, solubility, reactivity, and coordination properties of the ILs can be changed according to the special requirements of the given application (9). Their applications in separation processes are very promising because of their unique properties, such as negligible vapor pressure, good thermal stability, tunable viscosity and miscibility with water and organic solvents, and high ionic conductivity (10). In recent years, ILs have been immobilized onto silica or polymeric supports (known as supported ionic phases-SILPs) in order to combine the advantages of IL with those of porous solid supports (11). SILP technology is regarded as a fundamental and new approach to obtain liquid-containing solid materials that do not evaporate, made through surface modification of porous solid by dispersing a thin film of ILs onto it (9). SILP are resulting in materials of low toxicity, which are environmentally benign and have a wide range of separation applications. These materials are prepared by covalent attachment of an IL to a support surface or simply impregnation of the IL phase (12).

In recent years, several researchers have focused on the use of novel adsorbents impregnated with ionic liquids (3, 8-11). Al-Bishri *et al.* investigated the uptake of lead from the aqueous solution by imidazolium-based ionic liquid impregnated onto nano-silica

sorbents (13). Lupa *et al*. immobilized the aminophosphate-based ionic liquid onto the organic and inorganic supports in order to be used as adsorbents for the removal of thallium from aqueous solutions (14,15). Navarro *et al*. investigated the bismuth(III) recovery from hydrochloric acid solution using Amberlite XAD-7 impregnated with a tetraalkylphosphonium ionic liquid (16). The improvement of Cu (II) ion sorption performance of the nano-silica and nano-alumina particles by the immobilization of 1-ethyl-3-methyl imidazolium bis (trifluorosulfonyl) imide [$Emim^{+}Tf_2N^{-}$] ionic liquid was investigated by Gizli and Arabacı (8).

In this study, the enhancement of Cr(VI) ion's sorption performance of the nanoparticles and polymeric supports were investigated by modifying them with three different types of ionic liquids. The diversity of support and ILs were selected of different porous properties and chemical structure among those commonly used in heavy metal removal processes. Modification was achieved via ultrasound-assisted physical impregnation method. Ultrasonification, as an unconventional method, is less time-consuming and ensures the effective distribution of IL onto solid supports (17). The physicochemical and morphological characteristics of the prepared adsorbents were investigated by Fourier-Transform Infrared Spectrospy (FTIR), Scanning Electron Microscopy (SEM), Brunauer–Emmett–Teller (BET) surface area analysis. On the other hand, thermal behaviors of the adsorbents were investigated by Thermal Gravimetric Analysis (TGA). Cr(VI) ion sorption performance of adsorbents have been examined by considering the effect of sorption conditions (pH of solution, initial concentration, adsorbent dose) and loading ratio of IL per unit mass of solid supports. Fixed bed column sorption studies were also carried out to obtain the breakthrough performances of SILPs.

MATERIAL AND METHOD

Chemicals

In this study, three types of ionic liquids such as tricapryl methyl ammonium chloride [A336][Cl] known as Aliquat® 336, 1-ethyl-3-methylimidazolium bis(trifluoromethylsulfonyl)imide [$EMIMTf_2N$] and tricapryl methyl ammonium nitrate [A336][NO_3] were used. Although [A336][Cl] and $EMIMTf_2N$ was obtained from Sigma Aldrich, [A336][NO_3] was synthesized. Chemical structures of ionic liquids are shown in Figure 1.

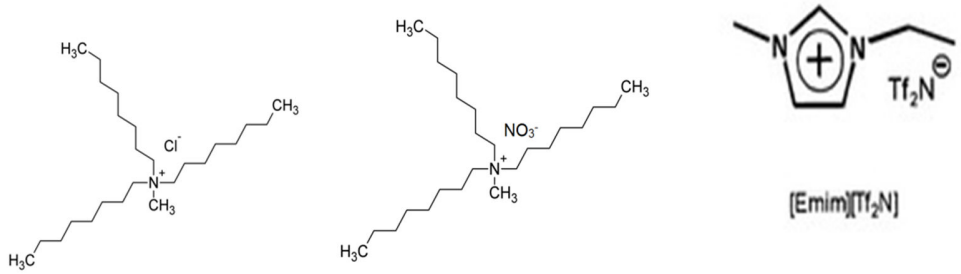

Figure 1 Chemical structures of ionic liquids.
a) Aliquat® 336 (left), b) [A336][NO_3] (middle), c) [EMIMTf_2N] (right).

The stock solution of Cr(VI) (1000 mg/ L) was prepared by dissolving an appropriate amount of $K_2Cr_2O_7$ in deionized water. The working solutions of different concentrations were prepared by diluting the stock solution. The $K_2Cr_2O_7$ salt was supplied from Merck, Germany.

Nano-silica (Aerosil TT600 and Aerosil MOX 80) particles from Evonic Industries and polymeric particles *(*Amberlite XAD-16) from Fluka, were used as supporting materials*.* Properties of polymeric and nanoparticles are given in Table 1 and Table 2, respectively.

Table1. Properties of polymeric support (Amberlite XAD-16).

Properties	**Value**
Density (dry) [g/mL]	1.08
Surface area [m^2/g]	900
Pore Size [A°]	100
Mesh size (wet)	20-60
Pore Volume [mL/g]	1.82

Table 2. Properties of nanoparticles.

	Commercial Name	
Properties	**Aerosil TT600**	**AerosilMOX80**
Particle Size [nm]	40	30
Surface Area[m^2/g]	200	80
pH	3.5-4.5	3.5-4.5
Content	SiO_2 (%100)	SiO_2(%99)/Al_2O_3 (%1)

EXPERIMENTAL PROCEDURE

Task-Specific Ionic Liquid Synthesis

Task-specific ionic liquid, A336 [NO_3] was prepared by anion metathesis reaction as shown in the following equation.

$$A336\ [Cl] + KNO_3 \rightarrow A336\ [NO_3] + KCl \quad \text{(Eq. 1)}$$

To achieve the reaction, commercial Aliquat® 336 ionic liquid and 2 M of KNO_3 solutions were contacted for 1 hour during vigorous stirring. The phases were then separated by using a separating funnel followed by washing with distilled water. These steps were repeated for 4 times. Completion of the reaction was controlled by checking the Cl^-ion content of the ionic liquid by using $AgNO_3$ indicator.

Preparation of the Ionic Liquid Impregnated Adsorbents

SILP adsorbents were prepared by the impregnation of the ionic liquid onto polymeric- and silica-based nanoparticle supports through ultrasound-assisted physical impregnation method (18). The solid supports were immersed into 25 mL of ethanol to swell in the solvent media. Then, a proper amount of ionic liquid was added and sonicated at a frequency rate of 35 Hertz during 60 minutes. The particles were then left to dry at ambient conditions. The IL content of adsorbents were varied between 0.1 ~ 2.0 g-IL/g-solid support and the prepared SILPs are abbreviated as given in the Table 3.

Table 3. Abbreviation of prepared SILPs.

ID	Ionic Liquid	Solid Support	Structure of Solid Support
XAD-A	Aliquat 336	XAD-16	SDVB polymer
XAD-TS	[A336] [NO_3]	XAD-16	SDVB polymer
XAD-IL	[EMIMTf_2N]	XAD-16	SDVB polymer
TT600-A	Aliquat 336	Aerosil TT600	Silica based nano particles
TT600-TS	[A336] [NO_3]	Aerosil TT600	Silica based nano particles
TT600-IL	[EMIMTf_2N]	Aerosil TT600	Silica based nano particles
MOX80-A	Aliquat 336	Aerosil MOX 80	Silica based nano particles
MOX80-TS	[A336] [NO_3]	Aerosil MOX 80	Silica based nano particles
MOX80-IL	[EMIMTf_2N]	Aerosil MOX 80	Silica based nano particles

Characterization of Adsorbents

The chemical structures of prepared SILPs were investigated by a Fourier Transform Infrared Spectrometer (FTIR), (Perkin Elmer Spectrum 100) within the wavenumber range of 650-4000 cm^{-1} to identify the functional groups both before and after the modification of the

support materials with IL. The surface morphologies of adsorbents were analyzed by using Scanning Electron Microscopy (SEM), (Philips XL 30S FEG) operating at an accelerating voltage of 2.00 kV. The particles were coated with a gold layer in order to make them conductive. Surface areas and pore volumes of silica adsorbents were investigated by Brunauer–Emmett–Teller (BET) analysis (Micromeritics Gemini V model). Thermal Gravimetric Analysis (TGA) was carried out using Perkin Elmer Diamond TG/DT model to investigate thermal behavior of the support materials before and after modification with IL.

Adsorption Studies

Batch Sorption Studies*:* Adsorption studies were carried out by contacting 10 mL of Cr(VI) (50 mg/L) solution with 0.2 g SILP at 25°C during 24 h. Chromium ion concentrations were measured by Atomic Absorption Spectrophotometer (AAS) (Varian 10+) before and after adsorption studies.

The uptake of Cr(VI) by the adsorbent was calculated from the following equation,

$$q_e = \frac{(C_0 - C_e) * V}{W} \quad \text{(Eq. 2)}$$

Where q_e is the uptake of Cr(VI) by SILP at equilibrium (mg/g), C_0 and C_e are the initial and equilibrium Cr(VI) concentrations in the aqueous phase (mg/L), V is the volume of solution (mg/L), and W is the amount of adsorbent (g).

The sorption percentage of the nanoparticles was calculated as given in Equation (3),

$$Sorption(\%) = \frac{(C_0 - C_e)}{C_0} * 100 \quad (3)$$

Column Sorption Studies*:*

Column sorption studies were carried out by passing 0.01 M of Cr(VI) solution through a packed bed column having 0.7 cm inner diameter and filled with 1 mL of adsorbent. The flow rate of the solution has been fixed as 15 bed-volumes per hour (BV/h) by the help of peristaltic pump (Peristaltic PR-2003).

RESULTS AND DISCUSSION

Characterization of Adsorbents

The FTIR spectra of nanoparticles (TT600 and MOX80) before and after modification with $EMIMTf_2N$ ionic liquid are shown in Figure 2.

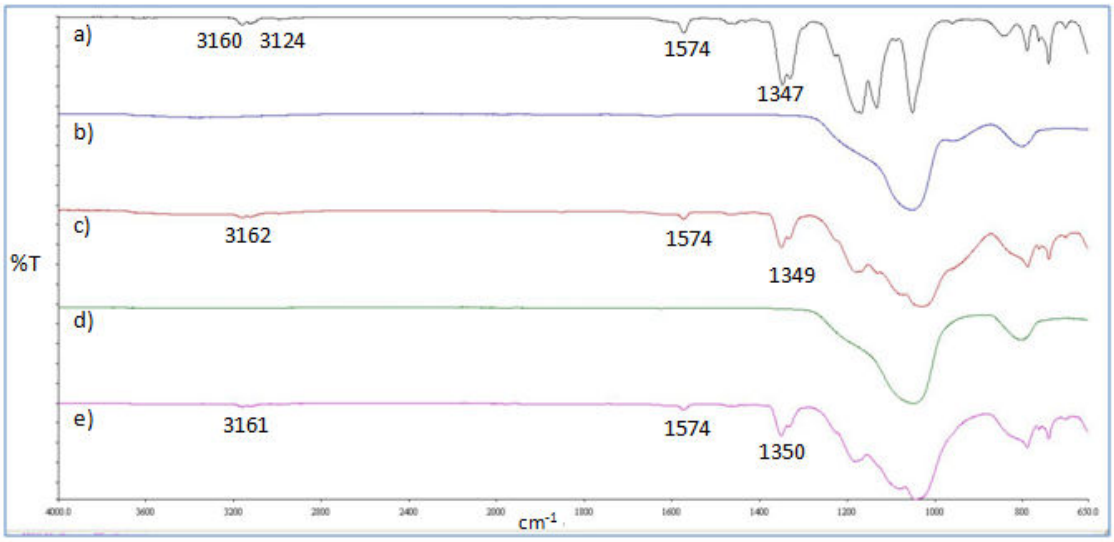

Figure 2. FTIR spectrum of nanoparticles prepared with [$EMIMTf_2N$].
a) $EMIMTf_2N$ ionic liquid b) TT600- before modification c) TT600-after modification d) MOX80-before modification e) MOX80- after modification.

The characteristic peaks of the $EMIMTf_2N$ ionic liquid are seen around 3160 cm^{-1} and 1574 cm^{-1} in Figure 2-a can be attributed to the C-H and C=C vibrations of the imidazole ring of ionic liquid. In addition, the infrared region of the ionic liquid spectrum between 1400 cm^{-1} and 1000 cm^{-1} is mainly dominated and characterized by several peak assignments that are related to the anionic moiety (19). In all spectra of the silica nanoparticles (Figure 2 b,c,d,e), the bands around 1090 cm^{-1} assigning the stretching vibrations of the Si-O-Si groups of the silica backbone are observed. It can also be seen in all the spectra of modified nanoparticles that two new absorption peaks at the position of 3161 cm^{-1} and 1574 cm^{-1} appeared after nanoparticles are treated with IL. These adsorption peaks confirm the modification of nanoparticles with ionic liquid.

The FTIR spectrum of SDVB particles (XAD-16) before and after modification with [A336][NO_3] ionic liquid is shown in Figure 3.

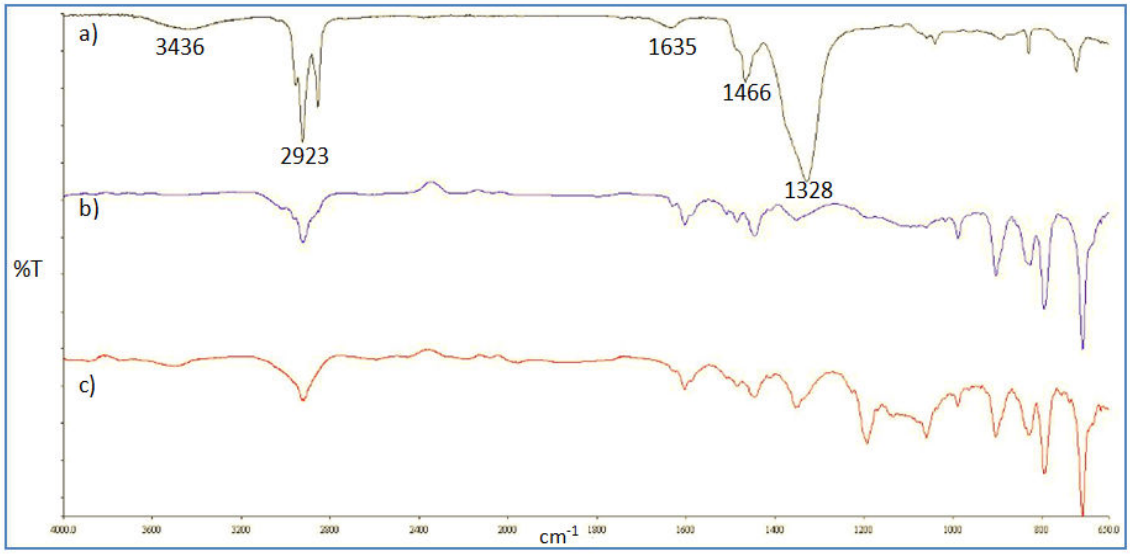

Figure 3. FTIR of p-SILP prepared with [A336][NO_3] a) ionic liquid [A336][NO_3]. b) XAD-16- before modification c) XAD-TS after modification.

In the spectra of [A336][NO_3] (Figure 3.a), the peaks around the position of 2923 cm^{-1} can be attributed to the characteristic absorption of -CH_3 of alkyl chain and at the position of 1466 and 1328 cm^{-1} are based on the structure of quaternary ammonium moiety of the ionic liquid. The peak located at 1328 cm^{-1} (Figure 3-c) is pronounced after modification of polymer particles with ionic liquid.

The morphological change of polymeric support by modification with A336 [NO_3] can be quantified from SEM images presented in Figure 4.

It is evident from Figure 4 that immobilization of the ionic liquid on the surface of polymeric particles lead to a characterized change on the morphology. It is clearly observed that porous structures of the particles are filled with ionic liquid.

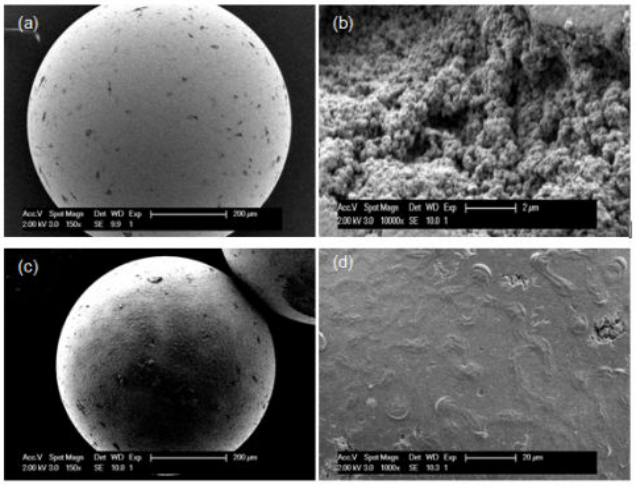

Figure 4. SEM images of SILP adsorbent (loading ratio = 1:1 [g-IL: g-support]). a) Before impregnation (X150), b) Before impregnation (X10000), c) After impregnation (X150), d) After impregnation (X1000).

The change in surface morphology of nanoparticles by immobilization of IL at various ratios is shown in Figure 5.

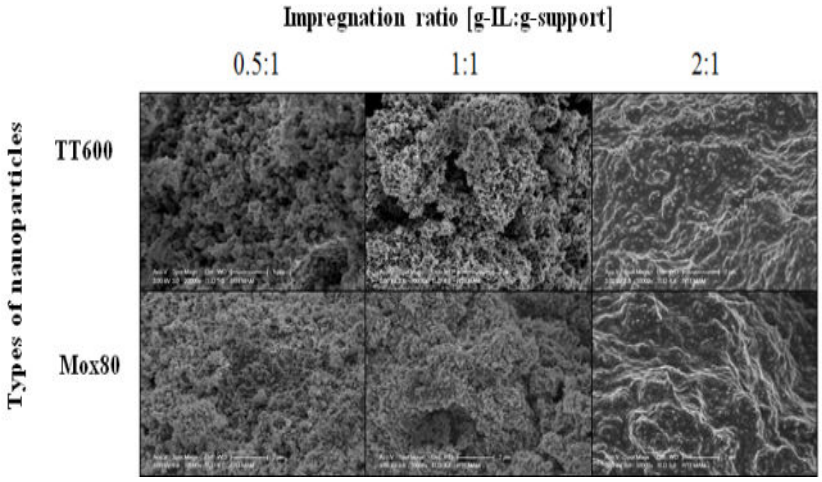

Figure 5.SEM images of nanoparticles impregnated with ionic liquid at the loading rate of 0.5:1, 1:1, 2:1 (g-IL: g-support).

It is evident from Figure 5 that immobilization of IL on the surface of the nano-silica and nano-alumina particles resulted in a pronounced and characterized change on the surface morphology. It is clearly observed that ILs cover the surface of the nanoparticles which lead to a decrease in the surface area by modification.

The surface pore characteristics of the solid supports modified by various amount of ILs were examined by BET and surface area analyzer. BET results are given in Supplementary

Documents, (Tables A1 and A2 and Figure A1). In BET analysis results, there are noticeable declines in the surface area (m^2/g) pore volume (cm^3/g) and pore size values after modification of the all type of solid supports with ionic liquid. Surface area of nanoparticles decreased from 200 (m^2/g) to 9.3 (m^2/g) for TT600 and from 80 (m^2/g) to 19.7 (m^2/g) for MOX80. All support materials follow the same trend as drastic decline in the surface area with increasing in the ionic liquid loading ratio. These can be concluded that ILs are filled into the pores of solid supports.

Thermal behaviors of the adsorbents were characterized by TGA analysis (given in the Supplementary Document). It is evident from Figure 2.A that [$Emim^+Tf_2N^-$] started to decompose at 350 °C and decomposed almost completely at 500 °C. The weight loss of the nanoparticle adsorbents prepared at the impregnation ratio of 1:1 (g-IL/g-support) were below 3% at the temperature range of 20-350 °C. However, the nanoparticle supports started to decompose at moderately low temperatures (around 30 °C) and the mass loss of all types of nanoparticles were around 15% at the temperature range of 20-600 °C. SDVB polymeric type solid support also started to decompose at the temperatures below 100 °C but decomposition temperature of such type of supports were elevated to 200 °C by modification with ionic liquids. It can be concluded that the immobilization of ionic liquids may lead to improvement in the thermal stability of nano-silica and SDVB polymeric particles at the temperature range of 20-300 °C.

Cr(VI) Adsorption Experiments

Batch Sorption Studies: A series of batch sorption tests were carried out to obtain the optium sorption parameters such as adsorbent type, adsorbent dose, pH and concentration of adsorbate for the removal of Cr(VI) from aqueous solutions.

The results of the a comparative study for the sorption performance of prepared sorbents are shown in Figure 6.

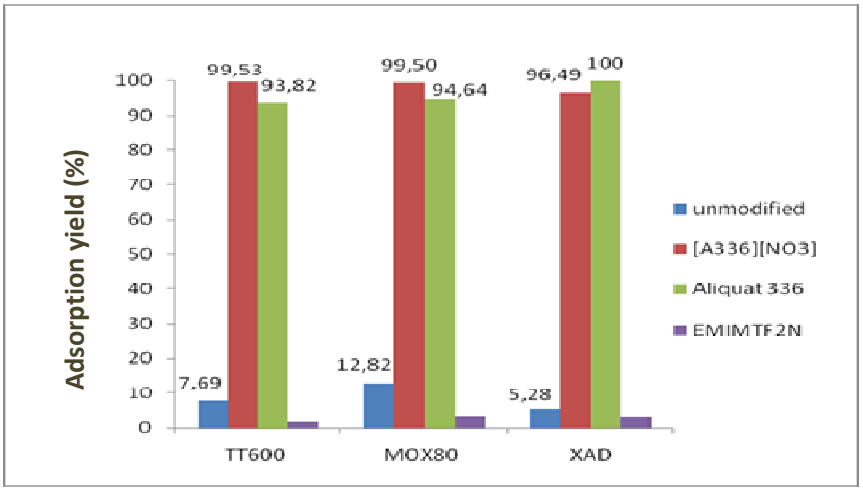

Figure 6. Adsorption performance of prepared adsorbents for Cr(VI) removal.

As seen in Figure 6, it is clearly observed that there is a significant increase in the adsorption percentage of all type of support materials after modification with Aliquat® 336 and A336[NO_3] type ionic liquids. Adsorption yield of polymeric (XAD) adsorbent is increased from 5.28% to almost 100% after impregnation with Aliquat® 336 and A336[NO_3]. Similar adsorption performances are also achieved by TT600 and MOX 80 nanoparticles. However, the sorption performances of all type of sorbents containing EMIMTf_2N ionic liquid dramatically decreased comparing to the others. It can be concluded that Aliquat® 336 and A336[NO_3] type ionic liquids might be attached to the solid support by electrostatic interactions and sorption takes place under the effect of anion exchange reaction. Since Cr(VI) occurs predominantly in the form of $(HCrO_4)^-$ ions in aqueous phase at working pH value. On the other hand, EMIMTf_2N ionic liquid does not play a role in an ion exchange reaction and repulsion effect is observed for that working pH range.

Effect of IL Loading Ratio on the Sorption of Cr(VI) Ions

The effect of the amount of ionic liquid loading ratio on the Cr(VI) adsorption percentages were investigated by using SILP containing various amount of IL(g) per solid support (g). The impregnation ratio was selected as 0.2:1, 0.5:1, 0.7:1, 1:1, 1.2:1, and 2:1 (g-IL/g-support). The effect of IL loading ratio on Cr(VI) removal performances for XAD, TT600, and MOX 80 are shown in Figure 7-9, respectively.

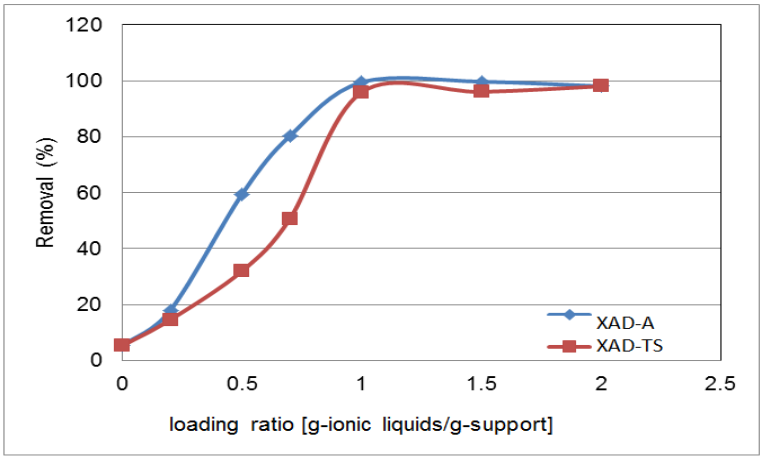

Figure 7. Effect of ionic liquid loading ratio on Cr(VI) removal performance of XAD supports.

At these conditions, it can be clearly seen from Figure 7 the increasing in the IL loading ratio of both XAD-A and XAD-TS increase the percentage of adsorption until the loading ratio of (1:1 g-IL/g-support and adsorption percentages are found nearly 100% and 96% for XAD-A and XAD-TS, respectively.

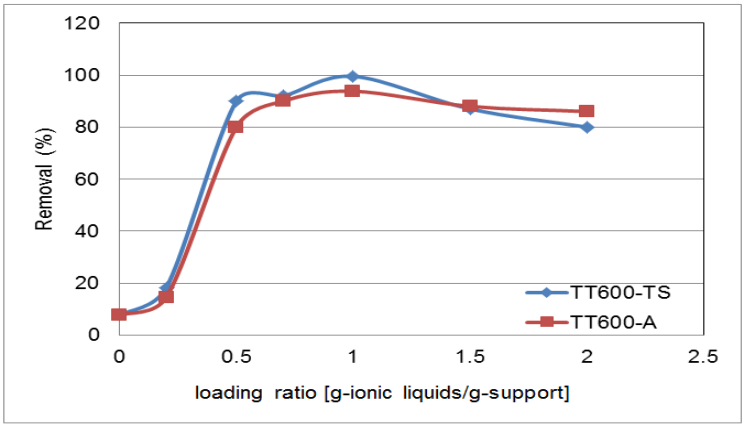

Figure 8. Effect of ionic liquid loading ratio on Cr(VI) removal performance of TT600.

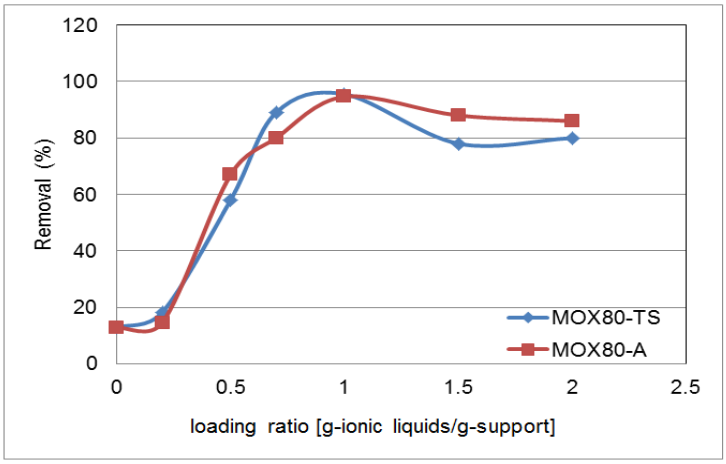

Figure 9. Effect of ionic liquid loading ratio on Cr(VI) removal performance of MOX 80.

In Figures 8 and 9, it is clearly seen that up to a certain value (1 g /g support) the adsorption yield of the ionic liquid increases with increasing loading ratios. After this value, it can be attributed that adsorption yield decreases with decreasing in the value of surface area because of the filling the pores of particle with IL for nanoparticles. Impregnation with A336[NO_3] type ionic liquids demonstrated higher achievement compared to commercial ionic liquid for both MOX 80 and TT600. For further studies, IL loading ratio is chosen as 1:1 (g-IL/g-support) for all type of SILPs.

Effect of Solution pH

The solution pH is one of the most important parameter to find out the adsorption capacity of adsorbents for Cr(VI) ions.

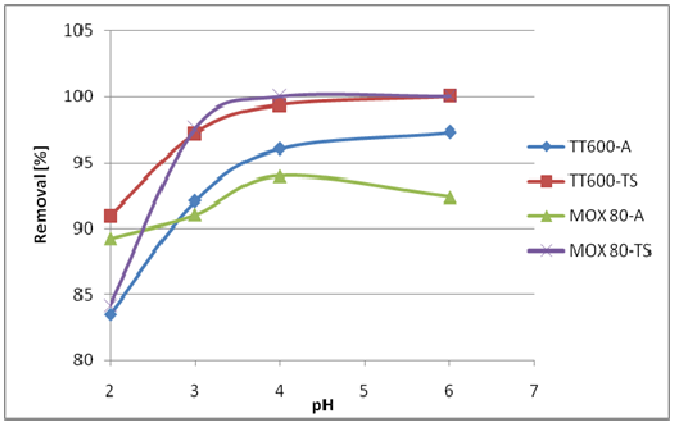

Figure 10. Effect of pH on the adsorption of Cr(VI) onto adsorbent (TT600 and MOX80).

In Figure 10, it is shown that the removal of Cr(VI) ion increases with increasing pH from 2 to 4. After the pH value of 4, nearly no further changes in percentage of adsorption yield is

observed. This situation can be explained by the predominant formation of $HCrO_4^-$ ions reacted with anionic group of ionic liquid by ion exchange reactions in pH values between 2 and 4. Above pH 4 predominantly form of $CrO_4^{2-}$was formed in the solution.

The effects of pH on the adsorption of Cr(VI) onto SILP with polymeric support are shown in the Figure 11.

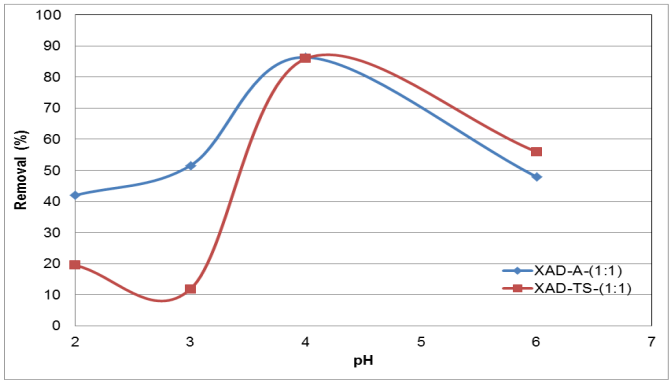

Figure 11. Effect of pH on the adsorption of Cr(VI) onto SILP adsorbent.

In Figure 11 it can be clearly seen that removal of Cr(VI) ions increases with increasing pH between 2 and 4. After pH 4, a sudden decrease is observed in the percentage removal. According to Figures 10 and 11, the optimal pH value is specified as 4.

Effect of Adsorbent Dose

The amount of sorbent significantly affects the extent of Cr(VI) sorption. Increase in sorbent dose leads to more surface areas which are available for adsorption resulting in an increase in the active sites on the sorbent. The effect of adsorbent dose (g) on the adsorption of Cr(VI) was studied in the range of 0.01~0.35 g adsorbent by contacting with 10 mL of solution at 30 °C during 24 hours. The initial concentration of Cr(VI) ion was set as 50 mg/L, and pH of the solution was adjusted to the value of 4.

The effects of adsorbent amount of nano particles (TT600 and MOX80) are shown in Figure 12 and 13.

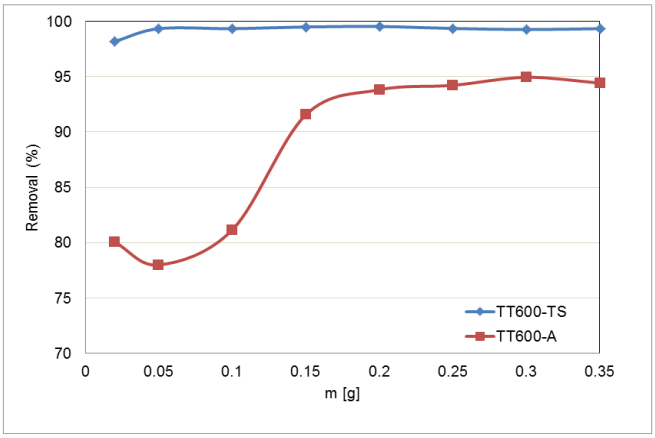

Figure 12. Effect of adsorbent dose on the adsorption of Cr(VI) onto SILP (TT600).

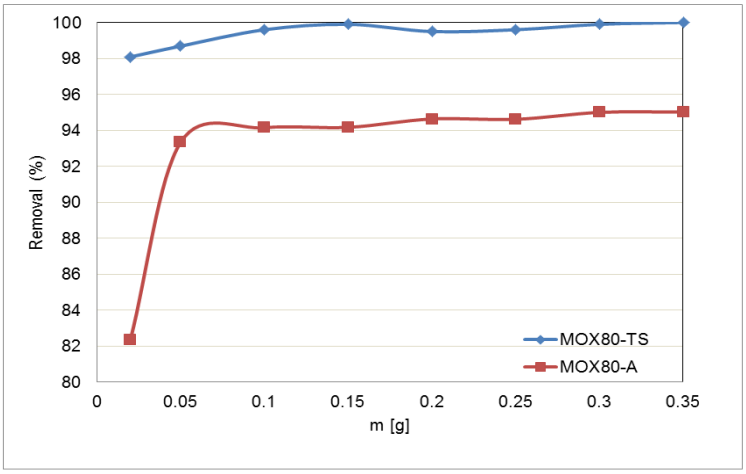

Figure 13. Effect of adsorbent dose on the adsorption of Cr(VI) onto SILP (MOX 80).

It is observed from Figure 12 and Figure 13 that the percentage removal of Cr(VI) ions reach to almost 100% for TT600-TS and MOX80-TS. Optimum adsorbent dose is determined as 0.1 g per 10 mL of Cr(VI) solution since the highest adsorption percentages is obtained at that condition.

TT600-TS and MOX 80-TS exhibited higher Cr(VI) sorption performance than that of TT600-A and MOX 80-A. The percentage removal of Cr(VI) ions increases from 82% to 94 %, with the increasing in the adsorbent amount of TT600-A from 0.1 to 0.2 g. Then, adsorption percentage value reaches a plateau with increasing amount of the adsorbent. Therefore, for TT600-A, the optimum adsorbent dose is selected as 0.2 g for the rest of the experimental studies. In Figure 13, similar trend can be observed for MOX80 with TT600. In

Figure 12, it can be explained that high adsorption efficiency is reached at around 0.1 g. Therefore, optimum adsorbent dose is determined as 0.1 g for MOX80-A. After this value it reaches to the plateau as seen in Figure 13.

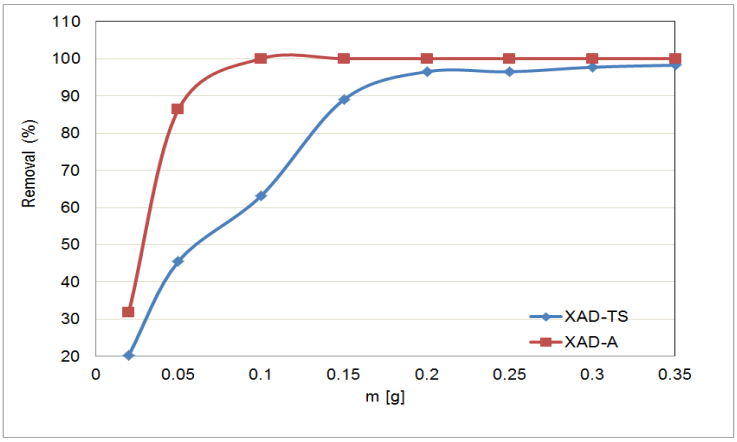

Figure 14. Effect of sorbent dose on the adsorption of Cr(VI) onto SILP (XAD).

On the other hand, polymeric adsorbents XAD-A exhibited higher performance than that of XAD-TS. While optimum sorbent dose is specified as 0.1 g for XAD-A support, 0.2 is chosen as optimum adsorbent dose for XAD-TS.

Equilibrium Studies

The equilibrium adsorption isotherms are some of the most important data for determining the sorption performances of the modified particles through the potential affinity between the metal ion and the adsorbent, the bond energy, and the sorption capacity. The most commonly employed models, namely the Langmuir and Freundlich adsorption models, were used in this study in order to describe the relationship between the amount of Cr(VI) ion adsorbed per unit weight of the modified nanoparticles (qe) and the liquid-phase equilibrium concentration (C_e) of the Cr(VI) ions. The linear forms of the Langmuir and Freundlich isotherms are represented by the following equations (4) and (5) respectively.

$$\frac{C_e}{q_e} = \frac{1}{q_{max}b} + \frac{C_e}{q_{max}} \qquad \text{(Eq. 4)}$$

Where C_e is the equilibrium concentration (mg/L), q_{max} is the monolayer adsorption capacity (mg/g) and b is the constant related to the free adsorption energy (Langmuir constant, L/mg).

$$logq_e = logk_F + \frac{1}{n} logC_e \quad \text{(Eq. 5)}$$

Where k_F is a constant indicative of the adsorption capacity of the adsorbent (mg/g) and the constant 1/n indicates the intensity of the adsorption.

The adsorption equilibrium data are conveniently represented by adsorption isotherms, which correspond to the relationship between the mass of the solute adsorbed per unit mass of adsorbent, q_e (mg/g), and the solute concentration for the solution at equilibrium, C_e (mg/L).

The preceding step, adsorption of Cr(VI) ions on the SILPs was studied according to Cr(VI) concentration range of 20-200 mg/L at optimum conditions. Equilibrium behaviors of TT600-TS, MOX80-TS and XAD-A are shown in Figure 15.

According to the values of correlation coefficient (R^2) for Langmuir and Freundlich models, it can be seen that Langmuir model represents a good fit with the experimental data for all adsorbents. The Langmuir and Freundlich adsorption isotherm constants along with the correlation coefficients are given in Table 4.

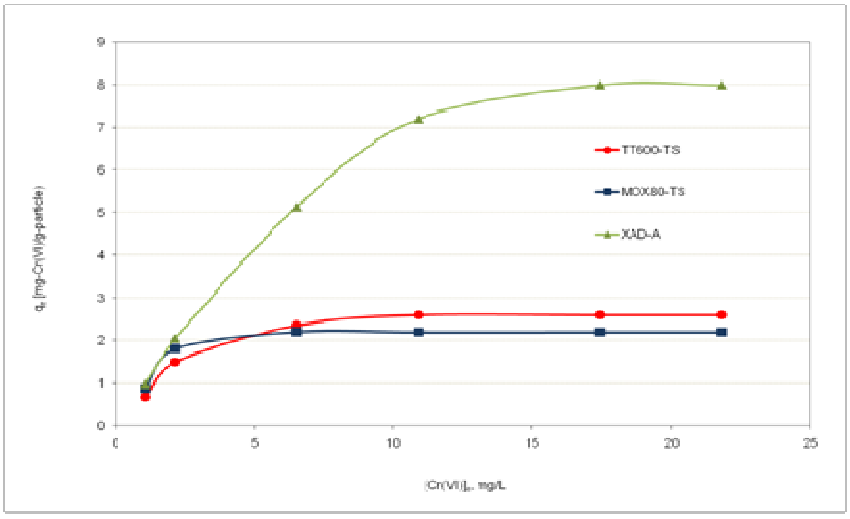

Figure 15. Equilibrium behavior of SILPs.

Table 4. Langmuir and Freundlich constants for the sorption of Cr(VI) on to SILPs.

MODEL	Constants	TT600-TS	MOX80-TS	XAD-A
Langmuir	q_{max} *(mg/g)*	2.6137	2.2452	8.2508
	b	3.0929	7.5109	0.9106
	R^2	0.9986	0.9992	0.9963
Freundlich	k (mg/g)	1.5628	1.6562	3.0068
	n	0.2883	0.1835	0.4982
	R^2	0.7768	0.6303	0.9283

Maximum adsorption capacities (q_{max}) for TT600-TS, MOX80-TS and XAD are found to be 2.61, 2.25 and 8.25 mg/g, respectively.

Column Sorption Study

Continuous studies were carried out in a packed bed column of 0.7 cm inner diameter and breakthrough curves are shown in Figure 16 in this regard.

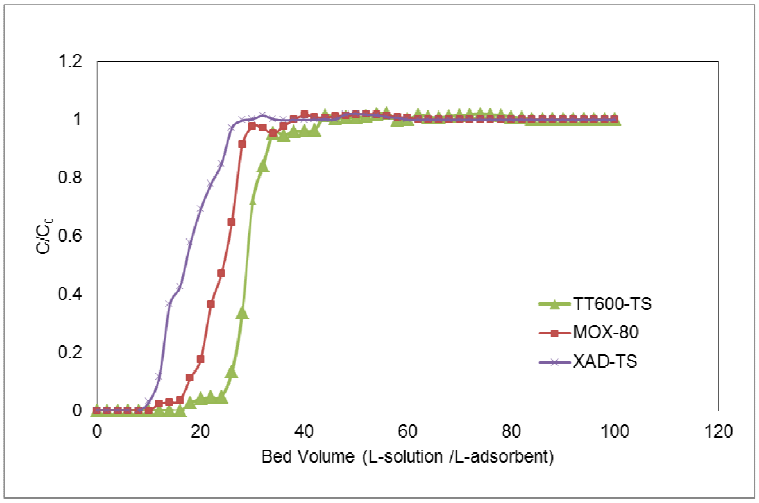

Figure 16. Breakthrough Curve.

When the breakthrough point is considered as the concentration of 5 mg/L; TT600-TS, MOX80-TS and XAD-A exhibited 15, 11 and 8 bed-volumes (L-solution /L-adsorbent) break through capacities.

CONCLUSION

In this study, supported ionic liquid phase (SILP) adsorbents were prepared by modification of nanosilica and SDVB polymeric particles with commercial and task-specific ionic liquids in order to enhance the Cr(VI) sorption capacities. The FTIR, SEM, and BET surface area analysis applied to the adsorbents proved the fact that the nanosilica and SDVB polymeric

supports were impregnated with the studied ionic liquids and also put in evidence in morphological changes.

Optimal conditions for the removal of Cr(VI) ions from aqueous solutions were determined by series of batch sorption studies. The sorption performance of prepared adsorbents was directly affected by the amount of IL confined (mL-IL: g-nanoparticle). The impregnation of the supports at a ratio of 1:1 showed higher sorption percentages up to 90%. Further increasing in the impregnation ratio led to decrease in Cr(VI) ion removal percentage. Optimal pH value was found to be 4 for all types of prepared adsorbents.

Adsorption isotherm data were well fit with Langmuir model representing favorable behavior with maximum sorption capacities up to 2.6, 2.2 and 8.2 mg Cr(VI)/g-SILP for TT600-TS, MOX80-TS, XAD-A, respectively. The column mode sorption performances of silica and SDVB particles were achieved for Cr(VI) removal and 5 mg/L was considered as the breakthrough point.

All the experimental data showed that the ionic liquid synthesized as Task-Specific (TS) impregnated nanoparticles and polymeric supports shows promising performance in the removal of Cr(VI) ions from aqueous solutions.

ACKNOWLEDGMENTS

This study is supported by TUBITAK with the contract no 213M537 and Ege University Scientific Research Foundation 15MÜH005.

REFERENCES

1. Fu F, Wang Q. Removal of heavy metal ions from wastewaters: A review. J Environ Manage. 2011; 92 (3): 407–418. DOI: 10.1016/j.jenvman.2010.11.011.

2. Galán B, Castañeda D, Ortiz I. Removal and recovery of Cr(VI) from polluted ground waters: A comparative study of ion-exchange technologies. Water Res. 2005; 39 (18): 4317–4324. DOI: 10.1016/j.watres.2005.08.015.

3. Abdel Salam OE, Reiad NA, ElShafei MM. A study of the removal characteristics of heavy metals from wastewater by low-cost adsorbents. J Adv Res. 2011; 2 (4): 297–303. DOI: 10.1016/j.jare.2011.01.008.

4. Hosseini SS, Bringas E, Tan NR, Ortiz I, Ghahramani M, Alaei Shahmirzadi MA. Recent progress in development of high performance polymeric membranes and materials for metal plating wastewater treatment: A review. J Water Process Eng. 2016; 9: 78–110. DOI: 10.1016/j.jwpe.2015.11.005.

5. Patil DS, Chavan SM, Oubagaranadin JUK. A review of technologies for manganese removal from wastewaters. J Environ Chem Eng. 2016; 4 (1): 468–487. DOI: 10.1016/j.jece.2015.11.028.

6. Aydin H, Bulut Y, Yerlikaya Ç. Removal of copper (II) from aqueous solution by adsorption onto low-cost adsorbents. J Environ Manage. 2008; 87 (1): 37–45. DOI: 10.1016/j.jenvman.2007.01.005.

7. Ahmad A, Siddique JA, Laskar MA, Kumar R, Mohd-setapar SH, Khatoon A, et al. New generation Amberlite XAD resin for the removal of metal ions : A review. J Environ Sci. 2015; 31: 104–123. DOI: 10.1016/j.jes.2014.12.008.

8. Gizli N, Arabacı M. Enhanced Sorption of Cu (II) Ions from Aqueous Solution by Ionic Liquid Impregnated Nano-silica And Nano-alumina Particles. Chem Ind Chem Eng Q J. 2016; in press. DOI: 10.2298/CICEQ160121034G.

9. Hauman, M., Schönweiz, A., Breitzk, H., Buntkowsky, G., Werner, S. and Szesni N. Supported Ionic Liquids: Fundamentals and Applications. Vol. 35, Chemical Engineering Technologies. 2012. 1421 p. ISBN (print): 978-3-527-32429-3.

10. Liu JF, Jiang G Bin, Jönsson JÅ. Application of ionic liquids in analytical chemistry. Trends Anal Chem. 2005; 24(1): 20–7. DOI: 10.1016/j.trac.2004.09.005.

11. Fontanals N, Borrull F, Marcé RM. Ionic liquids in solid-phase extraction. Trends Anal Chem. 2012; 41: 15–26. DOI: 10.1016/j.trac.2012.08.010.

12. Zapp E, Brondani D, Vieira IC, Scheeren CW, Dupont J, Barbosa AMJ, et al. Biomonitoring of methomyl pesticide by laccase inhibition on sensor containing platinum nanoparticles in ionic liquid phase supported in montmorillonite. Sensors Actuators, B Chem. 2011; 155(1): 331–339. DOI: 10.1016/j.snb.2011.04.015.

13. Al-Bishri HM, Abdel-Fattah TM, Mahmoud ME. Immobilization of [Bmim +Tf 2N -] hydrophobic ionic liquid on nano-silica-amine sorbent for implementation in solid phase extraction and removal of lead. J Ind Eng Chem. 2012;18(4): 1252–1257. DOI: 10.1016/j.jiec.2012.01.018.

14. Lupa L, Negrea A, Ciopec M, Negrea P, Vodă R. Ionic liquids impregnated onto inorganic support used for thallium adsorption from aqueous solutions. Sep Purif Technol. 2015; 155: 75–82.

15. Lupa L, Popa A, Dragan ES, Ciopec M, Negrea A, Negrea P. Adsorption performance of the organic solid support impregnated with ionic liquid in the removal process of Tl(I) from aqueous solutions. Process Saf Environ Prot. 2016; (1): 1–7. DOI: 10.1016/j.psep.2016.08.015.

16. Navarro R, Ruiz P, Saucedo I, Guibal E. Bismuth(III) recovery from hydrochloric acid solutions using Amberlite XAD-7 impregnated with a tetraalkylphosphonium ionic liquid. Sep Purif Technol. 2014; 135: 268–277. DOI: 10.1016/j.seppur.2014.02.023.

17. Kalidhasan S, Santhana Krishna Kumar A, Vidya Rajesh, Rajesh N. An efficient ultrasound assisted approach for the impregnation of room temperature ionic liquid onto Dowex 1x8 resin matrix and its application toward the enhanced adsorption of chromium (VI). J Hazard Mater. 2012; 213–214: 249–257. DOI: 10.1016/j.jhazmat.2012.01.093.

18. Kabay N, Cortina JL, Trochimczuk A, Streat M. Solvent-impregnated resins (SIRs) - Methods of preparation and their applications. React Funct Polym. 2010; 70 (8): 484–496. DOI: 10.1016/j.reactfunctpolym.2010.01.005.

19. Afkhami A, Saber-Tehrani M, Bagheri H. Simultaneous removal of heavy-metal ions in wastewater samples using nano-alumina modified with 2,4-dinitrophenylhydrazine. J Hazard Mater. 2010; 181 (1–3): 836–844. DOI: 10.1016/j.jhazmat.2010.05.089.

Türkçe Öz ve Anahtar Kelimeler

Nanosilika ve Polimerik Destek Malzemelerin Sulu Ortamlardan Cr(VI) İyonlarını Uzaklaştırma Performanslarının İyonik Sıvı Emdirilerek Geliştirilmesi

Nilay Gizli, Merve Arabacı

Öz: Bu çalışmada, sulu ortamlardan hekzavalent krom, Cr(VI) iyonlarının uzaklaştırılması için destekli iyonik sıvı faz (SILP) tutucular, iyonik sıvıların nanosilika ve polimerik destek malzemelere tutuklanması ile hazırlanmıştır. Trikapril metil amonyum nitrat [A336][NO_3], trikapril metil amonyum klorür (Aliquat® 336) ve 1-etil-3-metilimidazolyum bis(triflorometilsülfonil)imid (EMIMTf_2N) olmak üzere üç çeşit iyonik sıvı, ultrases varlığında fiziksel emdirme yöntemi izlenerek katı destek malzemelere başarı ile emdirilmiştir. Hazırlanan tutucuların modifikasyon öncesi ve sonrası kimyasal ve morfolojik yapılanmaları, FTIR, SEM ve BET analizleri ile incelenmiştir. Ayrıca, iyonik sıvı emdirilmiş katı taneciklerin ısıl davranışlarındaki değişim, TGA analizleri ile tanımlanmıştır. Hazırlanan tutucuların Cr(VI) iyonlarını tutma başarımları ise termodinamik ve kinetik davranışları temelinde incelenmiştir. İyonik sıvı yükleme oranı, çözelti pH'ı, tutucu miktarı, metal iyon derişiminin başlangıç değeri gibi analitik değişkenlerin tutucuların adsorplama verimi üzerine etkileri incelenmiştir. Hazırlanan tüm tutucu türleri için çözelti pH'ının 2-4 aralığında ve emdirme oranının 1 g-iyonik sıvı/g-destek malzeme olduğu koşullarda Cr(VI) iyonlarının dikkate değer bir biçimde uzaklaştırıldığı gözlemlenmiştir. Bununla birlikte, TT600-TS, MOX80-TS ve XAD-A tutucuları için krom iyonu uzaklaştırma yüzdeleri sırasıyla 99.53%, 99.50% ve 100%, olarak bulunmuştur. Ayrıca tutucuların denge davranışlarının Langmuir Denge İzotermlerine uyduğu sonucuna ulaşılmıştır.

Anahtar kelimeler: Adsorpsiyon, iyonik sıvı, destekli iyonik sıvı faz sistemleri, krom.

Sunulma: 03 Ekim 2016. **Düzeltme:** 16 Kasım 2016. **Kabul:** 03 Aralık 2016.

(This article was initially submitted to National Chemical Engineering Congress and reviewed by JOTCSB editorial staff).

Preparation of 3A Zeolite-Loaded Membrane for Hydrogen Recovery from Waste Gas

Filiz Ugur Nigiz*, Nilufer Durmaz Hilmioglu

Kocaeli University, Chemical Engineering Department, 41380, Kocaeli, Turkey

Abstract: In this study, carboxymethyl cellulose based mixed matrix membranes were prepared to remove H_2/CH_4 and CO/CH_4 gas mixtures and characterization experiments were performed. Zeolite 3A was selected as the inorganic material. It is essential in gas separation process that the membrane should be non-porous, therefore, the structure of the membrane was determined by means of polarized light microscope and contact angle test. The thermal behavior of membrane under high temperature condition was determined by using thermogravimetric analysis (TGA).

Keywords: Gas separation; mixed matrix membrane; carboxymethyl cellulose.

Submitted: October 04, 2016**. Revised:** December 12, 2016**. Accepted:** December 12, 2016.

Cite this: Ugur Nigiz F, Durmaz Hilmioglu N. Preparation of 3A Zeolite-Loaded Membrane for Hydrogen Recovery from Waste Gas. JOTCSB. 2017;1(1):71–80.

*Corresponding author. E-mail: filiz.ugur@kocaeli.edu.tr.

INTRODUCTION

Today, the recycling of valuable gases from the waste stream is a very important issue for the chemical industry in terms of both economic and environmental aspects. Particularly, the recovery of hydrogen from the petrochemical waste stream has become the significant treatment step in the petrochemical industry. Additionally, the separation of hazardous gas from flue gases contributes to decrease the greenhouse effect.

For the separation of desired gas from gas mixtures; cryogenic distillation, pressure swing adsorption and membrane gas separation methods are commercially used. Cryogenic distillation is a selective gas recovery technique. It depends on liquefying procedure of the hydrocarbons under low temperature and high pressure conditions (1). The pressure swing adsorption is a process in which the gas is adsorbed through an adsorbent at high pressure. This method is applied without need any heat treatment process (2). However, high pressure is required to obtain ultra-pure hydrogen. Membrane gas separation is an alternative technique to recover very pure hydrogen from the other hydrocarbons by using a selective membrane. Differently from the mentioned methods, membrane separation unit covers less space. It is easy to operate this process with low operating cost. Moreover, very high purity hydrogen (99%) can be separated (1, 3) effectively.

Membrane fouling, concentration polarization, and instability in the membrane performance directly affect the performance and total operating cost of the system. One of the major factors limiting the commercial expansion of the system is the structural membrane failure under the harsh operating conditions. Additionally, low gas flux and unstable membrane selectivity restrict the commercial usage of the membrane in a gas separation method. Therefore, almost the all-academic studies related to the membrane gas separation focus on suitable membrane material selection and membrane production.

The separation pathway of a gas through a non-porous membrane has been shown in Figure 1.

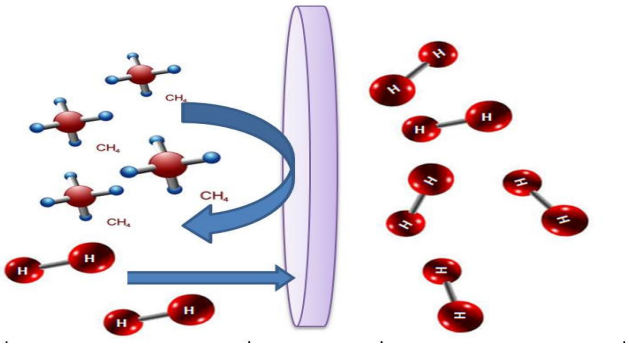

Figure 1. Molecular passage through the non-porous membrane.

In this system, selected gas molecule is removed from the gas mixture according to the molecular size of the gas and its affinity to the membrane. In the membrane gas separation system, non-porous membranes are used (4, 5). Separation behavior through the non-porous membrane is mostly explained by solution-diffusion model. This model depends on selective sorption of the gas on the membrane surface, diffusion through the membrane and desorption to the downstream side of the membrane. Membrane strength, stability, selectivity, and permeability value directly affect the performance of the system. In the membrane gas separation, driving force is the partial pressure difference between the sides of the membranes (6). Therefore, separation is maintained by the pressure difference. However, it is not the only effective parameter in this process. Besides the operating conditions such as pressure, temperature or gas composition, and structural properties of membrane material have critical importance in this system. The structural properties of the membrane are directly related to the nature of the membrane material. Inorganic, polymeric or mixed matrix dense membranes can be used as a selective membrane. Inorganic materials show resistant to severe operating conditions. However, it is difficult and expensive to manufacture inorganic membrane. Polymeric membranes are frequently used as gas separation membrane (7, 8). It is easy to form polymeric materials as a membrane with a different module. Yet, the polymeric membranes have relatively low chemical and thermal resistance. Hence, the operating lifetimes of the polymeric membranes are relatively short. Polymeric membranes can be characterized into two main classes; rubbery and glassy types according to the segmental structure of polymers. Because of the limited free volume of glassy ones, they are preferable to be used for the separation of small gas molecules from hydrocarbons (such as hydrogen removal from carbon dioxide or methane). In order to increase the stability of polymeric materials, inorganic filler incorporated polymeric membranes have been improved. Homogeneous distribution of inorganic particles in a polymeric matrix also increases the tortuous pathway and improves the selectivity of small-size gas molecules through the membrane. For these purposes, zeolites, clays, and inorganic or metallic based materials can be used (3).

The aim of this study is to manufacture a selective membrane to be used to separate hydrogen from methane and carbon dioxide. Hydrogen has a relatively small kinetic diameter than that of methane and carbon dioxide, therefore, it is important to manufacture a selective membrane that has small free volume. It is known that the glassy polymers have limited free volume spaces. Hence, carboxymethyl cellulose (CMC) has been chosen as the polymeric matrix. In order to restrict the free volume spaces and the chain mobility of the polymeric matrix, zeolite 3A has been selected as the inorganic filler. It is also expected to increase the thermal resistance of the membrane by zeolites incorporating. Additionally, a cross-linking procedure has been applied to

restrict the chain mobility of the polymer.

MATERIALS AND METHODS

Materials

Carboxymethyl cellulose, 3A zeolite, and glutaraldehyde were purchased from Aldrich Chemicals, Turkey. HCl, acetone, and ethanol were supplied from Merck Chemicals, Turkey.

Method

In this study, 3A distributed CMC mixed matrix membrane was prepared by phase inversion method. For this purpose, 7 wt. % CMC-water solution was prepared and stirred at 55 °C until a homogeneous solution was obtained. Afterward, 3A zeolites (with weight ranging between 10% - 50%) were added to the polymer solution by using "priming method" which was described in the previous study (9). Priming is a procedure to prevent a non-adhesive contact between the polymer and inorganic particle. It is important to combine these two different structures for preparation a good selective membrane. A possible incompatible area between the polymer and zeolite may cause a reduction in gas selectivity values. Especially, in the case of the selective hydrogen recovery, the diameters of almost all organic chemicals are larger than the size of a hydrogen molecule. Hence, it is possible to restrict the non-selective passage of other molecules by preventing contact-free region between the polymer and zeolite.

Characterization

In this study, several characterization experiments were performed to determine the structural properties of the membrane, which would affect the membrane gas permeability. Sessile drop water contact angles of the pristine and loaded membranes were measured by using Attension KVS Instrument. Thermogravimetric analysis (TGA) of the membrane was taken by using Mettler Toledo TGA Instrument. The TGA method was identified by the changing the temperature from 25 °C to 600 °C routinely and by recording the weight loss. Zeolite distributions in the CMC were analyzed by using Nikon Eclipse Polarized Microscope.

RESULTS AND DISCUSSION

Contact Angle Measurement

In this study, a glassy carboxymethyl cellulose polymeric membrane was used to produce a hydrogen-selective membrane. Despite the CMC was a rigid polymer, it had also flexible chain mobility and large free volume. Therefore, it was predicted that CMC could give low hydrogen selectivity without a structural improvement. To improve that failure, 3A zeolite was incorporated

into CMC matrix. 3A has very small cage size that only allows to hydrogen molecule passage over the methane and carbon dioxide. Additionally, 3A zeolite contributes to decelerate the diffusions of the larger ions by increasing the tortuous pathway. Contact angle measurements were shown in Figure 2.

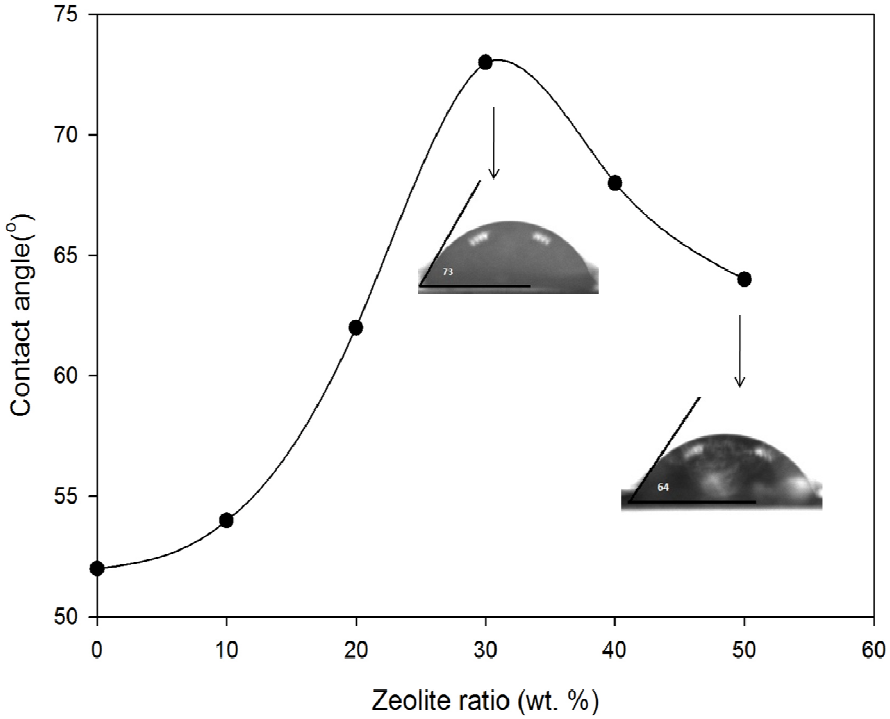

Figure 2. Contact angle measurement of mixed matrix membrane.

Addition of zeolite particles into CMC increased the water uptake capacity of the membrane. However, after a certain loading, angles decreased due to the tight and continuous zeolite phase in the membrane. With the help of the contact angle measurements, it is possible to predict that the decreasing molecular species could restrict the non-selective passage of other molecules and could increase the hydrogen selectivity.

Polarized Electron Microscope Results

In Figure 3, electron microscopy images under polarized light are shown. While the dark region represented the polymeric matrix, light phase showed the zeolite particles on the surface of the membrane.

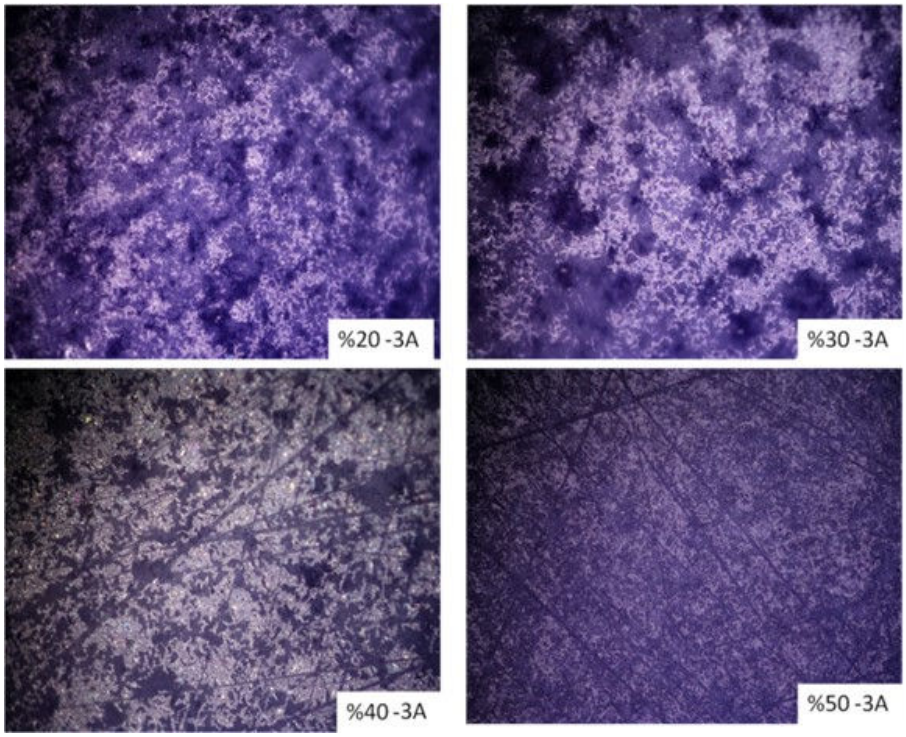

Figure 3. Zeolite distribution on polymeric matrix.

As seen in Figure 3, when the amount of zeolite increased in the membrane, the continuous phase distribution of the zeolite on the membrane surface increased. Despite this increment, there was no aggregation on the surface. A homogeneous dispersion was observed from the microscopy images. It was also found that the surface of 40 wt. % and 50 wt. % of zeolite loaded membranes were fully coated by zeolite.

Thermogravimetric Analysis

One of the biggest disadvantages of the polymeric membrane usage is the low thermal resistance of polymeric materials. It is known that the inorganic particle addition into polymeric membrane improves the thermal resistance of the membrane according to the rule of mixture (10). The industrial waste gases are generally produced followed by hot processes. Therefore, the membrane to be used in gas separation system should have high thermal resistance. Besides the high selective separation properties of the membrane, this study focused on the improving of thermal resistance of membrane by zeolite addition as well. Figure 4 shows the thermal behavior of pristine and zeolite loaded CMC membrane. As such, it can be evaluated from the figure that the thermal resistance of the membrane increased by zeolite addition.

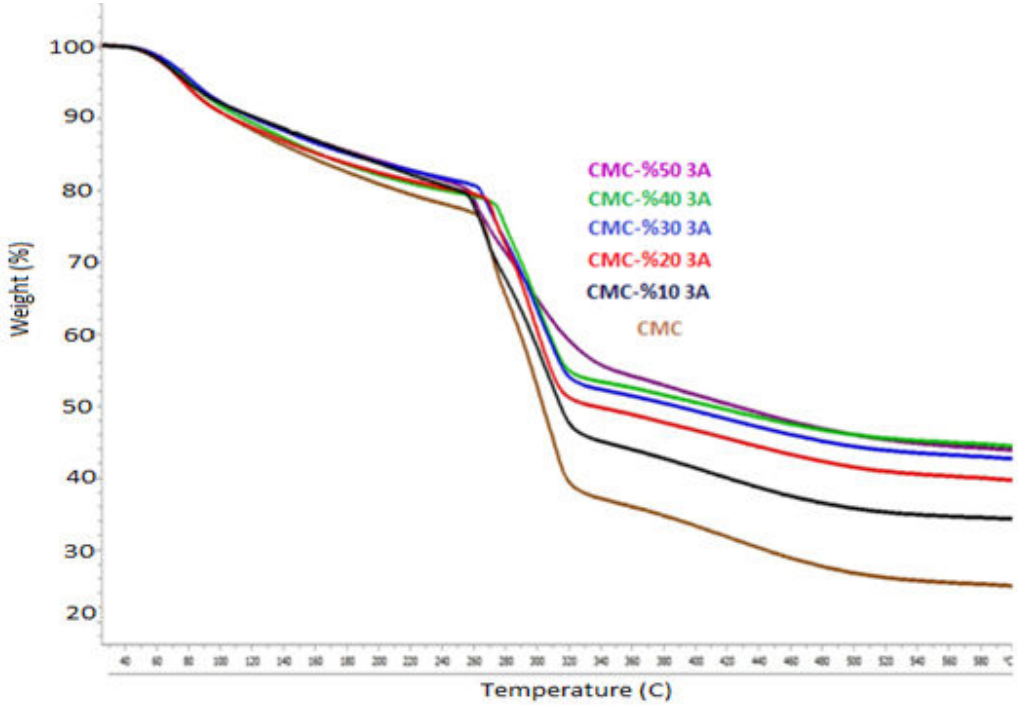

Figure 4. TGA results of pristine and zeolite loaded membrane.

CONCLUSIONS

In this study, 3A loaded carboxymethyl cellulose mixed matrix membrane was prepared to be used for hydrogen recovery from other gases such as carbon dioxide or methane and characterization tests were performed. As a result of the characterization tests, it was seen that the thermal resistance of the membrane increased by zeolite addition. It is clear from the characterization findings that the physical and chemical properties of membranes changed from polymeric to inorganic by zeolite addition. When the zeolite ratio increased, the capacity of water penetration in the membrane surface was increased and it was confirmed by contact angle measurements. In other words, the mixed matrix membrane restricted the molecular void spaces of the polymer. As a result, it is possible to consider that the prepared mixed matrix membrane is suitable for selective hydrogen recovery by membrane gas separation method.

ACKNOWLEDGMENTS

This study was financially supported by the Scientific Research Center of Kocaeli University (Grant Number:2016/066).

REFERENCES

1. Faraji S, Gharebagh RS, Mostoufi N. Hydrogen Recovery from Refinery Off-gases. Journal of Applied Sciences. 2005;5:459-464. URL: http://docsdrive.com/pdfs/ansinet/jas/2005/459-464.pdf.

2. Sanders DF, Smith ZP, Guo R, Robeson LM, McGrath JE, Paul DR, Freeman BD. Energy-efficient polymeric gas separation membranes for a sustainable future: A review. Polymer. 2013; 54: 4729–4761. DOI: 10.1016/j.polymer.2013.05.075.

3. Ismail A, David LIB. A review on the latest development of carbon membranes for gas separation. Journal of Membrane Science. 2001;193: 1-18. DOI: 10.1016/S0376-7388(01)00510-5.

4. Ulbricht M. Advanced functional polymer membranes. Polymer. 2006; 47: 2217–2262. DOI: 10.1016/j.polymer.2006.01.084.

5. Abedini R, Amir N. Application Of Membrane In Gas Separation Processes: Its Suitability And Mechanisms. Petroleum & Coal. 2010;52:69-80. URL: https://www.researchgate.net/publication/45601637_Application_of_membrane_in_gas_separation_processes_Its_suitability_and_mechanisms.

6. Bernardo P, Drioli E, Golemm G. Membrane Gas Separation: A Review/State of the Art. Ind. Eng. Chem. Res., 2009;48:4638–4660. DOI: 10.1021/ie8019032.

7. Yang T, Chung TS. High performance ZIF-8/PBI nano-composite membranes for high temperature hydrogen separation consisting of carbon monoxide and water vapor. International Journal of Hydrogen Energy. 2013; 38: 229-239. DOI: 10.1016/j.ijhydene.2012.10.045.

8. Han J, Lee W, Choi JM, Patel R, Byoung-Ryul M. Characterization of polyethersulfone polyimide blend membranes prepared by a drywet phase inversion Precipitation kinetics, morphology and gas separation. Journal of Membrane Science.2010; 351: 141-148. URL: 10.1016/j.memsci.2010.01.038.

9. Nigiz F, Dogan H, Hilmioglu N. Pervaporation of ethanol/water mixtures using clinoptilolite and 4A filled sodium alginate membranes. Desalination. 2012;300:24-31. DOI: 10.1016/j.desal.2012.05.036

10. Liu G. A step-by-step method of rule-of-mixture of fiber- and particle-reinforced composite materials. Composite Structures. 1997;40(3-4):313-322. DOI: 10.1016/S0263-8223(98)00033-6.

Türkçe öz ve Anahtar Kelimeler

Atık Gazlardan Hidrojen Gerikazanımı için 3A Zeoliti Katkılı Selüloz Membranların Hazırlanması

Filiz UĞUR NİGİZ, Nilüfer DURMAZ HİLMİOĞLU

ÖZET: Bu çalışmada, H_2/CH_4 ve CO/CH_4 ayrılmasına yönelik karboksimetil selüloz temelli karma matrisli membranlar hazırlanmış ve karakterizasyon testleri yapılmıştır. Inorganik malzeme olarak 3A zeoliti seçilmiştir. Membranın gözeneksiz olması yüksek seçicilik için önemlidir bu nedenle gözeneksiz yapı polarize ışınlı mikroskop ve temas açısı testleri ile belirlenmiştir. İnorganik malzeme eklenmesi ile membranın yüksek sıcaklığa dayanması amaçlandığı için 3A katkısının termal dayanıma etkisi termal test (TGA) ile belirlenmiştir.

Anahtar Kelimeler: Gaz ayırma; karma matrisli membran.

Sunulma: 04 Ekim 2016**. Düzeltme:** 12 Aralık 2016**. Kabul:** 12 Aralık 2016.

This article was initially submitted to the UKMK 2016 (National Chemical Engineering Congress) and finally evaluated by the JOTCSB editorial staff.

Preparation of Photocatalytic Materials for Water Clarification via Organic Waste

İlker ERDEM*, M. Furkan BALTACIOĞLU, M. Furkan BİLGİ

Abdullah Gül University (AGU), Faculty of Engineering, 38100, Kayseri, Türkiye

Abstract: Photocatalytic oxidation is a preferable method for clarification of fresh water polluted by colourful pollutants, pesticide-like hard-to-treat organic pollutants, and microbiological metabolites. Titanium dioxide (TiO_2), having superior physicochemical properties, is one of the most common catalyst in heterogeneous photocatalysis. Free electron formed by the absorption of light by titanium dioxide triggers formation of free radicals and results in oxidation of polluting compounds. Titanium dioxide is photocatalytically more active under the relatively shorter (100 nm < λ < 400 nm) UV wavelength region. This forces the usage of UV lamps for supplying UV light, which is only present at low ratios in the sunlight (8%). Doping with various elements, preparing of its composites with different oxides, usage of dyes absorbing sunlight were investigated for enhancing the photocatalytic activity of titanium dioxide and using the sunlight as energy source and some enhancements were reported. Using titanium dioxide in nano-size was also reported to be enhancing its photocatalytic activity. In this work, while organic wastes rich in carbon were milled to increase their surface area, nano-sized titanium dioxide was synthesised via sol-gel method. Using these two materials C element and titanium dioxide in couple possible enhancement of the photocatalytic activity of the synthesised material was investigated. Walnut shells were used as organic waste.

Keywords: Photocatalysis; titania; sol-gel; organic waste.

Submitted: September 26, 2016**. Revised:** October 18, 2016**. Accepted:** December 12, 2016.

Cite this: Erdem İ, Baltacıoğlu M, Bilgi M. Preparation of Photocatalytic Materials for Water Clarification via Organic Waste. JOTCSB. 2017;1(1):81–90.

*Corresponding author. E-mail: ilker.erdem@agu.edu.tr

INTRODUCTION

The amount and variety of the wastewaters is increasing with the increase in the number and quantity of chemically synthesised products. This results in the insufficiency of conventional applications for water treatment. Therefore, research on improving present conventional methods, introducing new and effective water treatment methods and usage of them integrated to conventional ones has been carried out. (1)

Photocatalytic oxidation is one of the methods preferred for clarification of fresh water contaminated by colourful pollutants, hard-to-clean pesticide-like persistent organic pollutants (POPs), and microbiological metabolites (1–4). Hydroxyl radicals occurring during photocatalytic oxidation are strong oxidising agents, which may react with plenty of organic and inorganic water-soluble pollutants at high reaction rates (1,3).

Titanium dioxide (titania, TiO_2) is a widely used catalyst in heterogeneous catalysis due to its superior physicochemical properties (4–6). The free electron formed by absorption of light energy by titanium dioxide triggering the formation of free radicals results in oxidation of pollutants in the environment (1). It has the potential to oxidise many of the organic pollutants to relatively non-hazardous pollutants; CO_2 and H_2O (3). Titania may be present in different crystallographic phases. Most abundant ones of these phases are anatase, rutile and brookite (2,6). Results about highest photocatalytic activities for different reactions have been reported for pure anatase phase or pure rutile phase or mixture of anatase and rutile phase (as in the commercial titania; Degussa P-25) (1,5). Titanium dioxide mainly shows its photocatalytic activity at the presence of low wavelength ultraviolet (UV) light (100 nm < λ < 400 nm). This enforces the usage of special light sources for supplying UV which is only present in a small ratio in the daylight (8%). Research has been performed on doping of different elements in titania, preparation of its composites with different oxides and utilisation of daylight absorbing dye materials as additives for the use of daylight as light source and increasing the photocatalytic efficiency of titania and some enhancements have been reported (2,4,5). The photocatalytic property of titania was reported to be increased when titania is used in nano-size (6). In this work, organic residues were ground to increase their surface area and nano-sized titania was prepared via sol-gel method. The possible enhancement of photocatalytic activity of the composite material was investigated which was synthesised by combining carbon-rich organic residue and synthesised nano-titania. Clarification (decolourisation) experiments of a resistant dying material; methylene blue, of which resistance to exogenous factors is high (7), were performed for this purpose.

MATERIALS AND METHODS

Sol (Ti-Sol) which was prepared via sol-gel method as described in previous work (8,9) was used as the titania source for synthesising the novel material in this work. Titanium(IV) isopropoxide (97%, Sigma-Aldrich), nitric acid (67%, Merck), isopropyl alcohol (99.8%>, Merck, Emsure) and deionised water were used in preparation of Ti-Sol. The particle size distribution of the sol was determined via a laser light scattering instrument (NanoZS, Malvern).

Shells of walnuts purchased from a local market were used as organic waste. Walnut shells were mechanically crushed first, following grinding via ball-milling (Retsch MM400) and finally sieved through 400-micron sieve. The grounded particles passed through the sieve were used for the experiments.

The Ti-sol and ground walnut shell were heat treated at appropriate temperature (400-500 °C) under modified atmosphere (with nitrogen gas introduction). The ground walnut shell was used with two aims. First, it would be a support for the photocatalyst (titania) and second the carbon-rich material was expected to increase the activity of photocatalyst.

Photocatalytic experiments were performed in the biosafety cabinet (Faster) equipped with both visible (vis) and ultraviolet (UV) light sources. Methylene blue (MB) (Sigma) solutions (500 ppm) were used as substrates for these reactions. Photocatalytic materials were added to one of the MB solution (2 g/L) and not added to the other solution (0 g/L), which was used as blank sample for that experiment. Commercial nano-sized titania (Aldrich-718467, 21 nm (TEM)) was used for comparing the photocatalytic activity of the novel material (C-TiO_2) prepared via ground walnut shell and nano-titania prepared via sol-gel method. The substrate (MB) solutions both photocatalytic material added and not were magnetically stirred under different light sources (UV or vis) and the change in absorbance values (λ = 664 nm) in time were determined via a spectrophotometer (Shimadzu UV-1800). The absorbance readings were continued for samples kept at dark overnight (AN) in the following day. The intensities of the light sources used were determined as 1 and 4 W/m^2 for UV and visible (vis) light sources, respectively (Apogee Solar Radiation, MP-200).

RESULTS AND DISCUSSION

The average particle size (Stoke's diameter) of the Ti-sol was determined as 23 nm via laser light scattering, which would assist formation of a fine microstructure after heat treatment. Most of the

particles in the sol were around 3 nm with some agglomerated impurities, which increased the average particle size.

The results for photocatalytic experiments performed via commercial nano-sized titania under visible light (vis) are shown in Figures 1 & 2. There is no considerable difference between the decolourisation (clarification) ratios for samples with and without photocatalyst addition.

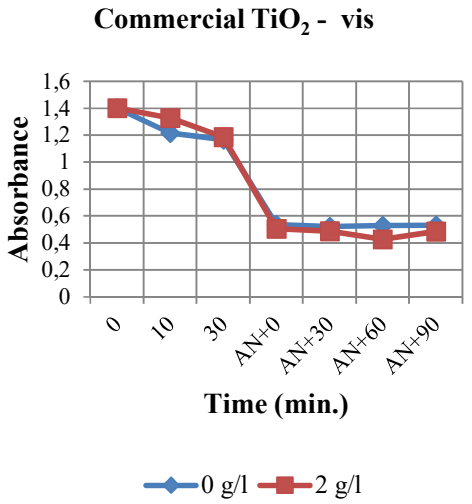

Figure 1: The change of absorbance in time for sample with and without commercial nano-sized titanium dioxide (Aldrich, 21 nm) exposed to visible light (vis).

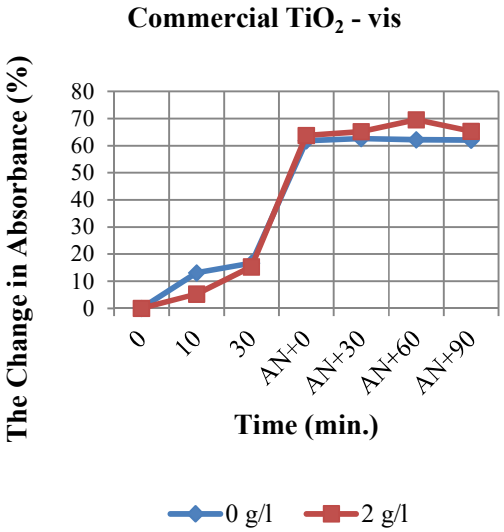

Figure 2: The change of absorbance (%) in time for sample with and without commercial nano-sized titanium dioxide (Aldrich, 21 nm) exposed to visible light (vis).

The results for photocatalytic experiments performed via commercial nano-sized titania under UV are shown in Figures 3 & 4. A decolourisation rate of 69% was observed for the sample with

commercial photocatalyst. It was only 33% for the sample without the commercial photocatalyst.

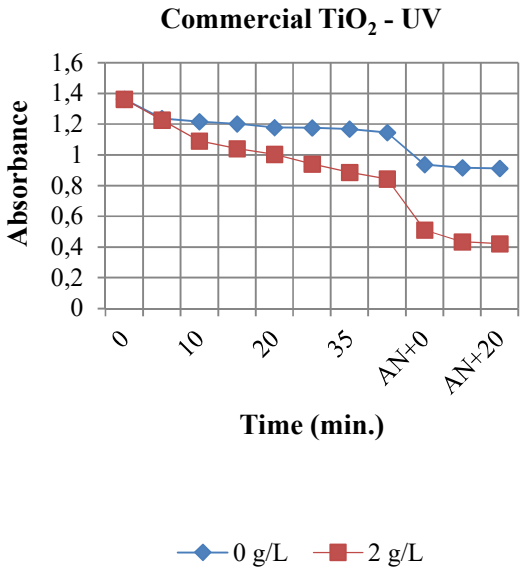

Figure 3: The change of absorbance in time for sample with and without commercial nano-sized titanium dioxide (Aldrich, 21 nm) exposed to ultraviolet light (UV).

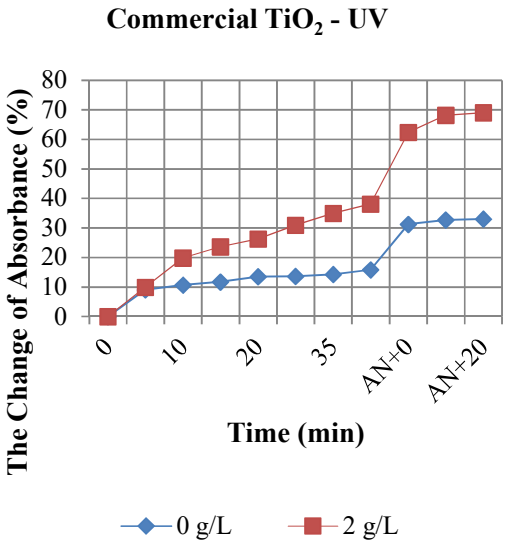

Figure 4: The change of absorbance (%) in time for sample with and without commercial nano-sized titanium dioxide (Aldrich, 21 nm) exposed to ultraviolet light (UV).

The results for photocatalytic experiments performed via synthesised material (C-TiO_2) under UV are shown in Figure 5 & 6. A decolourisation rate of 84% was observed for the sample with synthesised photocatalyst. It was 22% for the sample without it.

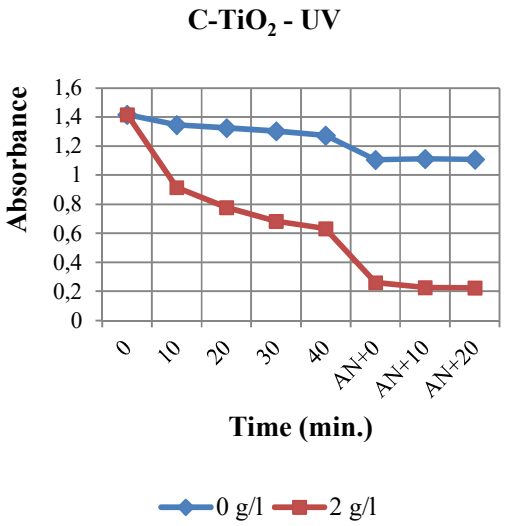

Figure 5: The change of absorbance in time for sample with and without synthesised material (C-TiO_2) exposed to ultraviolet light (UV).

The results for photocatalytic experiments performed via synthesised material (C-TiO_2) under visible light (vis) are shown in Figure 7 & 8. A decolourisation rate of 58% was observed for the sample with synthesised photocatalyst. The decolourisation was only 20% for the sample without it.

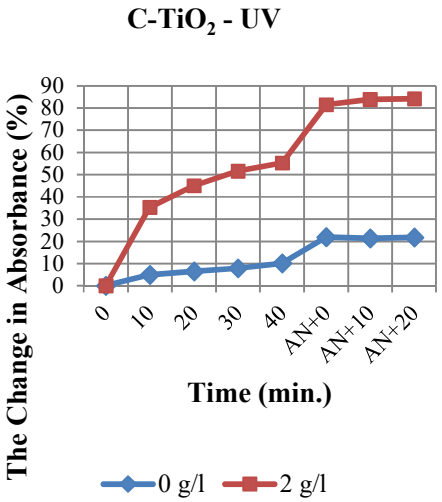

Figure 6: The change of absorbance (%) in time for sample with and without synthesised material (C-TiO_2) exposed to ultraviolet light (UV).

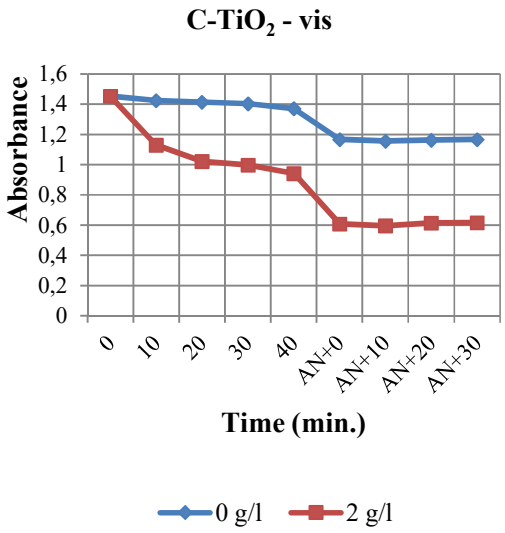

Figure 7: The change of absorbance in time for sample with and without synthesised material (C-TiO_2) exposed to visible light (vis).

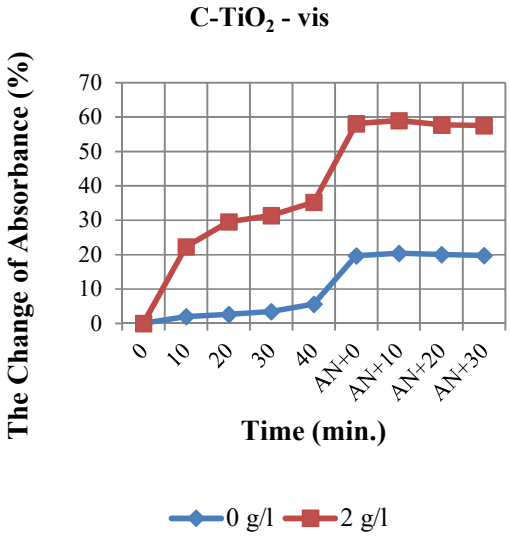

Figure 8: The change of absorbance (%) in time for sample with and without synthesised material (C-TiO_2) exposed to visible light (vis).

It was observed that the photocatalytic activities of materials were different from each other under different light sources (UV/Vis) and decolourisation occurs mainly under UV exposure. The synthesised material (C-TiO_2) was more efficient in decolourisation compared to the commercial nano-sized titania. The decolourisation rates for the samples with and without commercial titania were almost similar when exposed to visible light. There was an enhancement when UV was the light source, where the decolourisation for the sample with the commercial photocatalyst was 33% better than the sample without commercial photocatalyst. The decolourisation rates for the

synthesised material (C-TiO_2) were relatively higher at both experiments with different light sources (UV/vis). The decolourisation of the sample with synthesised material (C-TiO_2) exposed to visible light was 38% better than the sample without photocatalyst. The best enhancement for decolourisation rate was observed for the sample with synthesised photocatalytical material addition under UV exposure, which was 62% higher than the sample without photocatalyst addition. The initial rates of decolourisation observed for the synthesised material (C-TiO_2) also shows a relatively higher rate of decolourisation than the commercial photocatalyst.

The decrease in absorbance continued for the samples left in the dark overnight (AN). One of the most probable reasons of this incidence is considered to be adsorption of the dye on the surface of the photocatalyst. Therefore, more research activities should be performed for determining the ratios of two main possible decolourisation mechanisms on the process: photocatalysis and surface adsorption. The effect of parameters like the synthesis conditions and concentration of the synthesised photocatalytic material will be the subject of the following works.

REFERENCES

1. Gogate PR, Pandit AB. A review of imperative technologies for wastewater treatment I: oxidation technologies at ambient conditions. Adv Environ Res. 2004 Mar;8(3–4):501–51. DOI: 10.1016/S1093-0191(03)00032-7.

2. Fujishima A, Zhang X, Tryk DA. TiO2 photocatalysis and related surface phenomena. Surf Sci Rep. 2008 Dec 15;63(12):515–82. DOI: 10.1016/j.surfrep.2008.10.001.

3. Microsoft Word - 376-385_598_Stasinakis_10-3.doc - 376-385_598_Stasinakis_10-3.pdf [Internet]. [cited 2016 Sep 20]. Available from: http://journal.gnest.org/sites/default/files/Journal%20Papers/376-385_598_Stasinakis_10-3.pdf.

4. WANG JL, XU LJ. Advanced Oxidation Processes for Wastewater Treatment: Formation of Hydroxyl Radical and Application. Crit Rev Environ Sci Technol. 2012 ubat;42(3):251–325. DOI: 10.1080/10643389.2010.507698.

5. Carp O, Huisman CL, Reller A. Photoinduced reactivity of titanium dioxide. Prog Solid State Chem. 2004;32(1–2):33–177. DOI: 10.1016/j.progsolidstchem.2004.08.001.

6. Madhusudan Reddy K, Manorama SV, Ramachandra Reddy A. Bandgap studies on anatase titanium dioxide nanoparticles. Mater Chem Phys. 2003 ubat;78(1):239–45. DOI: 10.1016/S0254-0584(02)00343-7.

7. Kushwaha AK, Gupta N, Chattopadhyaya MC. Removal of cationic methylene blue and malachite green dyes from aqueous solution by waste materials of Daucus carota. J Saudi Chem Soc. 2014 Jul;18(3):200–7. DOI: 10.1016/j.jscs.2011.06.011.

8. Preparation of ceramic composite membranes for protein separation [Internet]. [cited 2016 Sep 20]. Available from: http://openaccess.iyte.edu.tr/handle/11147/4713.

9. Investigation of effects of microstructural and surface properties of ultrafiltration/ nanofiltration ceramic membranes on their performance [Internet]. [cited 2016 Sep 20]. Available from: http://openaccess.iyte.edu.tr/handle/11147/2871.

Türkçe Öz ve Anahtar Kelimeler

Organik Atıklar Kullanılarak Su Temizleme için Fotokatalitik Malzemelerin Hazırlanması

İlker ERDEM, M. Furkan BALTACIOĞLU, M. Furkan BİLGİ

Öz: Fotokatalitik yükseltgeme, renkli kirliliklerle, pestisit benzeri ve muamelesi zor organik kirliliklerle ve mikrobiyolojik metabolitlerle kirlenmiş içme suyunun temizlenmesi için tercih edilen bir yöntemdir. Titanyum dioksit (TiO_2) üstün fizikokimyasal özellikleriyle heterojen fotokatalizde en yaygın kullanılan katalizördür. Titanyum dioksit tarafından ışığın soğurulması ile oluşan serbest elektron serbest radikallerin oluşmasını tetikler ve kirlilik verici bileşiklerin yükseltgenmesi ile sonuçlanır. Titanyum dioksit fotokatalitik olarak, nispeten kısa (100 nm < λ < 400 nm) UV dalgaboyuna sahip olan ışıkla daha aktiftir. Bu da UV ışığını sağlamak amacıyla UV lambalarının kullanılmasını zorunlu kılar, bu lambaların sağladığı ışık güneş ışığının küçük bir kısmını (%8) oluşturur. Çeşitli elementlerle aşılama, farklı oksitlerle kompozit hazırlama, güneş ışığını soğuran boyar maddeleri kullanma yöntemleri titanyum dioksidin fotokatalitik aktivitesinin artırılmasında incelenmiş ve güneş ışığı enerji kaynağı olarak kullanılmış ve varılan bazı ilerlemeler bildirilmiştir. Nano boyutta titanyum dioksidin kullanılması fotokatalitik aktivitesini artırmak için denenmiş ve bildirilmiştir. Bu çalışmada, yüzey alanını artırmak için karbonca zengin organik atıklar değirmende öğütülmüş ve sol-jel yöntemiyle nano boyutta titanyum dioksit sentez edilmiştir. Karbon elementi ve titanyum dioksit kullanılarak sentez edilmiş malzemenin fotokatalitik aktivitesindeki olası artış incelenmiştir. Ceviz kabukları organik atık olarak kullanılmıştır.

Anahtar kelimeler: Fotokataliz; titanya; sol-jel; organik atık madde.

Sunulma: 26 Eylül 2016**. Düzeltme:** 18 Ekim 2016**. Kabul:** 12 Aralık 2016.

(This article was initially submitted to National Chemical Engineering Congress and reviewed by JOTCSB editorial staff)

Reaction Kinetics of Carbon Dioxide with Nonaqueous Solutions of Sterically Hindered Amines

F. Pınar Gördesli Duatepe[1,*], Erdoğan Alper[2]

1. Izmir University of Economics, Faculty of Engineering, Izmir 35330, Turkey
2. Hacettepe University, Faculty of Engineering, Chemical Engineering Department, Ankara 06900, Turkey

Abstract: Due to existing energy intensive CO_2 capture processes and rising fuel costs, alternative and affordable solvents or technologies for CO_2 capture have gained importance in the research of reducing global warming. To that effect, sterically hindered amines have been introduced which have high CO_2 absorption capacities by means of the formation of unstable carbamate ions. Another factor leading to an affordable solvent for CO_2 capture could be using nonaqueous solvents instead of aqueous solvents in the process. This is important because nonaqueous solvents can eliminate some of the problems of aqueous solvents such as corrosion and high thermal requirements. To that end, in this study, we investigated the reaction kinetics of CO_2 and two sterically hindered amines; 2-amino-2-methyl-1,3-propanediol (AMPD) and 2-amino-2-ethyl-1,3-propanediol (AEPD) in ethanol. The pseudo–first-order reaction rate constants of the reactions between CO_2 and sterically hindered amines were measured in ethanol at 288, 298 and 308 K by using direct stopped-flow technique. The measured rate constants were then analyzed by using the equations of termolecular reaction mechanism. The orders of the reactions (n) between CO_2-AMPD and CO_2-AEPD were found as 1 and 2, respectively.

Keywords: Carbon dioxide absorption; fast reaction kinetics; global warming; sterically hindered amines; stopped-flow technique.

Submitted: November 04, 2016. **Revised:** November 29, 2016. **Accepted:** December 31, 2016.

Cite this: Gördesli Duatepe F, Alper E. Reaction Kinetics of Carbon Dioxide with Nonaqueous Solutions of Sterically Hindered Amines. JOTCSB. 2017;1(1):91–102.

Corresponding author. E-mail: pinar.gordesli@ieu.edu.tr.

INTRODUCTION

The enhanced greenhouse effect resulting from the extensive use of fossil fuels to produce energy is one of the universal concerns nowadays. Therefore, there is a vital need to control the emission of greenhouse gases into the atmosphere, especially carbon dioxide (CO_2), due to its high abundance, so as to mitigate their greenhouse effect [1-3]. It is projected that the increase in energy efficiency and the use of renewable energy sources will not provide the required reductions in CO_2 emissions. On the other hand, the capture of CO_2 from industrial flue gases prior to its release into the atmosphere and subsequent storage of the captured CO_2 away from the environment seems to be a promising approach towards reducing global climate change due to the enhanced greenhouse effect [4, 5]. Today, the most effective method for the separation and capture of CO_2 from a gas mixture is the absorption of CO_2 into amine solutions with a reversible reaction [6, 7]. The CO_2 capture technology conventionally used in large scale is the absorption/desorption process in which aqueous monoethanolamine (MEA) solution is frequently used as solvent [8-10]. Among conventional amines, MEA is often used in industry due to its high CO_2 absorption rate. However, MEA has a low CO_2 absorption capacity (amine/CO_2 < 0.5) and a high thermal requirement for its regeneration due to stable carbamate formation. MEA also has a high degradation rate and a corrosive property [11]. For these reasons, sterically hindered amines which can absorb high amounts of CO_2 (amine/CO_2 = 1) and form unstable carbamates have been introduced [12] and obtaining rate constants of the reactions between CO_2 and sterically hindered amines to estimate the efficiency of the CO_2 absorption have gained importance in recent years [13-18]. Sterically hindered amines which are proposed as alternatives to conventional amines can be designed for specific applications, have increased resistance to degradation and can also be produced from renewable resources. In addition, compared to aqueous systems, the use of non-aqueous systems (*i.e.*, ethanolic or methanolic system) is considered to be a promising alternative method for CO_2 capture, due to high solubility and capacity, low corrosiveness and low energy consumption for the regeneration of used solvents [19-22].

In this study, reaction kinetics of CO_2 with different concentrations of two sterically hindered amines namely, 2-amino-2-methyl-1,3-propanediol (AMPD) and 2-amino-2-ethyl-1,3-propanediol (AEPD) in ethanol were investigated at 288, 298 and 308 K. The pseudo-first order reaction rate constants k_o (s^{-1}) were directly measured using stopped-flow technique. Termolecular reaction mechanism was used to model the kinetics of the system and to calculate forward reaction rate constants. Interest in AMPD and AEPD comes from the fact that

both of them can be produced from renewable sources, that is from 1,2-propanediol and 1,3-propanediol which are abundant as side products of biodiesel process [23, 24].

MATERIALS AND METHODS

Chemicals

Sterically hindered amines, AMPD and AEPD of purities ≥ 99.8%, and ethanol of purity ≥ 99.9% were supplied by Merck (Darmstadt, Germany) and J.T. Baker, respectively. Carbon dioxide with a purity of 99.9% was supplied by Linde (Munich, Germany). The experiments were carried out in ethanolic solution using 0.25–1.00 kmol/m^3 of AMPD and 0.25–1.25 kmol/m^3 of AEPD, at 288, 298 and 308 K.

Apparatus

The stopped-flow apparatus (model SF-61SX2; Hi-Tech Scientific, Salisbury, UK) with a conductivity detector is a direct standard technique used for kinetic study of the fast reactions between amines and CO_2. The equipment consists of four main units: a sample handling unit, a conductivity cell, an A/D converter, and a microprocessor unit. The entire flow circuit is encased in a thermostat and maintained at a constant temperature by an external water bath within ± 0.1 K. "Kineticasyst" software was used to activate the pneumatically controlled drive plate, which pushes separately the amine and CO_2 solutions in equal volumes into the conductivity detection cell through a mixing loop. For each experimental run, equal volumes of solution were suddenly pushed into and mixed in the stopped flow mixer cell. In the conductivity cell, solutions react to generate ions that conduct electricity through platinum electrodes placed across the cell. The conductivity detection system directly measures the intrinsic rate of the rapid homogeneous reaction. The reaction software automatically calculates the observed pseudo–first order rate constant (k_o) based on least square regression. To satisfy the pseudo–first order condition, concentration ratios of the amine (AMPD or AEPD) to that of CO_2 were maintained at about 10:1 for all experiments. Further details of the equipment and the experimental procedure can be found elsewhere [19, 25, 26].

Experimental procedure

According to termolecular reaction mechanism, which was first proposed by Crooks and Donnellan [27], there is a loosely bound encounter complex formed as initial product in the reaction between amine and CO_2. In this mechanism, the bonding between amine and CO_2 and the proton transfer take place simultaneously, involving only a single step as represented by Eq. (1). Here, carbamate formation involves the transfer of a proton from the amine functionality.

$$\mathrm{CO_2 + RNH_2 \cdots B \leftrightarrow RNHCOO^- \cdots BH^+} \quad \textbf{(Eq. 1)}$$

It should be noted that for sterically hindered amines the carbamate ion is unstable, leading to the following reaction [26]

$$\mathrm{CO_2 + RNH_2 + H_2O \leftrightarrow HCO_3^- + RNH_3^+} \quad \textbf{(Eq. 2)}$$

The observed carbon dioxide absorption rate in amine solutions is given as

$$r_{obs} = k_o[\mathrm{CO_2}] \quad \textbf{(Eq. 3)}$$

The observed pseudo–first order reaction rate constant (k_o) in aqueous systems is given as

$$k_o = k_{H_2O}[\mathrm{H_2O}][\mathrm{RNH_2}] + k_{RNH_2}[\mathrm{RNH_2}]^2 \quad \textbf{(Eq. 4)}$$

According to Eq. 1, in nonaqueous systems such as in ethanol (EtOH), k_o will be

$$k_o = k_{EtOH}[\mathrm{EtOH}][\mathrm{RNH_2}] + k_{RNH_2}[\mathrm{RNH_2}]^2 \quad \textbf{(Eq. 5)}$$

Note that the base (B) which is weakly bonded to amine in Eq. (1) could be any base in the environment such as amine or ethanol in a nonaqueous system. Considering that EtOH concentration remains constant for dilute nonaqueous amine solutions, then, introducing constant k, where

$$k = k_{EtOH}[\mathrm{EtOH}] \quad \textbf{(Eq. 6)}$$

Thus, the observed pseudo-first order reaction rate constant in ethanol system will be

$$k_o = k[RNH_2] + k_{RNH_2}[RNH_2]^2 \quad \textbf{(Eq. 7)}$$

RESULTS AND DISCUSSION

The reaction kinetics of carbon dioxide with AMPD or AEPD in ethanol were investigated at 288, 298, and 308 K. Table 1, Figure 1 and Figure 2 show the experimentally obtained pseudo–first order reaction rate constants for the sterically hindered amines dissolved in ethanol. It is clearly seen that the reaction rate constants increased with increasing temperature at a constant amine concentration. Similarly, the rate constants also increased with increasing amine concentration at a constant temperature. Due to the limited solubility of AMPD in ethanol, the maximum 1.00 kmol/m^3 concentration of solution could be successfully prepared.

Table 1. Measured pseudo-first order rate constants of the reactions between CO_2-AMPD and CO_2-AEPD in ethanol at 288, 298 and 308 K

[AMPD] (kmol/m^3)	$k_{o(288\ K)}$ (s^{-1})	$k_{o(298\ K)}$ (s^{-1})	$k_{o(308\ K)}$ (s^{-1})
0.25	2.9	6.0	8.5
0.50	6.9	11.0	17.0
0.75	10.2	19.9	31.6
1.00	19.2	32.3	45.0
[AEPD] (kmol/m^3)	$k_{o(288\ K)}$ (s^{-1})	$k_{o(298\ K)}$ (s^{-1})	$k_{o(308\ K)}$ (s^{-1})
0.25	2.3	3.0	3.9
0.5	8.3	9.6	10.5
0.75	19.4	21.6	26.2
1.00	30.2	35.6	44.2
1.25	53.8	61.4	73.4

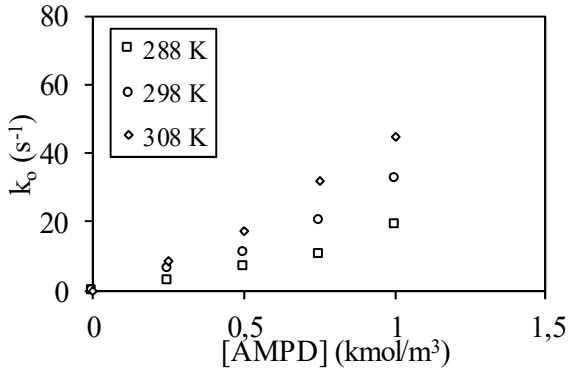

Figure 1. Effect of AMPD concentration on the measured pseudo-first order rate constants of the reaction between CO_2-AMPD in ethanol at 288, 298 and 308 K.

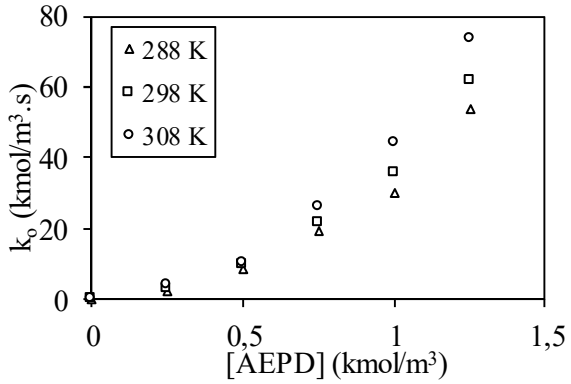

Figure 2. Effect of AEPD concentration on the measured pseudo-first order rate constants of the reaction between CO_2-AEPD in ethanol at 288, 298 and 308 K.

The obtained values of pseudo-first order reaction rate constants (k_o) were generally low in comparison to that of MEA systems. Considering that AMPD and AEPD are sterically hindered amines, this trend is comparable to that of other hindered amines [16-18, 25]. In addition, CO_2-amine reaction rates in nonaqueous solution such as ethanolic solution used in our study were observed to be lower than the reaction rates in aqueous solution. For example, in our previous study [16] the pseudo–first order reaction rate constant (k_o) measured between CO_2 and aqueous AMPD [0.5 kmol/m^3] at 298 K was found to be 55.9 s^{-1}. Compared to that, the measured rate constant (k_o) of the reaction between AMPD [0.5 kmol/m^3] and CO_2 in ethanol at 298 K was found to be 11.0 s^{-1} (Table 1). Similarly, the measured reaction rate constants for CO_2-AEPD in ethanol were lower than the rate constants obtained for the same reaction in aqueous solution [17]. This trend can be linked to the lower basicity of ethanol compared to that of water.

Empirical power law plots for the CO_2-AMPD system (Figure 3) gave reaction orders of 1.31, 1.20 and 1.21 at 288, 298 and 308 K, respectively (Table 2). In other words, according to termolecular reaction mechanism, the base which is weakly bonded to amine was either EtOH or amine itself for all temperatures investigated. However, due to the fact that the degrees obtained were very close to 1, the base was mostly EtOH. The measured rate constant k_o (s^{-1}) of the reaction between CO_2 and AMPD in ethanol solution can be shown as below:

$$k_o = k_{EtOH}[EtOH][AMPD] + k_{AMPD}[AMPD]^2 \qquad \textbf{(Eq. 8)}$$

Table 2. Forward reaction rate constants and reaction orders (n) of CO_2-AMPD and CO_2-AEPD in ethanol at 288, 298 and 308 K.

Temperature (K)	k (m^3/kmol.s)	k_{AMPD} (m^6/$kmol^2$.s)	n
288	6	12.4	1.31
298	14	17.7	1.20
308	27	18.0	1.21
Temperature(K)		k_{AEPD} (m^6/$kmol^2$.s)	n
288		33	1.93
298		38	1.90
308		46	1.85

In the literature, the CO_2-AMPD reaction was examined indirectly in aqueous media and related solubility or kinetic data were reported [13-15]. To the best of our knowledge, no kinetic studies in ethanol media was reported for CO_2-AMPD system. The kinetic studies for CO_2-AMPD system performed in aqueous media at different temperatures (278-298 K) has revealed that the reaction order of CO_2 with AMPD varies between 1.12 and 1.25 ([AMPD] = 0.10-1.50 kmol/m^3). This leads to the conclusion that the base which is weakly bonded to amine in CO_2-AMPD system is the solvent used in the system.

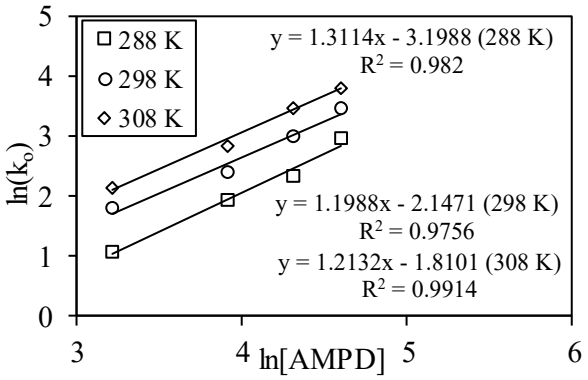

Figure 3. Empirical power law plots for CO_2-AMPD system in ethanol at 288, 298, and 308 K.

When CO_2-AEPD reaction in ethanolic media was investigated, the empirical power law plots for the system (Figure 4) gave reaction orders of 1.93, 1.90 and 1.85 at 288, 298 and 308 K, respectively (Table 2). It implies that, for CO_2-AEPD system, the base which is weakly bonded to amine was mostly amine itself for all temperatures investigated.

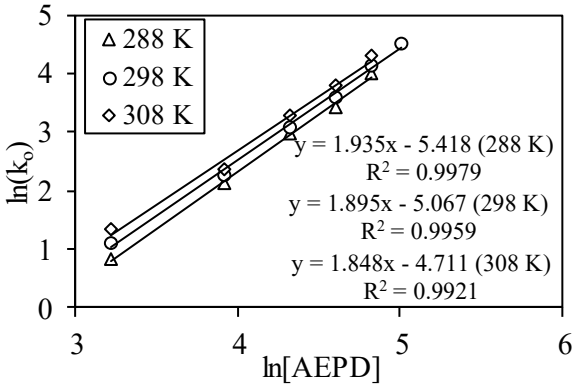

Figure 4. Empirical power law plots for CO_2-AEPD system in ethanol at 288, 298, and 308 K.

If the effect of EtOH as a base is neglected, then the measured rate constant k_o (s^{-1}) of the reaction between CO_2 and AEPD in ethanol solution can be shown as below:

$$k_o = k_{AEPD}[AEPD]^2 \qquad \textbf{(Eq. 9)}$$

Previously we have found that the reaction order of CO_2 with aqueous AEPD varies between 1.04 and 1.14 for temperatures between 278 and 298 K ([AEPD] = 0.03-1.00 kmol/m^3) [17]. Similarly in another study [18] the reaction order of CO_2-AEPD in aqueous solution was reported to be as 1 at temperatures between 303 and 318 K ([AEPD] = 0.41-2.15 kmol/m^3). To conclude, the reaction orders and reaction rate constants of the CO_2-AEPD system in aqueous and nonaqueous solutions are different from each other. The results obtained in this respect are important in order to estimate the efficiency of the CO_2 absorption to occur, since they are not previously found in the literature and are obtained directly using the stop-flow technique.

The forward reaction rate constants for CO_2-AMPD reaction, k ($k_{EtOH}[EtOH]$, m^3/kmol.s) and k_{AMPD} (m^6/$kmol^2$.s), and for CO_2-AEPD reaction, k_{AEPD} (m^6/$kmol^2$.s) were obtained by polinomial regressions (Table 2). For both reactions, the forward rate constants increased with increasing temperature. However, all rate constants obtained for CO_2-sterically hindered amine reaction are very slow relative to the rate of an amine solution commonly used in the industry, such as MEA. In the case of large-scale CO_2 absorption processes, activator-associated solutions of sterically hindered amines will need to be used.

ACKNOWLEDGMENTS

This study was financially supported by Turkish Scientific and Technological Research Council (TUBITAK) through a research project (Project No.: 106M034).

REFERENCES

1. Third Assessment Report. IPCC Climate Change, Intergovernmental Panel on Climate Change; 2001. http://www.ipcc.ch/ipccreports/tar/

2. McCann N, Maeder M, Attalla M. Simulation of enthalpy and capacity of CO_2 absorption by aqueous amine systems. Ind. Eng. Chem. Res. 2008; 47:2002–2009. DOI: 10.1021/ie070619a

3. Raupach MR, Marland G, Ciais P, Le Quéré C, Canadell JG, Klepper G, Field CB. Global and regional drivers of accelerating CO_2 emissions. Proc. Natl. Acad. Sci. 2007; 104:10288–10293. DOI: 10.1073/pnas.0700609104

4. Metz B, Ogunlade D, de Coninck H, Loos M, Meyer L. Intergovernmental Panel on Climate Change Special Report on Carbon dioxide Capture and Storage. Cambridge University Press, New York, United States: 2005. https://www.ipcc.ch/report/srccs/

5. Metz B, Davidson, OR, Bosch PR, Dave R. IPCC: Summary for Policymakers, in Climate Change: Mitigation. Contribution of Working Group III to the Fourth Assessment Report of the Intergovernmental Panel on Climate Change. Cambridge University Press, New York, United States: 2007.
https://www.ipcc.ch/publications_and_data/publications_ipcc_fourth_assessment_report_wg3_report_mitigation_of_climate_change.htm

6. de Koiejer G, Solbraa E. High pressure gas sweetening with amines for reducing CO_2 emissions. 7th International Conference on Greenhouse Gas Control Technologies. Vancouver, Canada: 2004. http://www.sciencedirect.com/science/book/9780080447049

7. Kvamsdal HM, Maurstad O, Jordal K, Bolland O. Benchmarking of gas turbine cycles with CO_2 capture. 7th International Conference on Greenhouse Gas Control Technologies. Vancouver, Canada: 2004. http://www.academia.edu/14972806

8. Danckwerts PV. The reaction of CO_2 with ethanolamines. Chem. Eng. Sci. 1979; 34:443–446. DOI:10.1016/0009-2509(79)85087-3

9. Alejandre J, Rivera JL, Mora MA, de la Garza VJ. Force field of monoethanolamine. Phys. Chem. B 2000; 104:1332–1337. DOI: 10.1021/jp993101w

10. da Silva E, Svendsen HF. Study of the carbamate stability of amines using ab initio methods and free-energy perturbations. Ind. Eng. Chem. Res. 2006; 45:2497–2504. DOI: 10.1021/ie050501z

11. Sartori G, Savage DW. Sterically hindered amines for carbon dioxide removal from gases. Ind. Eng. Chem. Fundam. 1983; 22:239-249. DOI: 10.1021/i100010a016

12. Baek JI, Yoon JH. Solubility of carbon-dioxide in aqueous-solutions of 2-amino-2-methyl-1,3-propanediol. J. Chem. Eng. Data 1998; 43:635-637. DOI: 10.1021/je980024

13. Baek JI, Yoon JH, Eum HM. Prediction of equilibrium solubility of carbon dioxide in aqueous 2-amino-2-methyl-1,3-propanediol solutions. Korean J. Chem. Eng. 2000; 17:484-487. DOI: 10.1007/BF02706866

14. Bouhamra W, Bavbek O, Alper E. Reaction mechanism and kinetics of aqueous solutions of 2-amino-2-methyl-1,3-propandiol and carbon dioxide. Chem. Eng. J. 1999; 73:67-70. http://dx.doi.org/10.1016/S1385-8947(99)00017-0

15. Gordesli FP, Ume CS, Alper E. Mechanism and kinetics of carbon dioxide capture using activated 2-amino-2-methyl-1,3-propanediol. Int. J. Chem. Kinetics 2013; 45:566-573. DOI: 10.1002/kin.20787

16. Ume CS, Alper E, Gordesli FP. Kinetics of carbon dioxide reaction with aqueous mixture of piperazine and 2-amino-2-ethyl-1,3-propanediol. Int. J. Chem. Kinetics 2013; 45:161-167. DOI: 10.1002/kin.20752

17 .Yoon JH, Baek JI, Yamamoto Y, Komai T, Kawamu T. Kinetics of removal of carbon dioxide by aqueous 2-amino-2-methyl-1, 3-propanediol, Chem. Eng. Sci. 2003; 58:5229-5237. http://dx.doi.org/10.1016/j.ces.2003.08.019

18. Ali SH, Merchant SQ, Fahim MA. Kinetic study of reactive absorption of some primary amines with carbon dioxide in ethanol solution. Sep. Purif. Technol. 2000; 18:163−175. http://dx.doi.org/10.1016/S1383-5866(99)00064-7

19 .Bratzler K, Doerges A. Amisol process purifies gases. Hydrocarbon Process 1974; 53:78−80. DOI: 10.1002/14356007.a12_169.pub2

20. Kadiwala S, Rayer AV, Henni A. Kinetics of carbon dioxide (CO_2) with ethylenediamine, 3-amino-1-propanol in methanol and ethanol, and with 1-dimethylamino-2-propanol and 3-dimethylamino-1-propanol in water using stopped-flow technique. Chem. Eng. J. 2012; 179:262−271. http://dx.doi.org/10.1016/j.cej.2011.10.093

21. Sada E, Kumazawa H, Osawa Y, Matsuura M, Han Z. Reaction kinetics of carbon dioxide with amines in non-aqueous solvents. Chem. Eng. J. 1986; 33:87−95. DOI:10.1016/0300-9467(86)80038-7

22. Miyazawa T, Koso S, Kunimori K, Tomishige K. Glycerol hydrogenolysis to 1,2-propanediol catalyzed by a heat-resistant ion-exchange resin combined with Ru/C. Appl. Catal. 2007; A 329:30−35. http://dx.doi.org/10.1016/j.apcata.2007.06.019

23. Yuan Z, Wang J, Wang L, Xie W, Chen P, Hou Z, Zheng X. Biodiesel derived glycerol hydrogenolysis to 1,2-propanediol on Cu/MgO catalysts. Bioresour. Technol. 2010; 101:7088–7092. http://dx.doi.org/10.1016/j.biortech.2010.04.016

24. Alper E. Reaction mechanism and kinetics of aqueous solutions of 2-amino-2-methyl-1-propanol and carbon dioxide. Ind. Eng. Chem. Res. 1990; 29:1725–1728. DOI: 10.1021/ie00104a023

25. Gordesli FP, Alper E. The kinetics of carbon dioxide capture by solutions of piperazine and N-methyl piperazine. Int. J. Global Warm. 2011; 1:67–76. http://dx.doi.org/10.1504/IJGW.2011.03837

26. Crooks JE, Donnellan JP. Kinetics and mechanism of the reaction between carbon dioxide and amines in aqueous solution. J. Chem. Soc. Perkin Trans. 1989; 2:331–333. DOI: 10.1039/P29890000331

Türkçe Öz ve Anahtar Kelimeler

Sterik Olarak Engelli Aminlerin Susuz Çözeltileriyle Karbon Dioksidin Reaksiyon Kinetikleri

F. Pınar Gördesli Duatepe, Erdoğan Alper

Öz: Şu anda var olan CO_2 tutuklama süreçleri ve artan yakıt maliyetlerinden ötürü, küresel ısınmayı azaltacak araştırmalarda CO_2 tutuklama için ucuz çözücüler veya teknolojilerin kullanılması önem kazanmıştır. Bu anlamda, sterik olarak engelli aminler, kararsız karbamat iyonlarının oluşumu yoluyla yüksek CO_2 soğurma kapasitelerine sahip moleküller olarak bilim dünyasının dikkatine sunulmuştur. CO_2 tutuklanması için ucuz bir faktör de süreçte sulu çözücüler yerine susuz çözücülerin kullanılmasıdır. Bu değişiklik önemlidir, çünkü sulu çözücülerin korozyon ve yüksek ısıl gereksinimleri gibi bazı sorunları giderilmektedir. Bu bakımdan çalışmada CO_2 ve iki sterik olarak engelli amin (2-amino-2-metil-1,3-propandiol, AMPD ve 2-amino-2-etil-1,3-propandiol, AEPD) reaksiyon kinetikleri etanollü çözeltide çalışılmıştır. CO_2 ve sterik olarak engelli aminler arasındaki yalancı birinci mertebeden reaksiyon hızı sabitleri etanol içinde 288, 298 ve 308 K sıcaklıklarda doğrudan durdurulmuş akış tekniği ile ölçülmüştür. Ölçülen hız sabitleri üç moleküllü reaksiyon mekanizması kullanılarak analiz edilmiştir. CO_2-AMPD ve CO_2-AEPD arasındaki reaksiyonların mertebeleri (n) sırasıyla 1 ve 2 olarak tespit edilmiştir.

Anahtar kelimeler: Karbon dioksit soğurulması; hızlı reaksiyon kinetikleri; küresel ısınma; sterik olarak engelli aminler; durdurulmuş akış tekniği.

Sunulma: 04 Kasım 2016. **Düzeltme:** 29 Kasım 2016. **Kabul:** 31 Aralık 2016.

(This article was initially submitted to National Chemical Engineering Congress and reviewed by JOTCSB editorial staff).

Removal of Sulfur From Iron Ore with Physical and Chemical Methods

Buğra ÇAVUŞOĞLU[1] Hüseyin KARACA*[1]
[1]Department of Chemical Engineering, Inonu University, Malatya, Turkey

Abstract - In this study, sulfur was removed from Kahramanmaras Elbistan iron ore, which has a high sulfur content, by application of microwave and chemical methods (H_2SO_4 / H_2O_2) together. Low-grade iron ore, with a high sulfur content, constitutes a significant bottleneck especially in technical applications. Various physical and chemical methods for removal of sulfur from a high sulfur content iron ore are applied. However, the sulfur removal process must be economical to be applicable reasonably. Therefore, both physical and chemical methods for removal of sulfur were investigated in this study. In the first part, iron ore was heated to a high temperature by microwave to decompose pyritic sulfur, which is one of the sulfur species in the ore (FeS_2), into sulfur dioxide (SO_2), ferrous sulfate ($FeSO_4$), and pyrrhotite (FeS). Then, the ore obtained by this process was extracted (leaching) with H_2SO_4/H_2O_2 solution at a determined concentration. The highest sulfur removal was obtained at 2.75 GHz and 900W microwave heating time of 210 sec and 0.03 N H_2SO_4/10% H_2O_2 treatment conditions at 60 min reaction time and ambient conditions. According to the obtained results, removal of sulfur content of the iron ore was not significantly affected at high microwave power, high H_2SO_4 and H_2O_2 concentration and high temperature conditions. By applying microwave and chemical methods (H_2SO_4/H_2O_2) together, sulfur content of iron ore was removed approximately by 84%.

Keywords: Iron ore; sulfur removal; physical and chemical methods.

Submitted: September 17, 2016. **Revised:** December 25, 2016. **Accepted:** December 26, 2016.

Cite this: Çavuşoğlu B, Karaca H. Removal of Sulfur From Iron Ore with Physical and Chemical Methods. JOTCSB. 2017;1(1):103–14.

*Corresponding author. E-mail: huseyin.karaca@inonu.edu.tr.

INTRODUCTION

World steel production is in continuous growth. Today, it is not even possible to imagine a life without steel. While the annual steel production in the world was 28 million tonnes in 1900, it reached 780 million tonnes at the end of the century. North America with a 14.5% share and Continental Europe, including the former Soviet Union and Eastern Block, with a 36% share became the steel producer blocks following Asia [1].

Problematic iron ore deposits containing silica, sulfur, copper, carbonate, alumina, titanium, phosphorus, and arsenic and directly affecting the cost, quality, and production in the sector are present in Turkey. These deposits with iron tenors between 20-54% are located in Malatya, Sivas, Erzincan, Bingöl, Kayseri, Kahramanmaraş, Balıkesir, Aydın, Ankara, and Kırşehir. Among these problematic deposits, 500-600 thousand tonnes are produced annually from siderite ore in Malatya-Hekimhan, containing 39% Fe and 4% Mn, and used in the sinter blend especially in İsdemir at the rates of 20%. Iron ore reserves determined following the studies conducted by the General Directorate of Mineral Research and Exploration are divided into 3 groups, based on the usage of iron and steel plants:

a) Workable iron ore reserve

These are the deposits, the exploration works limited to a certain extent and production of almost all of which have been made until today. Their ore tenors change between 51-62% Fe. Their current reserves are around 137 million tonnes in which 23 deposits are present.

b) Problematic iron ore reserve

The exploration works of this type of deposits have been performed, and the apparent probable reserve potential has been determined; however, the deposits were partially mined during certain periods since they contained some impurities which were undesired by integrated plants. Today, a significant part of these deposits are not active. Their ore tenors change between 19-54% Fe.

c) Potential iron ore reserve

Not enough exploration activities have been performed in Turkey, and a total of approximately 320 million tonnes of potential reserves has been determined in 27 fields. The tenors of these deposits change between 14-52% Fe. It is not possible to mine these deposits without determining the ore reserve and solving the technological problems for certain [2]. Almost all of the iron ore deposits in Turkey contain impurities in a range not approved by integrated plants. It is not possible to mine these deposits without determining the ore reserve

and solving the technological problems for certain [2]. Sulfur, phosphorus, oxygen, hydrogen, and nitrogen are the dangerous impurities contained in steel. These are also known as interstitial atoms since they settle into interstitial spaces in the iron cage. The most important effects of these impurities on steel are ductility, impact resistance, and reduction of the resistance to corrosion. Oxygen and sulfur are also the source of non-metallic particles in steel, known as inclusion. These inclusions should be removed from steel as far as possible since they have dangerous effects on the properties of steel. Carbon is also a similar interstitial atom; however, it is generally not acknowledged as a dangerous impurity and its amount should be in accordance with the specification. However, new steel types that should contain carbon at a rate as low as possible have been developed nowadays. Sulfur is present in iron ore in the form of sulfatic, pyritic (FeS_2) and other sulfurous mineral salts. This is an unwanted content as stated in the iron-steel industry. It should be removed from the environment with physical and chemical methods at the ore stage or the pot stage. While sulfate sulfur can be easily removed from the environment with proper solvents, pyritic sulfur and sulfur in the form of mineral salts cannot be removed easily [3]. There are many methods for the removal of pyritic sulfur. However, the most effective method is the chemical method [4-8]. Furthermore, it is possible to transform pyritic sulfur into pyrrhotite (FeS) by exposing it to thermal decomposition (pyrolysis). This decomposition reaction is as follows [4]:

$$FeS_2 \rightarrow Fe_{(1-x)}S \rightarrow FeS \quad \text{or} \quad FeSO_4 \ (0<x<0{,}125)$$

With the decomposition of pyrite to pyrrhotite, elemental sulfur gas, pyrrhotite, and iron (II) sulfate are formed. Magnetic susceptibility of pyrrhotite is approximately a hundred times more than that of pyrite [5]. While elemental sulfur is removed at the gas phase, a part of pyrite in the environment is degraded to sulfate form. This facilitates the removal of a part of sulfur in the ore through dissolution. Microwave heating ensures selective and rapid heating. Pyrite is present at low rates compared to the iron and oxygen compounds in the ore. Ferromagnetic iron alloys such as magnetite provide rapid, effective and selective heating by absorbing microwave rays. Therefore, while pyrite reaches the decomposition temperature faster, energy loss is prevented [6-8]. Pyrite that undergoes no decomposition in the environment after microwave heating is oxidized to a structure that can be dissolved with proper solvents by oxidizing with H_2O_2.

Oxidation is shown as follows [4]:

$$H_2O_2 \rightarrow H_2O + {}^{1}/_{2}O_2$$

$$2\ FeS_2 + {}^{11}/_{2}\ O_2 \rightarrow\ Fe_2O_3 + 4SO_2$$
$$2\ FeS_2 + 7\ O_2 \rightarrow\ Fe_2(SO_4)_3 + SO_2$$
$$SO_2 + ½\ O_2 \rightarrow\ SO_3$$
$$Fe_2O_3 + 3\ SO_3 \rightarrow\ Fe_2(SO_4)_3$$

The formed $FeSO_4$ compound can easily be dissolved with H_2SO_4 in water. Dissolution is provided as follows:

$$4FeSO_4 + 2H_2SO_4 + O_2 \rightarrow 2\ Fe_2(SO_4)_3 + 2\ H_2O$$

H_2SO_4 is known to increase the oxidation degree of H_2O_2 [4]. The effects of this interaction on the ore at room conditions (1 atm, 25 ^oC) are also examined. Parameters at room conditions are chosen to reduce the cost.

MATERIALS AND METHODS

The analysis of the raw iron ore is given in Table 1. Iron ore to be used in experiments was ground with a grinder and sifted through a sieve with 0.75 μm pores. The sifted sample was dried for 48 hours at room conditions. Approximately 40 g of the ore, prepared for the process, was taken to silica crucibles by being weighed at 0.001 g accuracy, and 5 different samples, prepared in this way, were treated in a home type microwave oven at 2.45 GHz frequency and 900 Watt for 30, 60, 90, 120, 180 and 240 sec. The treated ore was left to cool in a desiccator just after the microwave treatment.

For the process of sulfur removal with H_2O_2 solution, approximately 40 g of iron ore was weighed at 0.001 g accuracy and put in a 400 mL Erlenmeyer flask in a way that the "amount of ore (g)/volume of H_2O_2 solution (mL)" ratio will be approximately 1/5. During 60 min of the reaction time at room temperature, they were mixed with hydrogen peroxide solutions with 1%, 5% 10%, 20% and 30% concentrations throughout the reaction time. Afterwards, the treated ore samples, filtered with a rough filter paper, were dried for 6 hours under 160 mmHg of constant vacuum pressure and at 100 °C constant temperature.

For the process of sulfur removal with H_2SO_4 solution, approximately 40 g of ore was weighed at 0.001 g accuracy and put in 400 mL Erlenmeyer flask in a way that the "amount of ore (g)/volume of H_2SO_4 solution (mL)" ratio will be approximately 1/5 in specific sulfuric acid concentrations. For 60 min of the reaction time at room temperature, they were mixed with

H_2SO_4 solutions in 0.01 N, 0.03 N, 0.05 N, 0.07 N and 0.1 N concentrations throughout the reaction time. Afterwards, the treated samples, filtered with a rough filter paper, were washed 6 times with 20 mL of hot water and dried for 6 hours under 160 mmHg of constant vacuum pressure and at 100 °C constant temperature. The total sulfur and sulfate sulfur contents of the raw ore sample and treated ore samples were determined in accordance with TS 329 and TS 363 standards, respectively [9-10]. Since no organic sulfur was present in the sample, pyritic sulfur was calculated from the difference.

Table 1. The analysis of the raw iron ore (wt.%)

Fe	FeO	Al_2O_3	SiO_2	Na_2O	K_2O	P	S	Cu	S_{SOx}	$S_{pyritic}$
63,02	20,31	0,11	5,37	0,07	0,09	0,02	5,505	0,01	0,048	5,457

RESULTS AND DISCUSSION

The Effect of H_2SO_4 concentration

Upon increase of the sulfuric acid in the media during the leaching of the iron ore, removable sulfur amount firstly increases then decreases. This results from the porous nature of the ore. A high amount of sulfur exists inside the solution remaining as the hygroscopic moisture in the pores of the ore after the filtration. This content is crystallized after drying process and causes an increase in the sulfur rate of the ore. Therefore, dissolving effect of the leaching solution reduces in partially lower sulfuric acid concentrations. Thus, the residual solution following the leaching process bears low sulfur. As clear from Figures 1 and 2, sulfuric acid concentration is at optimum value around 0.03 N. High acid concentrations have a negative effect on the sulfur removal process. Furthermore, for the process costs, higher levels of acid concentrations negatively affect the sulfur removal process.

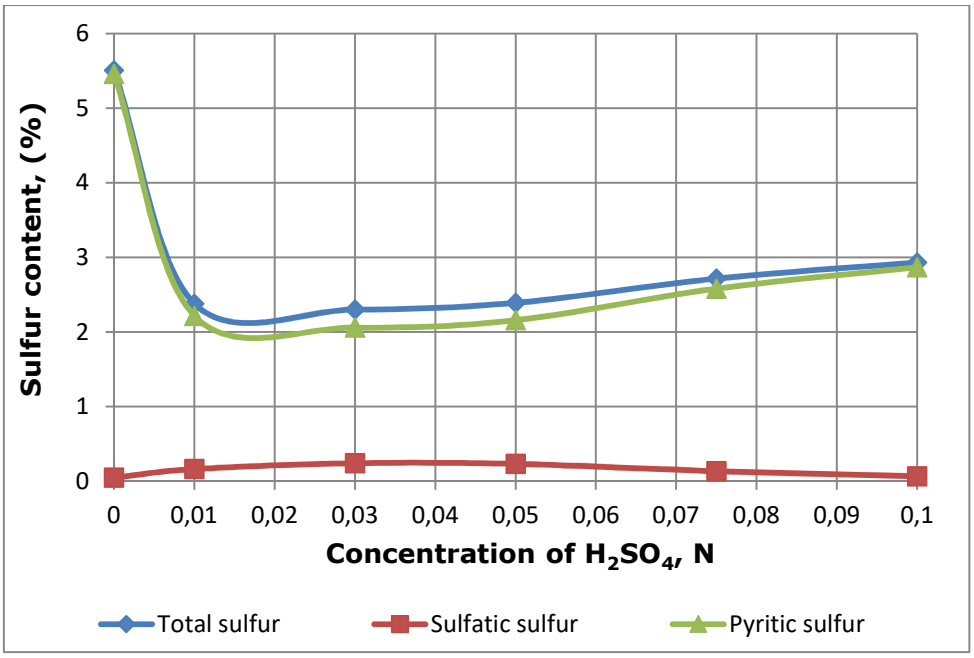

Figure 1. Effect of H_2SO_4 concentrations on sulfur content of the iron ore.

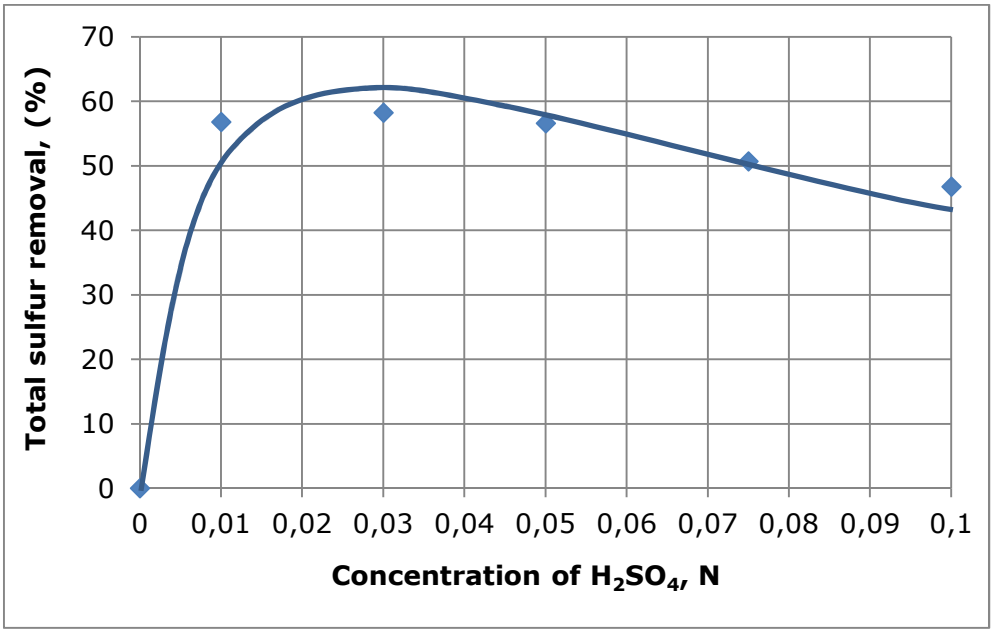

Figure 2. Effect of H_2SO_4 concentrations on total sulfur removal of the iron ore.

The Effect of H_2O_2 Concentration

In the leaching process of the iron core with hydrogen peroxide solution, pyritic sulfur and other sulfur compounds, highly available in the iron core, are oxidized to the sulfatic sulfur. In Figures 3 and 4, the most suitable H_2O_2 concentration for both total sulfur and sulfur types content and total sulfur removal is 10%. For high concentrations of H_2O_2, no significant change

has occurred in the total sulfur and sulfur type contents. Moreover, some part of the sulfatic sulfur are attached to iron ions like $Fe_2(SO_4)_3$. This would cause loss of iron during leaching of H_2SO_4. Therefore, high concentrations of H_2O_2 were not preferred.

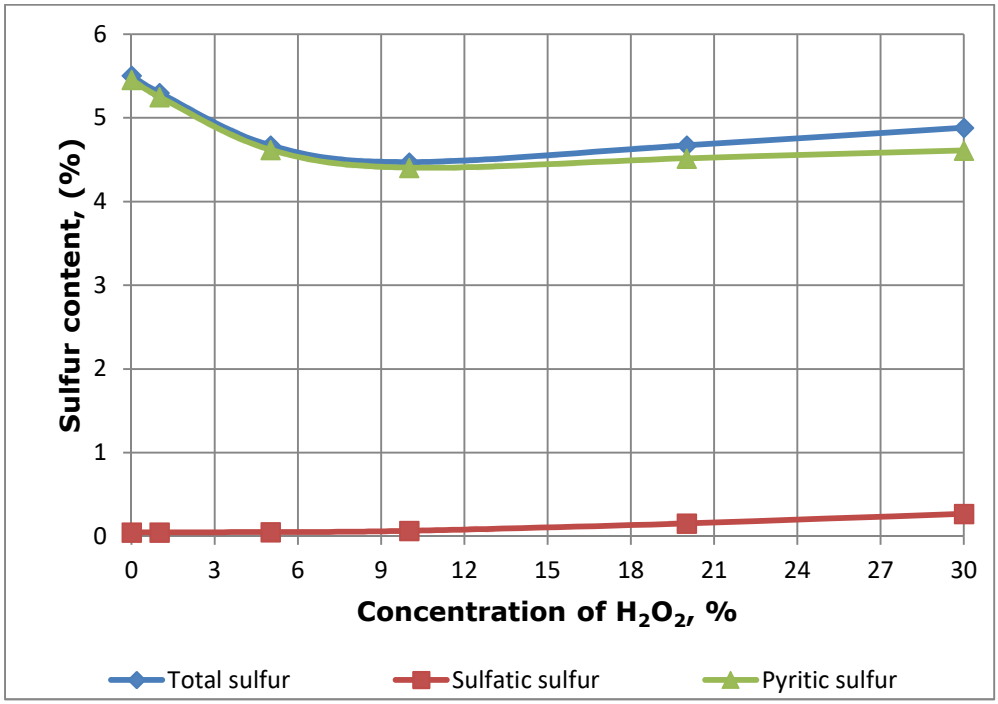

Figure 3. Effect of H_2O_2 concentrations on sulfur content of the iron ore.

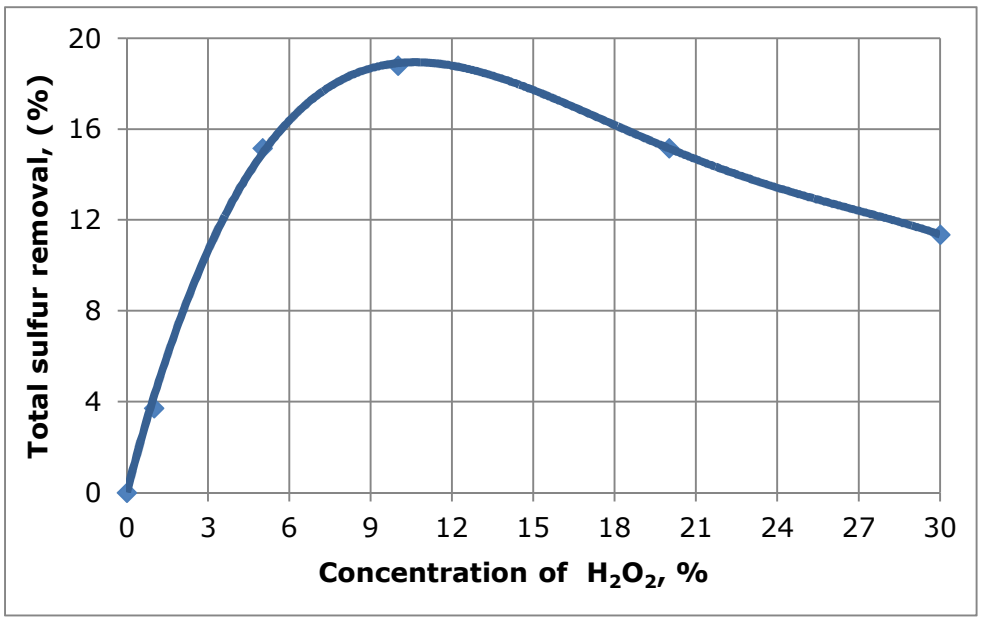

Figure 4. Effect of H_2O_2 concentrations on total sulfur removal of the iron ore.

The Effect of Heating by Microwave

A microwave oven of 2.75 GHz and 900 Watt was utilized to remove sulfur from the iron ore. The process of removing sulfur from the iron ore through the microwave method has allowed us to examine the effect of microwave rays in different durations on total sulfur and sulfur types. As stated above, a significant amount of pyritic sulfur is available in the iron ore. Therefore, pyrite and other sulfur compounds heat up very quickly via the microwave rays. Due to the liberated heat during this process, temperature goes up and thus decomposition of pyrite accelerates. Because the system used for the sulfur removal from the iron ore via microwave method is open to the atmosphere, significant part of the sulfur is oxidized and goes away as SO_2 and other sulfur oxide compounds. As clear from Figure 5 and 6, the most suitable microwave heating span is 210 s for both total sulfur and sulfur types content and also the total sulfur removal. Increasing the time over 210 s has not changed the total sulfur and sulfur types content significantly. Since the pyritic sulfur is decomposed until approximately 210 s, not a significant change has occurred in total sulfur removal in high microwave heating times.

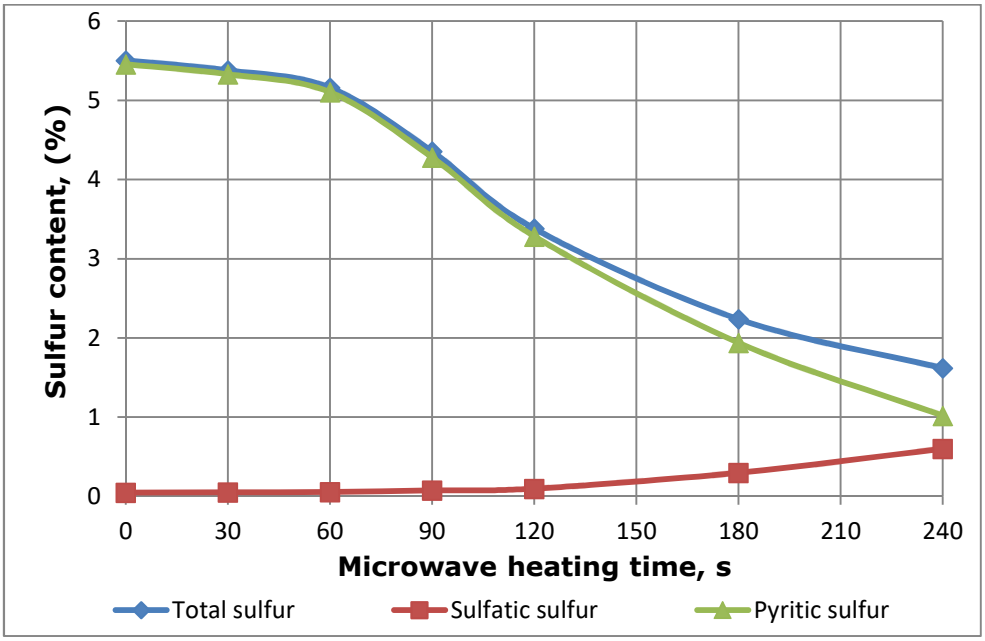

Figure 5. Effect of microwave heating time on sulfur content of the iron ore.

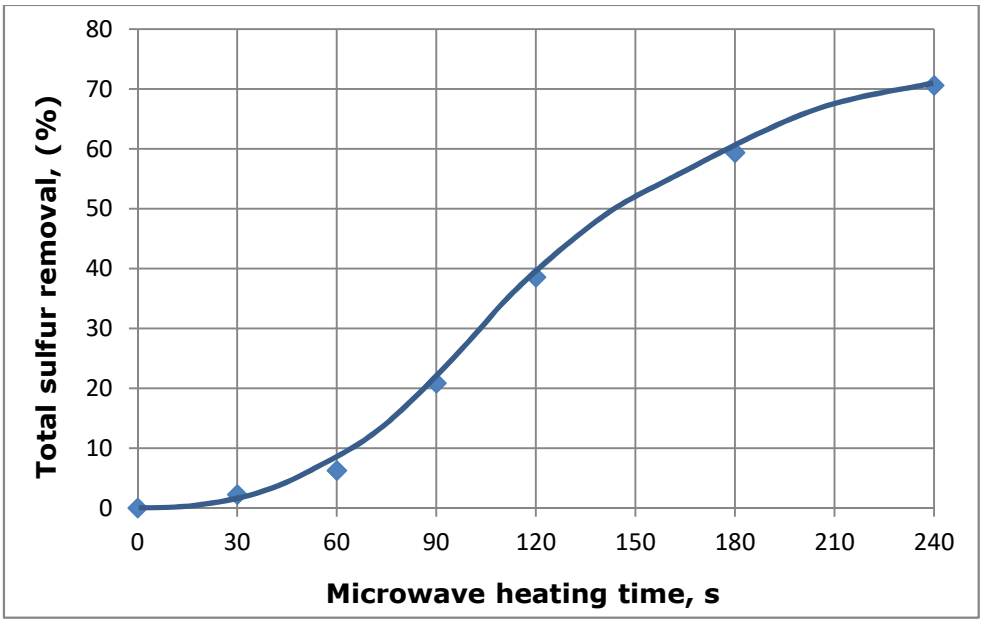

Figure 6. Effect of microwave heating time on total sulfur removal of the iron ore.

According to the results obtained, the optimum process parameters were briefly determined as 210 sec of heating with a microwave at 2.75 GHz and 900 W, H_2SO_4 concentration; 0.03 N, H_2O_2 concentration; and 10% in the removal of sulfur from iron ore with physical and chemical methods.

Following the treatment of the ore, pre-treated with a microwave at 2.75 GHz and 900 Watt, with 0.03 N H_2SO_4 and 10% H_2O_2 solutions at room conditions for 1 hour, the total sulfur content of iron ore was reduced from 5.505% to 0.894%, pyritic sulfur content was reduced from 5.457% to 0.894% and sulfate sulfur was removed completely. Since no organic sulfur is present in the iron ore sample, the total sulfur content is equal to the sum of sulfate and pyritic sulfur. Since no sulfate sulfur is present in the treated sample, the total sulfur is equal to pyritic sulfur. Therefore, the total sulfur and pyritic sulfur contents of the treated sample are the same (0.894%). At the end of these processes, the total sulfur content of the raw iron ore was removed at the rate of approximately 84%. It is considered that the rate of sulfur removal from raw iron ore can be increased and the cost of the process can be reduced with a study in which the power, frequency and heating rate of the microwave based on these parameters change.

REFERENCES

[1] 2003, Demir-Çelik Sektörü, Birleşik Metal İşçileri Sendikası, Birleşik Metal-İş Yayınları , Sayı: 2, İstanbul.

[2] 2001, Sekizinci Beş Yıllık Kalkınma Planı, Madencilik ÖİK Raporu Metal Madenler Alt Komisyonu Demir Çalışma Grubu Raporu, Ankara.

[3] Socha, L., Michalek, K., Bazan, J., GRY, K., Machovc P., OPLERE, A., STYRNAL, P., 2014, Svaluation of Influence of Briquetted Synthetic Slags on Slags Regime and Process of Steel Desulphurization, Archives of Metallurgy and Material, Volume: 59, Page: 809.

[4] Karaca, H., Ceylan, K., 1995, Chemical cleaning of Turkish lignites by leaching with aqueous hydrogen peroxide, Fuel Processing Technology, Volume: 50, Page: 19.

[5] Toroman Ö.Y., Depçi, T., 2007, Kömürde Mikrodalga ile Önişlem Uygulamaları, Madencilik, Cilt: 46, Sayı: 3, Sayfa: 43.

[6] Jarjoni, E., Rezai, B., Vossoughi, M., Osanloo, M., 2004, Desulfurization of Tabascoal with Microwaveirration/Peroxyaceticacid Washing at 25 ^{o}C and 55 ^{o}C, Fuel, Volume:83, Page: 943.

[7] Uslu, T., Atalay, Ü., Microwaveheating of Coal for Enhanced Magnetic Removal of Pyrite, 2003, Fuel Processing Technology, Volume: 85, Page: 21.

[8] Asmatülü, R., İpekoğlu, B., 1995, Desulphurization of Coal at Coal by Using Sequebtial Process, İstanbul Üniversitesi Mühendislik Fakültesi Yerbilimleri Dergisi, Cilt: 9, Sayı: 2, Sayfa: 85.

[9] Turkish Standards, 1966, TS 329.

[10] Turkish Standards, 1979, TS 363.

Türkçe Öz ve Anahtar Kelimeler

Fiziksel ve Kimyasal Yöntemlerle Demir Cevherinden Kükürdün Uzaklaştırılması

Buğra ÇAVUŞOĞLU, Hüseyin KARACA

Öz: Bu çalışmada kükürt, yüksek kükürt içeriğine sahip Kahramanmaraş Elbistan demir cevherinden mikrodalga ve kimyasal yöntemlerle (H_2SO_4 /H_2O_2) uzaklaştırılmıştır. Düşük kaliteli demir cevherinde yüksek kükürt içeriği vardır, özellikle teknik uygulamalarda bir darboğaz yaratmaktadır. Yüksek kükürtiçerikli demir cevherinden kükürdün giderilmesi için çeşitli yöntemler uygulanmıştır. Ancak, kükürt giderme sürecinin makul bir şekilde uygulanabilmesi için ekonomik olması gerekir. Bu nedenle, kükürt giderme için fiziksel ve kimyasal yöntemler incelenmiştir. İlk kısımda, demir cevheri pirit kükürdünü (FeS_2, cevherde bulunan kükürt türlerinden biridir) mikrodalga ile yüksek sıcaklığa ısıtılıp kükürt dioksit (SO_2), demir(II) sülfat ($FeSO_4$) ve pirotit (FeS) elde edilmiştir. Bunun ardından H_2SO_4 / H_2O_2 çözeltisi ile soz konusu cevher örneği belirlenen derişimlerde ekstrakte edilmiştir (liçing). En yüksek kükürt giderme performansı 2,75 GHz ve 900 W ısıtma ile (210 saniye) elde edilmiştir, kimyasal yöntemde ise 0,03 N H_2SO_4 / %10 H_2O_2 karışımı 60 dakika süreyle ve oda şartlarında kullanılmıştır Elde edilen sonuçlara göre, demir cevherinden kükürt gidermesinde yüksek mikrodalga gücü, yüksek H_2SO_4 ve H_2O_2 derişimi ve yüksek sıcaklık parametreleri belirgin bir şekilde etkili olmamıştır. Mikrodalga ve kimyasal yöntem (H_2SO_4 / H_2O_2) beraber kullanıldığında demirin kükürt içeriği yaklaşık %84 oranında giderilmiştir.

Anahtar kelimeler: Demir cevheri; kükürt giderme; fiziksel ve kimyasal yöntemler.

Sunulma: 17 Eylül 2016. **Düzeltme:** 25 Aralık 2016. **Kabul:** 26 Aralık 2016.

This article was initially submitted to the UKMK 2016 (National Chemical Engineering Congress) and finally evaluated by the JOTCSB editorial staff.

Development of a Gold Nanoparticle-Based Electrochemical Biosensor for Detection of Phenolic Compounds

Melike KIZILKAYA[1], Ülfet EREN[2], İlker POLATOĞLU[1*]

1. Celal Bayar University, Faculty of Engineering, Bioengineering Department, 45140 Muradiye- Manisa, Turkey
2. Kâtip Çelebi University, Graduate School Of Natural And Applied Science, Biomedical Technologies, Çiğli-İzmir, Turkey

Abstract: In this study, an enzymatic biosensor was developed with gold nanoparticles and its performance was tested for detection of phenolic compounds. Different combinations of chitosan (Chit), as a support, gold nanoparticle (GNP), and tyrosinase enzyme (T) were coated on glassy carbon working electrode (GCE) to form the enzymatic biosensor. The sensor's components (Chit, GNP and T) were characterized by cyclic voltammetry (CV) and electrochemical impedance spectroscopy (EIS) while its performance and selectivity to catechol (as a model phenolic compound) were tested by chronoamperometric method. An amplified sensor signal was observed depending on high conductivity of gold nanoparticles. Developed sensor has wide linear range (0.046-50 μM), low detection limit (13.8 nM) and high sensitivity (1.144 A/M). The results reported here indicate that this kind of biosensors is a potential candidate for cheap, fast, and simple detection of phenolic compounds.

Keywords: Electrochemical enzyme biosensor; gold nanoparticle; phenol detection.

Submitted: September 21, 2016. **Accepted:** December 13, 2016.

Cite this: Kızılkaya M, Eren Ü, Polatoğlu İ. Development of a Gold Nanoparticle-Based Electrochemical Biosensor for Detection of Phenolic Compounds. JOTCSB. 2017;1(1):115–26.

*Corresponding author. E-mail: ilker.polatoglu@cbu.edu.tr.

INTRODUCTION

Phenolic compounds have been used in the production process of many important components including pesticides, petrochemical products, and wood protectors (1). These compounds are harmful for environment because of their toxicity (2) threating human health and ecological balance (3). Therefore, true and fast detection of phenolic compounds becomes significant. The methods such as spectrophotometry and chromatography are unpractical due to the fact that they are time consuming, expensive and they require trained personnel (4). Biosensor technology is a promising alternative for detection of phenolic compounds (5, 6).

The working principle of biosensors is based on the measurements of the sensor signal that results from the interaction of the analyte with the electrode surface coated by the biofilm (7). Biological agents which will react with the analyte can be enzyme, nucleic acid, microorganism, tissue, antibody, or cells (8). Enzymatic biosensors depending on their substrate interaction capabilities and biocatalytic properties have been developed by using the enzymes as a biological element such as glucoseoxidase (GOD), horseradish peroxidase (HRP) and glutamate dehydrogenase (GDH) for the detection glucose, heavy metals, and pesticides (9). Besides, tyrosinase enzyme is cheaper and extensively studied for detection of phenolic compounds.

Various polymers have been used as support materials for enzyme immobilization. Among them, chitosan is the natural and biocompatible biopolymer and it has special properties such as high mechanical strength, permeability, antimicrobial, cheap, harmless nature, and good biofilm capability (10, 11). Chitosan produced by deacetylation of chitin from mushroom or insect's skeleton interacts with materials having protein structure because of its ability of protonation in acidic conditions (12).

Due to their high surface area, nanoparticles are widely used for sensor construction in order to achieve sensitive detection of lower analyte concentration with wide linear range. Especially gold nanoparticles increase the surface stability for enzyme immobilization (13). These nanoparticles are favored as a sensor component with chitosan based biosensor due to being ability to form biofilm with excellent electrical properties as a result of interaction with positive charges (14). Therefore, they allow electrochemical sensing by providing electrochemical communication between enzyme and bulk electrode materials without the need of external electron transfer mediators (15).

In this work, an electrochemical enzyme biosensor is developed based on tyrosinase immobilized chitosan-gold nanoparticle films coated on working electrode to detect the catechol as a model phenolic compounds.

MATERIALS AND METHODS

Chemicals

Tyrosinase from mushroom (T3824, 25KU/4.3mg), chitosan (Chit), gold nanoparticles (GNP, 20 nm, in 0.1 mM phosphate buffer solutions suspension), catechol (Cat), potassium nitrate (KNO_3), and potassium hexacyanoferrate(II) trihydrate ($K_4[Fe(CN)_6].3H_2O$) were purchased from Sigma Aldrich. Hydrochloric acid (HCl, 37%), disodium hydrogen phosphate dihydrate ($Na_2HPO_4.2H_2O$) and sodium dihydrogen phosphate monohydrate ($NaH_2PO_4.H_2O$) were purchased from Merck. All solutions were prepared with ultra pure water (18.2 MΩ).

Apparatus

All electrochemical measurements (cyclic voltammetry, electrochemical impedance spectroscopy, and chronoamperometry) were conducted by using triple electrode system (reference electrode: Ag/AgCl, counter electrode: Pt wire and working electrode: 5 mm glassy carbon electrode).

Experimental Procedure

A 50 mM pH: 6.5 phosphate buffer solution (PBS) was prepared with $Na_2HPO_4.2H_2O$ and $NaH_2PO_4.H_2O$. Tyrosinase (T) stock solution (4.3 mg/mL) and 2 mM Cat solution were prepared with 50 mM pH: 6.5 PBS. Chitosan powder was dissolved in 0.1 M HCl while GNP solution was first exposed to ultrasonication for 4 hours and an additional 15 minutes of sonication was conducted before each use. 0.5 mM $K_4[Fe(CN)_6]$ containing 0.5 M KNO_3 solution was prepared with 18 MΩ cm^{-1} ultra-pure water for CV and EIS characterizations.

The surface of 5 mm GCE was cleaned by ultrasonication, polishing with 0.05 μm alumina powder and then washing with ethanol and water to achieve a better biofilm coating. 10 μL of sensor components obtained according to Table 1 were dropped on 5 mm cleaned GCE and then dried in vacuum oven (40 cm Hg, 25 °C) about an hour. Enzyme containing electrodes (Chit-T, Chit-GNP-T) was washed in 10 mL pH: 6.5 PBS solution (200 RPM) for 30 minutes to remove non-immobilized enzymes on electrode surface.

Table 1: Combining ratio of biocomposite films.

Sensor component	Mixing with volume ratio respectively
Chit	From stock solution
Chit-GNP	1/1
Chit-T	1/4
Chit-GNP-T	1/1/4

Impedance measurements were performed in the frequency range of 10^5 - 0.1 Hz with 0,005 V amplitude while CV measurements were conducted both in 0.5 mM $K_4[Fe(CN)_6]$ containing 0.5 M KNO_3 solution and pH 6.5, 0.1 mM Cat containing PBS solution in ±0.6 V potential range and at 0,01 V/s scan rate. Optimum working potential of developed enzyme electrode (Chit-GNP-T) was determined by potential scanning in the range of ±1 V both in the absence and presence of 0.1 mM Cat containing PBS solution. Reusability of the biosensor was tested by 30 successive determinations in 10 µM Cat solution. Analytic performance of the biosensor was determined by chronoamperometric method in the range of 0.2-145 µM Cat concentration. Lower detection limit (LOD) was also calculated by using the equation:

$$LOD = \frac{(3.S_{y/x})}{a} \quad \text{(Eq. 1)}$$

Where *a* is the sensitivity (linear part of calibration curve for Cat) of the method and $S_{y/x}$ is the standard deviation of the fit.

RESULTS AND DISCUSSION

Interface properties of biocomposite films were determined by EIS characterization. Semicircle diameters shown in Figure 1 indicate the electron transfer resistance which controls the electron transfer kinetic on electrode surface. Due to non-conductive properties of Chit and T, increase in semicircle diameter was observed after coating the surface of GCE with Chit and Chit-GNP-T. On the other hand, Nyquist curve diameter decreased with the addition of conductive GNP to the Chit structure (Chit-GNP). Electron transfer resistances were evaluated by fitting the Nyquist curves to an equivalent circuit model in order to clarify the interface mechanism.

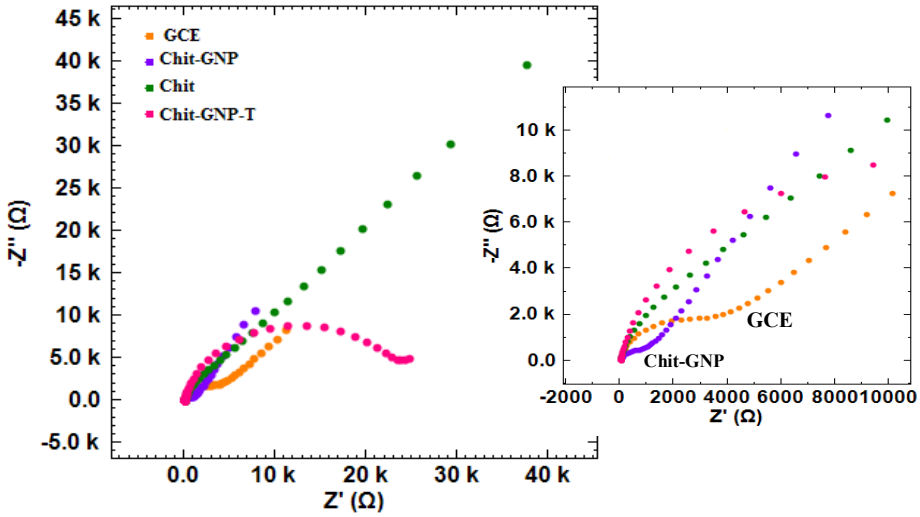

Figure 1. Nyquist diagram of GCE, Chit, Chit-GNP and Chit-GNP-T coated electrode in 0.5 mM $K_4[Fe(CN)_6]$ containing 0.5 M KNO_3 solution. Frequency range: 10^5-0.1 Hz, amplitude: 0,005 V.

In the equivalent circuit model shown in Figure 2, R_s refers to solution resistance, R_{ct} refers to electron transfer resistance, $Y0_1$ and $Y0_2$ refers to constant phase elements.

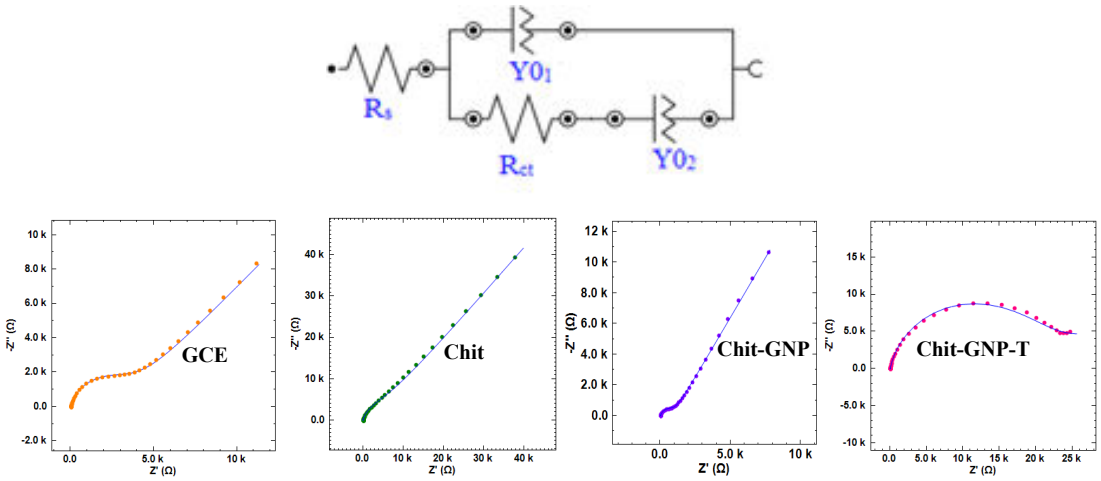

Figure 2. Nyquist diagram of GCE, Chit, Chit-GNP and Chit-GNP-T coated electrode fitted to equivalent circuit model.

The electron transfer resistance (R_{ct}) was estimated as 3.72 kΩ, 6.84 kΩ and 15.6 kΩ for the GCE, Chit and Chit-GNP-T respectively as represented in Table 2. It indicates that Chit and Chit-GNP-T obstructed the electron transfer of $[Fe(CN)_6]^{4-}$ which causes an increase in the electrode impedance. In addition, the obvious increase in R_{ct} for Chit-GNP-T point out the successful immobilization of tyrosinase. The decrease in R_{ct} value for Chit-GNP (1.06 kΩ) with respect to Chit (6.84 kΩ) indicated that GNP accelerate the electron transfer of the electrochemical probe.

Table 2. Electrical paremeters of GCE, Chit, Chit-GNP and Chit-GNP-T coated electrodes.

Electrode	R_s (Ω)	R_{ct} (kΩ)	Y01 (μMho)	Y02 (μMho)
GCE	14.6	3.72	3.45	109
Chit	14.4	6.84	2.72	21.9
Chit-GNP	13.5	1.06	4.62	101
Chit-GNP-T	14.8	15.6	2.94	98.0

CV measurement was also performed in 0.5 mM $K_4[Fe(CN)_6]$ containing 0.5 M KNO_3 solution to demonstrate the enhancement of GNP used for biosensor design. An increase in the redox peak was observed (Figure 3a) in Chit-GNP biocomposite film due to rapid electron transfer depending on conductive properties of GNP parallel to EIS result. Figure 3b depicts the cyclic voltammograms of Chit-T and Chit-GNP-T coated electrodes in the absence and presence of 0.1 mM Cat containing PBS solution. There was no redox peak in the absence of Cat while distinct reduction peak was observed in its presence both for Chit-T and Chit-GNP-T coated electrodes.

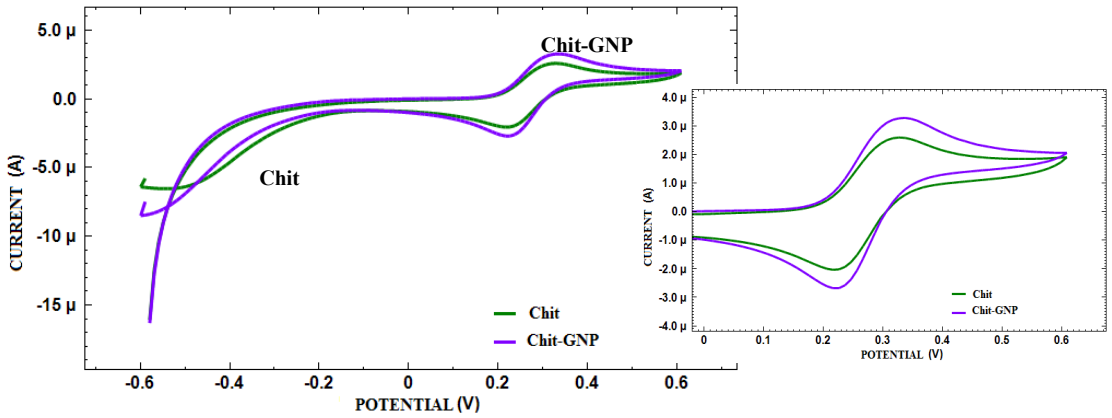

(a)

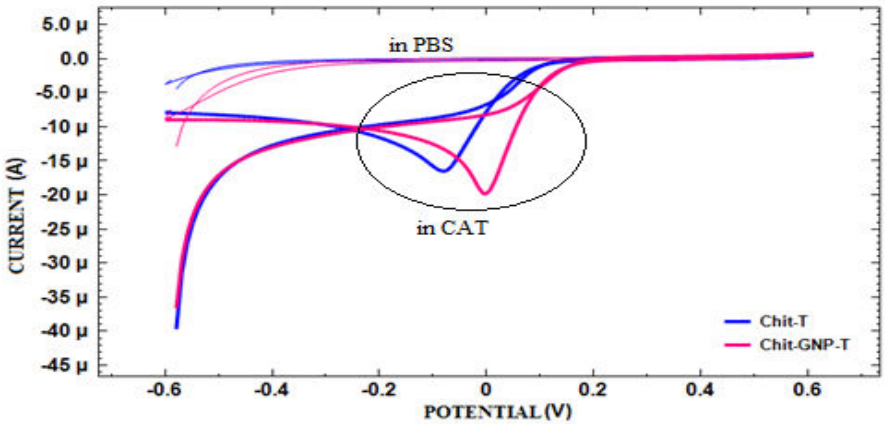

(b)

Figure 3. Cyclic voltammetry of Chit and Chit-GNP coated electrodes. Potential range: ±0.6 V, scan rate: 0.01 V/s. (a) in 0.5 mM $K_4[Fe(CN)_6]$ containing 0.5 M KNO_3 solution. (b) in the absence and presence of 0.1 mM Cat containing PBS solution.

The observed reduction peak was attributed to the reduction of o-quinone on the electrode surface shown in Figure 4. Comparison of the reduction peak currents at Chit-T and Chit-GNP-T clearly demonstrates that GNPs result in a dramatic enhancement of the electrochemical signal (Figure 3b). Therefore the most suitable sensor components were chosen as Chit-GNP-T.

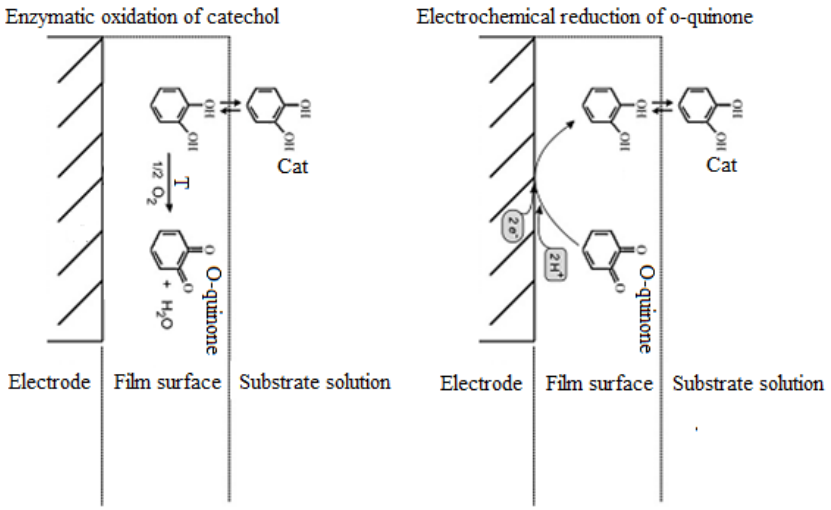

Figure 4. Enzymatic oxidation of catechol and electrochemical reduction of o-quinone.

In this work, optimal working potential was determined to detect the Cat chosen as the phenolic compound by using amperometric method. A higher signal difference was obtained at -0.6 V potential value which was used for further amperometric measurements as seen in Figure 5.

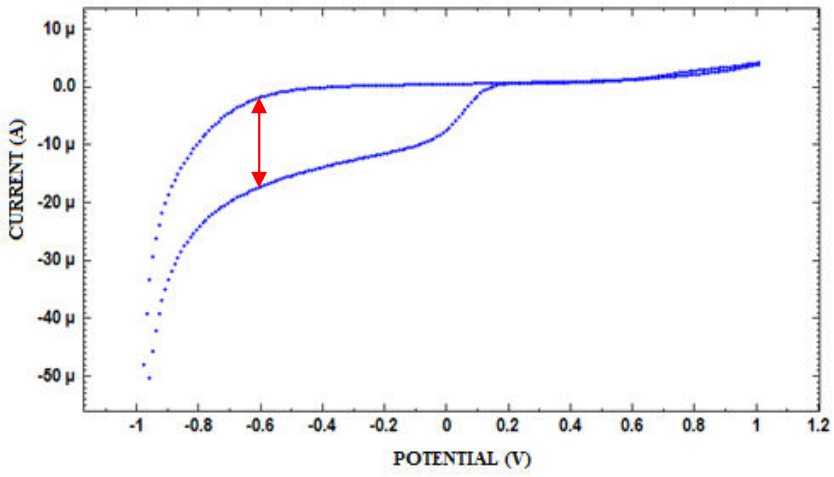

Figure 5. The effect of working potential on amperometric response of developed sensor (Chit-GNP-T) in the absence and presence of 0.1 mM Cat containing PBS solutions.

The phenolic compound "Cat" was detected by developed sensor (Chit-GNP-T) in the concentration range of 0.2-145 µM and calibration curve (Figure 6) was obtained from typical time-current plot (amperometric responses). Kinetic parameters (K_m, I_m) were also calculated by fitting the experimental data to Michaelis-Menten model equation.

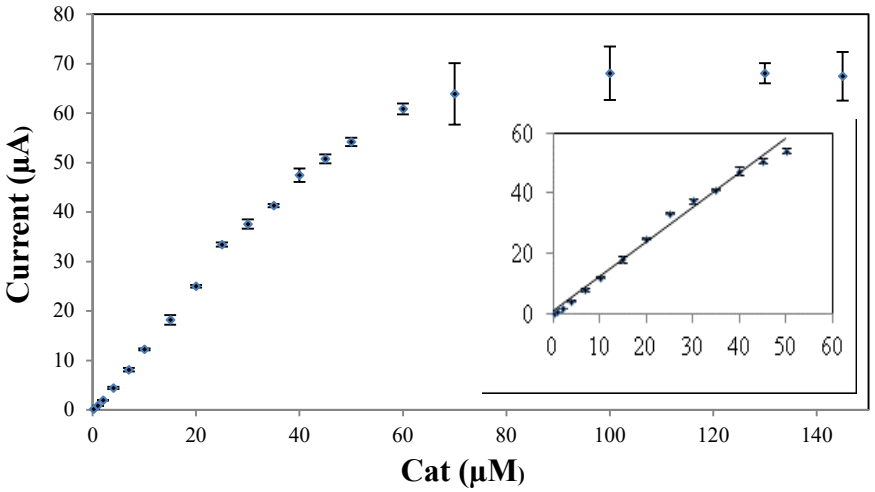

Figure 6. Calibration curve for Cat obtained Chit-GNP-T biosensor.

Analytical performance of developed biosensor including linear range, correlation coefficient, detection limit and sensitivity are summarized in Table 3. Chit-GNP-T biosensor has wide linear range with high correlation coefficient. Compared with the literature, Chit-GNP-T biosensor developed in this study has low detection limit (13.8 nM) with highest sensitivity. The low K_m value demonstrated that Chit-GNP-T biosensor exhibited a high affinity to Cat. Relative standard deviation value of 3.1% for ten successive measurements also indicates good repeatability for developed biosensor.

Table 3. Analytical performance of developed biosensor in Cat containing media.

Analytical performance	This work	Wang *et al*.	Han *et al*.	Obrero *et al*.
Linear range (µM)	0.046-50	0.083-70	0.001-20	0.2-10
Correlation coefficient	0.991	0.999	0.997	0.999
Detection limit (nM)	13.8	25	0.3	353
Sensitivity (A/M)	1.144	0.514	0.561	0.055
K_m (µM)	47.7	96.9	5.21	84.4
I_m (µA)	98.3	83.6	-	-

In this work, an electrochemical biosensor enhanced with gold nanoparticles was developed for detection of phenolic compounds. Sufficient amount of enzyme loading was provided by nanobiocomposite film as understood from electrochemical

characterizations. The designed biosensor demonstrated good analytical performance without extra mediators to increase electrode signal, and showed high sensitivity, low detection limit, and good reusability. The design strategy can lead to develop different types of electrochemical enzyme biosensor.

ACKNOWLEDGMENTS

This study was supported financially by the Scientific and Technological Research Council of Turkey (TUBITAK Grant Number 114Z417).

REFERENCES

1. Han E, Yang Y, Cai J, Zhang X, Dong X. Development of tyrosinase biosensor based on quantum dots/chitosan nanocomposite for detection of phenolic compounds. Analytical Biochemistry. 2015; 486: 102. DOI: 10.1016/j.ab.2015.07.001.

2. Yu C, Gou L, Zhou X, Bao N, Gu H. Chitosan-Fe_3O_4 nanocomposite based electrochemical sensors for the determination of bisphenol A. Electrochimica Acta.2011; 56: 9056.DOI: 10.1016/j.electacta.2011.05.135.

3. Yang L, Xiuhua Z, Wang S. A novel tyrosinase biosensor based on chitosan-carbon-coated nickel nanocomposite film. Bioelectrochemistry. 2012; 84: 44. DOI: 10.1016/j.bioelechem.2011.11.001.

4. Moldoveanu SC, Kiser M. Gas chromatography/massspectrometry versus liquid chromatography/fluorescence detection in the analysis of phenols in main stream cigarette smoke. Journal of Chromatography A. 2007; 1141: 90. DOI: 10.1016/j.chroma.2006.11.100.

5. Mehrotra P. Biosensors and their applications – A review, Journal of Oral Biology Craniofacial Research. 2016; 6: 153. DoI: 10.1016/j.jobcr.2015.12.002.

6. Turner APF. Biosensors: sense and sensibility. Chemical Society Reviews. 2013; 42(8): 3175. DOI: 10.1039/C3CS35528D.

7. Grieshaber D, MacKenzie R, Vörös J, Reimhult E. Electrochemical Biosensors - Sensor Principles and Architectures. Sensors. 2008; 8: 1400. DOI: 10.3390/s8031400.

8. Thevenot DR, Toth K, Durst RA, Wilson, GS. An acetylcholinesterase (AChE) biosensor with enhanced solvent resistance based on chitosan for the detection of pesticides, Talanta. 2016; 146: 279. DOI: 10.1016/j.talanta.2015.08.030.

9. Amine A, Mohammadi H, Bourais I, Palleschi G. Enzyme inhibition-based biosensors for food safety and environmental monitoring. Biosensors and Bioelectronics. 2006; 21: 1405. DOI: 10.1016/j.bios.2005.07.012.

10. Dalkiran B, Kaçar C, Erden PE, Kiliç E. Amperometric xanthine biosensors based on chitosan- Co_3O_4-multiwall carbon nanotube modified glassy carbon electrode. Sensors and Actuators B. 2014; 200: 83. DOI: 10.1016/j.snb.2014.04.025.
11. Bhatt AS, Bhat DK., Santosh MS. Electrical and magnetic properties of chitosan-magnetite nanocomposites. Physica B. 2010; 405: 2078. DOI: 10.1016/j.physb.2010.01.106.

12. Rajasree R and Rahate KP. An Overview on Various Modifications Of Chitosan And It's Applications. International Journal Of Pharmaceutical Sciences and Research. 2013; 4(11):4175-93.URL: http://search.proquest.com/docview/1491065138/abstract/F53148E17E8342AEPQ/1?accountid=11638.

13. Pingarro JM, Yanez-Sedeno P, Gonzalez-Cortes A. Gold nanoparticle-based electrochemical biosensors. Electrochimica Acta. 2008; 53: 5848. DOI: 10.1016/j.electacta.2008.03.005.

14. Feng D, Wang F, Chen Z. Electrochemical glucose sensor based on one-step construction of gold nanoparticle–chitosancomposite film. Sensors and Actuators B. 2009; 138: 539. DOI: 10.1016/j.snb.2009.02.048.

15. Sanz VC, Mena ML, Gonzalez-Cortes A, Yanez-Sedeno P, Pingarron JM. Development of a tyrosinase biosensor based on gold nanoparticles-modified glassy carbon electrodes Application to the measurement of a bioelectrochemical polyphenols index in wines. Analytica Chimica Acta. 2005; 528: 1. DOI: 10.1016/j.aca.2004.10.007.

16. Obrero GS, Mayén M, Miguel J, Mellado JMR, Amaro RR. New Biosensor for Phenols Compounds Based on Gold Nanoparticle-Modified PVC/TTF-TCNQ Composite Electrode. *Int. J. Electrochem. Sci.* 2012; 7: 10952. URL: http://electrochemsci.org/papers/vol7/71110952.pdf.

Türkçe Öz ve Anahtar Kelimeler

Fenolik Bileşiklerin Tayini İçin Altın Nanopartikül Esaslı bir Elektronik Biyosensörün Geliştirilmesi

Melike KIZILKAYA, Ülfet EREN, İlker POLATOĞLU

Öz: Bu çalışmada, altın nanopartikül kullanılarak bir enzimatik biyosensör geliştirilmiş ve fenolik bileşiklerin tayininde kullanılmıştır. Farklı kitosan (Chit), destek olarak, altın nanopartikül (GNP) ve tirozinaz enzimi (T) camsı karbon çalışma elektrodu (GCE) üzerine kaplanmış ve enzimatik biyosensör oluşturulmuştur. Sensörün bilşenleri olan Chit, GNP ve T döngülü voltametri (CV) ve elektrokimyasal impedans spektroskopisi (EIS) ile karakterize edilmiş ve model fenolik bileşik olarak katekole karşı seçimlilik performansı test edilmiştir. Altın nanopartiküllerin yüksek iletkenliği nedeniyle artmış bir sensör sinyali gözlenmiştir. Geliştirilen sensörün geniş bir lineer aralığı (0,046 – 50 µM), düşük tayin sınırı (13,8 nM) ve yüksek hassasiyet (1,144 A/M) içerdiği bulunmuştur. Burada bildirilen sonuçlara göre bu türden biyosensörler fenolik bileşiklerin ucuz, hızlı ve basit bir şekilde tayinine olanak tanıyan potansiyel adaylardır.

Anahtar Kelimeler: Elektrokimyasal enzim biyosensörü; altın nanopartikül; fenol tayini.

Sunulma: 21 Eylül 2016. **Kabul:** 13 Aralık 2016.

(This article was initially submitted to the UKMK 2016 (National Chemical Engineering Congress) and finally evaluated by the JOTCSB editorial staff).

Design and Simulation of Semiconducting Polymers for Optoelectronic Applications by Using Quantum Mechanical Tools

Özge Özkılınç[1], Birnur Kaya[1] and Hakan Kayı[1,*]

[1] Atılım University, Chemical Engineering and Applied Chemistry Department, Computational Chemistry Laboratory, 06836, Ankara, Turkey

Abstract: In this study, polymers containing furan, thiophene, and selenophene units as electron donating groups and benzooxadiazole, benzothiadiazole and benzoselenadiazole units as electron acceptor groups are theoretically designed and their electronic band gaps are calculated with the help of density functional theory. The lowest energy structures of the monomers of these systems are revealed with the help of conformational analysis by using the B3LYP/6-31G(d) and B3LYP/LANL2DZ methods. While the electronic band gap values of monomers are obtained at the same levels of theory, the ones for the polymers are obtained by performing periodic boundary conditions calculations, PBC-DFT. First, accuracy of the methodology is tested by comparing the band gaps with the ones previously studied in the literature, and then structural and electronic properties of the new semiconducting polymers are revealed.

Keywords: Density functional theory, semiconducting polymers, electronic band gap, selenophene.

Submitted: October 11, 2016. **Revised:** November 30, 2016. **Accepted:** December 07, 2016.

Cite this: Özkılınç Ö, Kaya B, Kayı H. Design and Simulation of Semiconducting Polymers for Optoelectronic Applications by Using Quantum Mechanical Tools. JOTCSB. 2017;1(1):127–34.

*Corresponding author. E-mail: hakan.kayi@atilim.edu.tr.

INTRODUCTION

Today, the need to use renewable energy resources in the most effective way that constitutes a driving force for the scientific studies about the high-efficiency and low-cost photovoltaic devices (1). Development of organic, polymer-based photovoltaic materials exhibits the low cost and easy energy generation potential from the sunlight. These materials are promising for the future applications due to their improved electronic and optical properties, low product cost, functionality, thin film flexibility, ease of handling and processing, ease of storage in the form of thin films. Conjugated polymers usually have a band gap of around 1.5-3 eV, and it causes the polymer to make weak absorption in the longer wavelength region of the solar spectrum. This results with the undesirable situations like low electrical charge generation and low stability (2). Conceptually, in order to have a better control on the band gap and energy levels, new strategies need to be developed. One of the most effective strategies is to tune the band gap by utilizing electron donor-acceptor approach. In this approach, various electron donor and electron acceptor units are used in monomer structures and then they are polymerized to tune the band gap of the polymer. These polymers are generally known as donor-acceptor-donor (*D-A-D*) type conjugated polymers. Using of different *D* and *A* units in the form of *D-A-D* is one of the most successful approaches in the design and synthesis of low band gap conjugated polymers (3,4).

Because of the importance of these polymers in practical applications, theoretical studies have also gained great attention in literature. Some of these studies focused to reproduce experimental findings and hence to validate the theoretical methods used. And some others focused on the revelation of the electronic and optical properties of these polymers by using different *D* and *A* units in the monomer design. For example, Alguno *et al*. calculated the band gap of thiophene monomer and dimer using B3LYP and B3P86 methods and 6-31G(d, p) basis set but their findings were in error by more than 1 eV comparing with experimental results (5). Liu *et al*. calculated the band gap of furo-, thieno-, selenopheno-thiophene and benzo-dithiophene (PBDTFPD, PBDTTPD, PBDTSePD) containing *D-A-D* type conjugated polymers at the PBE0/6-31G(d), O3LYP/6-31G(d), TD-O3LYP/6-31G(d)//O3LYP/6-31G(d) and PBC-O3LYP/6-31G(d) levels of theory and they obtained comparable results to experimental data (6). Fu *et al.* worked on the electronic structures of dithienothiophene based *D-A* conjugated polymers (TTP-DTT, DTP-DTT, TBT-DTT) and investigated the effect of *D/A* ratio used within the monomer on the electronic properties of the polymer using B3LYP/6-31G(d) and PBC/B3LYP/6-31G level calculations (7). They obtained the most effective results when *D/A = 2/1* ratio was used. Kose used thiophene (S) as the donor unit and investigated the band gap of a group of *D-A-D* type monomers (S-X-S) systematically as a function of different acceptor (X) units using B3LYP/6-31G(d) method (8). That work was limited

to monomers, and properties of the corresponding polymer systems were not investigated. In the other study, polymers of OOO, SOS and SeOSe systems were studied experimentally and also by using periodic boundary conditions method PBC-B3LYP/6-31G(d) (9). Previously reported abnormally low band gap value, 0.83 eV, for the SSeS polymer and excessively high value, 1.80 eV, for the SSS polymer indicate the possible errors in experimental and theoretical methods used (10). Therefore, studies on these systems need to be examined. In our previous studies, we extensively studied OSO and OSeO systems by performing detailed conformational analyses on the structures from monomers to tetramers and then calculated the band gap of polymers using different levels of density functional theory (11,12).

In this study, five different *D-A-D* type conjugated polymeric systems are investigated. For all systems, furan (*X = O*), thiophene (*X = S*) and selenophene (*X = Se*) groups are used to be electron donor units, and benzooxadiazole (*Y=O*), benzothiadiazole (*Y = S*) and benzoselenadiazole (*Y = Se*) groups are used as electron acceptor units.

MATERIALS AND METHODS

First, detailed conformational analyses on the monomers of all OOO (*X, Y = O*), SOS (*X = S, Y = O*), SSS (*X, Y = S*), SSeS (*X = S, Y = Se*) and SeSSe (*X = Se, Y = S*) systems are performed using density functional theory at the B3LYP/6-31G(d) and B3LYP/LANL2DZ levels of theory. Starting geometries of the different monomer conformers are prepared under the guidance of our previous studies based on OSO (11) and OSeO (12) systems. The lowest energy monomer structure for each system is obtained as a result of conformational analysis. HOMO-LUMO energy levels and electronic band gap values of the monomers are calculated by the Pipek-Mezey population localization analysis. Subsequently, the band gap values (E_g) of the polymers are calculated with the help of the most stable monomer structure of each system using the periodic boundary conditions (PBC) calculations at the PBC-B3LYP/6-31G(d) and PBC-B3LYP/LANL2DZ levels of theory.

While the obtained band gap values of the OOO, SOS, SSS, and SSeS systems are compared with experimental ones in the literature, the one for the SeSSe polymer is revealed.

Gaussian 09 Rev. D.01 (13) software package is utilized for all the quantum chemical calculations and GaussView 5.0.9 (14) for the molecular visualizations.

RESULTS AND DISCUSSION

Three different stable monomer conformations are obtained for each of the five different systems studied, as a result of the conformational analyses performed at the B3LYP/6-31G(d) and B3LYP/LANL2DZ levels. Chemical structures of these conformers are given in Figure 1, and their relative energies are shown in Table 1.

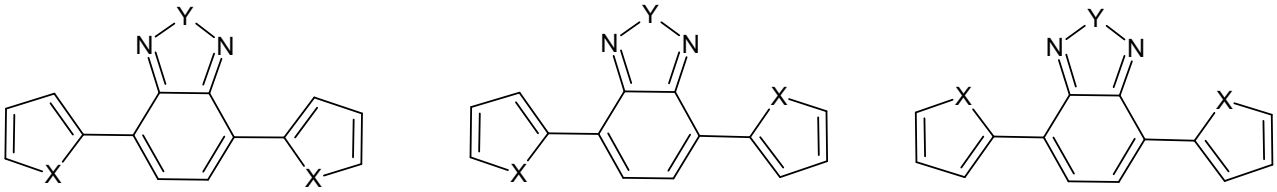

Figure 1. A representation of the chemical structures of monomer conformers obtained from the B3LYP/6-31G(d) and B3LYP/LANL2DZ calculations. (*X = O, S, or Se* and *Y = O, S, or Se*)

Table 1. Relative energies of different monomer conformations for each system calculated at the B3LYP/6-31G(d) and B3LYP/LANL2DZ levels of theory (in E_{rel}, kJ mol^{-1}).

Monomer	E_{rel} B3LYP/6-31G(d)	E_{rel} B3LYP/LANL2DZ
OOO-a	0.0	0.0
OOO-b	13.4	19.8
OOO-c	27.7	41.3
SOS-a	0.0	0.0
SOS-b	5.6	10.5
SOS-c	11.1	21.1
SSS-a	0.0	0.0
SSS-b	2.5	8.1
SSS-c	5.0	16.5
SSeS-a	0.0	0.0
SSeS-b	1.4	7.0
SSeS-c	2.8	14.4
SeSSe-a	7.5	1.5
SeSSe-b	3.4	0.3
SeSSe-c	0.0	0.0

As shown in Table 1, the conformation *a* is found to be the lowest energy structure for the OOO, SOS, SSS and SSeS systems, whereas the conformation *c* is the lowest energy monomer structure for the SeSSe system which is given in Figure 2. Non-bonding interaction between selenium and

nitrogen atoms stabilizes the structure *c* as it was also suggested by Pati and coworkers (15). Therefore, electronic band gap calculation of these systems with the periodic boundary conditions method is based on the SeSSe-c, OOO-a, SOS-a, SSS-a and SSeS-a structures, and the obtained results are given in Table 2.

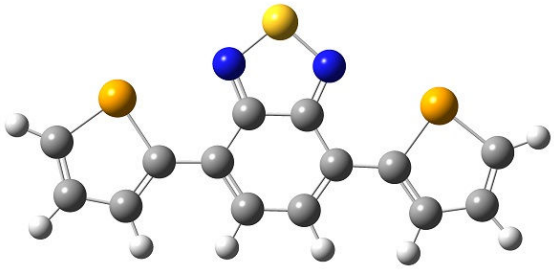

Figure 2. The lowest energy monomer conformation (SeSSe-c) of the SeSSe system.

Table 2. Electronic band gap values of the studied monomers and polymers.

Monomer E_g (eV)			
System	**B3LYP/6-31G(d)**	**B3LYP/LANL2DZ**	**Experimental**
OOO	2.81	2.61	2.46[a]
SOS	2.83	2.59	2.47[a]
SSS	2.74	2.44	2.43[a]
SSeS	2.61	2.42	2.29[b]
SeSSe	2.58	2.28	2.33[a]
Polymer E_g (eV)			
System	**PBC-B3LYP/6-31G(d)**	**PBC-B3LYP/LANL2DZ**	**Experimental**
OOO	1.68	1.47	1.66[c]
SOS	1.68	1.38	1.62[c]
SSS	1.67	1.32	1.50[d]
SSeS	1.59	1.31	1.46[d]
SeSSe	1.41	1.28	-

[a]Ref(15); [b]Ref(16); [c]Ref(9); [d]Ref(17)

When the theoretical results for the polymers are compared with the experimental ones, quite low deviations, from 0.02 eV to 0.13 eV, are obtained through the PBC-B3LYP/6-31G(d) level calculations as they are presented in Table 2.

In this study, we designed the SeSSe polymer, whose monomer was experimentally studied in the literature (15), and we calculated its electronic band gap for the first time by using two different calculation levels PBC-B3LYP/6-31G(d) and PBC-B3LYP/LANL2DZ to be 1.41 eV and 1.28 eV,

respectively. Polymer E_g values in Table 2 clearly indicate that the 6-31G(d) basis set produces slightly higher values and the LANL2DZ produces lower values comparing with the experiments for all the systems studied. Hence it is foreseeable that if the SeSSe polymer is synthesized and its E_g value is measured experimentally, it is highly possible that its electronic band gap value will lie in the given range provided by our calculations. In addition, the lowest E_g value is obtained for the SeSSe polymer amongst all five systems studied. Our findings suggest that increasing the period number in the group VI-A of the periodic table when choosing the X and Y atoms *e.g.*, using a heavy atom such as Se instead of O, for the XYZ system defined in this study directly leads to lower electronic band gap values for the these polymers. We believe that these findings will serve as a guide in the future for both theoretical and experimental design and synthesis studies of the novel low band gap conjugated polymers.

REFERENCES

1. Tang CW. Two-layer organic photovoltaic cell. Appl Phys Lett. 1986;48(2):183. DOI : 10.1063/1.96937.

2. McConnell RM, Godwin WE, Baker SE, Powell K, Baskett M, Morara A. Polyfuran and co-polymers: A chemical synthesis. Int J Polym Mater. 2004;53(8):697–708. DOI: 10.1080/00914030490472908.

3. Beaujuge PM, Ellinger S, Reynolds JR. The donor–acceptor approach allows a black-to-transmissive switching polymeric electrochrome. Nat Mater. 2008;7(10):795–9. DOI: 10.1038/nmat2272.

4. Steckler TT, Abboud KA, Craps M, Rinzler AG, Reynolds JR. Low band gap EDOT–benzobis(thiadiazole) hybrid polymer characterized on near-IR transmissive single walled carbon nanotube electrodes. Chem Commun. 2007;(46):4904. DOI: 10.1039/B709672K.

5. Alguno, Arnold C, Chung, Wilfredo C, Bantaculo, Rolando V, Vequizo, Reynaldo M. Ab initio and density functional studies of polythiophene energy band gap. NECTEC Tech J. 2001;II(9):215–8. URL: http://citeseerx.ist.psu.edu/viewdoc/download?doi=10.1.1.510.5901&rep=rep1&type=pdf.

6. Liu X, He R, Shen W, Li M. Theoretical design of donor-acceptor conjugated copolymers based on furo-, thieno-, and selenopheno[3,4-c] thiophene-4,6-dione and benzodithiophene units for organic solar cells. J Mol Model. 2013;19(10):4283–91. DOI: 10.1007/s00894-013-1939-0.

7. Fu Y, Wang X, Chen M, Shen W. The effects of electron-acceptor strength and donor-to-acceptor ratio on the electronic properties of thieno[3,2-b]thiophene-based donor–acceptor copolymers. Mol Simul. 2014;40(6):439–48. DOI: 10.1080/08927022.2013.819429.

8. Köse ME. Evaluation of Acceptor Strength in Thiophene Coupled Donor–Acceptor Chromophores for Optimal Design of Organic Photovoltaic Materials. J Phys Chem A. 2012;116(51):12503–9. DOI: 10.1021/jp309950f.

9. Pati PB, Das S, Zade SS. Benzooxadiazaole-based D-A-D co-oligomers: Synthesis and electropolymerization. J Polym Sci Part Polym Chem. 2012;50(19):3996–4003. DOI: 10.1002/pola.26195.

10. Sun X, Lei X, Hu Y. Synthesis and Characterization of Conjugated Polymers Based on Benzoselenadiazole. Asian J Chem. 2015;27(7):2427–30. DOI: 10.14233/ajchem.2015.17885.

11. Kayi H. A computational study on 4,7-di(furan-2-yl)benzo[c][1,2,5]thiadiazole monomer and its oligomers. J Mol Model. 2014;20(6). 2269-2275. DOI: 10.1007/s00894-014-2269-6

12. Kayi H, Elkamel A. A theoretical investigation of 4,7-di(furan-2-yl)benzo[c][1,2,5]selenadiazole-based donor–acceptor type conjugated polymer. Comput Theor Chem. 2015;1054:38–45. DOI: 10.1016/j.comptc.2014.12.011.

13. Frisch, M J, Trucks, G W, Schlegel, H B, Scuseria, G E, Robb, M A, Cheeseman, J R, et al. Gaussian 09, Rev. D.01. Wallington CT: Gaussian Inc.; 2013.

14. Dennington, R, Keith, T, Millam, J. GaussView, Ver. 5.0.9. Shawnee Mission KS: Semichem Inc.; 2009.

15. Pati PB, Senanayak SP, Narayan KS, Zade SS. Solution Processable Benzooxadiazole and Benzothiadiazole Based D-A-D Molecules with Chalcogenophene: Field Effect Transistor Study and Structure Property Relationship. ACS Appl Mater Interfaces. 2013;5(23):12460–8. DOI: 10.1021/am403559a.

16. Acharya R, Cekli S, Zeman CJ, Altamimi RM, Schanze KS. Effect of Selenium Substitution on Intersystem Crossing in π-Conjugated Donor–Acceptor–Donor Chromophores: The LUMO Matters the Most. J Phys Chem Lett. 2016;7(4):693–7. DOI: 10.1021/acs.jpclett.5b02902.

17. Cihaner A, Algı F. A Novel Neutral State Green Polymeric Electrochromic with Superior n- and p-Doping Processes: Closer to Red-Blue-Green (RGB) Display Realization. Adv Funct Mater. 2008;18(22):3583–9. DOI: 10.1002/adfm.200801094.

Türkçe Öz ve Anahtar Kelimeler

Kuantum Mekanik Araçlar Kullanarak Optoelektronik Uygulamalar için Yarıiletken Polimerlerin Tasarımı ve Simülasyonu

Özge Özkılınç, Birnur Kaya and Hakan Kayı

Öz: Bu çalışmada, furan, tiyofen ve selenofen birimlerinin electron verici olarak ve benzooksadiazol, benzotiyadiazol ve benzoselenadiazol birimlerinin de elektron çekici olduğu polimerler teorik olarak tasarlanmış ve elektronik bant genişlikleri yoğunluk fonksiyonel teorisi yardımıyla hesaplanmıştır. Bu sistemlerdeki monomerlerin en düşük enerji yapıları B3LYP/6-31G(d) ve B3LYP/LANL2DZ yöntemlerinin yardımıyla ortaya çıkarılmıştır. Monomerlerin elektronik bant genişlikleri teori ile aynı seviyelerde elde edilmekteyken polimerler için elde edilen değerler periyodik sınır koşulları hesaplamaları (PBC-DFT) yapılarak elde edilmiştir. Öncelikle, yöntemin doğruluğu literatürde daha önce çalışılmış moleküllerin bant genişlikleri ile kıyaslama yapılarak test edilmiş, daha sonra da bu yeni yarıiletken polimerlerin yapısal ve elektronik özellikleri ortaya çıkarılmıştır.

Anahtar kelimeler: Yoğunluk fonksiyonel teori; yarıiletken polimerler; elektronik bant genişliği; selenofen.

Sunulma: 11 Ekim 2016. **Düzeltme:** 30 Kasım 2016. **Kabul:** 07 Aralık 2016.

(This article was initially submitted to National Chemical Engineering Congress and reviewed by JOTCSB editorial staff)

Effect of Temperature on SO_2 Absorption

Hayrunnisa MAZLUMOĞLU*[1] and Mustafa Şahin GÜLABOĞLU[1]

[1]Department of Chemical Engineering, Atatürk University, 25240 Erzurum, Turkey.

Abstract: Wet flue desulfurization methods are commonly used to absorb sulfur oxides produced by burning in large coal-fired power stations. The reaction between aqueous suspensions containing appropriate absorbents and the sulfur oxides in the flue gas forms the basis of these methods. As a result, the effect of temperature on the absorption rates of SO_2 in a solution prepared from Mazıdağı phosphate rock, with appropriate characteristics identified in previous studies, and in pure water were investigated and changes to the rock were observed. In an aquatic environment the effect of temperature on SO_2 absorption rate is negative, though the rate of absorption in the phosphate rock suspension was found to increase up to 30 ºC. According to this result, it was concluded that the Mazıdağı phosphate rock should be investigated for use in a flue gas desulfurization system.

Keywords: Phosphate rock; wet flue gas desulfurization; SO_2 absorption; three-phase reactor; lime/limestone.

Submitted: November 14, 2016. **Second round:** November 28, 2016. **Accepted:** January 16, 2017.

Cite this: Mazlumoğlu H, Gülaboğlu M. Effect of Temperature on SO2 Absorption. JOTCSB. 2017;1(1):135–48.

*Corresponding author. E-mail: h.mazlumoglu@hotmail.com.

INTRODUCTION

Especially since the 20th century, the concept of energy has become one of the most important elements used to ensure competitive advantage for countries. At the same time, it is an important factor in economic and social development and plays a vital role in raising living standards. However, thermal power stations used to produce energy cause secondary problems like air and water pollution. As a result, attempts have been made to reduce the waste amounts and types caused by thermal power station technologies and incineration processes day to day with a variety of improvements (1, 2).

The most effective method used in flue gas scrubbing units in power stations is the soil alkaline metal processes using lime/limestone. In the lime/limestone process, flue gas is initially cooled and later washed in an absorption tower with a suspension of limestone or aqueous lime. The SO_2 within the gas mixture forms calcium sulfide and/or sulfate and reacts with the suspension. The scrubbed gas is released into the atmosphere (3-6).

The mechanism of SO_2 absorption within limestone sludge may be obtained from the following steps (7);

$$SO_{2(g)} \rightarrow SO_{2(aqueous)} \quad (1)$$

$$SO_{2(aqueous)} + H_2O \rightarrow H_2SO_3 \quad (2)$$

$$H_2SO_3 \rightarrow H^+ + HSO_3^- \quad (3)$$

$$HSO_3^- \rightarrow H^+ + SO_3^{-2} \quad (4)$$

$$CaCO_{3\,(k)} \rightarrow CaCO_{3\,(aqueous)} \quad (5)$$

$$CaCO_{3\,(aqueous)} \rightarrow Ca^{+2} + CO_3^{-2} \quad (6)$$

$$H^+ + CO_3^{-2} \rightarrow HCO_3^- \quad (7)$$

$$H^+ + HCO_3^- \rightarrow CO_2 + H_2O \quad (8)$$

$$SO_2 + HCO_3^- \rightarrow HSO_3^- + CO_2 \quad (9)$$

$$SO_2 + SO_3^{-2} + H_2O \rightarrow 2HSO_3^- \quad (10)$$

$$CO_3^{-2} + HSO_3^- \rightarrow HCO_3^- + SO_3^{-2} \quad (11)$$

The majority of currently used flue gas desulfurization systems aim to absorb SO_2 with assessment of products formed a secondary concern. However, assessing these products has great importance for the economics of the process. It is generally expensive to regenerate the absorbent materials used in SO_2 absorbent systems as they contain SO_2. As a result, systems discard the material adsorbing SO_2 at the end of the process and appear to be cheaper in terms of investment. However, as the areas of use of the sludge or dry waste materials formed by these systems are limited, storage difficulties arise. If the solid absorbent in flue gas desulfurization can be used in industry after the reaction, it will both solve the solid waste problem and make the process more economical (8).

The Mazıdağı phosphate rock, outcropping over a large area in the Mazıdağı region of Mardin in Turkey, contains a very small amount of silica in addition to large amounts of calcite. The phosphate rock cannot be used in production of orthophosphoric acid and super phosphate due to a variety of problems such as consuming a high amount of sulfuric acid and creating foaming and blockage. However, this rock was determined to have high porosity and appropriate pore distribution during research into gas-solid reactions. Linked to these properties the Mazıdağı phosphate rock had high SO_2 adsorption efficiency rarely seen in the literature (9-12). Thus, the solid obtained after use of active-structured Mazıdağı phosphate rock in wet flue desulfurization systems contains both phosphate and sulfate and it will be possible to use it in the phosphoric acid and fertilizer industry.

Firstly, it was necessary to investigate the effect of temperature on the SO_2 absorption rate in an aquatic phosphate rock suspension and investigate changes in its structure.

MATERIAL AND METHOD

The phosphate rock used in our research was obtained from the Şemikan deposit in the Mardin-Mazıdağı region. The ore was fragmented with a laboratory-type jaw crusher and ground in a ball mill. After homogenization, chemical analysis was performed. The results are shown in Table 1.

Table 1. Chemical Analysis of Phosphate Rock

Component	%wt
SiO_2	1.60
P_2O_5	25.84
Al_2O_3	1.39
F_2	1.69
CaO	47.11
MgO	1.61
Fe_2O_3	0.71
Loss of ignition (CO_2)	13.79 (13.02)

According to these results, the sample with moderate degree phosphate ore contains a very high amount of carbonate.

Mineralogical analysis of the sample used the X-ray powder diffraction method and the spectrum is given in Figure 1. In this diagram, the peaks for two mineral types containing phosphate, fluorapatite, and carbonate fluorapatite are clearly observed. In addition to these, $CaCO_3$ is clearly identified. Different from these three minerals, SiO_2 peaks are observed; apart from these, other minerals could not be determined due to low amounts.

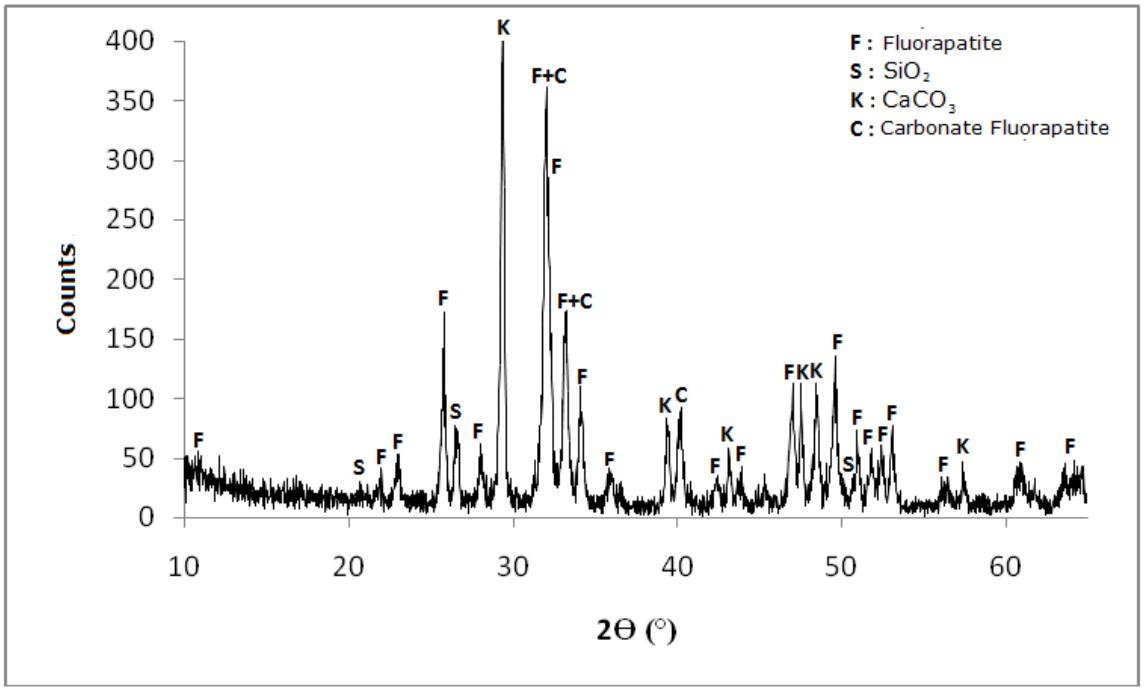

Figure 1. X-ray diffraction spectrum of raw phosphate rock.

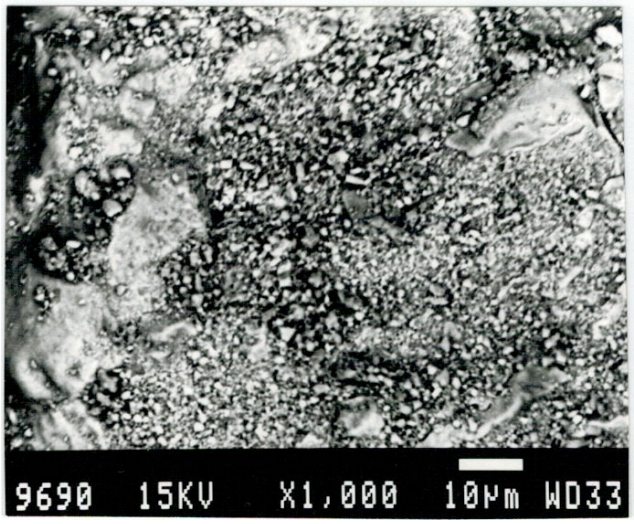

Figure 2. SEM images of raw phosphate rock.

SEM images of raw phosphate rock are given in Figure 2. Here, the large shiny particles and small particles between them are observed. The nearly 2 µm calcite particles between the large phosphate particles are agglomerated. The shiny surface of the phosphate particles indicates a non-porous compact structure. The pore volume in this phosphate rock is 0.0867 cm^3/g with specific surface area identified as 15.68 m^2/g (13).

The TG-DTG-DTA diagram of the raw rock is given in Figure 3. The total weight loss in this diagram appears to agree with the results obtained from chemical analysis. Up to 600 ºC in addition to the weight loss due to water loss and other volatile compounds, there is a slight exothermic peak observed on the DTA curve and the weight loss around 500 ºC is equivalent to combustion of the remaining organic material before evaporation. The weight loss in the region from 600 ºC to 760 ºC is the result of disintegration of $CaCO_3$. At 760 ºC, the shoulder on the DTA curve and following weight loss supports the presence of carbonate fluorapatite identified on the X-ray powder diffraction spectrum and again shows good compatibility with the results of the chemical analysis.

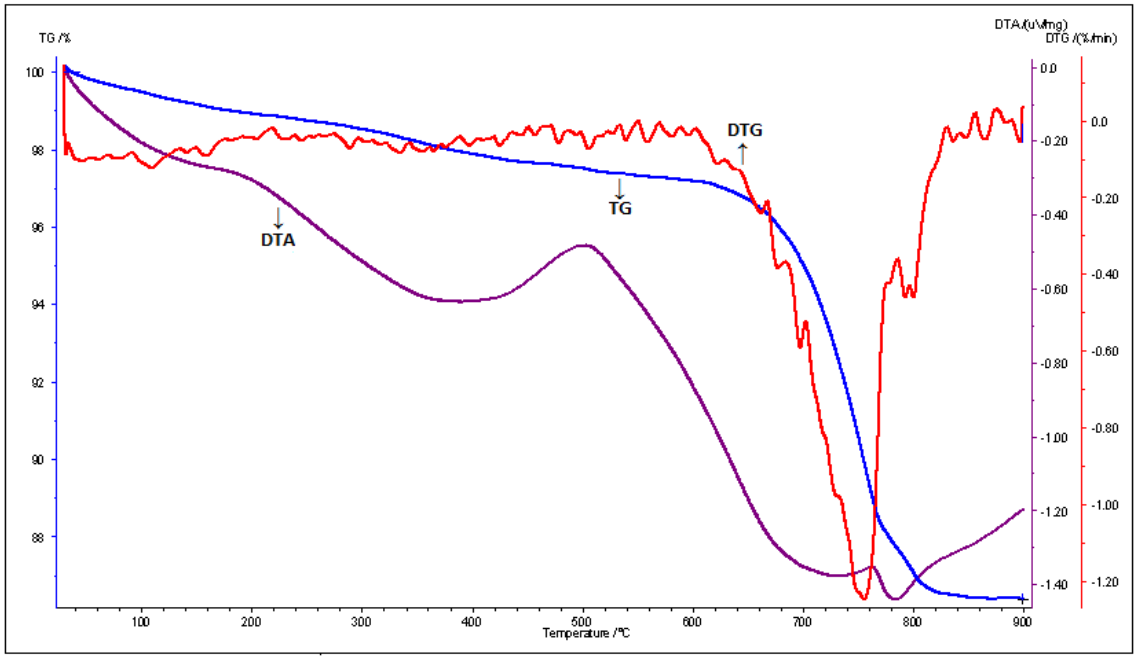

Figure 3. Results of thermal analysis of raw phosphate rock.

To investigate the effect of temperature on SO_2 absorption using the Mardin Mazıdağı phosphate ore and observe changes in the ore, a three-phase reactor as described in the literature was used and the experimental setup is given schematically in Figure 4. The reactor was made of plexi-glass material designed with a fixed surface area to allow contact between fluid and gas phases and to fix the temperature heating or cooling were ensured with the aid of a jacket inside the wall. Additionally it allowed mixing of fluid and gas phases separately at different rates. Air sent into the reactor was heated to the required temperature and humidified before mixing with the determined SO_2 amount. A portion of the "air + SO_2"

mixture was sent to a direct IR spectrometer and the entry concentration of SO_2 was identified. On the far side some of the output gas from the reactor was disposed of, while a portion was sent back to the same analyzer for SO_2 analysis. The values read by the analyzer were recorded with the aid of a computer. Thus the entry and exit values of the "air + SO_2" mixture were identified and the amount of absorbed SO_2 was calculated in terms of molar flux with the aid of the following equation;

$$N_{SO_2} = \frac{P\dot{V}(Y_{SO_2,\text{input}} - Y_{SO_2,\text{output}})}{RTA} \quad (12)$$

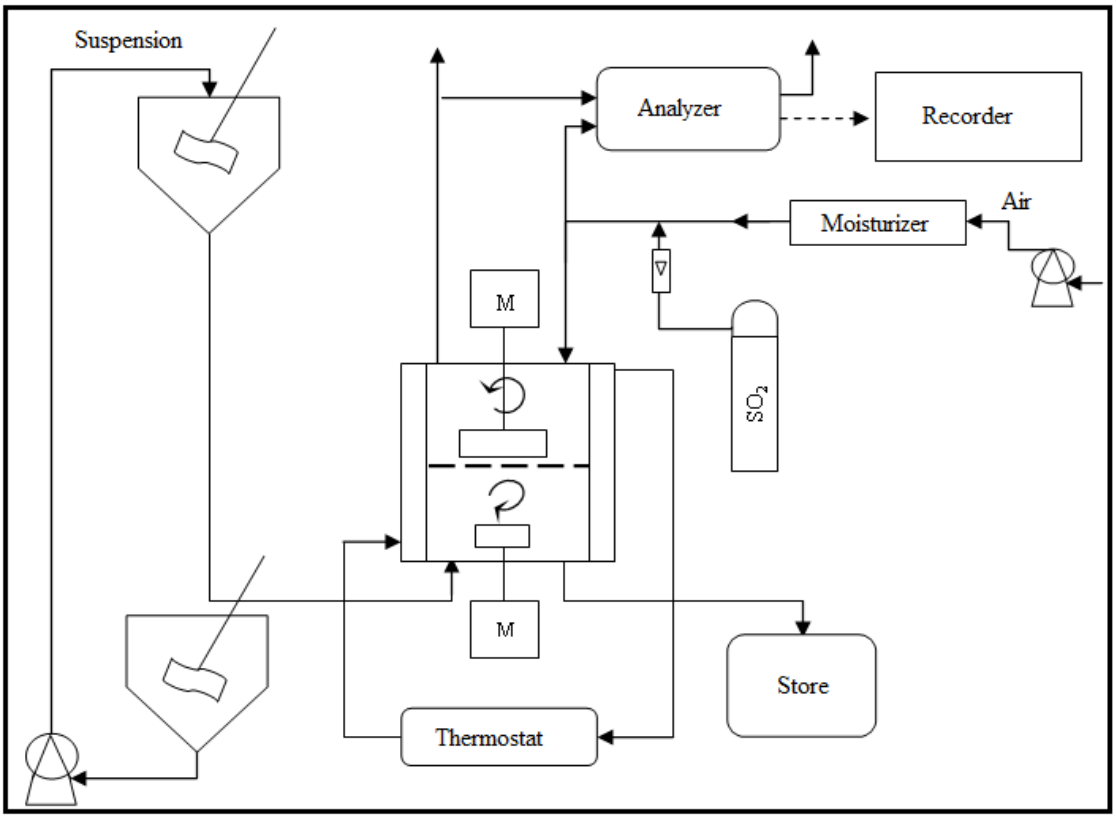

Figure 4. Experimental setup of wet flue gas desulfurization.

Experiments for wet flue gas desulfurization were completed in Erzurum with atmospheric pressure of 610 mmHg.

RESULTS AND DISCUSSION

During experiments to investigate the effect of temperature on absorption, temperature was varied while gas concentration, gas flow, sludge flow, mixing rates and sludge concentration were fixed. Experiments were completed with 3000 ppm SO_2, 4000 mL/min gas flow, 500 mL/min sludge flow, 900 rpm gas mixing rate, 300 rpm fluid mixing rate and 6% sludge concentration. Additionally, measurements were completed under the same conditions with water containing no phosphate rock. The $N_{SO2,s}$ statement is for the suspension (sludge), while

the $N_{SO2,w}$ refers to the molar flux obtained for water. The results calculated from experimental data are shown in Figure 5.

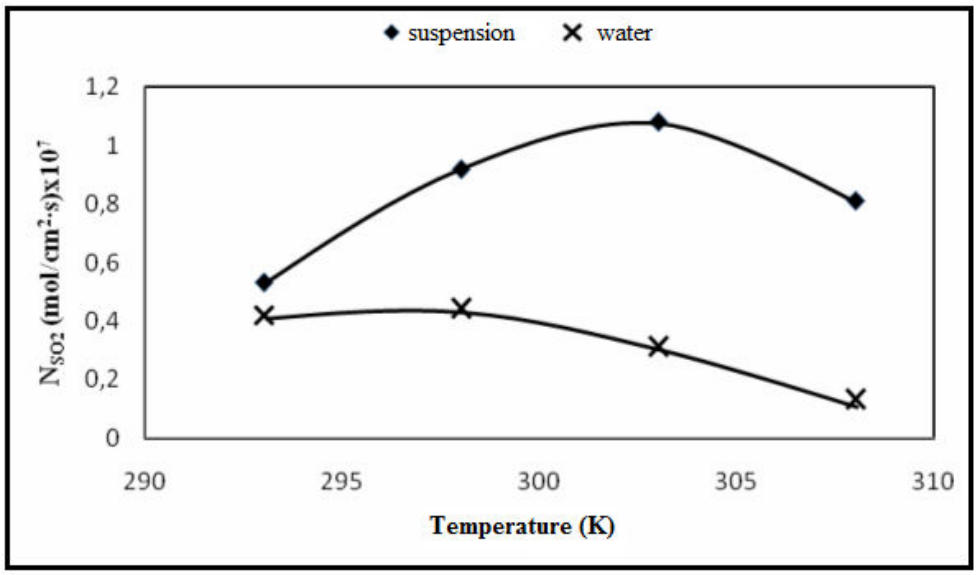

Figure 5. Variation of SO_2 molar flux with temperature.

As the transformation of the solid in this measurement system was very low, the analysis could not be completed so the following procedural examples were prepared. The suspension prepared using phosphate ore obtained from the Şemikan deposit in the Mardin-Mazıdağı region was left in the humidified "Air + SO_2" mix within the semi-batch operated reactor for 16 hours. The experiment used the above experimental conditions; however it was completed on the fluid side with non-flux semi-batch procedure. The sludge was later filtered, dried and investigated with x-ray powder diffraction, SEM and thermal analysis methods.

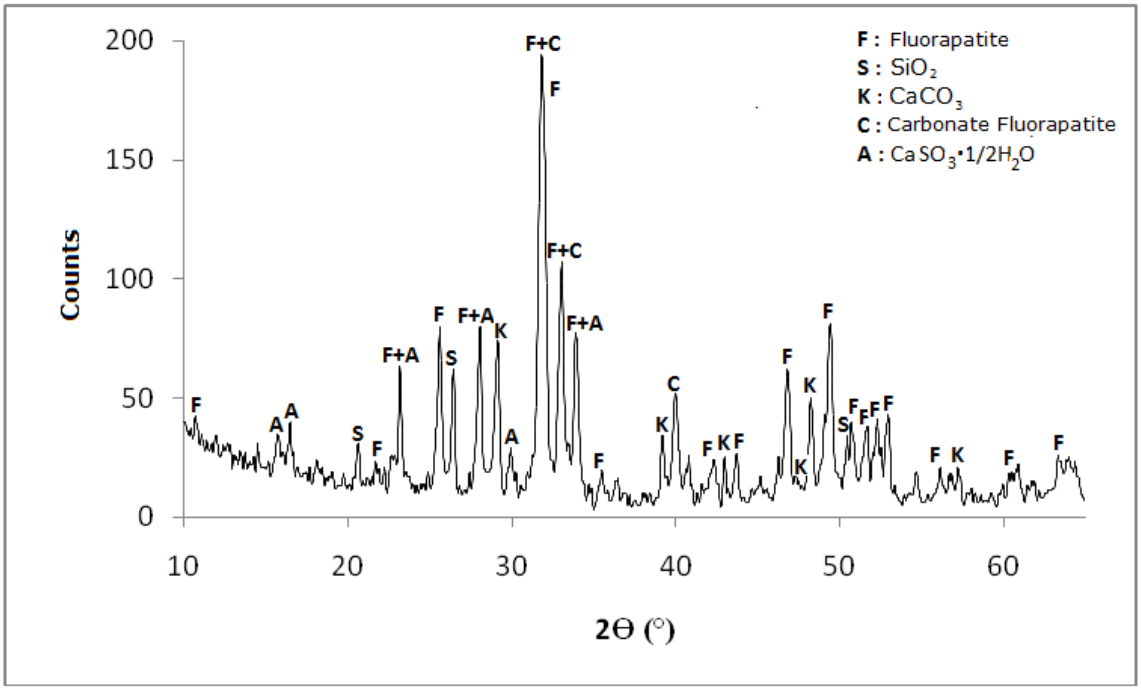

Figure 6. X-ray powder diffraction spectrum of rock processed for 16 hours.

The X-ray powder diffraction diagram for this sample (Figure 6) did not show any significant changes in fluorapatite, carbonate fluorapatite and silicon dioxide peaks. However, the calcium carbonate peak weakened significantly and new peaks shown by A were formed. These peaks were determined to belong to $CaSO_3 \cdot ½H_2O$ compound.

On the thermal analysis diagram shown in Figure 7, the weight loss up to 300 ºC has thermal analysis results similar to raw ore. However, after the rapid weight loss at 400 ºC, there was a weight increase after 550 ºC. This did not occur with the raw ore and is considered to be a result of the reactions occurring between SO_2 and the rock. Later the weight loss beginning around 700 ºC is similar to the behavior of the raw rock. The shoulder belonging to carbonate fluorapatite is repeated with no change observed in the value.

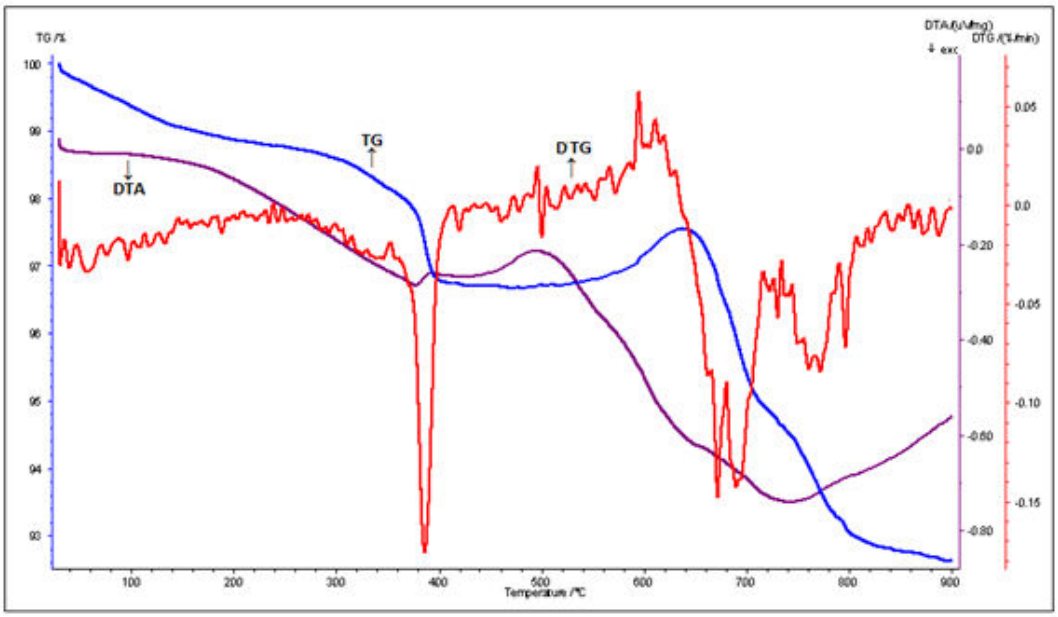

Figure 7. Results of thermal analysis of phosphate rock processed for 16 hours.

Figure 8, in addition to showing the SEM images of the samples, shows the phosphorus and sulfur distribution. From the diagram, it is noteworthy that the large particles rich in phosphorus have less involvement with sulfur. In this way, the small particles are rich in sulfur, which appears to accumulate on all surfaces. Additionally, the measured SEM image shown in Figure 9 confirms that all surfaces of the small $CaSO_3 \cdot ½H_2O$ crystalline agglomerates are covered.

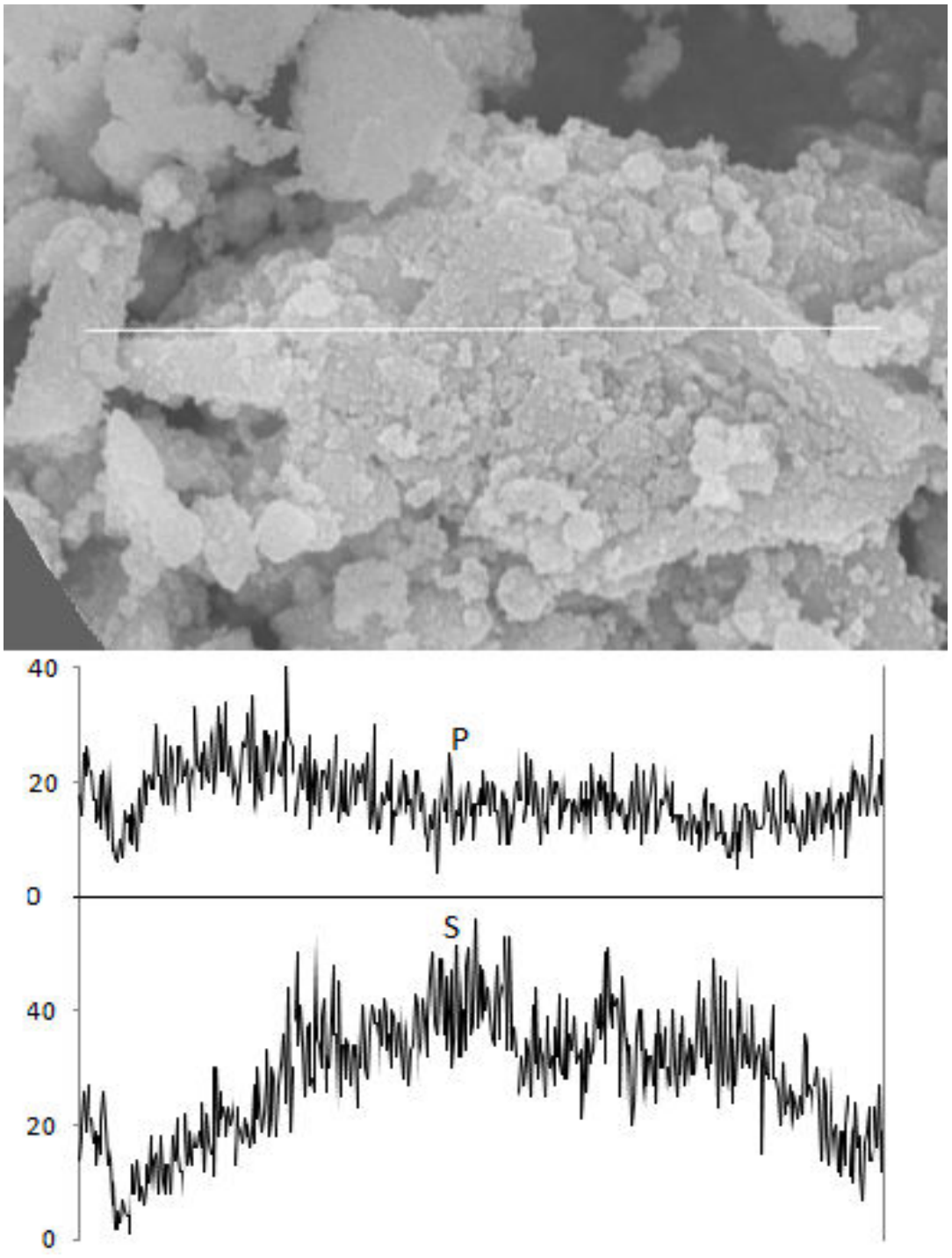

Figure 8. SEM image and elements distribution of the rock processed for 16 hours.

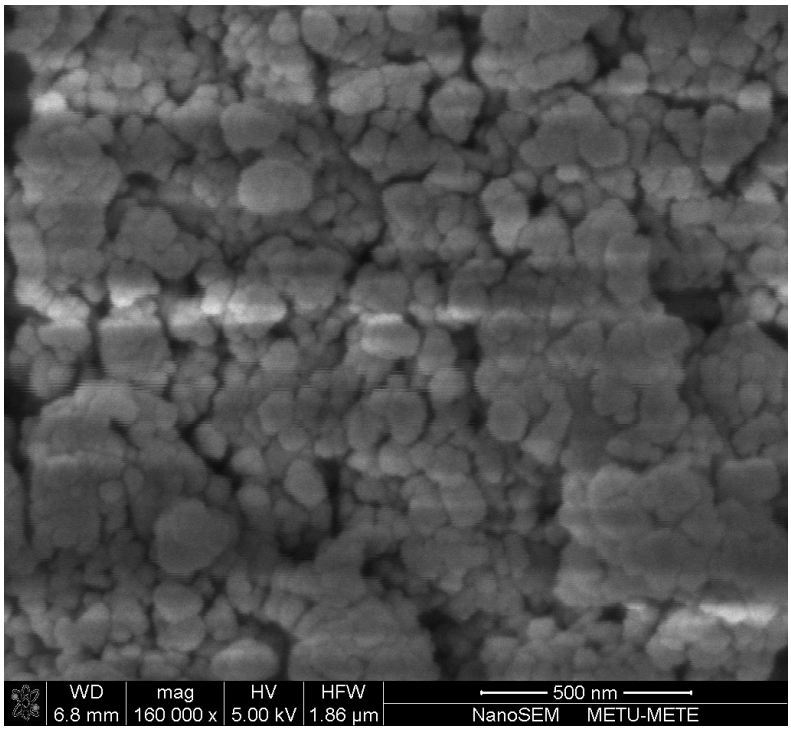

Figure 9. SEM image and elements distribution of the rock processed for 16 hours.

CONCLUSION

In this study, phosphate ore obtained from the Şemikan deposit in the Mardin-Mazıdağı region had chemical and structural characteristics determined with a variety of chemical and instrumental methods. Later, in a multi-phase reactor the suspension containing finely ground ore was placed in contact with "Air + SO_2" gas mix with unchanging surface to investigate the effect of temperature on gas absorption. Analyses were performed to identify changes occurring in the ore. Below these investigations are discussed separately.

As seen in Figure 5, the SO_2 molar flux of the suspension containing phosphate rock initially increased with the increase in temperature and then later reduced. The molar flux in water initially rose slightly but then a significant reduction was observed as temperature increased. Experiments by Long *et al.* (2005) and Mao *et al.* (2008) on chemical reaction absorption concluded that temperature initially increased molar flux by a certain amount and then later reduced it. As observed in Figure 5, the experiments completed in water initially had an insignificant increase in molar flux followed by a significant degree of reduction. Kiil *et al.* (1998) and Mao *et al.* (2008) stated that this situation was based on the reduction in solubility of SO_2 in water at high temperatures. These observed results are in accordance with the reduction in solubility of SO_2 in water identified by Bjerle *et al.* (1972). This variation difference occurring in water and in suspension may be explained by SO_2 transferred into water being directed by the solubility balance, while the SO_2 transferred into the suspension medium has difficulty reaching balance due to chemical linkages (14-17).

As the transformation of products obtained from the continuous system was very small, to identify these products a semi-batch system that could run for longer was used in a 16-hour experiment.

Analysis of samples obtained did not show a reduction in the ratios of fluorapatite and carbonate fluorapatite in the ore structure, though there was a significant reduction in calcite ratio. The X-ray diffractometry diagram showed that it contained the compound $CaSO_3 \cdot ½H_2O$. On SEM images, the agglomeration of small particles described in the literature (18) was clearly observed. Apart from this, in the diagram under the SEM image, the greater intensity of the sulfur peaks compared to phosphorus is clearly observed. The larger scale image of this formation (Figure 9) is in accordance with the agglomerations described by Chu *et al.* (1997).

In conclusion, domestic phosphate rock may be said to easily react with SO_2 with high efficiency under conditions appropriate to wet flue gas desulfurization. With more detailed investigation of conditions and transformation of the product into more stable sulfate form, it will be possible to apply this method in the industry. Local raw phosphate rock cannot be used in H_3PO_4 production as it causes excessive acid consumption due to high carbonate content and because of technological problems like causing foaming and blockage in the system. However, the creation of unused waste by sorbents after use in flue gas desulfurization and the environmental problems caused by these led to consideration of the applicability of a basic sorbent of phosphate rock. As seen in this study, the ore may be a good flue gas sorbent and produces a good raw material for use in H_3PO_4 production. With large reserves and no use due to high carbonate content, Turkey's phosphate deposits may be used for this aim contributing to the country's economy and as an alternative sorbent for use in flue gas desulfurization; as such we believe this study is a pioneer for future studies.

NOMENCLATURE

N_{so2}	SO_2 molar flux, mol cm^{-2} s
P	partial pressure, Pa
v	gas flow, mL min^{-1}
$Y_{SO2,input}$	SO_2 input mole fraction
$Y_{so2,output}$	SO_2 output mole fraction
R	gas constant, J mol^{-1} K^{-1}
T	temperature, K
A	surface area, cm^2

REFERENCES

1. Kavak K. Dünyada ve Türkiye'de Enerji Verimliliği ve Türk Sanayiinde Enerji Verimliliğinin incelenmesi. Devlet Planlama Teşkilatı Uzmanlık Tezi, Yayın No: DPT. 2005; 2689

2. Davutoğlu C. Termik Santral Baca Gazı Arıtma Tesisi Kaynaklı Koagülasyon Çamurunda Florür Giderimi. Y. Lisans Tezi, Çukurova Üniv., Adana. 2008

3. Hamm V H, Hüller R. Das zweistufige Knauf-Research-Cottrell-Verfahren zur Rauchgas-entschwefelung am Beispiel des Kraftwerkes Franken. Zement-Kalk-Gips. 1982; 6: 313-17.

4. Mohn U. Steinmüller–Rauchgasent-schwefelung. VDI-Berichte. 1984; 495: 83-9.

5. Schönbucher B. Rauchgasentschwe-felungsanlagen im Kraftwerk Heilbronn. VDI-Berichte. 1984; 495: 93-100.

6. Çavuşoğlu H, Gülaboğlu M Ş. Yaş Baca Gazı Desülfürizasyon Yöntemleri. Pamukkale Üniversitesi Mühendislik Bilimler Dergisi. 2013; 19 (4): 187-194.

7. Takashina T, Honjo S, Ukawa N, Oishi T. Effect of Limestone Concentration and Particle Size on SO2 Absorption in Wet FGD Process. Journal Chemical Engineering of Japan. 2001; 34: 810-18.

8. Özer A K. Mazıdağı Fosfat Kayası ile Baca Gazı Desülfürizasyonu. Doktora Tezi, Atatürk Üniv., Erzurum. 1996.

9. Özer A K, Gülaboğlu M Ş, Bayrakçeken S, Weisweiler W. Flue Gas Desulfurization with Phosphate Rock in a Fluidized Bed. Fuel. 2002; 81: 41-9.

10. Özer A K, Gülaboğlu M Ş, Bayrakçeken S, Weisweiler W. Changes in Physical Structure and Chemical Composition of Phosphate Rock during Calcination in Fluidized and Fixed Bed. Advanced Powder Technol. 2006; 17(5): 481-94.

11. Sınırkaya M, Bayrakçeken H, Özer A K, Gülaboğlu M Ş. The Effect of Carbon Dioxide during the Desulfurization of Flue Gas with Mardin-Mazıdagı Phosphate Rock. Flue. 2008; 87: 3200-206.

12. Naktiyok J, Bayrakçeken H, Özer A K, Gülaboğlu M Ş. Flue Gas Desulfurization by Calcined Phosphate Rock and Reaction Kinetic. Energy and Fuels. 2013; 27: 1466-72.

13. Özer A K, Gülaboğlu M Ş, Bayrakçeken S. Physical Structure and Chemical and Mineralogical Composition of the Mazidagı (Turkey) Phosphate Rock. Ind. Eng. Chem. Res. 2000; 39: 679-83.

14. Long X, Xiao W, Yuan W. Kinetics of Gas-Liquid Reaction between NO and $Co(en)_3^{+3}$. Ind. Eng. Chem. Res. 2005; 44: 4200-205.

15. Mao Y P, Bi W, Long X L, Xiao W D, Li W, Yuan W K. Kinetics for the Simultaneous Absorption of Nitric Oxide and Sulfur Dioxide with the Hexamminecobalt Solution. Separation Purification Technology. 2008; 62: 183-191.

16. Kiil S, Michelsen M L, Dam-Johansen K. Experimental Investigation and Modeling of a Wet Flue Gas Desulphurization Pilot Plant. Industrial and Engineerin Chemistry Research. 1998; 37: 2792-2806.

17. Bjerle I, Bengtsson S, Farnkvist K. Absorption of SO_2 in $CaCO_3$-slurry in a laminar jet absorber. Chemical Engineering Science. 1972; 27: 1853-61.

18. Chu K J, Yoo K S, Kim K T. Charactaristics of Gypsum Crystal Growth over Calcium-Based Slurry in Desulfurization Reactions. Materials Research Bulletin. 1997; 32 (2): 197-204.

Türkçe Öz ve Anahtar Kelimeler

SO_2 Soğurulması Üzerine Sıcaklığın Etkisi

Hayrunnisa MAZLUMOĞLU ve Mustafa Şahin GÜLABOĞLU

Öz: Kömür kullanan büyük enerji santrallerinde yanma ürünü olan kükürtoksitlerin tutulması amacıyla yaş baca gazı desülfürizasyon yöntemleri sıklıkla kullanılmaktadır. Uygun absorban içeren sulu süspansiyonların baca gazındaki kükürtoksitler ile olan reaksiyonu, bu yöntemlerin temelini oluşturmaktadır. Bu yüzden daha önceki çalışmalarda uygun özellikleri tespit edilmiş Mazıdağı fosfat kayasından hazırlanmış süspansiyonda ve saf suda SO_2 çözünme hızı üzerine sıcaklığın etkisi incelenmiş ve kullanılan cevherde meydana gelen değişimler gözlenmiştir. Sulu ortamda SO_2'nin çözünme hızı üzerine sıcaklığın etkisinin negatif olmasına karşın fosfat kayası süspansiyonundaki hızın 30 °C'ye kadar artış gösterdiği tespit edilmiştir. Bu sonuca göre yaş baca gazı desülfürizasyon sistemi için Mazıdağı fosfat kayasının incelenmesi sonucuna varılmıştır.

Anahtar kelimeler: Fosfat kayası; yaş baca gazı desülfürizasyonu; SO_2 absorsiyonu; üç fazlı reaktör; kireç/kireçtaşı.

Sunulma: 14 Kasım 2016. **İkinci tur:** 28 Kasım 2016. **Kabul:** 16 Ocak 2017.

(This article was initially submitted to National Chemical Engineering Congress and reviewed by JOTCSB editorial staff).

Concentration of Skim Milk and Dairy Products by Forward Osmosis

Ayça Hasanoğlu[1]*, Kübra Gül[1]
[1]Yıldız Technical University, İstanbul, Turkey

Abstract: The concentration of liquid foods such as fruit-vegetable juices and milk by removing its water content is an important chemical process in terms of concentration of food nutrition, shelf-life and stability extension, decrease of the bacterial activities and cost reduction of transportation and storage. Milk can be consumed as concentrated milk by removing its water content at certain rates. Eliminating the water content in milk at certain proportions is also an essential step during several dairy product manufacture processes such as cheese, yogurt and milk powder production. In this study, milk concentration is carried out by means of forward osmosis using membrane contactors as an alternative process to conventional evaporation processes. In this process, milk is circulated through the shell side of the hydrophobic membrane contactor while a draw solution of $CaCl_2$ is circulated through the lumen side. Thus water is transferred from the milk solution to the brine solution because of the activity difference between these two solutions. In forward osmosis the effect of process parameters such as feed and draw solution rates, draw solution concentration, temperature on water fluxes was investigated and it was found that water can be removed efficiently and rapidly using this process. The concentration was carried out until the milk volume reduced in half and flux values at investigated process conditions were found to be in the range of 155-387 mL. h^{-1} m^{-2} .

Keywords: Forward osmosis; membrane contactor; milk concentration.

Submitted: September 30, 2016. **Revised:** November 21, 2016. **Accepted:** December 30, 2016.

Cite this: Hasanoğlu A, Gül K. Concentration of Skim Milk and Dairy Products by Forward Osmosis. JOTCSB. 2017;1(1):149–60.

*Corresponding author. E-mail: aycameric@yahoo.com.

INTRODUCTION

In order to provide microbiological and chemical stability, milk is generally concentrated using multi-stage evaporators. When the focus is to prepare concentrated milk to be consumed, the dry matter content in milk should be increased from 8-12% to 20-25% [1]. Since the volume is reduced, stock and transfer costs decrease in this way. On the other hand, in most dairy product production such as cheese, yogurt, and milk powder, milk is used as its concentrated form by removing its water content at certain rates. For example, in milk powder process milk is concentrated until 50% dry matter content before it is sent to spray dryer [2]. Ramirez *et al.* (2006) made an analysis of energy consumption and energy efficiency for the dairy industry in four European countries and indicated that milk concentration, together with drying, can be considered as the most energy intensive operations of the dairy industry [3]. In general, in the dairy industry, evaporation is mainly done in falling film evaporators employing multiple stage evaporators [3]. However, conventional thermal evaporation can result in a loss of aroma compounds and color and taste degradation in liquid foods due to the thermal effects [4]. Therefore, non-thermal alternative concentration techniques have been gaining importance recently. The use of membrane separation techniques in liquid food concentration have several advantages over conventional separation processes including improved product quality, easy scale-up and lower energy consumption [4]. In the literature, several liquid food concentration studies such as fruit juices using forward osmosis have been reported [4-7], however milk concentration was not encountered using this process. Although there are reported studies of milk processing with the use of membrane processes such as reverse osmosis and ultrafiltration [8, 9], there are few works in the literature focused on the use of membrane contactors for milk concentration. Hausmann *et al.* proposed membrane distillation which employs membrane contactors for milk and whey processing [10, 11]. In their study, water transfer through the membrane is achieved by a temperature difference provided on both sides of the hydrophobic membrane contactor. They studied skim milk and whey concentration by membrane distillation where the driving force is the temperature difference between two sides of the membrane. They concluded that the retention of dissolved solids was found to be close to %100, indicating the potential use of the membrane contactors in dairy product processing. On the other hand, several reports in literature indicate that that forward osmosis has several advantages over membrane distillation [12, 13]. In forward osmosis the driving force for the water transfer through the hydrophobic membrane contactor is provided by activity difference of water between two sides of the hydrophobic membrane contactor. Alves and Cohelso (2005) carried out a comparative study of forward osmosis and membrane distillation for orange juice concentration and concluded that the fluxes are lower in membrane distillation due to the temperature gradient created between the

bulk and the membrane interface, which reduces the driving force for water transport [12]. Dinçer *et al.* (2016) carried out a comparative study of forward osmosis and membrane distillation for black mulberry juice concentration [13]. They indicated that forward osmosis was generally superior in comparison to membrane distillation process especially in maintaining nutrient content and volatile components in the feed. In this study, forward osmosis process is proposed for milk concentration. The effect of important process parameters that influence milk processing by forward osmosis such as feed flow rate, draw solution flow rate, draw solution concentration, feed/draw solutions volume ratios, and temperature on water fluxes was investigated. Thus optimum conditions for the process were obtained. The studies in the literature and the obtained results in this work lend credence to potential use of the osmotic distillation in dairy processing.

MATERIALS AND METHODS

Chemicals

$CaCl_2$ was purchased from Carlo Erba in its anhydrous powder form. The milk used in the experiments was prepared by using 9 wt.% dry milk powder purchased from local brand of Pınar. NaOH and sodium azide were purchased from Sigma Aldrich.

Apparatus

X50 Liqui-cel® 1.7×5.5 Minimodules purchased from Membrana GmbH were used as membrane contactors. The membrane contactors have 7400 microporous polypropylene fibers which provide 0.58 m^2 contact surface.

Experimental procedure

In forward osmosis, the aim is to transfer the water molecules from the feed solution with higher activity to the draw solution with lower activity where the driving force is the activity difference of water molecules between two sides of the membrane. The transfer of the water through the membrane pore is achieved by three steps: (1) Vaporization of water in feed-membrane interface on the boundary layer, (2) the transport of the water vapor through the membrane pore to the other interface, (3) the condensation of water in brine- membrane interface on boundary layer. Since the water molecules in milk have higher activity than the ones in brine, they transfer to the brine side. Thus milk is concentrated by continuous removal of its water content. The illustration of mass transfer can be seen in Figure 1. The membrane material is polypropylene, which shows hydrophobic characteristics and thus the pores cannot be wetted by the water. The water is evaporated at the pore mouth; it diffuses through the pore and then condensates on the brine side boundary layer so only vapor form of water can be transferred through the pores.

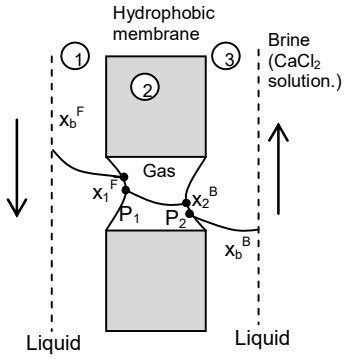

Figure 1 Mass transfer through the membrane.

The experimental setup for forward osmosis is illustrated in Figure 2. The feed solution, which is milk in this case, was circulated through the shellside of the membrane by a peristaltic pump while the brine solution was circulated through the lumen side of the membrane by another peristaltic pump. Both the temperatures of feed and brine were controlled using a thermostatic water bath. Every 10 minutes, the volume reduction in milk was recorded and the experiments were carried out until the dry matter in milk is reached to 20% wt from 9% wt.

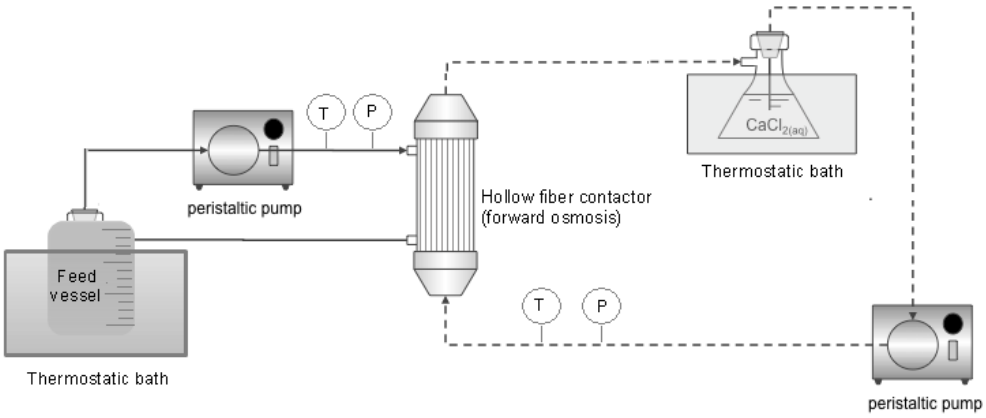

Figure 2: Experimental setup of forward osmosis process.

The process parameters and operating conditions studied in forward osmosis process are given in Table 1. The experiments were carried out to investigate the effect of the velocities of feed and brine solutions, brine concentration, feed/brine volume ratio, and temperature on the fluxes. The experiments that investigate the parameters apart from the temperature were carried out at 25°C.

Table 1: Operating conditions and process parameters of forward osmosis.

Parameter/Condition	Value/Range	Unit
Feed volume	400	mL
Temperature	25-40	°C
Solution flowrates	800-2000	mL min^{-1}
$CaCI_2$ concentration	3-5	M
V_{feed}:V_{brine}	1:1, 1:2, 1:3, 1:4	Volume ratios

RESULTS AND DISCUSSION

Since forward osmosis is a process in which the driving force is the activity difference between two sides of the membrane, the concentration of the brine is an important process parameter which affects directly the magnitude of this driving force. The experiments were carried out using 3, 4 and 5 M $CaCl_2$ brine solutions to investigate the effect of brine concentration on water fluxes. In Figure 3, the volume reduction of feed and water fluxes with time is given at different brine concentrations.

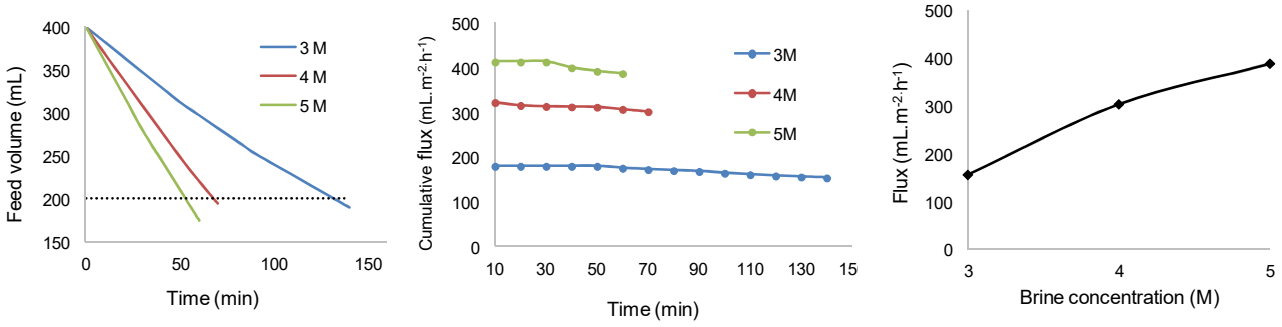

(a) (b) (c)

Figure 3: The effect of brine concentration on water permeation: (a) The volume change of milk with time, (b) cumulative water fluxes with time, (c) the fluxes at different brine concentrations.

As can be seen from Figure 3, fluxes increase with increasing brine concentration. As the brine concentration increases, the activity difference between two sides of the membrane increases and consequently the process becomes more rapid and operation time decreases for the required volume reduction. As can be seen from Figure 3a, the operation time for a volume reduction by half using 4 M brine is relatively closer to the operation time attained with 5 M brine. Thus considering the $CaCl_2$ consumption, an optimum concentration of 4 M brine was chosen for the further experiments. In Figure 3, it can be observed that fluxes tend to decrease slightly with time. This tendency is resulted from the decrease of activity difference with time because of the dilution of brine with the permeation of water continuously. Kujawski *et al.* investigated

concentration of red grape juice by forward osmosis using $CaCl_2$ as draw solution [14]. They measured the change of the driving force difference in water activities between feed and draw solutions as a function of time of experiment using an initial draw solution of 50 wt% $CaCl_2$ and juice concentration of 5°Brix. They concluded that in extended time of experiment activity difference decreases continuously because of the dilution of the brine and concentration of the juice by time. Hence it is important to operate at brine volumes that is not affected by the dilution dramatically. Thus different feed volume to brine volume ratios including 1:1, 1:2, 1:3 and 1:4 were studied to investigate optimum ratio and results are presented in Figure 4.

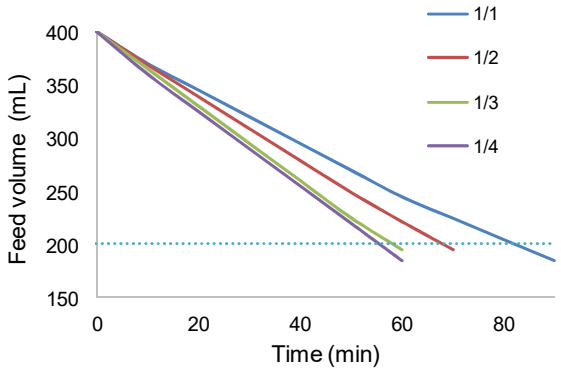

Figure 4: Feed volume reduction with time at different feed/brine volume ratios.

As can be seen from Figure 4, as the brine volume increases compared to the feed volume, the dilution of the brine becomes less significant and thus, operation time for a volume reduction by half decreases. However as the brine volume increases the consumption of $CaCl_2$ increases significantly, thus an optimum ratio should be considered for a more economic operation. Considering the optimum operation time and $CaCl_2$ consumption, the ratio of feed to brine was chosen as 1:2 in all experiments.

In order to investigate the effect of the feed velocity on fluxes, experiments were carried out at different feed velocities. The velocity of feed was changed as 800, 1200, 1600 and 2000 $mL.min^{-1}$ while the brine solution velocity was kept at 1600 $mL.min^{-1}$. The volume reduction and fluxes are presented in Figure 5 at various feed velocities.

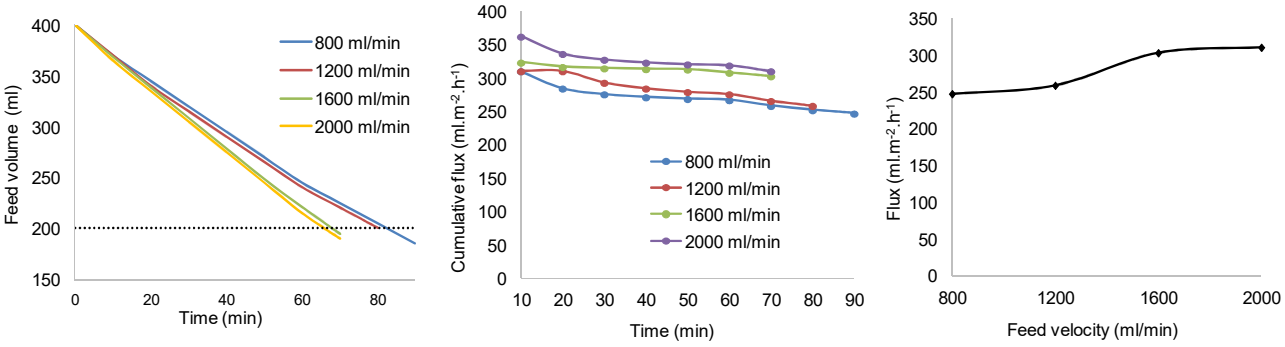

(a) (b) (c)

Figure 5: Effect of feed velocity on flux (a) The volume change of milk with time (b) Cumulative fluxes with time (c) Fluxes at different feed velocities.

As can be seen in Figure 5, as the feed velocity increases fluxes increase slightly and the operation time reduces accordingly. This is resulted from increase of the Re numbers and the decrease of the feed boundary layer thickness which presents resistance for the mass transfer. Since the mass transfer through the membrane requires the transfer of water molecules from feed boundary layer, membrane pores and brine boundary layer respectively, the overall mass transfer coefficient is expressed as follows according to resistance-in-series model:

$$K = \left(\frac{1}{K_f} + \frac{1}{K_m} + \frac{1}{K_d}\right)^{-1} \qquad \textbf{(Eq. 1)}$$

where $1/K_f$, $1/K_m$ and $1/K_d$ are the transport resistances of feed boundary layer, membrane and draw solution boundary layer respectively. Thus, in forward osmosis process, it is important to define the resistances in order to describe the mass transfer through the membrane. After investigating the effect of the feed velocities, experiments were carried out at different brine velocities at fixed feed velocity in order to investigate the effect of brine velocity on fluxes. The brine velocities were in the range of 800-2000 $mL.min^{-1}$ while feed velocity was kept at 1600 $mL.min^{-1}$. The results are presented in Figure 6.

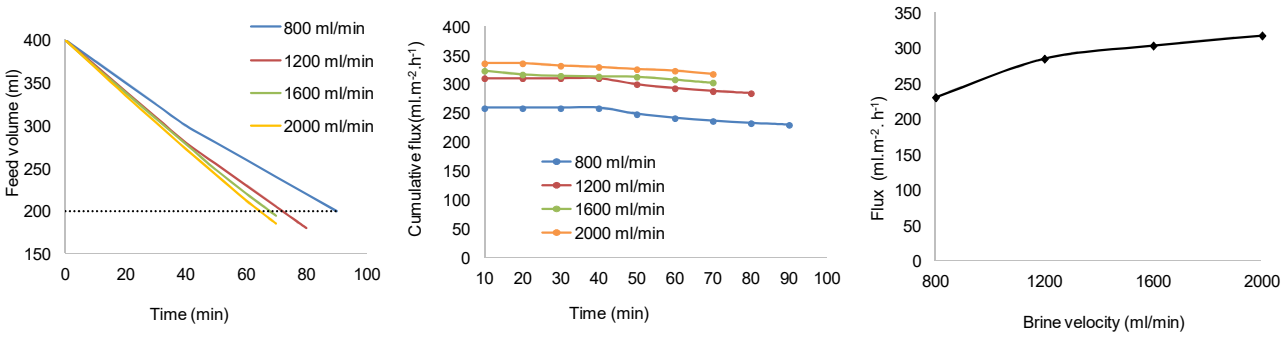

(a) (b) (c)

Figure 6: Effect of brine velocity on flux (a) The volume changes of milk with time, (b) Cumulative fluxes with time, (c) Fluxes at different brine velocities.

Figure 6 indicates that water fluxes increase with increasing brine velocity. At 800 mL.min^{-1} brine velocity, the operation time is longer. At this velocity value brine boundary layer presents a larger resistance for the mass transfer. As the velocity was increased to 1200 mL.min^{-1} operation time decreased however further increase in brine velocities did not affect the fluxes and consequently operation times significantly. Thus it can be concluded that although both feed and brine resistances affect the mass transfer, the mass transfer is dominated by feed side resistance and the brine boundary layer resistance affects the overall resistance less than the feed side. In general, increasing the feed or draw solution flow rate improves the water trans-membrane flux in osmotic distillation. This phenomenon can be attributed to the reduction in the related hydrodynamic boundary layer thickness [5]. Dova *et al*. (2007b) studied osmotic concentration of several model fruit juice solutions containing sucrose and glucose using a brine solution of NaCl [15]. They developed a model to analyze the resistances of water transport through the membrane and determined the magnitude of the two fluid resistances, namely the one on the side of osmotic medium containing salt solutions and the one on the side of the feed liquid containing sugar molecules. They showed that increasing the velocities of each sides affect the overall resistance and a detailed comparison of the two resistances indicated that feed side resistance was greater than the respective resistance of the osmotic medium. In this study also the effect of feed boundary layer resistance was found to be more dominant. This can be attributed to the difference in the magnitude of the tendencies of formation of fouling layers on each side. Since milk contains large protein and lactose molecules, the fouling is expected to be more severe on feed side. Thus change in hydrodynamic conditions on feed side affects the water flux more significantly.

The experiments were carried out at different temperatures in the range of 25-40 °C to investigate the effect of the temperature on the fluxes. In some experiments both feed and brine solution were heated to the same temperature while in some of the experiments the temperature of feed was kept slight higher than that of brine to generate a temperature difference between two sides of the membrane to enhance the driving force. The results are presented in Figure 7.

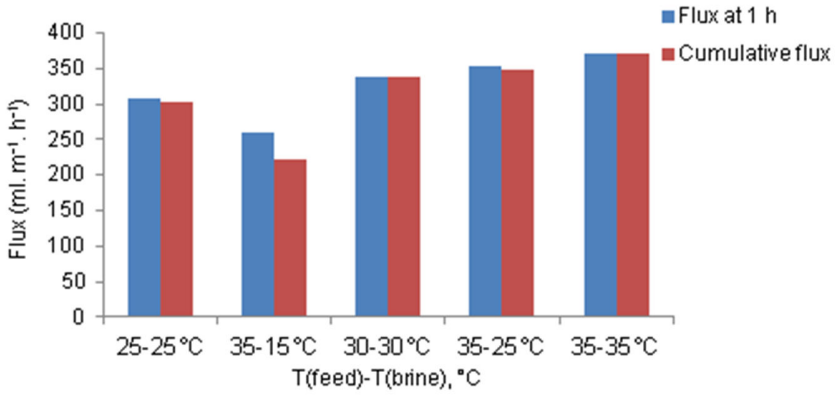

Figure 7: Water fluxes at various temperatures of brine and feed solutions.

When the feed and brine solutions are used at the same temperature, fluxes increase with increasing temperature. On the other hand, when the feed and brine solution have different temperatures, the temperature difference between two sides of the membrane gets closer during the experiment because of the evaporation-condensation steps of the water molecules as they release the latent heat to the brine solution. By this way, the temperature difference between the solutions decreases because of the temperature polarization and the system acts as at unique temperature. The fluxes attained at feed and brine temperatures of 35-25 °C respectively were slightly higher than the fluxes attained at 35-35 °C indicating a very small temperature difference may enhance the driving force. Nevertheless, the experiments carried out at feed and brine temperatures of 35-25 °C respectively have higher fluxes than the experiments carried out at 35-15 °C of feed-brine temperatures. Although the temperature difference is higher in the latter case, the total thermal energy given to the system is higher in the former case thus the fluxes are higher at 35-25 °C of feed and brine compared to the case at 35-15°C. In general, increasing the process temperature positively affects the fluxes. The viscosity of solutions to be processed decreases with increasing temperature and the diffusion coefficients increase with the temperature, and consequently water fluxes transmembrane increase. Similar results were obtained about the effect of temperature in literature. Thanedgunbaworn *et al.* (2007) reported that increasing bulk temperature from 25 to 35 °C, flux increased by 20% during the osmotic concentration of fructose [6]. Babu *et al.* (2006) indicated that increasing the process temperature from 25 to 45°C enhanced the water flux by 78% when they concentrated the

pineapple juice by osmotic distillation [16]. These results show that temperature is an important process parameter in osmotic distillation.

CONCLUSION

In this work, several process parameters on water flux were investigated and optimum conditions were determined for the concentration of milk by forward osmosis. As the draw solution concentration increased, the fluxes increase due to the increase of the water activity difference on both sides of the membrane. When the effect of the different feed and draw solution flow rates were compared, the impact of the feed velocity was found to be slightly higher than that of brine velocity indicating that the feed side resistance is more significant especially when the viscosity increases in feed boundary layer during operation. As the temperatures of feed and brine increase, fluxes increase generally. A very small temperature difference between feed and draw solution generated around room temperatures enhances the fluxes. These results show that fluxes obtained at mild temperatures were satisfactory for a reasonable operation time. The flux values at investigated process conditions were found to be in the range of 155-387 mL. h^{-1} m^{-2} while the operation time was in the range of 50-120 min for the concentration process carried out until the volume reduction by half. In general, the concentration of milk was performed efficiently using forward osmosis process. Based on the results obtained, forward osmosis can be considered as an alternative process to conventional evaporation.

ACKNOWLEDGEMENTS

The authors acknowledge the support of the Scientific and Technological Research Council of Turkey (Project TÜBİTAK 115M137).

REFERENCES

1. Van Den Berg J. C. T.. Evaporated and condensed milk. In: Milk Hygiene, A monograph from WHO, Geneva, Switzerland: WHO Monograph series No:48, 1962. 321-345 p.

2. Liu DZ, Dunstan DE, Martin GJO. Evaporative concentration of skimmed milk: Effect on casein micelle hydration, composition, and size. Food Chemistry. 2012 Oct;134(3):1446–52. DOI: 10.1016/j.foodchem.2012.03.053.

3. Ramirez C, Patel M, Blok K. From fluid milk to milk powder: Energy use and energy efficiency in the European dairy industry. Energy. 2006 Sep;31(12):1984–2004. DOI: 10.1016/j.energy.2005.10.014.

4. Jiao B, Cassano A, Drioli E. Recent advances on membrane processes for the concentration of fruit juices: a review. Journal of Food Engineering. 2004 Aug;63(3):303–24. DOI: 10.1016/j.jfoodeng.2003.08.003.

5. Sant'Anna V, Marczak LDF, Tessaro IC. Membrane concentration of liquid foods by forward osmosis: Process and quality view. Journal of Food Engineering. 2012 Aug;111(3):483–9. DOI: 10.1016/j.jfoodeng.2012.01.032.

6. Thanedgunbaworn R, Jiraratananon R, Nguyen MH. Mass and heat transfer analysis in fructose concentration by osmotic distillation process using hollow fibre module. Journal of Food Engineering. 2007 Jan;78(1):126–35. DOI: 10.1016/j.jfoodeng.2005.09.023.

7. Zambra C, Romero J, Pino L, Saavedra A, Sanchez J. Concentration of cranberry juice by osmotic distillation process. Journal of Food Engineering. 2015 Jan;144:58–65. DOI: 10.1016/j.jfoodeng.2014.07.009.

8. Wenten IG, Khoiruddin. Reverse osmosis applications: Prospect and challenges. Desalination. 2016 Aug;391:112–25. DOI: 10.1016/j.desal.2015.12.011.

9. Keogh MK, Murray CA, O'Kennedy BT. Effects of ultrafiltration of whole milk on some properties of spray-dried milk powders. International Dairy Journal. 2003 Jan;13(12):995–1002. DOI: 10.1016/S0958-6946(03)00123-7.

10. Hausmann A, Sanciolo P, Vasiljevic T, Ponnampalam E, Quispe-Chavez N, Weeks M, et al. Direct Contact Membrane Distillation of Dairy Process Streams. Membranes. 2011 Jan 4;1(4):48–58. DOI: 10.3390/membranes1010048.

11. Hausmann A, Sanciolo P, Vasiljevic T, Kulozik U, Duke M. Performance assessment of membrane distillation for skim milk and whey processing. Journal of Dairy Science. 2014 Jan;97(1):56–71. DOI: 10.3168/jds.2013-7044.

12. Alves VD, Coelhoso IM. Orange juice concentration by osmotic evaporation and membrane distillation: A comparative study. Journal of Food Engineering. 2006 May;74(1):125–33. DOI: 10.1016/j.jfoodeng.2005.02.019.

13. Dincer C, Tontul I, Topuz A. A comparative study of black mulberry juice concentrates by thermal evaporation and osmotic distillation as influenced by storage. Innovative Food Science & Emerging Technologies. 2016 Dec;38:57–64. DOI: 10.1016/j.ifset.2016.09.012.

14. Kujawski W, Sobolewska A, Jarzynka K, Güell C, Ferrando M, Warczok J. Application of osmotic membrane distillation process in red grape juice concentration. Journal of Food Engineering. 2013 Jun;116(4):801–8. DOI: 10.1016/j.jfoodeng.2013.01.033.

15. Dova MI, Petrotos KB, Lazarides HN. On the direct osmotic concentration of liquid foods: Part II. Development of a generalized model. Journal of Food Engineering. 2007 Jan;78(2):431–7. DOI: 10.1016/j.jfoodeng.2005.10.011.

16. Babu BR, Rastogi NK, Raghavarao KSMS. Effect of process parameters on transmembrane flux during direct osmosis. Journal of Membrane Science. 2006 Sep;280(1–2):185–94. DOI: 10.1016/j.memsci.2006.01.018.

Türkçe Öz ve Anahtar Kelimeler

İleri Osmozla Yağsız Süt ve Süt Ürünlerinin Derişiklendirilmesi

Ayça Hasanoğlu, Kübra Gül

Öz: Meyve-sebze suları, süt gibi su içeren sıvı gıdaların suyunun giderilerek derişiklendirilmesi, gıdadaki besinsel değerin yoğunlaştırılması, raf ömrü ve stabilitenin arttırılması, bakteriyel faaliyetlerin azaltılması, depolama ve taşınım maliyetlerinin düşürülmesi açısından önemli bir kimyasal süreçtir. Süt, içerdiği suyun belli oranlarda uzaklaştırılmasıyla derişik süt olarak kullanılabilir. Aynı zamanda yoğurt, peynir, süt tozu, peynir altı suyu tozu gibi süt ürünlerinin yapımında sütteki suyun belli bir orana kadar uzaklaştırılarak derişiklendirilmesi şarttır. Bu çalışmada derişik süt üretimi, geleneksel buharlaştırma prosesine alternatif olarak membran kontaktörlerin kullanımıyla ileri osmoz süreci ile gerçekleştirilmiştir. Bu süreçte süt hidrofobik membran kontaktörün gövde kısmından geçerken, çekme çözeltisi olarak kullanılan $CaCl_2$ çözeltisi kontaktörün iç kısmından geçmektedir. Böylece suyun aktivitesi yüksek olan süt çözeltisinden, aktivitesinin düşük olduğu $CaCl_2$ çözeltisine geçişi sağlanmıştır. İleri osmoz sürecinde besleme ve çekme çözeltisi hızı, çekme çözeltisi konsantrasyonu, sıcaklık gibi işletme parametreleri incelenmiş ve suyun bu süreçle hızlı ve etkin bir şekilde sütten uzaklaştırılabildiği görülmüştür. Sütün hacmi yarıya düşene kadar derişiklendirme işlemi yapılmış ve incelenen süreç şartlarında akı değerleri 155-387 mL. h^{-1} m^{-2} aralığında bulunmuştur.

Anahtar kelimeler: İleri osmoz; membran kontaktör; sütün derişiklendirilmesi.

Sunulma: 30 Eylül 2016. **Düzeltme:** 21 Kasım 2016. **Kabul:** 30 Aralık 2016.

This article was initially submitted to the UKMK 2016 (National Chemical Engineering Congress) and finally evaluated by the JOTCSB editorial staff.

Application of a Hydrothermal Gasification Method in the Treatment of Wastewater Generated from the Afyonkarahisar-Alkaloid Plant

Nihal Ü. Cengiz[1,*], Mehmet Sağlam[1], Mithat Yüksel[1], Levent Ballice[1]

1. Ege University, Department of Chemical Engineering, İZMİR, Turkey

Abstract: The wastewater coming from the alkaloid production plant, located in the province of Afyon, must satisfy the discharge limits specified in the "Water Pollution Control Regulations, 2004" to be safely discharged into the environment. Treatment of the alkaloid plant wastewater with the existing treatment method, which is a combination of the biological (aerobic / anaerobic) and chemical treatment, is not sufficient. In this study, hydrothermal gasification (or supercritical water gasification, SCWG) is proposed as an alternative and advanced treatment technique. The other objectives of the study are to show the producibility of methane and hydrogen as a renewable energy source and to investigate, as to what extent was the removal of chemical oxygen demand and polluting compounds as a spontaneous result of gasification. The effect of a catalyst in the highest conversion of an organic carbon content in wastewater, to a gaseous product rich in H_2 and CH_4, and the maximum efficiencies in total organic carbon (TOC) and chemical oxygen demand (COD) removals. Hydrothermal gasification studies of alkaloid wastewater were carried out without a catalyst and with Na_2CO_3 (N). The experiments were performed at the reaction temperatures of 400, 500, and 600 °C with and without 0.12 g of catalyst and 15 mL of wastewater. The gaseous products were analyzed using gas chromatography, and the TOC and COD content of the aqueous products and raw wastewater were analyzed using a TOC analyzer and COD analysis set. The variation of the product distribution and yields, TOC and COD removal by temperature and catalysis were examined. The initial TOC, and COD values of the wastewater studied were 15,000 mg/L and 35,000 mg/L, respectively.

Keywords: Supercritical water gasification; methane; hydrogen; hydrothermal gasification; alkaloid wastewater.

Submitted: November 08, 2016. **Revised:** December 29, 2016. **Accepted:** February 03, 2017.

Cite this: Ü. Cengiz N, Sağlam M, Yüksel M, Ballice L. Application of a Hydrothermal Gasification Method in the Treatment of Wastewater Generated from the Afyonkarahisar-Alkaloid Plant. JOTCSB. 2017;1(1):161–70.

*Corresponding author. E-mail . nihal.cengiz@ege.edu.tr

INTRODUCTION

In recent years, the gasification of biomass in supercritical wastewater is investigated with a growing interest. The choice of materials to be used as raw material [1-3], selection of the catalyst, [4-6], optimization of the operating conditions [7, 8], investigation in the behavior of the model compounds during the hydrothermal gasification period [9, 10], and thermodynamic calculations [11, 12] are the most investigated topics in this field. This new technique is also used in wastewater gasification and the production of valuable chemicals. The wastewater used in energy production and evaluated using the supercritical water gasification method has become one of the new types of raw materials [13-15]. There are two studies with black liquor which is generated from cellulose production by the sulfate method [15-16], a study with olive mill wastewater [13], and another study with wood gasification wastewater [17]. Besides wastewater coming from the amino acid production process [18], acrylonitrile plant wastewater [19], and coking plant wastewater [20] are also used as raw materials in hydrothermal gasification studies.

The wastewater generated by an Opium Alkaloid Factory is 840 m^3 per day and is discharged into Eber Lake by way of the river Akarcay after successive treatment processes. According to literature data, the COD value of this wastewater varies between 18.3 - 42.5 O_2/ liters [21]. This wastewater contains toxins and poisons, inhibiting microorganism activity, and biodegradation-resistant materials. Therefore, it must be treated to below 1500 mg O_2/liter before being discharged into the environment due to the Water Pollution Control Regulations published in 2004.

There are many studies on the treatment of this wastewater using chemical, biological, (aerobic and anaerobic medium), and wet air oxidation (oxidation with air in the liquid phase) [22-25]. It has been reported that the COD value of the wastewater could be reduced by approximately 33 to 80%. According to this ratio, the COD of the treated wastewater is at least 6000 mg. This is more than four times the discharge limit. The reason to choose this wastewater as a raw material is the high organic carbon content and to propose this method as a solution to the environmental problems caused by this wastewater in and around Lake Eber.

All these studies indicate that the Opium Alkaloids Plant wastewater shows a high resistance to treatment because of its complex structure, and has revealed that it is difficult to treat adequately.

The Opium Alkaloids Plant wastewater, which is a waste of a specific industry, has not been considered for the evaluation of hydrogen and methane production as an energy source using hydrothermal gasification in literature so far. This wastewater was not studied using this technique as a treatment alternative in any research.

RESULTS AND DISCUSSION

Hydrothermal gasification studies were carried out in a batch autoclave reactor system shown in Figure 1 in the absence of a catalyst and in the presence of Na_2CO_3 at various reaction temperatures. The pressures reached at studied runs changed within the range of 235-440 bar. The experiments were performed at the reaction temperatures of 400, 500 and 600 °C with and without 0.12 g of catalyst and 15 mL of wastewater. The effects of reaction temperature and the catalyst addition on the product yields and COD, TOC removals were investigated. The reactor was sealed tightly and the air inside it was purged with nitrogen then heated at a rate of 8 - 10 K/min to the reaction temperature. It is maintained constant during the reaction time of 1 h with a PID controller. Table 1 contains the studied experimental conditions. The selection of the alkali catalyst is based on enhancing the gasification efficiencies and providing high COD and TOC removal efficiencies.

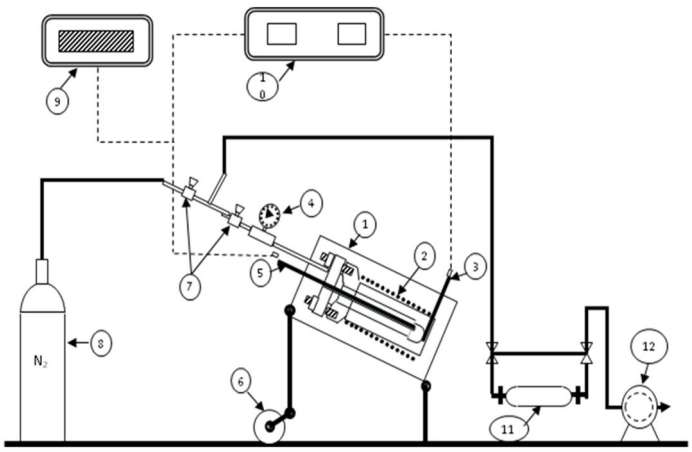

Figure 1: Schematic of the autoclave reactor.

Table 1: Hydrothermal gasification conditions (T:temperature, 4:400°C, 5:500°C, 6:600°C, and N: Na_2CO_3)

Exp Code	*T,°C*	*P, bar*	*Catalyst*	*Catalyst amount, g*
AF-T4	400	240	-	-
AF-T5	500	365	-	-
AF-T6	600	440	-	-
AF-T4N	400	235	Na_2CO_3	0.12
AF-T5N	400	355	Na_2CO_3	0.12
AF-T6N	400	415	Na_2CO_3	0.12

The other criterion for catalyst selection is the increasing effect on the percentage of H_2 and CH_4 in the gaseous product mixture.

The gaseous products were analyzed using gas chromatography (Agilent Technologies HP 7890A, USA). It is equipped with serially arranged 7 columns (Hayesep Q 80/100 mesh (0.5 m long × 2 mm i.d.), a Hayesep Q 80/100 mesh (1.8 m long × 2 mm i.d.), a Molsieve 5A 60/80 mesh (2.4 m long × 2 mm i.d.), a Hayesep Q 80/100 mesh (0.9 m long × 2 mm i.d.), a Molsieve 5A 60/80 mesh (2.4 m long × 2 mm i.d.), a DB-1 (pre-column), and HP-Plot Al_2O_3 S (25 m long × 0.32 mm i.d.). 3 detectors were serially connected with a special adapter (2 thermal conductivity detectors (TCD), and a flame ionization detector (FID)), and the TOC and COD content of the aqueous products and raw wastewater were analyzed using a TOC analyzer (Shimadzu TOC-VCPH, Japan). Chemical Oxygen Demand (COD) of the raw wastewater and aqueous products were determined with COD analysis equipment formed of thermo-reactor (MERCK, Spectroquant TR320) and spectrophotometer (MERCK, Spectroquant Nova 60), and kits (500-10,000 ppm and 150-1,000 ppm) depending on the COD level of the aqueous product. The distribution (molar percentage, %) and the yields (mol/kg C) of the compounds in the gaseous product are given in Figs. 2 and 3. The COD and TOC values and removal efficiencies are shown in Figs. 4 and 5.

Total Organic Carbon Removal Efficiency (TOC_{RE}, %) and Chemical Oxygen Demand Removal Efficiency (COD_{RE}, %) were expressed by using the following formulas;

Total Organic Carbon Removal Efficiency:

$$(TOC_{RE}, \%) = \frac{TOC_{ww} - TOC_{aq}}{TOC_{ww}} x100$$

Chemical Oxygen Demand Removal Efficiency:

$$(COD_{RE}, \%) = \frac{COD_{ww} - COD_{aq}}{COD_{ww}} x100$$

The effect of parameters on product distribution and yields were determined.

Table 2: Experimental results of catalytic and non-catalytic runs at studied reaction temperatures.

Exp Code	*TOC RE, %*	*COD RE, %*	*H_2 yield (mmol/kg C)*	*CH_4 yield (mmol/kg C)*
AFALT4	40.9	42.6	11.3	3.5
AFALT5	74.5	80.0	20.4	16.8
AFALT6	85.6	91.2	33.3	25.1
AFALT4N	52.7	45.4	16.1	5.9
AFALT5N	89.2	87.4	26.8	20.9
AFALT6N	90.3	93.3	37.2	29.8

The effect of the parameters on product distribution and yields were determined.

The proposed reactions associated with hydrothermal decomposition of organic carbon containing biomass in water are given below. Considering these reactions, for the carbon-containing organic pollutants and biomass in wastewater, assessing the results will be useful.

$$C_6H_{12}O_6 + 6H_2O \leftrightarrow 6CO_2 + 12H_2 \quad \text{(Eq. 1)}$$

$$CO + 3H_2 \leftrightarrow CH_4 + H_2O \quad \text{(Eq. 2)}$$

$$CO_2 + 4H_2 \leftrightarrow CH_4 + 2H_2O \quad \text{(Eq. 3)}$$

$$CO + H_2O \leftrightarrow CO_2 + H_2 \quad \text{(Eq. 4)}$$

The gaseous product is composed of H_2, CO_2, CO, CH_4, C_2H_6, C_2H_4, C_3H_8, and C_4H_{10}. Smaller amounts were determined for C_2H_6, C_2H_4, C_3H_8, and C_4H_{10}, so the total amounts of these compounds were given as the C_2 - C_4 group in the plots for easier evaluation. The major products were detected as H_2, CO_2, CH_4, and CO. Hydrogen and carbon dioxide were formed by degradation of the organic compounds in the wastewater and the water gas shift reaction via reactions 1 and 4 dominantly. Methane is formed by the further reactions of the degradation products in reactions 2 and 3. As it is seen in Figure 2, the catalyst and reaction temperature has significant effects on the gas product distributions.

While the gaseous product distribution is considered in terms of molar percentage of H_2, in the absence of a catalyst, it is seen that there is no significant change with temperature and is partially reduced in the presence of Na_2CO_3. The yields were increased with increasing both the temperature and adding a catalyst as expected. The molar percentage and yields of CH_4 were promoted and clearly seen in Figures 2 and 3 from 400 to 600 °C with the increasing temperature in both the catalytic and non-catalytic cases. There is a significant reduction in the CO_2 percentage in the gas product related to the effect of the catalyst. The effect of temperature, on

the molar percentage of CO_2 in the gaseous product varies according to the catalyst usage. It decreases as the temperature increases in the studies without a catalyst while an ordered decrease or increased is not mentioned in the studies with Na_2CO_3.

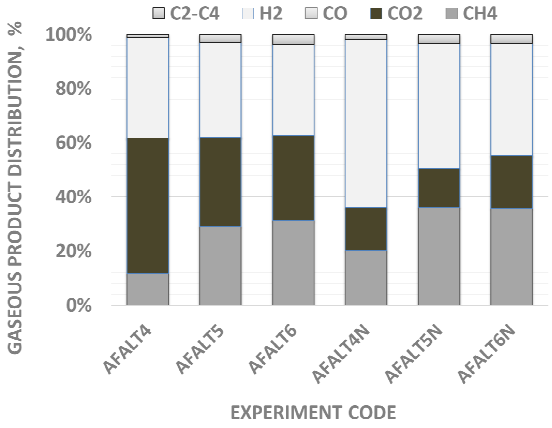

Figure 2: The effect of a catalyst and temperature on the gaseous product distribution.

Figure 3 shows the change in the number of gaseous products and the first noticeable inference is that the increasing temperature dramatically increases the total amount of product.

It is clearly seen that the yields of CH_4 and H_2 which were targeted to produce in this study reached the maximum yield at 600°C. While temperature is increasing from 400 to 600 °C, the yields of CH_4 and H_2 increased from 3.51 to 25.11 mmol / kg C and from 11.33 to 33.30 mmol / kg C, respectively.

At a specified reaction temperature, a significant decrease in the amount of CO_2 was seen by the effect of the alkaline catalyst. However, the amount of CH_4 and H_2 were promoted. In the presence of a catalyst, the CO_2 was converted to CH_4 via the 3rd reaction given above. It can be said that more organic compounds degraded with regards to the effect of the catalyst and converted to H_2 via reaction (1).

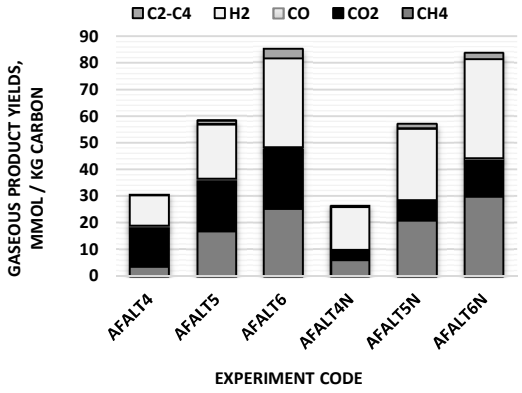

Figure 3: The effect of a catalyst on the gaseous product distribution and yields (mmol/kg C).

The TOC and COD content of the aqueous product decreases with the effect of the rising

temperature dramatically in both the absence and presence of a catalyst. Temperature is the dominant factor in the removal COD and TOC. From 500 °C to 600 °C, the change in TOC and COD has a downward acceleration magnitude. So, the operating temperature should be selected as 500 °C as the optimum. The maximum TOC removal efficiencies were obtained as 85% without a catalyst and 90% with Na_2CO_3.

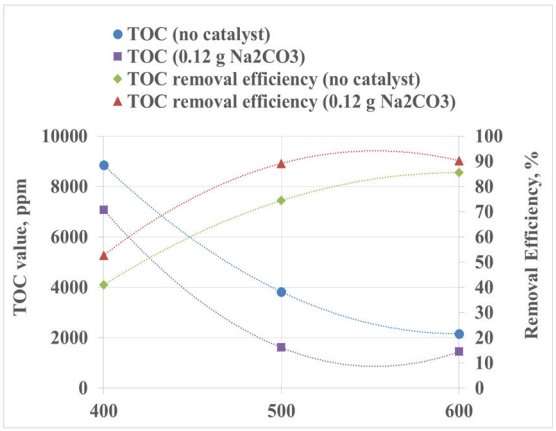

Figure 4: The variation of total organic carbon (TOC) in the aqueous product and TOC removal efficiencies with a catalyst and temperature.

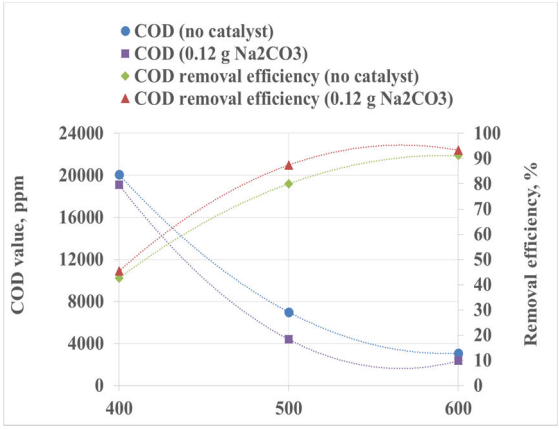

Figure 5: The variation of chemical oxygen demand (COD) in the aqueous product and COD removal efficiencies with a catalyst and temperature.

The highest COD removal efficiencies obtained were 91% without a catalyst and 93% with Na_2CO_3 as seen in Figure 5 at 600 °C. The economy of the process is taken into consideration to determine the most appropriate condition which is 500 °C as the reaction temperature. The catalyst should be added to improve efficiencies and yields.

CONCLUSION

Hydrothermal gasification of opium alkaloid wastewater in supercritical water was investigated at a temperature range of 400 °C – 600 °C. The effect of reaction temperature and the catalyst (Na_2CO_3, 0.12 g) added were represented in a batch autoclave reactor system for a reaction time of 1 h. The yields of CH_4 and H_2 promoted by increasing temperature from 3.5 to 25.1 mmol / kg C and from 11.3 to 33.3 mmol / kg C, respectively. Na_2CO_3 enhance the CH_4 and H_2 yields,

while decreasing yields of CO_2. TOC removal increased by catalyst addition significantly but COD removal was not affected by catalyst remarkably. Treatment of alkaloid wastewater by the proposed method is accomplished due to high COD and TOC removal results obtained at 500 °C and above it.

It can be emphasized that hydrogen and methane production was succeeded by supercritical water gasification method providing also good treatment characteristics.

Acknowledgement: We gratefully appreciate the financial support of Ege University -Aliye Üster Vakfı and Ege University-EBILTEM (Project No: 15 MÜH 055).

REFERENCES

1. T. Güngören Madenoğlu, Boukis N, Sa M. Supercritical water gasification of real biomass feedstocks in continuous flow system. 2011;(6):5–12.

2. He C, Chen C-L, Giannis A, Yang Y, Wang J-Y. Hydrothermal gasification of sewage sludge and model compounds for renewable hydrogen production: A review. Renew Sustain Energy Rev. 2014 2015 Nov;(39):1127–42.

3. Guo L, Cao C, Lu Y. Supercritical Water Gasification of Biomass and Organic Wastes. Biomass. 2010. Sciyo:downloaded from SCIYO.COM ;2010. p. 113–8.

4. Azadi P, Afif E, Azadi F, Farnood R. Screening of nickel catalysts for selective hydrogen production using supercritical water gasification of glucose. Green Chemistry. 2012;(14):1766-1777.

5. Onwudili J a., Williams PT. Enhanced methane and hydrogen yields from catalytic supercritical water gasification of pine wood sawdust via pre-processing in subcritical water. RSC Advances. 2013;(3):12432-12442.

6. Sinag A, Kruse A and Rathert J. Influence of the Heating Rate and the Type of Catalyst on the Formation of Key Intermediates and on the Generation of Gases During Hydropyrolysis of Glucose in Supercritical Water in a Batch. Ind. Eng. Chem. Res. 2004;(43):502–508.

7. Güngören Madenoğlu T, Sağlam M, Yüksel M, Ballice L. Simultaneous effect of temperature and pressure on catalytic hydrothermal gasification of glucose. Journal of Supercritical Fluids. 2013 ;(73):151–60.

8. Mohammadali E, Sheikhdavoodi MJ, Almassi M, Kruse A, Bahrami H. Effect of Reaction Temperature and Type of Catalyst on Hydrogen Production in Supercritical Water Gasification of Biomass. Iranica J. Energy & Environ. 2012;(3):202–209.

9. Sinag A, Kruse A, Schwarzkopf V. Key Compounds of the Hydropyrolysis of Glucose in Supercritical Water in the Presence of K2CO3. Ind. Eng. Chem. Res. 2003;(42):3516–21.

10. Madenoğlu TG, Üremek NC, Sağlam M, Yüksel M, Ballice L. Catalytic Gasification of Mannose for Hydrogen Production in Near- and Super-Critical Water. J Supercritical Fluids. 2016; (107):153-162

11. Gutiérrez Ortiz FJ, Ollero P, Serrera A. Thermodynamic analysis of the autothermal reforming of glycerol using supercritical water. Int J Hydrogen Energy. 2011;36 (19):12186–99.

12. Voll FAP, Rossi CCRS, Silva C, Guirardello R, Souza ROMA, Cabral VF, et al. Thermodynamic analysis of supercritical water gasification of methanol, ethanol, glycerol, glucose and cellulose. Int J Hydrogen Energy 2009; 34(24):9737–44.

13. Kıpçak E, Söğüt O Ö, Akgün M. Hydrothermal gasification of olive mill wastewater as a biomass source in supercritical water. J Supercrit Fluids. 2011;(57):50–57.

14. García Jarana MB, Sánchez-Oneto J, Portela JR, Nebot Sanz E, Martínez de la Ossa EJ. Supercritical water gasification of industrial organic wastes. J Supercrit Fluids. 2008;(46):329–34.

15. Sricharoenchaikul V. Assessment of black liquor gasification in supercritical water. Bioresource Technol. 2009;100 (2):638–43.

16. C.Cao, L. Guo, Y. Chen, S. Guo, Y. Lu. Hydrogen Production from Supercritical Water Gasification of Alkaline Wheat Straw Pulping Black Liquor in Continuous Flow System. International Journal of Hydrogen Energy. 2011;(36): 1328-13535.

17. C. D. Blasi, C. Branca, A. Galgano, D. Meier, I. Brodzinski, O. Malmros. Supercritical Gasification of Wastewater from Updraft Wood Gasifiers. Biomass and Bioenergy. 2007;31:802-811.

18. I. G. Lee, S.K. Ihm. Hydrogen Production by SCWG Treatment of Wastewater from Amino Acide Production Proscess. Ind. Eng. Chem. Res. 2010;(49):10974-10980.

19. Shin, Young Ho Shin, Nae Chul Veriansyah, Bambang Kim, Jaehoon Lee, Youn Woo, Supercritical water oxidation of wastewater from acrylonitrile manufacturing plant, Journal of Hazardous Materials .2009;163 (2-3): 1142-1147.

20. Xin Dua, Rong Zhang , Zhongxue Gan, Jicheng Bi. Treatment of high strength coking wastewater by supercritical water oxidation. Fuel 2013;(104):77–82

21. Bural CB, Demirer GN, Kantoglu O, Dilek FB. Treatment of opium alkaloid containing wastewater in sequencing batch reactor (SBR) — Effect of gamma irradiation. R Radiation Physics and Chemistry. 2010;79(4):519–26.

22. Aydin AF, Altinbas M, Sevimli MF, Öztürk I, Sarıkaya HZ. Advanced treatment of high strength opium alkaloid industry effluents. Water Sci Technol 2002; 46(9):323–330.

23. Aydin AF, Ersahin ME, Dereli RK, Sarikaya HZ, Ozturk I. Long-term anaerobic treatability studies on opium alkaloids industry effluents Journal of Environmental Science and Health, Part A 2010;(45): 37–41.

24. Kunukcu YK, Wiesmann U. Activated Sludge Treatment and Anaerobic Digestion of Opium Alkaloid Factory. World Water and Environmental Resources Congress 2004 Utah, USA; ASCE Library.

25. Aytimur G, Atalay S. Treatment of an Alkaloid Industry Wastewater by Biological Oxidation and / or Chemical Oxidation Treatment of an Alkaloid Industry Wastewater 2004;(26):661–70.

Türkçe Öz ve Anahtar Kelimeler

Afyonkarahisar Alkaloid Tesisinden Üretilen Atıksuyun Terbiyesine Hidrotermal Gazlaştırma Yönteminin Uygulanması

Nihal Ü. Cengiz, Mehmet Sağlam, Mithat Yüksel, Levent Ballice

Öz: Afyon ilinde bulunan alkaloid üretim tesisinden gelen atıksu 2004 yılında yürürlüğe girmiş olan "Su Kirliliği Kontrol Yönetmeliği" kapsamında belirlenen deşarj sınırlamalarını karşılamalıdır. Biyolojik (aerobik / anaerobik) ve kimyasal terbiye yöntemlerinin bir karışımı olan mevcut terbiye yönteminde alkaloid tesisinin atıksuyunu terbiye etme yöntemi yeterli değildir. Bu çalışmada, hidrotermal gazlaştırma (ya da süperkritik su gazlaştırması, SCWG) bir alternatif ve ileri terbiye tekniği olarak önerilmektedir. Çalışmanın diğer amaçları, yenilenebilir bir enerji kaynağı olarak metan ve hidrojenin üretilebilirliğini göstermek ve gazlaştırmanın kendiliğinden olan bir sonucu olarak kirletici bileşiklerin ve kimyasal oksijen ihtiyacının ne kadar giderildiğini incelemektir. Atıksudaki organik karbon içeriğinin H_2 ve CH_4 açısından zengin gaz ürününe en yüksek mertebede dönüşümü için katalizör etkisi ve toplam organik karbon (TOC) ve kimyasal oksijen ihtiyacı (COD) giderimi için en yüksek etkinliklerin bulunması da amaçlanmıştır. Alkaloid atıksuyunun hidrotermal gazlaştırma çalışmaları katalizör olmadan ve katalizör olarak Na_2CO_3 (N) kullanarak yürütülmüştür. Deneyler 400, 500 ve 600 °C'de yürütülmüştür, katalizör kullanılacağı zaman, miktarı 0,12 g olarak belirlenmiştir ve atıksudan 15 mL alınmıştır. Gaz ürünler gaz kromatografisi ile analiz edilmiştir ve sulu ürünler ile ham atıksuyun TOC ile COD içeriği TOC analizörü ve COD analiz seti kullanılarak belirlenmiştir. Ürün dağılımı ve verimlerin değişmesi, sıcaklık ve katalizör ile TOC ve COD giderimi incelenmiştir. Atıksuya ait ilk TOC ve COD değerleri sırasıyla 15.000 mg/L ve 35.000 mg/L olarak bulunmuştur.

Anahtar kelimeler: Süperkritik su gazlaştırması; metan; hidrojen; hidrotermal gazlaştırma; alkaloid atıksuyu.

Sunulma: 8 Kasım 2016. **Düzenleme:** 29 Aralık 2016. **Kabul:** 03 Şubat 2017.

(This article was initially submitted to National Chemical Engineering Congress and reviewed by JOTCSB editorial staff).

GASIFICATION OF OLIVE MILL WASTEWATER WITH WATER PLASMA

Esra Yıldırım[1,*], Vuslat İbrahimoğlu[1], Salih Karasarı[1], Ahmet Zafer Özek[1]

1.Anadolu Plazma Teknoloji Enerji Merkezi, Gölbaşı Kampüsü Teknoplaza Binası, Gölbaşı, ANKARA

Abstract: Olive mill waste water(OMW) is formed as a result of olive oil production. Due to the abundance of organic matter, suspended solids, oil and grease and existence of phenolic compounds, it is a significantly dangerous type of wastewater. Since the pollution rate in OMW is high, its disposal and energy recovery from organic compounds within should be enabled. In this study, OMW is used as a raw matter and gasified with water plasma. Obtainable ideal gas composition is theoretically examined and results acquired from experimental studies are compared. The aim of this study is to identify the uncalculated effect of plasma by comparing the experimental studies with theoretical calculations. In theoretical studies, during gasification process, four basic reactions were used, compound equivalence has been established and gasification process has been simulated using MATLAB program with conversion balance. Ideal syngas composition was established at temperatures between 850 – 1000 K working within 0,05-0,7 S (water vapor/dry fuel) ratios. Experimental studies with low mass flow range olive mill wastewater feed were performed and in order to examine gas composition, gas chromatography analysis was executed. Results are proven to be consistent and when compared to the conventional gasification methods same ratio of syngas compounds have been achieved by plasma gasification at much lower temperatures. Since there is no literature on the gasification of OMW with plasma technology, this article carries a quintessential role in the study of waste recycling technology for energy recovery.

Keywords: Plasma gasification; syngas, olive mill wastewater.

Submitted: September 20, 2016**. Revised:** October 31, 2016**. Accepted:** February 16, 2017**.**

Cite this: Yıldırım E, İbrahimoğlu V, Karasarı S, Özek A. GASIFICATION OF OLIVE MILL WASTEWATER WITH WATER PLASMA. JOTCSB. 2017;1(1):171–82.

Corresponding author: Esra Yıldırım. E-mail: esrayildirimmmm@gmail.com.

INTRODUCTION

Industrial wastewaters that emerged after the world’s industrial development have become one of today's most important environmental problems as they contain components with high-polluting properties. As a result of olive oil production obtained industrial wastewater known as the Olive Mill Wastewater (OMW) contains organic matter, suspended solids, oil, and grease. Therefore, the treatment and disposal of olive mill wastewater is very important (1). The quantity and characteristics of OMW vary depending on olive species, climate, harvest time, and degree of maturity (2). 1 m^3 olive mill wastewater is equivalent to approximately 200 m^3 domestic wastewater (1).

Due to the high content of organic matter in the OMW, oxygen in water dissolves very quickly. Thus, aquatic macro- and micro-organisms are unable to survive. As the light permeability of water due to the color of the wastewater, it restricts the ability of photosynthesis of aquatic plants. The most significant damage to the atmosphere is a peculiar smell of OMW. Fermented OMW can evaporate from little ponds, plants, and soil to the atmosphere causing odor emissions. (3).

In order to reduce or eliminate the pollutant effect of OMW, many laboratory and industrial scale studies are being carried out and different treatment technologies are being developed both in Turkey and all over the world.

In literature, some examples of OMW treatment, disposal, or reduction of its harmful nature are listed below:

- Distillation (4),
- Adsorption (5,6),
- Electrolysis (7,8),
- Evaporation (9),
- Chemical Treatment (10,4,11),
- Aerobic Biological Treatment (12,4,13),
- Anaerobic Biological Treatment (14-18),
- Advanced Treatment Processes (19-23),

OMW, which is seen as a waste because of its properties, is actually an important energy source because of organic compound content and in addition to disposal, it will contribute to the national economy with efficient, valuable products through its evaluation. Studies on energy recovery are restricted due to moisture content in the raw material. For the studies on energy production from OMW liquor, gasification process was performed by Kipçak *et al*. in supercritical water conditions (24).

GASIFICATION TECHNOLOGY AND PLASMA GASIFICATION

Generally speaking, gasification is a technology that allows production of energy from solid or liquid fuels or of various chemicals. With conventional gasification processes, the raw material is treated with steam and a certain amount of oxidizer at a high temperature and pressure. Under these conditions, at a certain temperature value, volatile content of the raw material disappears and the remainder of the carbon reacts to form carbon monoxide, carbon dioxide, and hydrogen.

In this study, the energy required for the realization of the exothermic gasification reaction met with plasma technology. Plasma technology involves the formation of an electrical arc passing an electrical current through the gas. Since plasma gasification technology provides gasification with high purity and partial oxidation, it is usually known as "pure gasification" (25-27). Some of the advantages offered by the technology of plasma gasification technology are listed below:

-Clean and efficient synthesis gas with a high calorific value is obtained and it can be adjusted by controlling the content of the synthesis.

-Plasma, which has high energy density, is sufficient to provide energy for gasification in a short time and the reaction rate is increased because of its charged species. With the increase reaction rate, it reaches steady state conditions prematurely. It makes it possible to have a quick starting and stopping times.

-Can be used to dispose a wide range of waste types consisting of solid, liquid, and gas (28-33).

The high moisture content of Olive Mill Waste Water prevents the use of traditional methods for waste treatment technology aimed at energy recovery. However, for plasma technology the moisture content of the raw material is not important and as a result of plasma thermo-chemical process by ionizing raw material at a high temperature plasma gas is obtained.

MATERIALS AND METHODS

Apparatus

A 1.5 kW DC arc plasmatron was used during the experiments (patent no: 2012/03912). In order to provide efficient heat transmission, the feed head was specifically designed from copper material. 0.5 mm diameter holes located in the feed head has led to longer interaction

between OMW and plasma flame. In the experimental studies, lab-scale stainless steel fixed bed reactor, where the gasification reaction is carried out, was used. Plasma thermo-chemical reactions take place in the reactor and plasma gas rich in hydrogen and free radicals was formed as a result. Moisture within a plasma gas was removed and cooled by passing through a gas cooler. In the next phase, plasma gas was transferred to the gas chromatograph for component analysis.

EXPERIMENTAL PROCEDURE

MATLAB Simulation Studies

Gasification simulation analyses were performed by using MATLAB. Newton-Raphson numerical method, which is known as non-linear equation solving techniques, was used to obtain the simulation results. Newton-Raphson method used to obtain the given node balance for each load is given in Figure 1.

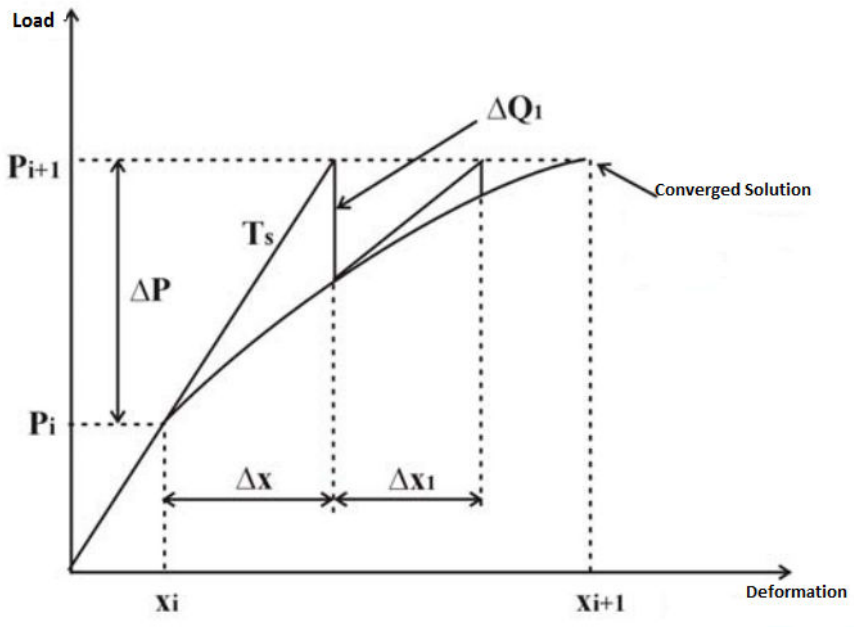

Figure 1. Calculation steps for non-linear analysis (34)

Simulation parameters were determined as change between 850-1000 K for temperature and mass parameters (S= kg steam/ kg dry fuel) ratio in the range of 0.05 to 0.7. It examined the effect of the parameters on the plasma gas composition. Elemental analysis values of the fuel used in the study is given in Table 1.

During simulation studies, while identifying the synthesis gas composition, kinetic data related to the ‘Water Gas Reaction’, ‘Boudouard Reaction’, ‘Water Gas Shift Reaction’ and ‘Methanation

Reaction' and mass balance for H_2, N_2, CO, CO_2, CH_4, H_2O compositions were simultaneously solved in MATLAB program.

Table 1. Elemental analysis values of the fuel used (%) (35).

	DRY BASED
C, %	42.85
H, %	5.88
O, %	21.15
N, %	2.08
S, %	-
Ash, %	28.04
Moisture, %	80.0

$$C + H_2O \leftrightarrows CO + H_2 \quad \text{(Eq. 1)}$$

$$C + CO_2 \leftrightarrows 2CO \quad \text{(Eq. 2)}$$

$$CO + H_2O \leftrightarrows H_2 + CO_2 \quad \text{(Eq. 3)}$$

$$C + 2H_2 \leftrightarrows CH_4 \quad \text{(Eq. 4)}$$

Experimental Studies

In experimental studies, waste treatment technology for energy recovery was used to gasify OMW with plasma method. The aim of this study is to compare experimental with theoretical studies.

In the experimental study, plasma gasification of OMW, low mass OMW flow was performed with specially designed feed head with 0.5 mm diameter holes and it interacted with the plasma flame closest to the plasmatron area.

Water was used as a plasma agent and S ratio (steam / dry fuel) was fixed at 0,2. During the experiments, average temperature was 850-1000 K and studied under atmospheric pressure. In order to study the gas composition of formed plasma gas, it was cooled and analyzed by the gas chromatography analyzer. OMW plasma gasification test system is given in Figure 2.

Figure 2. Plasma gasification test system.

RESULTS AND DISCUSSION

MATLAB Simulation Study Findings

Investigation of Water Vapor and Temperature Effects

The effect of temperature and water vapor are investigated under constant atmospheric pressure. Examples of component concentrations at different temperatures with a value of S = 0.2 at atmospheric pressure are shown on Figure 3. With the increase in temperature, H_2-CO rate is increased and CH_4-CO_2 rate is decreased.

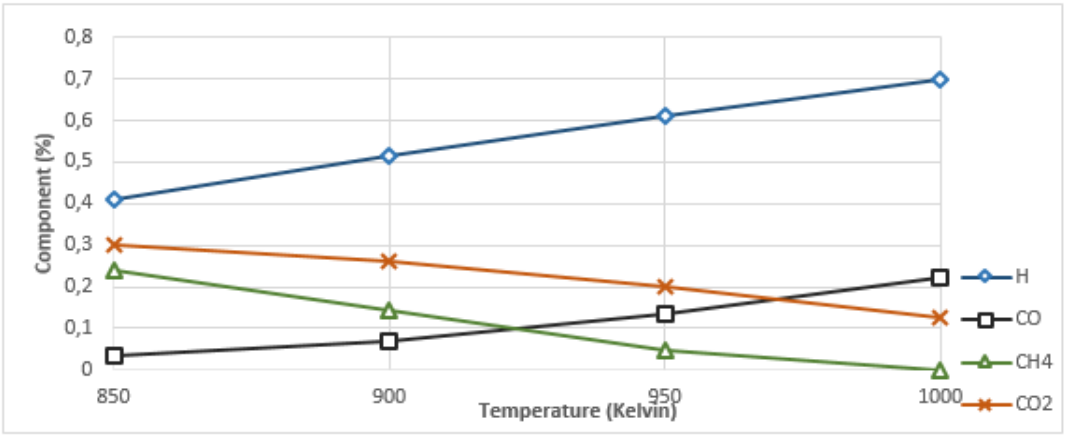

Figure 3. Temperature for S=0.2 % component replacement (P=1 atm).

Findings of Experimental Studies

Experimental studies were performed at atmospheric pressure and at constant steam/dry fuel at a 0.2 ratio. Due to the difficulties in temperature control of plasma, the average temperature values of the reactor were measured. The average temperature within the reactor is between 850-1000 K.

When considering the results obtained from experimental studies, probable fatty acids found in OMW suffered a thermochemical decomposition and carbon compounds turned into a hydrogen-rich gas plasma. The results are shown in Table 2 (1000 K).

The comparison of theoretical and experimental studies is shown in Table 3. The results of theoretical and experimental studies were obtained within the ratios of 1000 K and S value of 0,2.

In the theoretical studies while temperature was constant, with the increase of steam ratio, H_2/CO ratio has also been observed to increase. Increase of the temperature had similar effects on H_2 and CO. However, CH_4 and CO_2 concentration decreased.

The results from the comparison of theoretical and experimental studies are seen to be compatible. Other gases, apart from nitrogen, given in the results of the experimental study ethylene, propane, *etc*. are gases with combustion value and when comparing the calorific value, studies done with plasma technology are seen to be more efficient.

Theoretical and experimental studies have been carried out with this study and the possibility of energy recovery from Olive Mill Wastewater with high moisture content has been observed. Given the limited work done and available in this subject (24) this study has proven to be innovative and important.

Table 2. Experiment Results (1000 K),

	Experiment 1	Experiment 2	Experiment 3	Experiment 4	Experiment 5	Mean Value	StDev
Compound	(%v/v)	(%v/v)	(%v/v)	(%v/v)	(%v/v)	(%v/v)	
H_2	63.97	64.45	64.53	66.18	64.98	64.82	0.75
CO_2	7.81	13.1	10.56	10.03	6.82	9.66	2.20
CH_4	0.29	0.14	0.42	0.32	0.58	0.35	0.15
CO	1.34	1.86	1.57	1.49	2.18	1.68	0.29
Other	26.59	20.45	22.92	21.98	25.44	23.48	2.25

Table 3. Comparison of experimental and theoretical studies,

	Experimental Studies (1000 K)	Theoretical Studies (1000 K)
Compound	(%v/v)	(%v/v)
H_2	64.82	65.09
CO_2	9.66	12.75
CH_4	0.35	0.01
CO	1.68	22.4

ACKNOWLEDGMENTS

We would like to thank TKI institutions for their contributions to applied scientific studies. We would also like to thank Prof. Dr. Bekir Zuhtu Uysal for his scientific contributions.

REFERENCES

1. Şengül F, Özer A, Çatalkaya E, Oktav E, Evcil H, Çolak O, Sağer Y. Ebso projesi kapsamındaki zeytinyağı işletmeleri için durum tespiti, karasuyu karakterizasyonu, Karasu arıtılabilirlik çalışmaları ve sonuçlar. Dokuz Eylül Üniversitesi Mühendislik Fakültesi Çevre Mühendisliği Bölümü. 2013.

2. Acun T. Çapraz akışlı membran proseste zeytin karasuyun arıtımının incelenmesi. Atatürk Üniversitesi Fen Bilimleri Enstitüsü Yüksek Lisans Tezi. 2008. p. 1-10.

3. Kılıç M, Kaya G, Kestioğlu K. Kimyasal, biyolojik ve ileri arıtma yöntemleri ile zeytin karasuyunun arıtımına yönelik bir envanter çalışması. Uludağ Üniversitesi Mühendislik-Mimarlık Fakültesi Dergisi. 2009;14(2):185-187.

4. Oktav, E., Şengül, F. Zeytinyağı üretimi atıksularının distilasyon yöntemiyle arıtımı, SKKD. 2003;13(3).8-17.

5. El-Shafey, E.I., Correia, P.F.M., de Carvalho, J.M.R. An integrated process of olive mill wastewater treatment. Separation Science and Technology. 2007. p. 2841-2869.

6. Azzam, M.O.J., Al-Malah, K.I., Abu-Lail, N.I.. Dynamic post-treatment response of olive mill effluent wastewater using activated carbon. Journal of Environmental Science and Health Part A-Toxic/Hazardous Substances & Environmental Engineering. 2004;A39(1):269-280.

7. Israilides, C.J., Vlyssides M, V.N., Karvouni G. Olive oil wastewater treatment with the use of an electrolysis system. Bioresource Technology. 1999;61(2):163-170.

8. Oktav E, Özer A. Zeytinyağı Endüstrisi Atıksularının Özellikleri Ve Arıtım Alternatifleri, I. Zeytin Yağı Üretiminde Çevre Sorunları ve Çözümleri Uluslararası Çalıstayı Bildiriler Kitabı; 2002.

9. Niaounakis M, Halvadakis C. Olive processing waste management: literature review and patent survey. Elsevier, Amsterdam. 2006. p. 498.

10. Evcil, H. Pretreatment of olive oil mill wastewater. Master of Science Thesis, Graduate School of Natural and Applied Sciences, Environmental Science Program, Dokuz Eylül University. İzmir. 2005.

11. Ginos A, Manios T, Mantzavinos D. Treatment of olive mill effluents by coagulation–flocculation–h2o2 oxidation and effect on phytotoxicity. Journal of Hazardous Materials. 2006;B133:135-142.

12. Fadil K, Chahlaoui A, Ouahbi A, Zaida A, Borja R. Aerobic biodegradation and detoxification of wastewaters from the olive oil ındustry. International Biodeterioration and Biodegradation. 2003;51:37-41.

13. Benitez F.J, Beltran-Heredia J, Torregrosa J, Acero J.L. treatment of olive mill wastewaters by ozonation, aerobic degradation and the combination of both treatments. Journal of Chemical Technology and Biotechnology; 1999;74:639-646.

14. Azbar N, Tutuk F, Keskin T. Biodegradation performance of an anaerobic hybrid reactor treating olive mill effluent under various organic loading rates. International Biodeterioration & Biodegradation; 2009;63(6):690-698.

15. Beccari M, Majone M, Riccardi C, Savarese F, Torrisi L. Integrated treatment of olive oil mill effluents: effect of chemical and physical pretreatment on anaerobic treatability. Wat. Sci. Tech. 2009;40(1):347- 355.

16. Bressan M, Liberatore L, Dalessandro N, Tonucci L, Belli C, Ranali G. Improved combined chemical and biological treatments of olive oil mill wastewaters. Journal of Agricultural and Food Chemistry. 2004;52:1228-1233.

17. Khoufi S, Feki F, Aloui F, Sayadi S. Pilot-plant results of the electro-fenton treatment of olive mill wastewaters followed by anaerobic digestion. Water Science and Technology. 2007;55(12):259-265.

18. Khoufi S, Alouni F, Sayadi S. Treatment of olive oil mill wastewater by combined process electro-fenton reaction and anaerobic digestion. Water Research. 2006;40:2007-2016.

19. Uğurlu M, Kula İ, Gürses A. Removal of some organic compounds and color from olive mill wastewater by electrocoagulation. Fresenius Environmental Bulletin; 2006;15(10):1256-1265.

20. Adhoum N, Monser L. Decolourization and removal of phenolic compounds from olive mill waste water by electrocoagulation. Chemical Engineering and Processing. 2004;43:128-1287.

21. İnan H, Şimşek H, Karpuzcu M, Dimoglo A. Elektrokimyasal yöntemler ile zeytinyağı endüstrisi karasuyunun arıtılabilirliği, 1. Zeytinyağı üretiminde çevre sorunları ve çözümleri çalıştayı, Zeytinli, Edremit-Balıkesir, Bildiriler Kitabı; 2002. p. 97-107.

22. Tezcan Ü, Uğur S, Koparal A.S, Bakır Öğütveren Ü. Electrocoagulation of olive mill wastewaters. Separation and Purification Technology. 2006;52:136-141.

23. Tezcan Ü, Altay Ü, Koparal A.S, Bakir Öğütveren Ü. Complete treatment of olive mill wastewaters by electro-oxidation. Chemical Engineering Journal. 2008;139:445-452.

24. Kıpçak E, Akgün M. Catalytic gasification of olive mill wastewater as a biomass source under supercritical conditions. World Academy of Science, Engineering and Technology International Journal of Chemical, Molecular, Nuclear, Materials and Metallurgical Engineering. 2013. Vol:7. No:9

25. Ibrahimoglu B, Vural E.S, Yürek Ş, Demirel O. Plazma kömür gazlaştırma. Dünya Enerji Konseyi Türk Milli Komitesi, Türkiye 12. Enerji Kongresi. 2012.

26. İbrahimoğlu B, Yürek Ş, Demirel O. Plazma yöntemi ile kömürün gazlaştırılması. IV. Ulusal Hidrojen Enerjisi Kongresi ve Sergisi. 2009 Ekim.

27. Fridman A. Plasma chemistry. Cambridge University Press. 2008. p. 1-89.

28. Shin D. H, Hong Y. C, Lee S. J, Kim Y. J, Cho C. H, Ma S. H, Chun S. M and fri. A pure steam microwave plasma torch: gasification of powdered coal in the plasma. Surface & Coatings Technology. 2012;17552:4-7.

29. Janajreh I, Raza S.S, Valmundsson A.S. Plasma gasification process: modeling, simulation and comparison with conventional air gasification. Energy Conversion and Management. 2013;65:801–809.

30. Heberlein J, Murphy A.B. topıcal review thermal plasma waste treatment. J. Phys. D: Appl. Phys. 2008;41.053001:20

31. Gomez E, Rani D.A, Cheeseman C.R, Deegan D, Wise M, Boccaccini A.R. Thermal plasma technology for the treatment of wastes: a critical review. Journal of Hazardous Materials. 2009;161:614–626.

32. Balgaranova J. Plasma chemical gasification of sewage sludge. Waste Management & Research. 2003.

33. Hrabovsky M. Plasma aided gasification of biomass, organic waste and plastics. Belfast Northern Ireland UK, 30th ICPIG. 2011 August.

34. Değertekin Ö, Hayalioğlu S, Ülker M. Optimum design of nonlinear steel space frames via tabu search method. Journal of Engineering and Natural Sciences. 2006.

35. El Hajjouji H, Bailly J.R, Winterton P, Merlina G, Revel J.C, Hafidi M. Chemical and spectroscopic analysis of olive mill waste water during a biological treatment. Bioresource Technology; 2008;99:4958–4965.

Türkçe Öz ve Anahtar Kelimeler

GASIFICATION OF OLIVE MILL WASTEWATER WITH WATER PLASMA

Esra Yıldırım[1,*], Vuslat İbrahimoğlu[1], Salih Karasarı[1], Ahmet Zafer Özek[1]

Öz: Zeytinyağı üretimi sonrasında zeytin karasuyu açığa çıkmaktadır. Zeytin karasuyu; organik madde, askıda katı madde, yağ ve gres içeriği oldukça yüksek olan ve fenolik bileşikler sebebiyle çevre için önemli derecede tehlike oluşturan bir atık su çeşididir. İçerisinde bulunan yüksek kirlilik oranı ile hem bertarafı gerekmekte hemde içerisindeki organik bileşikler (yağ asitleri vs.), zeytin karasuyundan enerji elde edilebilmesine imkan tanımaktadır. Bu çalışmada, hammadde olarak zeytin karasuyu kullanılarak su plazması ile gazlaştırma yapılmıştır. Elde edilebilecek ideal plazma gazı kompozisyonu teorik olarak incelenmiş ve deneysel çalışmalar yapılarak elde edilen sonuçlar karşılaştırılmıştır. Bu çalışmadaki amaç, teorik ile deneysel çalışmaların karşılaştırılarak plazmanın tanımlanmayan etkisinin belirlenebilmesidir. Teorik çalışmalarda gazlaştırma sırasında oluşan dört temel gazlaştırma reaksiyonlarından yararlanılmış, bileşen denkliği kurulmuş ve denge dönüşümleri ile MATLAB programı kullanılarak gazlaştırma prosesi simüle edilmiştir. 850-1000 K arasında farklı sıcaklıklarda, 0,05-0,7 S (su buharı/kuru yakıt) oranlarında çalışılarak ulaşılabilecek ideal sentez gazı kompozisyonu belirlenmiştir. Deneysel çalışmalarda düşük kütlesel debi aralığına sahip karasu beslenmesi ile plazma gazlaştırma deneyleri yapılmış ve gaz bileşiminin incelenmesi amacıyla gaz kromatografisinde analizi yaptırılmıştır. Deneysel sonuçlar ile teorik hesaplamalar karşılaştırıldığında sonuçların uyumlu olduğu, gazlaştırma sonucu aynı bileşen oranlarına plazma gazlaştırma ile daha düşük sıcaklıklarda ulaşıldığı görülmüştür. Zeytin karasuyunun plazma teknolojisi ile gazlaştırılması hakkında bir literatür bulunmadığından bu makale enerji geri kazanımı için atık geri dönüşüm teknolojisinin incelenmesinde son derece önemli bir rol oynamaktadır.

Anahtar kelimeler: Plazma gazlaştırma; sentez gazı, zeytin karasu

Sunulma: 20 Eylül 2016**. Düzeltme:** 31 Aralık 2016**. Kabul:** 16 Şubat 2017**.**

SYNTHESIS AND CHARACTERIZATION OF COPPER HYDROXYNITRATE AND COPPER OXIDE BY HYDROTHERMAL METHOD

(This article was initially submitted to National Chemical Engineering Congress and reviewed by JOTCSB editorial staff).

Eda Keleş Güner[1] and Abdulkadir Özer[2]

[1]Department of Civil Defense and Firefighting, Üzümlü Vocational School, Erzincan University, 24150 Erzincan,Turkey
[2]Department of Chemical Engineering, Atatürk University, 25240 Erzurum, Turkey
eda.guner@erzincan.edu.tr; kadirozer@atauni.edu.tr

Abstract: In this study, copper hydroxynitrate ($Cu_2(OH)_3NO_3$) and copper oxide (CuO) were synthesized by using the reactants $Cu(NO_3)_2.3H_2O$ and $Na_2B_4O_7.10H_2O$ with the addition of SB12 surfactant by hydrothermal method. The prepared samples were characterized by X-ray diffraction (XRD), Thermal gravimetric analysis (TGA), Fourier Transform Infrared (FTIR) spectra, and scanning electron microscopy (SEM) techniques. According to X-ray diffraction results, copper hydroxynitrate was obtained by borax hydrolysis. Then, the monoclinic phase of copper oxide by calcination of $Cu_2(OH)_3NO_3$ at 400 ^oC was obtained. TG-DTA analysis showed single stage weight loss. The weight loss of 33.27% at 350°C represents a simultaneous dissociation of HNO_3 and H_2O. The FTIR analysis indicates the samples have O-H, O-NO_2, N-O and Cu-OH group bands. The SEM results reveal that the copper hydroxynitrate have micrometer-size elongated hexagonal plates.

Keywords: Hydrothermal Method, borax, copper nitrate, copper hydroxynitrate, copper oxide.

Submitted: October 25, 2016. **Revised:** January 03, 2017. **Accepted:** February 06, 2017.

Cite this: Keleş Güner E, Özer A. SYNTHESIS AND CHARACTERIZATION OF COPPER HYDROXYNITRATE AND COPPER OXIDE BY HYDROTHERMAL METHOD. JOTCSB. 2017;1(1):183–92.

Corresponding authors. E-mail: eda.guner@erzincan.edu.tr; kadirozer@atauni.edu.tr.

INTRODUCTION

Basic copper salts have become suitable precursor applicants for synthesis of unusual CuO nanostructures because of their unique and well-known layered structures. For example, $Cu_2(OH)_3NO_3$, $Cu_2Cl(OH)_3$, $Cu_2(OH)_2CO_3$, $Cu_4SO_4(OH)_6$, and $Cu_7Cl_4(OH)_{10}{\cdot}H_2O$ have been broadly used to prepare $Cu(OH)_2$ and CuO nanostructures with new morphologies (1). Copper-based hydroxynitrate (CuHN) with composition $Cu_2(OH)_3NO_3$ crystallizes in orthorhombic and monoclinic crystal systems (2). The crystal structure of monoclinic copper hydroxynitrate [$Cu_2(OH)_3NO_3$ or $Cu(OH)_{1.5}(NO_3)_{0.5}$] is comprised of copper hydroxide layers in which some of the hydroxyl ions (x = 0.5) are replaced by the nitrate ions and are directly coordinated to the sheets. Copper occupies two different distorted octahedral sites within the layer and the structure of copper hydroxynitrate ($Cu_2(OH)_3NO_3$) is shown in Figure 1.

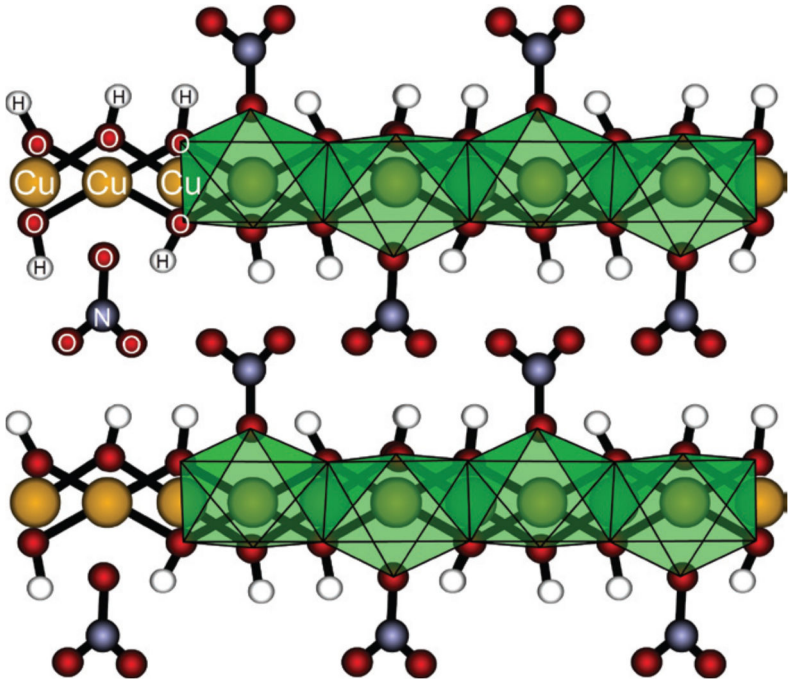

Figure 1. Schematic representation of the structure of copper hydroxynitrate, ($Cu_2(OH)_3NO_3$)(3).

Owing to such an extraordinary structure, copper hydroxyl nitrate has different applications, particularly for the swelling of vehicle airbags, low-ash solid propellants, ion exchangers and ignition compositions (4).

A diversity of inorganic and organic substances such as carbon materials, pure and doped metal oxides/hydroxides, and polymers have been successfully plated onto various substrates for particular aims (5). Metal oxide nanoparticles are crucial in inorganic material investigation owing to their numerous applications in catalysis, energy technology,

data storage and coating fields. One of them, namely copper oxide (CuO), gained increasing attention for its eventual practices in many areas (6). Copper oxide (CuO) is one of potential p-type semiconductors and gains considerable attention due to its excellent physical, electrical, optical and magnetic properties (7). CuO is widely used in gas sensors, photovoltaic cells, electrochemical cells, magnetic storage media, light emitters, thermoelectric materials, heat transfer nanofluids, and for catalysis (8).

There are several methods used to synthesize $Cu_2(OH)_3NO_3$ and copper oxide (CuO) such as chemical precipitation, ultrasound assisted synthesis, polyol mediated synthesis, thermal decomposition and hydrothermal synthesis methods, and so on (1, 3, 6, 9, 10). In the literature, (3) have prepared mixed metal hydroxynitrate such as $Cu_2(OH)_3$ (NO_3 using $Cu(NO_3)_2{\cdot}6H_2O$, and urea as starting material, (9) studied ($Cu(NO_3)_2.2.5H_2O$) and ($Na_2B_4O_7.10H_2O$) as reactants and Span 60 as surfactant by precipitation method, (10) prepared uniform $Cu_2(NO_3)(OH)_3$ nanoparticles using $Cu(NO_3)_2.2H_2O$ and $NaHCO_3$ by polyol-mediated method,

In this study, copper hydroxynitrate ($Cu_2(OH)_3NO_3$) and copper oxide (CuO) were prepared from $Cu(NO_3)_2.3H_2O$ and $Na_2B_4O_7.10H_2O$ as reactants with the addition of SB12 as the surfactant by hydrothermal method. The obtained particles were characterized by XRD, TGA, FTIR, and SEM techniques.

MATERIAL AND METHOD

Materials

Commercially available $Na_2B_4O_7{\cdot}10H_2O$ (borax, Merck, 99%) and copper(II) nitrate trihydrate ($Cu(NO_3)_2.3H_2O$; Merck, 99.5%), 3-(N,N-dimethyldodecylammonio) propanesulfonate (SB12;Fluka, 97%) deionized water and absolute alcohol were used in the experiments. All of the chemicals were of analytical grade.

Synthesis

The experimental procedure was as follows: 50 mL 0.1 M borax, 40 mL 0.5 M $Cu(NO_3)_2$ solution and required amount of surfactant zwitterionic SB12 in between its critical micellar concentration (CMC) range were mixed completely for 10 minutes at 60 °C. The critical micellar concentration of the surfactant (SB12) was $1.2x10^{-3}$ M (11). The solution was transferred to a 100 mL Teflon-lined stainless steel autoclave, stamped, and kept at 180 °C for 24 h without stirring and then was allowed inherently to cool to room temperature. The obtained sample was filtered, washed with deionized water and absolute alcohol, then dried at 80 °C for 8h. The sample was calcined at 400 °C for 2h.

Characterization

The morphology and structure of the synthesized products were studied by X-ray diffraction (XRD), Fourier transform infrared (FTIR), thermal gravimetric analysis (TGA/DTA) and scanning electron microscopy (SEM) techniques. Phase compositions of powder samples before and after calcination were characterized by X-ray diffraction (XRD, Rigaku advance powder X-ray diffractometer, λ=1.54 A°).Thermal gravimetric analysis and differential thermal analyses (TGA–DTA) curves were simultaneously obtained on a NETZSCH STA 409 PC Luxx at a heating rate of 10 °C min^{-1} under nitrogen atmosphere in the temperature range from 30 to 1000 °C using Al_2O_3 as the standard material. Fourier transform infrared (FTIR) spectra were recorded in the 500–4000 cm^{-1} range, using Perkin–Elmer Spectrum One FTIR spectrometer. The structure and morphology of the samples were observed by a scanning electron microscope (SEM, Zeiss Ls-10).

RESULTS AND DISCUSSION

Using $Cu(NO_3)_2.3H_2O$ and $Na_2B_4O_7.10H_2O$ as reactants with the addition of SB12 as the surfactant at 180ºC by hydrothermal method was synthesized copper hydroxynitrate ($Cu_2(OH)_3NO_3$). Powder XRD was very important in the identification of the phase formation. Powder X-ray diffraction patterns of both copper hydroxide nitrate and sample obtained by its calcination at 400 °C are shown in Figure 1, section (a) of which shows the powder X-ray diffraction patterns of copper hydroxynitrate obtained by borax hydrolysis. In the XRD patterns of ($Cu_2(OH)_3NO_3$), successive reflections, up to at least the third order, indicate the lamellar structure and could be indexed to monoclinic crystal system space using the JCPDS No. 75-1779 file.

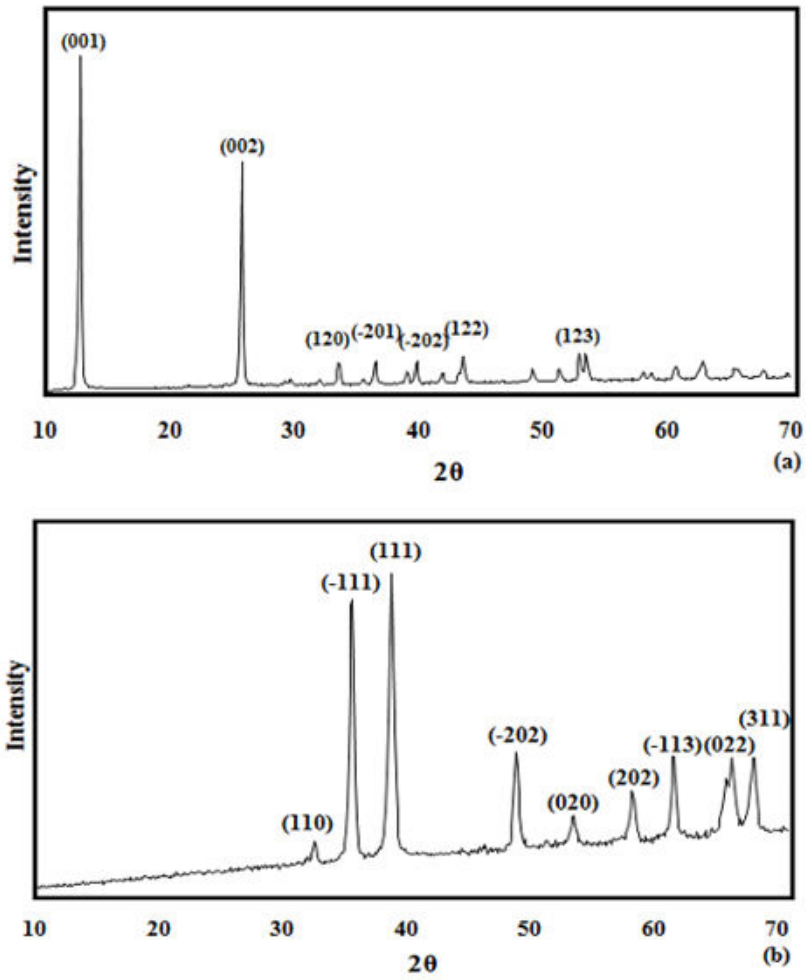

Figure 1. X-Ray diffraction of copper hydroxynitrate (a) raw and (b) calcined sample.

Fig. 1(b) shows the powder X-ray diffraction patterns of sample obtained by calcination at 400 °C of $Cu_2(OH)_3NO_3$. As can be seen from Figure 1(b), the decomposed product could be indexed to monoclinic phase of copper oxide (JCPDS No. 44-0706).

Thermal decomposition of layered hydroxynitrate follows dehydration, denitration, and disruption of layered framework under atmospheric conditions. The elimination of hydroxyl and nitrate groups from the precursors has great influence on the crystallinity of metal oxides, and new intermediate phase might also form during the disruption of the original structure.

TGA/DTA curves of $Cu_2(OH)_3NO_3$ shown in Figure 2. The total weight loss in the whole temperature range of 30–1000 °C is 33.26%, which is in good agreement with the theoretical value of $Cu_2(OH)_3NO_3$(33.6%). Meanwhile, most of the weight loss occurs within a narrow temperature range of 230–280 °C.

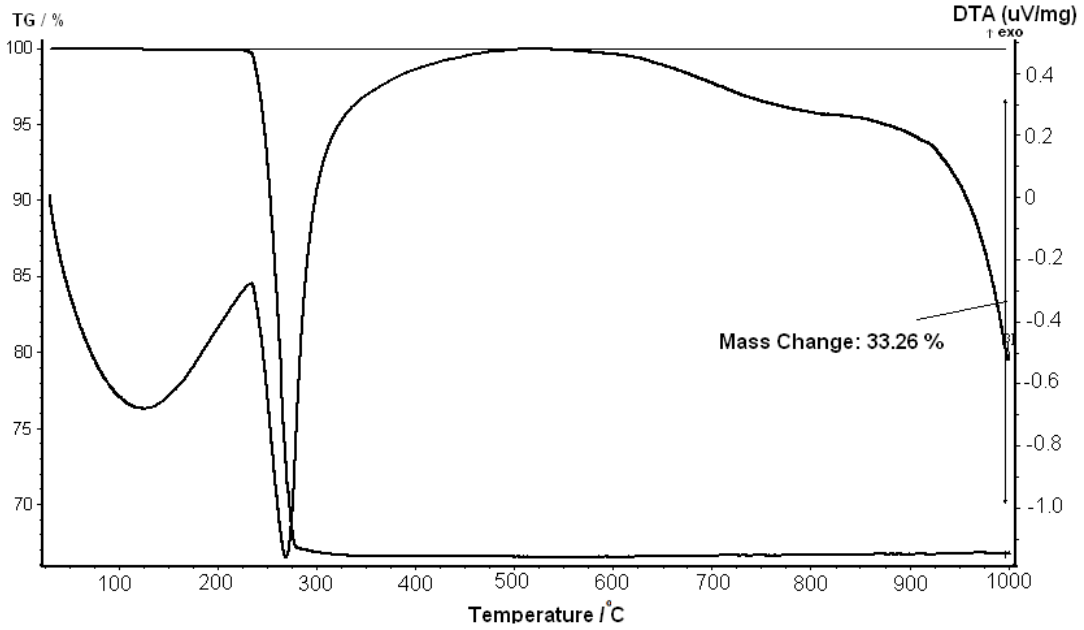

Figure 2. TGA/DTA curves of copper hydroxynitrate.

Thermal decomposition of copper hydroxynitrate occurs at single step in which dehydroxylation and decomposition of the nitrate in the interlayer space take place simultaneously leading to the destruction of the layered structure (Figure 2).

The copper hydroxynitrate undergoes decomposition in a single step producing CuO according to the equation:

$$Cu_2(OH)_3NO_3 \rightarrow 2CuO + HNO_3 + H_2O \qquad \text{(Eq. 1)}$$

It was shown that the results of TG/DTA curves was in agreement with the results obtained from the XRD analysis.

Fourier transform infrared (FTIR) spectroscopy analysis was carried out to identify the functional groups. FTIR results are given in Fig. 3.The peaks at 3539 and 3412 cm^{-1} belong to isolated and hydrogen bonded OH stretching peaks. The peaks at 1420 and 1347 cm^{-1} are asymmetric and symmetric stretching peaks of O-NO_2 respectively. The peak at 1046 cm^{-1} is connected to N-O stretching pulsation of monodentate O-NO groups. The peaks at 874, 771 and 665 $cm^{-1}$are due to bending vibrations of Cu-OH groups with different hydrogen bonds.

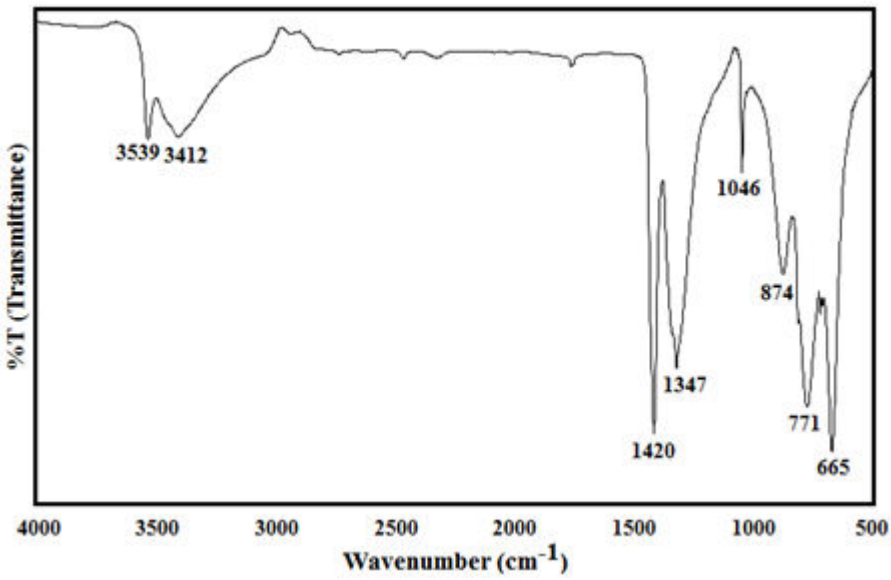

Figure 3. FTIR spectrum of copper hydroxynitrate.

Fig. 4 and 5 shows the scanning electron micrographs before and after calcination of obtained samples. It can be seen from Figure 4, copper hydroxyhydrate ($Cu_2(OH)_3NO_3$) exhibits well-defined and separated tabular particles with the micrometer-size elongated hexagonal plates. Their size was not accurately determined butSEM micrographs show that a 10 mm size is easily attained. The particles CuO obtained by calcination at 400 °C of $Cu_2(OH)_3NO_3$ are characterized by relatively different morphologies formed by disruption of hexagonal structure, which are displayed in the SEM micrographs in Fig. 5.

CONCLUSIONS

From the results that have been described above, some guidelines can be proposed concerning the production of copper hydroxynitrate ($Cu_2(OH)_3NO_3$) by a hydrothermal method starting from $Cu(NO_3)_2.3H_2O$ and $Na_2B_4O_7.10H_2O$ solutions.According to TG-DTA analysis, the synthesized products are seen that only a single sharp decomposition step, which is in accordance with a simultaneous dissociation of HNO_3 and H_2O. The FTIR analysis shows the samples have O-H, O-NO_2, N-O and Cu-OH group bands. In hydrothermal method at 180 °C synthesized the monoclinic copper hydroxynitrate ($Cu_2(OH)_3NO_3$)(gerhardite) hexagonal plate structure. On the other hand, working with the borax as a source of hydroxyl ions allows a slow and better controlled formation of the precipitate.

Figure 4. SEM image of copper hydroxynitrate.

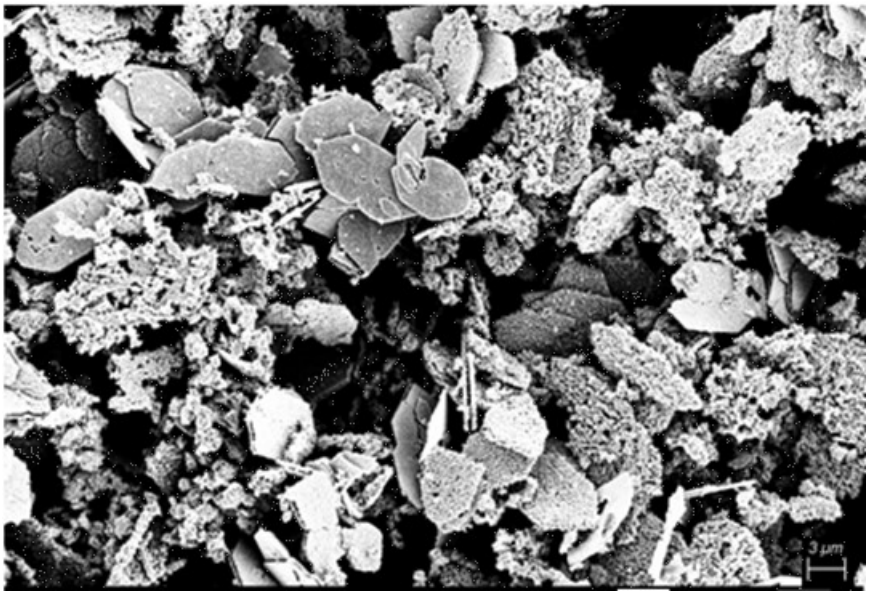

Figure 5. SEM image of copper oxide.

The present work has supplied an elementary and fast method to the micrometer-size well-defined elongated hexagonal plates of copper hydroxynitrate, which can be further processed to CuO structures. Particularly, the conversion of copper hydroxynitrate into CuO, which possess much more applications in vast technological fields, has also been demonstrated.

REFERENCES

1. Ba N, Zhu L, Li H, Zhang G, Li J, Sun J,.3D rod-like copper oxide with nanowire hierarchical structure: Ultrasound assisted synthesis from $Cu_2(OH)_3NO_3$ precursor, optical properties and formation mechanism. Solid State Sciences, 2016 (53):23–29.

2. Bovio B, Locchi S, Crystal structure of the orthorhombic basic copper nitrate, $Cu_2(OH)_3NO_3$.Journal of Crystallographic and Spectroscopic Research, 1982 (12);6:507–517.

3. Ramesh TN, Madhu L, Thermal Decomposition Studies of Layered MetalHydroxynitrates (Metal: Cu, Zn, Cu/Co, and Zn/Co). International Journal of Inorganic Chemistry,2015(11).

4. Anandan S, Wu JJ, Ashokkumar M, Sonochemical Synthesis of Layered Copper Hydroxy Nitrate Nanosheets.*ChemPhysChem.*, 2015 (16):3389–3391.

5. Ghotbi MY, Rahmati Z, Nanostructured copper and copper oxide thin films fabricated by hydrothermal treatment of copper hydroxide nitrate.Materials & Design, 2015(85):719–723.

6. Bozkurt G, Bayrakçeken A, Özer AK, Synthesis and characterization of CuO at nanoscale.Applied Surface Science, 2014(318): 244–250.

7. Phiwdang K, Suphankija S, Mekprasarta W, Pecharapaa W, Synthesis of CuO Nanoparticles by Precipitation Method Using Different Precursors. Energy Procedia, 2013(34): 740-745.

8. Dagher S, Haik Y, Ayesh AI, Tit N, Synthesis and optical properties of colloidal CuO nanoparticles. Journal of Luminescence, 2014(151): 149-154.

9. Alp B, Atakul Savrık S, Balkose D.Preparation and Characterization of Copper Borates as Lubricant Additives.Journal of Materials Science and Engineering B4, 2014 (4): 95-108.

10. Wolf S, Feldmann C, $Cu_2X(OH)_3$ ($X = Cl^-$, NO_3^-): Synthesis of Nanoparticles and its applicationfor room temperature deposition/printing of conductive copper thin-films. J. Mater. Chem, 2010 (20): 7694–7699.

11. Balouch, A, Enhancement of the analytical performance of spectral methods for the determination of metal cations, anions, and neutral organics via utilization of organized surfactant media, 2009. Ph. D. Thesis, Center of Excellence in Analytical Chemistry, University of Sindh, Jamshoro, Pakistan.

Türkçe Öz ve Anahtar Kelimeler

HİDROTERMAL YÖNTEM İLE BAKIR HİDROKSİ NİTRATIN SENTEZ VE KARAKTERİZASYONU

Eda Keleş Güner[1] ve Abdulkadir Özer[2]

Öz: Yapılan çalışmada, hidrotermal yöntemle bakır nitrat $Cu(NO_3)_2.3H_2O$ ve boraks ($Na_2B_4O_7.10H_2O$) başlangıç maddeleri ile SB12 surfaktanı kullanılarak bakır hidroksi nitrat ($Cu_2(OH)_3NO_3$) ve bakır oksit (CuO) sentezlenmiş ve elde edilen ürünler XRD, FTIR, TG ve SEM teknikleri ile karakterize edilmiştir. XRD sonuçlarına göre, 180 ºC'de hidrotermal yöntemle elde edilen örneklerin monoklinik bakır hidroksi nitrat ($Cu_2(OH)_3NO_3$) oluştuğu ve 400ºC'de kalsinasyonu sonucunda tamamen bakır oksit (CuO)'e dönüştüğü görülmektedir. Elde edilen bakır hidroksi nitratların TG analiz sonuçlarına bakıldığında sentezlenen ürünün HNO_3 ve H_2O'un eş zamanlı ayrışmasından meydana geldiği görülmektedir. Sentezlenen ürünün FTIR analizlerinde O-H, O-NO_2, N-O ve Cu-OH gruplarının bantları tespit edilmiştir. SEM analizi sonuçlarından, SB12 surfaktan ortamında altıgen plaka şeklinde nano/mikro yapıda partiküllerden oluştuğu görülmektedir.

Anahtar kelimeler: Hidrotermal yöntem; boraks; bakır nitrat; bakır hidroksi nitrat; bakır oksit.

Sunulma: 25 Ekim 2016. **Düzenleme:** 03 Ocak 2017. **Kabul:** 06 Şubat 2017.